

Quantum Dynamics of an Ion in a Quantum Gas

An Open System Approach

Dissertation

zur Erlangung des Doktorgrades

an der Fakultät für Mathematik, Informatik

und Naturwissenschaften

Fachbereich Physik

der Universität Hamburg

vorgelegt von

Lorenzo Oghittu

Hamburg

2024

Gutachter der Dissertation:

Prof. Dr. Ludwig Mathey
Dr. Juliette Simonet

Zusammensetzung der Prüfungskommission:

Prof. Dr. Michael Potthoff
Prof. Dr. Ludwig Mathey
Dr. Juliette Simonet
Prof. Dr. Henning Moritz
Prof. Dr. Dieter Jaksch

Vorsitzender der Prüfungskommission:

Prof. Dr. Michael Potthoff

Datum der Disputation:

31.05.2024

Vorsitzender des Fach-Promotionsausschusses PHYSIK:

Prof. Dr. Markus Drescher

Leiter des Fachbereichs PHYSIK:

Prof. Dr. Wolfgang J. Parak

Dekan der Fakultät MIN:

Prof. Dr.-Ing Norbert Ritter

Abstract

We present an open system approach to the study of the quantum dynamics of a single ion immersed in a bath of ultracold atoms. On this purpose, we derive a master equation in the limit of weak-coupling and Lamb-Dicke approximation for the reduced density matrix of the ion, which allows us to capture the dependence of the ion's temperature, position and velocity as a function of the parameters involved in the description. This approach is applied to different scenarios that are relevant for experiments involving ionic impurities in ultracold Fermi or Bose gases.

The master equation is first derived for a Paul-trapped ion, whereas the bath is represented by either a Bose gas below or above the critical temperature of condensation, or by a spin-polarized Fermi gas. Our numerical results show that the ion temperature averaged over the micromotion induced by the Paul trap saturates to a final value, which depends on the temperature of the bath and on the atom-ion scattering length. The density of the bath, on the other hand, only weakly affects the final temperature of the ion while strongly influencing the saturation time. As expected, the latter is shorter for a higher density. Interestingly, we find that for temperatures of the gas lower than the Fermi temperature, the gas statistics sensibly affects the final temperature of the ion. In particular, a Fermi bath allows the ion to reach lower temperatures.

A similar approach is then applied to the case of an untrapped ion moving inside a Bose-Einstein condensate with an initial finite momentum. We observe that the ion temperature is reduced by several orders of magnitude in a time scale on the order of microsecond for a $^{87}\text{Rb}^+$ ion in a ^{87}Rb Bose-Einstein condensate with a density between 10^{13} cm^{-3} and 10^{14} cm^{-3} . The aforementioned behavior is noticeably affected by the density of the condensate, with a higher density corresponding to faster cooling. The initial momentum of the ion, on the contrary, only weakly affects this dynamics. In the same time scale in which the cooling is observed, the ion velocity is also strongly reduced, making the position of the ion converge to a final value. Therefore, our findings predict the cooling and pinning of the ion due to the interaction with the Bose-Einstein condensate.

Furthermore, we consider the possibility of using an ionic impurity as a probe for the temperature of a Fermi gas. According to the thermometric protocol proposed by M. T. Mitchison *et al.* [Phys. Rev. Lett. **125**, 080402 (2020)] for a neutral impurity, the ion is considered as a two-level spin particle undergoing pure dephasing due to the coupling with the bath. By means of the theory of quantum estimation, we study how the performance of the thermometric measurement is affected by some of the parameters of the system, such as the temperature of the gas, the probing time and the atom-ion scattering length. Comparing our results with those obtained with a neutral impurity, we find that the long-range tail of the atom-ion potential has a profound impact on the thermometric performance: for certain values of the interaction parameter, it strongly enhances the sensitivity of the probe, making the ion a better sensor for the temperature of the Fermi gas.

Zusammenfassung

Wir stellen einen offenen Systemansatz vor, um die Quantendynamik eines einzelnen Ions zu untersuchen, das in ein Bad aus ultrakalten Atomen eingetaucht ist. Hierzu leiten wir eine Mastergleichung im Grenzfall der schwachen Kopplung und unter Anwendung der Lamb-Dicke-Näherung für die reduzierte Dichtematrix des Ions her. Diese Gleichung ermöglicht es uns, die Abhängigkeit der Temperatur, Position und Geschwindigkeit des Ions von den an der Beschreibung beteiligten Parametern zu erfassen. Unser Ansatz wird auf verschiedene Szenarien angewendet, die für Experimente mit ionischen Verunreinigungen in ultrakalten Fermi- oder Bose-Gasen relevant sind.

Die Mastergleichung wird zunächst für ein in einer Paul-Falle gefangenes Ion hergeleitet, wobei das Bad entweder durch ein Bose-Gas unterhalb oder oberhalb der kritischen Kondensationstemperatur oder durch ein spinpolarisiertes Fermi-Gas repräsentiert wird. Unsere numerischen Ergebnisse zeigen, dass die über die durch die Paul-Falle induzierte Mikrobewegung gemittelte Iontemperatur einen Grenzwert erreicht, der von der Temperatur des Bades und der Atom-Ionen-Streulänge abhängt. Die Dichte des Bades hat hingegen nur einen geringen Einfluss auf die Endtemperatur des Ions und beeinflusst die Sättigungszeit. Letzteres ist erwartungsgemäß bei höherer Dichte kürzer. Interessanterweise stellen wir fest, dass bei Temperaturen des Gases, die niedriger als die Fermi-Temperatur sind, die Statistik des Gases einen spürbaren Einfluss auf die Endtemperatur des Ions hat. Insbesondere ermöglicht ein Fermi-Bad, dass das Ion niedrigere Temperaturen erreicht.

Ein ähnlicher Ansatz wird dann auf ein nicht gefangenes Ion, das sich mit einem anfänglichen endlichen Impuls in einem Bose-Einstein-Kondensat bewegt. Wir beobachten, dass die Iontemperatur für ein $^{87}\text{Rb}^+$ -Ion in einem ^{87}Rb -Bose-Einstein-Kondensat mit einer Dichte im Bereich von 10^{13} cm^{-3} bis 10^{14} cm^{-3} auf einer Zeitskala von Mikrosekunden um mehrere Größenordnungen reduziert wird. Dieses Verhalten wird maßgeblich durch die Dichte des Kondensats beeinflusst, wobei eine höhere Dichte einer schnelleren Abkühlung entspricht. Der anfängliche Impuls des Ions beeinflusst diese Dynamik hingegen nur geringfügig. Im gleichen Zeitrahmen der Abkühlung wird auch die Ionengeschwindigkeit stark reduziert, wodurch sich die Position des Ions einem Grenzwert annähert. Daher prognostizieren unsere Ergebnisse die Abkühlung und Fixierung des Ions aufgrund der Wechselwirkung mit dem Bose-Einstein-Kondensat.

Darüber hinaus erwägen wir die Möglichkeit, eine Verunreinigung in Form eines Ions als Sonde für die Temperatur eines Fermi-Gases zu verwenden. Gemäß dem von M. T. Mitchison *et al.* [Phys. Rev. Lett. **125**, 080402 (2020)] vorgeschlagenen thermometrischen Protokoll wird das Ion als 2-Niveau-Spinteilchen betrachtet, das aufgrund der Kopplung mit dem Bad einer reinen Dephasierung unterliegt. Mithilfe der Theorie der Quantenabschätzung untersuchen wir, wie die Leistung der thermometrischen Messung durch einige Parameter des Systems beeinflusst wird, wie zum Beispiel die Temperatur des Gases, die Interaktionszeit und die Atom-Ionen-Streulänge. Im Vergleich unserer Ergebnisse mit jenen, die mit einer neutralen Verunreinigung erzielt wurden, stellen wir fest, dass der weitreichende Schwanz des Atom-Ionen-Potentials einen tiefgreifenden Einfluss auf das thermometrische Ergebnis hat: Bei bestimmten Werten des Interaktionsparameters erhöht er die Empfindlichkeit der Sonde erheblich. Dadurch wird das Ion zu einem präziseren Sensor für die Temperatur des Fermi-Gases.

Acknowledgments

I would like to express my deepest gratitude to all those who have accompanied me during the last years, providing scientific or emotional guidance.

A first thanks goes to my supervisor, Ludwig Mathey, and my co-supervisors, Antonio Negretti and Henning Moritz. The enlightening discussions and the precious advice they provided have been essential landmarks throughout my doctoral studies.

Next, I would like to thank René Gerritsma, Juliette Simonet and Philipp Wessels-Staarman for our fruitful collaboration. Working together was a great pleasure and a wonderful opportunity.

I am grateful to my colleagues and to all the people I met at the ZOQ, who have enriched my journey and made it truly memorable.

Finally, a huge thanks goes to family and friends for their unconditional support, which has been a constant source of strength and encouragement.

Contents

Preface	1
Introduction to atom-ion systems	3
1 Preliminary notions	5
1.1 Two-body properties of atom-ion systems	6
1.1.1 Atom-ion potential	6
1.1.2 Scattering properties	8
1.1.3 Regularized potential	12
1.2 Single ion in a Paul trap	14
1.2.1 Classical equations	14
1.2.2 Quantum description	16
1.2.3 Excess micromotion	18
2 Theoretical treatment	21
2.1 Master equation for a single ion in a quantum gas	22
2.1.1 Redfield equation	22
2.1.2 Hamiltonian description	24
2.1.3 Atom-ion master equation	27
2.1.4 Solution strategies	31
2.2 Temperature estimation with a two-level ion	33
2.2.1 Decoherence dynamics	33
2.2.2 Quantum Cramer-Rao bound	35
2.2.3 Thermometric protocol	36
3 Main results of author's publications	39
3.1 [L1] – Dynamics of a trapped ion in a quantum gas: effects of particle statistics	40
3.2 [L2] – Quantum-limited thermometry of a Fermi gas with a charged spin particle	43
3.3 [L3] – Cooling dynamics of a free ion in a Bose-Einstein condensate	46
Conclusions and outlook	51
Publications	55
Bibliography	111

Preface

This cumulative dissertation is based on the following publications, which will be referred with the initial "L" followed by their corresponding number in order to distinguish them from the other citations.

Author's publications

- [L1] Lorenzo Oghittu, Melf Johannsen, Antonio Negretti, and Rene Gerritsma. Dynamics of a trapped ion in a quantum gas: Effects of particle statistics. *Phys. Rev. A*, 104:053314, Nov 2021.
- [L2] Lorenzo Oghittu and Antonio Negretti. Quantum-limited thermometry of a Fermi gas with a charged spin particle. *Phys. Rev. Res.*, 4:023069, Apr 2022.
- [L3] Lorenzo Oghittu, Juliette Simonet, Philipp Wessels-Staarmann, Markus Drescher, Klaus Sengstock, Ludwig Mathey, and Negretti Antonio. Cooling dynamics of a free ion in a Bose-Einstein condensate. *Accepted on Phys. Rev. Res.*, Feb 2024.

Contributions to the publications All the authors were relevant for the fulfillment of the publications, with a special mention to Dr. Antonio Negretti who provided constant and careful support. The individual contributions to these works are listed below:

- L1: The first project took shape from the discussions between Dr. A. Negretti and Dr. R. Gerritsma before the beginning of my doctoral studies. The analytical calculations reported in [L1] were performed by Dr. A. Negretti, M. Johannsen and myself, while the numerical calculations and relative plots were mainly carried on by myself. The text was written by Dr. A. Negretti and myself.
- L2: The second project was suggested by Dr. A. Negretti. Analytical calculations and numerical simulations in [L2] were all performed by myself, with the constant advice from Dr. A. Negretti. The writing of the article was also done by myself with significant contributions from Dr. A. Negretti.
- L3: A discussion with all the authors of [L3] gave birth to the third project. Analytical calculations and numerical simulations were performed by myself with the constant support from Dr. A. Negretti and Prof. Dr. Ludwig Mathey. The text was initially written by myself with the advice from Dr. A. Negretti. Later, it was expanded and improved thanks to the contributions from Dr. J. Simonet, and Dr. P. Wessels-Staarmann, who also helped integrating the project with experimental insight.

Objectives of the projects The projects resulting in [L1] and [L3], aim to investigate the quantum dynamics of single ions immersed in ultracold quantum gases, and to unravel the behavior of ionic impurities in different possible configurations that are relevant from the experimental point of view. Specifically, we examine the dependence of various observables of the ion, such as its kinetic energy or velocity, on the parameters of the systems. To do that, we treat the surrounding gas as a bath and we rely on the master equation approach, that we apply to the case of a trapped ion in [L1] and a free ion in [L3]. On the other hand, the project that culminated in [L2] proposes the application of trapped ions as sensors for the temperature of ultracold Fermi gases. The study investigates the precision of a thermometric protocol based on the dephasing dynamics of the ion, which is considered as a two-level spin system. Comparing the results with the case of a neutral particle, it shows the advantages brought by the long-range character of the atom-ion potential in the application of the protocol and discusses its possible implementation.

Outline of the dissertation This cumulative dissertation starts with an introduction to the main experimental achievements and theoretical progresses in the field of ultracold hybrid atom-ion systems, preceded by a brief overview on the most important results in the two separate fields, namely ultracold atomic gases and trapped ions. In Chapter 1, some significant notions regarding the atom-ion two body properties and the trapping of a single ion are summarized. This information is relevant to the author's project and provides a general background which is necessary to contextualise the topics and results of the publications. Chapter 2 is devoted to the theory on which the author's publications are based. First, a complete overview of the master equation approach is given, with focus on the specific case of the trapped and free ion in an ultracold atomic bath, which are relevant to Ref. [L1] and Ref. [L3], respectively. Later, some results of the theory of quantum parameter estimation are reported with the aim of understanding the thermometric protocol underlying the arguments in Ref. [L2]. In Chapter 3 a selection of the most relevant results of the author's publications is summarized. Finally, a brief discussion is provided where we draw conclusions and highlight potential perspectives that have emerged from this project.

Introduction to atom-ion systems

Immersing ions in ultracold atomic gases offers a fruitful environment for investigating various fundamental aspects of quantum few- and many-body physics, as well as providing a unique platform for research in quantum technologies and quantum information. Referred to as hybrid systems of atoms and ions, they combine the advanced theoretical modeling and superb experimental controllability achieved in the two separate fields, yielding a whole new plethora of states and phenomena.

The study of ultracold atomic gases has enjoyed a rapid advancement in the last decades. Thanks to the refinement of cooling and trapping techniques [1–3], Bose-Einstein condensation (BEC) [4–6] and degeneracy in Fermi gases [7] were finally realized and observed by the end of the last century. Since then, the field has witnessed a remarkable growth punctuated by a multitude of groundbreaking achievements [8]. Noteworthy observations include matter wave interference [9], quantized vortices in rotating BECs [10], and superfluid phase transition in Fermi gases [11], among many others. The exceptional versatility of ultracold atomic gases as a tool for exploring the quantum world, stems from the ability to control various parameters. For instance, laser beams can be used in order to manipulate the spatial distribution of atomic clouds [12–14] while the interaction strength among the atoms can be precisely regulated by exploiting Feshbach resonances [15] through the application of external magnetic fields. When combined, these possibilities allow the scientists to cool large ensembles of atoms down to temperatures below 100 nK and to design the most diverse Hamiltonians, making ultracold atomic gases one of the most fertile mediums for quantum simulations of many-body systems [16–18].

On the other hand, the manipulation and control of ions have also reached an impressive level of sophistication. Modern trapping techniques have enabled the capture and long-term storage of individual atomic or molecular ions within radio-frequency traps, commonly known as Paul traps [19] or optical traps [20]. These traps can maintain ions for practically indefinite periods, allowing for extensive experimental investigation. Additionally, ions can be cooled to their lowest achievable energy state, known as the motional ground state [21]. Cooling of trapped ions is typically achieved using laser-based techniques [22, 23], although recent research has demonstrated the attainment of the quantum regime through buffer gas cooling methods [24]. Multiple ions can also be confined within the same trap, resulting in the formation of ordered crystal structures due to the interplay between the external potential and the repulsive Coulomb forces [25, 26]. The exquisite control of systems with single ions or ion chains, makes them ideal for numerous applications, including quantum computing [27–29], quantum simulations [30–32], atomic clocks [33] and quantum teleportation [34, 35].

By combining the two aforementioned systems, ultracold hybrid atom-ion systems are formed, unlocking new perspectives and applications that neither ultracold gases nor trapped ions alone could offer. The main factor that makes these systems intriguing is the potential governing the interactions between the ion and the atoms in the gas. This arises from the dipole moment induced by the charged particle on the neutral ones and can be described as proportional to $-1/r^4$ for values of the atom-ion separation r larger than a certain distance R_0 . The latter is typically on the order of a few Ångström [36, 37] and indicates the range below which the electronic clouds of the atom and ion start to overlap. The polarization potential in atom-ion systems exhibits a typical length scale on the order of hundreds of nanometers, which is much larger than the typical length of the van der Waals interaction between neutral particles. The long-range nature of atom-ion interactions leads to large cross-sections for elastic and inelastic processes at ultracold temperatures [36, 38] significantly impacting experimental observations. Furthermore, it complicates the theoretical description, making the use of the pseudopotential approximation infeasible [37, 39].

Since its inception, the hybrid atom-ion community has devoted a great deal of effort to surmounting the challenges posed by such systems [40–43]. Experiments with single trapped ions in ultracold atomic gases [44–46] have brought to light the richness of the physics involved, showing how the dynamics of the ions is affected by the interplay between the trapping potentials and the interactions with the surrounding atoms. One notorious example is the micromotion induced by Paul traps [47], which stands as the main obstacle to the attainment of the ultracold regime. However, in the very last years, a great progress was made in that direction [48, 49] and, thanks to the refinement of experimental techniques for radiofrequency [50] and optical traps [51], the first observations of quantum effects were finally accomplished, namely buffer gas cooling [24] and the presence of Feshbach resonances [52]. Other experimental achievements with trapped ions in ultracold atomic environments include the investigation of few-body processes and chemical reactions [53–58], the detection of interaction between trapped ions and Rydberg atoms [59, 60] and the observation of swap-cooling due to resonant charge exchange [61, 62] in homonuclear systems. On the other hand, experiments with untrapped ions obtained via ionization of Rydberg atoms [63, 64] have recently explored the transport properties of charges in Bose-Einstein condensates [65, 66] and the formation of Rydberg-atom-ion molecules [67, 68].

As far as the theoretical progress is concerned, many efforts have been made in recent years to grasp the complex features of hybrid atom-ion systems. Researchers have employed various advanced theoretical methods such as multi-configuration time-dependent Hartree methods, quantum Monte Carlo and diagrammatic techniques to explore the formation of large molecular ions within Bose-Einstein condensates [69], investigate novel polaronic states [70, 71] and to understand the role of the surrounding gas in mediating the interaction between two ions [72, 73]. Additionally, studies have been conducted to examine the quantum dynamics of ions immersed in ultracold bosonic or fermionic environments using the master equation approach [74], [L1, L3]. Other investigations have also led to proposals for utilizing such systems as quantum simulators [75–78] or sensors [L2], unveiling a wide range of potential uses for hybrid atom-ion systems and offering exciting prospects for further exploration and experimentation.

Preliminary notions

In this chapter, we provide an overview about the research on hybrid systems of atoms and ions in order to set the ground for a contextualised understanding of our own scientific contribution.

We start by summarizing in Sec. 1.1 the main properties of systems consisting of a single atom and a single ion. On this purpose, we introduce the potential governing their interaction and we take a look at the main features of atom-ion scattering dynamics at low energies. In Sec. 1.2 we provide some details about ion trapping and, specifically, about the motion of a single ion inside a Paul-trap.

1.1 Two-body properties of atom-ion systems

The main element that renders hybrid atom-ion systems a rich field of research is the potential arising from the interplay between ions and neutral atoms. Nevertheless, calculating the precise shape and features of the potential between a single ion and a single atom, presents a many-body problem that remains impractical to solve exactly, as the nuclei and electrons should be considered as separate parts interacting among each others. To address this complexity, the Born-Oppenheimer approximation comes into play, allowing to effectively simplify this intricate problem into a manageable two-body scenario. As we will see in the following sections, dealing with such a simplified picture allows to compute the main characteristics of the interaction and to describe atom-ion scattering events. Depending on the purpose of the study, however, it is often useful to further simplify the the potential, for instance by only considering its asymptotic form at large separations. This section provides a brief treatment of the two-body properties of atom-ion systems.

1.1.1 Atom-ion potential

The interaction energy in the Born-Oppenheimer approximation between the ion I^+ and the atom A can be written as

$$V_{I^++A} = E_{I^++A} - E_{I^+} - E_A \quad (1.1)$$

where E_{I^++A} is the energy of the interacting complex while E_{I^+} and E_A are the energies of the separated ion and atom. These energies can be computed with mean-field quantum chemical methods such as coupled-clusters or configuration-interaction [79, 80], yielding the interaction energy for different species of ions and atoms. We note that this kind of calculations depend on the specific electronic configuration of the two interacting systems and, therefore, each atom-ion pair will come with a spectrum of curves each one taking into account a precise set of electronic states. An example is in Fig. 1.1, where the interaction energies for the $(\text{Li} + \text{Yb})^+$ system are shown [81]. Similar studies include the investigation of $(\text{Na} + \text{Ca})^+$ [82], $(\text{Ba} + \text{Rb})^+$ [83], $(\text{Yb} + \text{Rb})^+$ [84], $(\text{Sr} + \text{Li})^+$ [85], and many others (see Ref. [42] fore an exhaustive list).

Asymptotic range When the separation between the atom and the ion is so large that the overlap between their wave functions can be safely neglected, a simple approximated expression for the atom-ion potential can be derived. The calculation based on Ref. [86] relies on the bipolar expansion of the Coulomb potential [87] and is carried out perturbatively around the states at infinite separation, where the atom and ion are unperturbed [88]. The leading term of the expansion corresponds to the interaction between the charge of the ion and the induced dipole moment on the atom. Indicating with r the atom-ion separation, the asymptotic expression of the potential reads [89]

$$V_{\text{ai}}(r) \approx -\frac{C_4}{r^4} \quad (1.2)$$

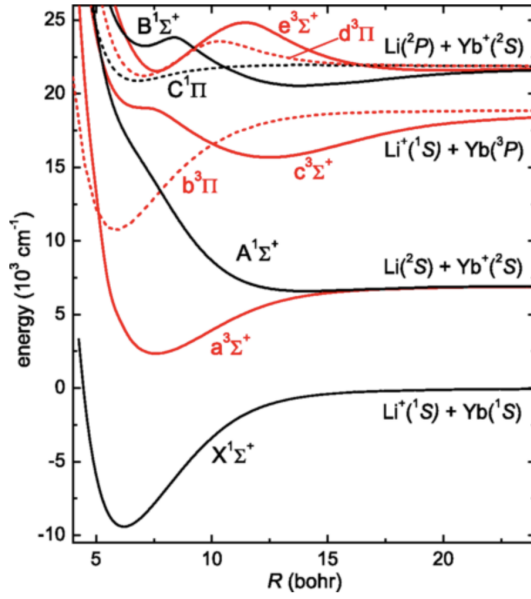


Figure 1.1: Interaction energy curves of the system $(\text{Li} + \text{Yb})^+$ for different electronic configurations. Figure reprinted with permission from Ref. [42].

with $C_4 = \alpha e^2 / (8\pi\epsilon_0)$, where α is the atom static polarizability, e is the elementary charge and ϵ_0 is the vacuum permittivity. The values of α are measured via atom interferometry for different atomic species, such as sodium [90], ytterbium [91], cesium, rubidium and potassium [92, 93]. The potential in Eq. (1.2) is known as the *polarization potential* and its long range character becomes clear when comparing it to the van der Waals interaction between neutral systems, which scales like $1/r^6$. The next-to-leading order terms in the expansion of the atom-ion potential are proportional to $-1/r^6$ and take into account the interaction of the ion with the induced quadrupole moment of the atom as well as the effect of dispersion interactions. Moreover, in case one of the two particles has a finite orbital angular momentum, the asymptotic expression takes a more complicated form. Since these details go beyond the scope of this dissertation, we refer the interested reader to Ref. [42, 83].

Short range In the regime where the electronic clouds overlap, calculations of the potential curves become exceedingly involved. Different methods can be adopted in order to address this problem and to include some information on the short-range behavior in a simple analytic potential.

One strategy consists of modeling the short-range part of the interaction by adding to the polarization potential in Eq. (1.2) a function of a few parameters, that are fitted with ab-initio data. For instance, exponential functions proportional to $\exp(-r)$ or $\exp(-r)/r$ were used in Ref. [36] and Ref. [82], respectively. Other choices comprehend Gaussian functions [94] or inverse powers of the atom-ion distance [95].

An alternative option is to regularize the divergence of the $-1/r^4$ potential at short distances by defining a function of one or more parameters that replicates the asymptotic behavior of the atom-ion potential at large distance and it is finite when $r \rightarrow 0$. One

example is the regularized potential introduced in Ref. [74], which is the one we used in our publications. We refer to Sec. (1.1.3) for an exhaustive description of its properties.

A more precise although sophisticated method relies on the so-called *quantum defect theory* (QDT), which was initially developed for potential scaling asymptotically like $-1/r^\alpha$ with $\alpha \leq 2$ [96–98] and more recently extended to the $\alpha > 2$ case [99, 100]. More precisely, multichannel QDT found its application in the description of atom-ion systems [101, 102] where it proved to be an accurate and precise approach for the study of scattering and bound states. The application of QDT to atom-ion systems relies on the scale separation between the characteristic length R^* of the potential (see Sec. 1.1.2 for the definition of R^*), and the distance R_0 at which the potential deviates from its asymptotic form. Due to the fact that $R_0 \ll R^*$, the information on the short-range dynamics can be summarized in a few constants that are independent of the energy and angular momentum and are determined by fitting experimental data. At the end of Sec. 1.1.2, we will see where QDT can be employed in the study of atom-ion scattering events. More details can be found in the cited literature.

1.1.2 Scattering properties

An important part of the research on hybrid atom-ion systems is represented by the study of scattering events. It was actually thanks to the groundbreaking works by Côté and his coworkers, where ultracold atom-ion collisions were investigated [36, 103], that the peculiarities of these systems were first unraveled to the scientific community in recent times. Earlier studies of a similar topic date back to the beginning of the previous century, when Langevin used classical trajectories to describe the scattering of a charged particle with a neutral particle [104].

According to the classical model by Langevin, two kinds of collisions can occur between a charged and a neutral particle. In particular, the model predicts the existence of a critical impact parameter b_c which depends on the collision energy E_{coll} . Collisions with impact parameter $b > b_c$ are referred to as *glancing collision* and result in a pure elastic event, where the trajectories are merely deflected by the long-range tail of the polarization potential. On the other hand, the so-called *Langevin collisions* occur when $b < b_c$, and result in a close spiraling motion of the two particles. During Langevin collisions, the short distance between the two scattering partners allows for large energy and momentum transfer.

Let us consider an atom and an ion approaching with collision velocity v_{coll} and impact parameter b . The collision energy is given by $E_{\text{coll}} = \mu v_{\text{coll}}^2/2$ while the classical angular momentum reads $L = \mu b v_{\text{coll}}$, where μ is the reduced mass. The total potential energy is given by the atom-ion potential plus the contribution $L^2/(2\mu r^2)$ from the angular momentum. The critical impact parameter is found by equating the collision energy to the maximum of the potential energy and reads

$$b_c = \left(\frac{2C_4}{E_{\text{coll}}} \right)^{\frac{1}{4}}. \quad (1.3)$$

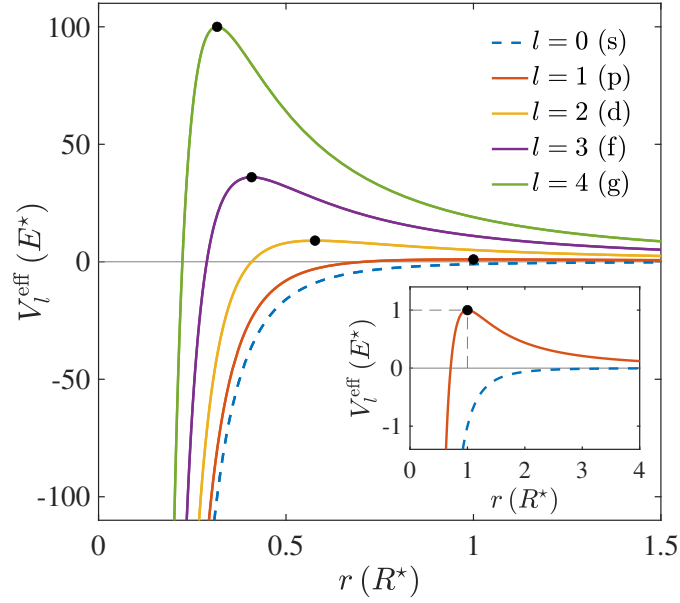


Figure 1.2: Atom-ion interaction in units of E^* for different partial waves as a function of atom-ion separation in units of R^* . Black dots indicate the centrifugal barriers. The inset shows a zoom on the $l = 0$ and $l = 1$ waves.

By definition, b_c represents the minimal value of the impact parameter for which the atom is able to overcome the centrifugal barrier. The Langevin cross section can be calculated as follows

$$\sigma_{\text{Langevin}}(E_{\text{coll}}) = 2\pi \int_0^{b_c} db b = \pi \sqrt{\frac{2C_4}{E_{\text{coll}}}}. \quad (1.4)$$

Considering an infinitely heavy ion immersed in an atomic gas, the collision rate is equal to the cross section multiplied by the relative velocity $v_{\text{coll}} = \sqrt{2E_{\text{coll}}/\mu}$ and the atomic density n_a :

$$\Gamma_{\text{Langevin}} = n_a 2\pi \sqrt{\frac{C_4}{\mu}}. \quad (1.5)$$

From Eq. (1.5) we observe that the classical Langevin collision rate is independent of the collision energy, which is a peculiarity of the polarization potential $-1/r^4$.

At the quantum level, in order to understand the role of the atom-ion interaction, we start by recalling that the total wave function of the system can be decomposed as the sum of different channel functions thanks to the isotropy of the potential. Different channels are referred to as partial waves, and are associated to different values of the angular momentum quantum number $l = 0, 1, \dots$, for which the corresponding effective potential is analogous to the classical case and reads

$$V_l^{\text{eff}}(r) = -\frac{C_4}{r^4} + \frac{\hbar^2 l(l+1)}{2\mu r^2}. \quad (1.6)$$

The effective potentials for the first five partial waves are shown in Fig. 1.2.

For every $l > 1$, one can find the position and height of the centrifugal barrier given by the second term on the right hand side of Eq. (1.6). Classically, values of the kinetic energy lower than the centrifugal barrier corresponding to a certain value of l , would allow that partial wave and the higher ones to be ignored. In a quantum description, the same argument cannot be applied due to tunnelling effect, and all partial waves should in principle be considered. For this reason, the regime where only the s -wave contributes is reached for collision energies much lower than E^* .

The lowest barrier, corresponding to $l = 1$ (p -wave), can be used to define the characteristic length R^* and energy E^* of the polarization potential:

$$R^* = \sqrt{\frac{2\mu C_4}{\hbar^2}}, \quad E^* = \frac{\hbar^2}{2\mu(R^*)^2}, \quad (1.7)$$

while the values corresponding to higher partial waves are given by

$$R_l^{\max} = \sqrt{\frac{2}{l(l+1)}} R^*, \quad E_l^{\max} = \frac{l^2(l+1)^2}{4} E^*. \quad (1.8)$$

Typical values of R^* are at least one order of magnitude larger than the characteristic length of van der Waals interactions between neutral particles, clearly indicating the long range character of the atom-ion potential. The characteristic quantities associated to different atom-ion systems are shown in Tab. 1.1.

atom-ion	M/m	R^* (nm)	E^*/k_B (μK)
${}^6\text{Li} - {}^{174}\text{Yb}^+$	28.92	69.77	8.57
${}^7\text{Na} - {}^{174}\text{Yb}^+$	7.57	129.85	0.708
${}^{87}\text{Rb} - {}^{138}\text{Ba}^+$	1.59	294.67	0.052
${}^{87}\text{Rb} - {}^{87}\text{Rb}^+$	1	267.81	0.079

Table 1.1: Values of mass ratio, R^* and E^* for different atom-ion systems.

To retrace the main steps of the quantum treatment of atom-ion scattering events, we explicitly write the total relative wave function as $\Psi(r, \theta_r, \varphi_r) = \sum_l Y_l^m(\theta_r, \varphi_r) \Phi_l(r)$, where the index l indicates the different partial waves and $Y_l^m(\theta_r, \varphi_r)$ are the spherical harmonics. We then write the two-body Schrödinger equation with the effective potential in Eq. (1.6) for the radial wave functions $\Phi_l(r)$:

$$\left[-\frac{\hbar^2}{2\mu} \frac{d}{dr^2} + V_l^{\text{eff}}(r) - E \right] \Phi_l(r) = 0. \quad (1.9)$$

This equation can be transformed into a Mathieu equation with imaginary argument [105–107] with the substitutions $\Phi_l(r) = \xi_l R^{1/2}$ and $r = e^z E^{-1/4}$. For each l we obtain two linearly independent solutions for the short-range limit

$$\Phi_l^a(r) \xrightarrow{r \rightarrow 0} r \sin(-R^*/r + \phi_l) \quad (1.10a)$$

$$\Phi_l^b(r) \xrightarrow{r \rightarrow 0} r \cos(-R^*/r + \phi_l). \quad (1.10b)$$

The short range phases ϕ_l , depend in general on the angular momentum l and the collision energy. However, since $R_0 \ll R^*$, we can assume that $\phi_l(E_{\text{coll}}) \equiv \phi$ and describe all the short-range dynamics with a single parameter which can only be determined experimentally. The solutions in Eq. (1.10a) and (1.10b) can also be obtained by solving the radial Schrödinger equation neglecting the centrifugal term. Moreover, Eq. (1.10a) is an analytic solution of Eq. (1.9) with $l = 0$ and $E = 0$, and is therefore valid at all r . Taking its limit for $r \rightarrow \infty$, we get the simple expression

$$a_{\text{ai}}^s = \cot(\phi) \quad (1.11)$$

relating the short-range phase to the s -wave scattering length.

In the opposite limit of large separation, the potential becomes negligible and the wave function approaches the free solution:

$$\Phi_l(r) \xrightarrow{r \rightarrow \infty} \sin[kr - l\pi/2 + \xi_l(k)], \quad (1.12)$$

where the phase shifts $\xi_l(k)$ take into account the long-range character of the atom-ion potential. Their dependence on l and k is computed by comparing Eq. (1.12) to the numerical solution of Eq. (1.9), or obtained by means of QDT, which gives analytical expressions. The phase shift is used to define the energy-dependent scattering length $a(k) = -\tan(\xi_0)/k$ [101]. This expression becomes equivalent to Eq. (1.11) in the zero-energy limit $k \rightarrow 0$. The reason for defining $a(k)$ is the difficulty in attaining the s -wave regime due to the low values of E^* . Unlike neutral-neutral systems, for which a pseudopotential approximations allows to parametrize the interaction with the s -wave scattering length alone [108, 109], the long-range of the atom-ion potential makes finite-energy corrections more likely to play a role in experiments.

The elastic cross section is also defined as a function of the phase shift

$$\sigma_{\text{el}} = \frac{4\pi}{k} \sum_{l=0}^{+\infty} (2l+1) \sin^2(\xi_l) \quad (1.13)$$

and becomes independent on the collision energy in the zero energy limit, where it takes the form $\sigma = 4\pi a_{\text{ai}}^s$. At higher energies, where several partial waves contribute, the phase shift can be estimated with a semiclassical approach. This gives $\xi_l \propto E_{\text{coll}}/l^3$, leading to $\sigma_{\text{el}} \propto E_{\text{coll}}^{-1/3}$ [36].

Finally, let us remark that QDT can be exploited for the calculations of other quantities of interest, such as the behavior of weakly bound states or charge exchange rates. Moreover, in the case of multichannel scattering problems, QDT can heavily reduce the computational effort required to numerically solve the coupled-channel equivalent of Eq. (1.9). We refer to Ref. [101, 102] for a complete treatment.

1.1.3 Regularized potential

In studies where the short-range features of the atom-ion potential are expected to play a marginal role, a precise description such as the one above is not necessary. As anticipated in Sec. 1.1.1, the behavior at short separation of the potential can be summarized by a short-range barrier whose shape is related to the scattering properties. Let us consider the regularized potential introduced in Ref. [74]:

$$V_{\text{reg}}(r) = -C_4 \frac{r^2 - c^2}{r^2 + c^2} \frac{1}{(b^2 + r^2)^2}, \quad (1.14)$$

where the parameters b and c control the s -wave scattering length and the number of bound states. This is the potential we used in all three of our publications, and here follows the procedure for the assessment of the b and c parameters.

The scattering amplitude in the first-order Born-Markov approximation corresponding to V_{reg} is proportional to its Fourier transform and reads

$$\begin{aligned} f(q) &= -\frac{\mu}{2\pi\hbar^2} \int_{\mathbb{R}^3} d\mathbf{r} e^{i\mathbf{q}\cdot\mathbf{r}} V_{\text{reg}}(r) \\ &= \frac{c^2\pi(R^*)^2}{(b^2 - c^2)^2 q} \left\{ e^{-bq} \left[1 + \frac{(b^4 - c^4)q}{4bc^2} \right] - e^{-cq} \right\}. \end{aligned} \quad (1.15)$$

The two parameters b and c are computed by imposing two physical conditions: (i) at zero energy, the scattering amplitude in Eq. (1.15) is equal to minus the atom-ion scattering length and (ii) the potential supports a single two-body bound-states. Note that the case of two or more two-body bound states can be treated analogously. However, the large energy separation between the bound states of the atom-ion polarization potential makes their occupation unlikely for typical atomic densities in hybrid atom-ion experiments. Therefore, a single bound state is sufficient of our purposes.

Condition (i) corresponds to the definition of the three-dimensional s -wave scattering length in the limit where the momentum transfer q goes to zero. This is given by

$$a_{\text{ai}}^s = -\lim_{q \rightarrow 0} f_s(q), \quad (1.16)$$

where $f_s(q)$ is the s -wave scattering amplitude at energy $\hbar^2 q^2 / (2\mu)$. Substituting f_s with the approximated definition in Eq. (1.15), the condition becomes $a_{\text{ai}}^s = -f(0)$. The

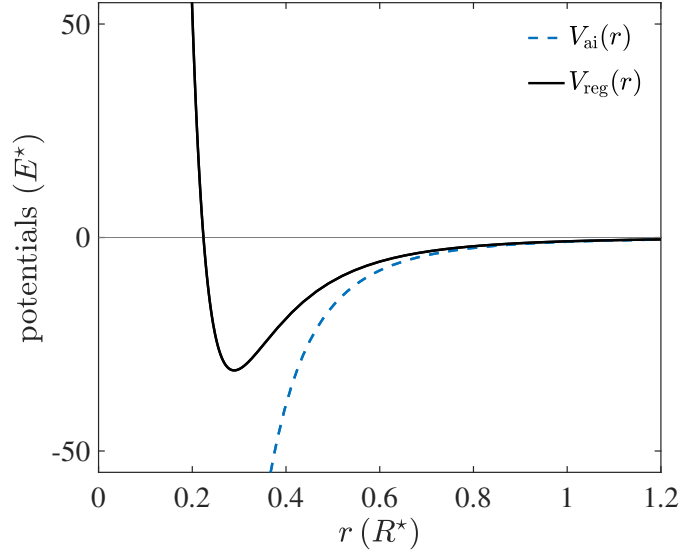


Figure 1.3: Atom-ion polarization potential (blue dashed) and regularized potential (black solid) in units of E^* as a function of atom-ion separation in units of R^* .

scattering amplitude at $q = 0$ can be computed by expanding the exponential functions and reads

$$f(0) = \pi(R^*)^2 \frac{b^2 + 2bc - c^2}{4b(b+c)^2}. \quad (1.17)$$

Condition (ii) is fulfilled by solving the radial time-independent Schrödinger equation for the scattering problem with the regularized potential in Eq. (1.14). This can be written in units of R^* and E^* as

$$\left[\frac{d}{dr^2} + \frac{r^2 - c^2}{r^2 + c^2} \frac{1}{(b^2 + r^2)^2} \right] \psi(r) = 0, \quad (1.18)$$

and can be solved with boundary conditions $\psi(0) = 0$ and $\psi'(0) = \epsilon$, where ϵ is a number smaller than one whose value does not affect the final result. Fixing the value of c , we can solve Eq. (1.18) iteratively for different values of b . For each solution ψ_b , we can compute the corresponding scattering length, which becomes a function of b and is given by

$$a_{\text{ai}}^s(b) = \lim_{r \rightarrow +\infty} \left[r - \frac{\psi_b(r)}{\psi_b'(r)} \right]. \quad (1.19)$$

Similarly, we can view the zero energy scattering amplitude in Eq. (1.17) as a function of the parameter b and seek for the value where it crosses with $-a_{\text{ai}}^s(b)$. In particular, we choose the value for which the first zero energy resonance occurs, indicating a single two-body bound state (see Fig. 1.4).

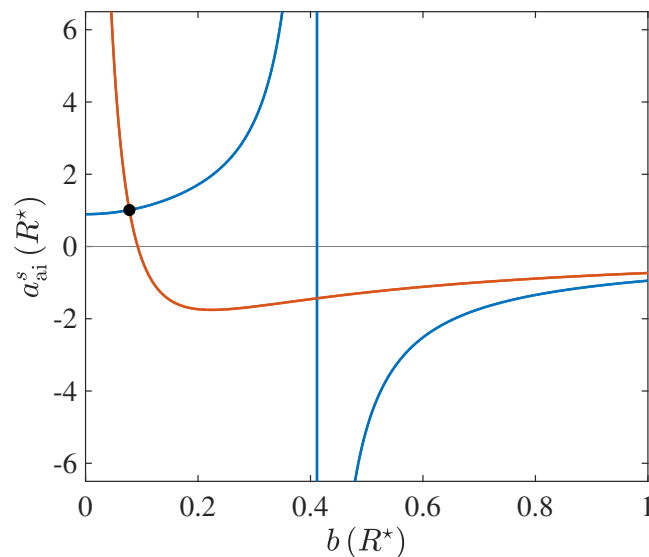


Figure 1.4: Atom-ion scattering length (blue) computed with Eq. (1.19) and minus the scattering amplitude at zero energy (orange) as defined in Eq. (1.17). The black dot indicates the selected point for fixed $c = 0.2239 R^*$, corresponding to $b = 0.07797 R^*$, a scattering length $a_{\text{ai}}^s = 1.0054 R^*$ and one two-body bound-state with energy $E_{\text{bs}} = -1.43 E^*$.

1.2 Single ion in a Paul trap

It is well known that charged particles cannot be trapped by static electric fields [110]. Therefore, ion traps have to rely on combinations of magnetic and static electric fields, as is the case of Penning traps [111], or time-dependent electric fields that take the name of Paul-traps [112]. The presence of collisions, however, affects the versatility of the two trapping systems: while Penning traps are unstable due to the lack of restoring forces on the radial plane [23], Paul traps are stable, allowing the application of buffer gas cooling. For this reason, Paul traps play a crucial role in experiments involving ions immersed in ultracold gases and, hence, in this dissertation. With the aim of setting the ground for the understanding of the calculations in Ref. [L1], we devote this section to the description of a single ion in a Paul trap. We refer to Ref. [19] for a complete treatment.

1.2.1 Classical equations

A Paul trap is essentially represented by a quadrupole potential $\Phi(x, y, z, t)$ which is assumed to be decomposed into a time-independent part, and another part oscillating at the radiofrequency Ω_{rf} :

$$\Phi(x, y, z, t) = \frac{U}{2}(\alpha x^2 + \beta y^2 + \gamma z^2) + \frac{\tilde{U}}{2} \cos(\Omega_{\text{rf}} t) (\alpha' x^2 + \beta' y^2 + \gamma' z^2). \quad (1.20)$$

The Poisson equation $\nabla^2\Phi = 0$ must be fulfilled at every time, leading to the conditions $\alpha + \beta + \gamma = 0$ and $\alpha' + \beta' + \gamma' = 0$. One of the most common configuration is the linear Paul trap, which is characterized by

$$\alpha + \beta = -\gamma > 0, \quad \alpha' = -\beta', \quad \gamma' = 0, \quad (1.21)$$

indicating static confinement along the z direction and dynamic confinement in the x - y plane.

Let us now consider a classical particle with mass M and charge $Z|e|$ in the quadrupole potential in Eq. (1.20). The force exerted on the particle is given by the Lorentz force $\mathbf{F} = e\mathbf{E}$, where $\mathbf{E} = -\nabla\Phi$ is the electric field of the Paul trap. The equation of motion x for the particle is therefore

$$\ddot{x}(t) = -\frac{Z|e|}{M} \frac{\partial\Phi}{\partial x} = -\frac{Z|e|}{M} \left[U\alpha + \tilde{U}\alpha' \cos(\Omega_{\text{rf}}t) \right] x(t), \quad (1.22)$$

which is conveniently rewritten as a Mathieu equation in its standard form:

$$\ddot{x}(\tau) + \left[a_x - 2q_x \cos(2\tau) \right] x(\tau) = 0, \quad (1.23)$$

where we defined the parameters $a_x = 4|e|Z\alpha U/(M\Omega_{\text{rf}}^2)$ and $q_x = -2|e|Z\alpha'\tilde{U}/(M\Omega_{\text{rf}}^2)$ and the dimensionless variable $\tau = \Omega_{\text{rf}}t$. The above equation is solved by means of the Floquet theorem [113] and is given by the following ansatz

$$x(\tau) = A_x e^{i\beta_x\tau} \sum_{n=-\infty}^{+\infty} C_{2n}^x e^{i2n\tau} + B_x e^{-i\beta_x\tau} \sum_{n=-\infty}^{+\infty} C_{2n}^x e^{-i2n\tau} \quad (1.24)$$

where the coefficients β_x and C_{2n}^x have to be found recursively, while the constants A_x and B_x are set by the initial conditions.

Inserting Eq. (1.24) into Eq. (1.23), we can join the cosine function of the radiofrequency driving field with the exponentials in the ansatz, obtaining the relations

$$C_{2n+2}^x - D_{2n}^x C_{2n}^x + C_{2n-2}^x = 0, \quad D_{2n}^x = \frac{a_x - (\beta_x + 2n)^2}{q_x}. \quad (1.25)$$

The iterative application of the equation on the left yields to the continued fractions

$$\frac{C_{2n}^x}{C_{2n+2}^x} = \frac{1}{D_{2n}^x - \frac{1}{D_{2n-2}^x - \frac{1}{D_{2n-4}^x - \dots}}}, \quad \frac{C_{2n}^x}{C_{2n-2}^x} = \frac{1}{D_{2n}^x - \frac{1}{D_{2n+2}^x - \frac{1}{D_{2n+4}^x - \dots}}} \quad (1.26)$$

from which we obtain an equation for the coefficient β_ξ :

$$\frac{a_x - \beta_x^2}{q_x} = \frac{1}{D_{-2}^x - \frac{1}{D_{-4}^x - \dots}} + \frac{1}{D_2^x - \frac{1}{D_4^x - \dots}}. \quad (1.27)$$

Note that the right hand side of Eq. (1.27) depends on β_x , q_x and a_x through the definition of D_{2n}^x , and the value of β_x has to be extracted by fixing q_x and a_x , and truncating the continued fractions to get the desired accuracy. Once the value of β_x is known, we can use Eq. (1.25) to compute the C_{2n}^x coefficients. Assuming $C_0^x = 1$ and $C_{2n}^x = 0$ for $|n| > N$, where N is a fixed positive integer, we can write a system of $2N$ coupled equations to be solved for the $2N$ coefficients C_{2n}^x with $-N \leq n \leq N$. We refer to Appendix C of Ref. [L1] for more details.

Let us remark that, as we can see from Eq. (1.24), the trapped particle is stable if the values of q_x and a_x guarantee $0 \leq \beta_x \leq 1$, and the same must be satisfied in all three direction. This leads to the presence of stability regions in the q_ξ - a_ξ planes ($\xi = x, y, z$), corresponding to the values for which the condition is fulfilled. The shape of these regions depend on the parameters in Eq. (1.20). Some examples are shown in Ref. [19].

Finally, we consider the case in which $a_x < |q_x| \ll 1$ and $p_x(0) = 0$. In this regime, the solution can be approximated with

$$x_{\text{approx}}(t) = \frac{2x(0)}{2 - q_x} \cos\left(\frac{\beta_x}{2} \Omega_{\text{rf}} t\right) \left[1 + \frac{q_x}{2} \cos(\Omega_{\text{rf}} t)\right] \quad (1.28)$$

with $\beta_\xi \approx \sqrt{a_x + q_x^2/2}$. The ion motion is the combination of a slow oscillation at frequency $\beta_x \Omega_{\text{rf}}/2$, called *secular motion*, and a fast oscillation at the frequency of the driving field Ω_{rf} , known as *micromotion*. A comparison between the approximated solution, the Floquet ansatz and a numerical solution is shown in Fig. 1.5.

1.2.2 Quantum description

A complete description of the phenomena arising in ultracold atom-ion experiments requires the ion to be treated quantum mechanically. Hence, a description for the dynamics of the ion in the Paul trap involving its quantized position and momentum operators has to be developed. On this purpose, let us consider Hamiltonian of a parametric oscillator

$$\hat{H}_\xi^{\text{trap}} = \frac{\hat{p}_\xi^2}{2M} + \frac{M}{2} W_\xi(t) \hat{r}_\xi^2 \quad \xi = x, y, z, \quad (1.29)$$

with the time-varying spring constant given by

$$W(t) = \frac{\Omega_{\text{rf}}^2}{4} [a_\xi + 2q_\xi \cos(\Omega_{\text{rf}} t)]. \quad (1.30)$$

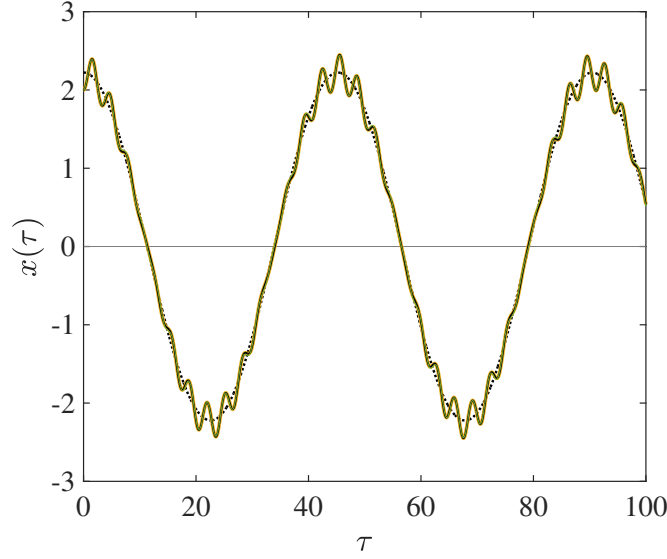


Figure 1.5: Ion motion in a Paul trap with $a_x = -0.001$, $q_x = 0.2$. The three solid lines correspond to three different solutions: numerical solution to Eq. (1.23) (thick yellow), Floquet ansatz in Eq. (1.24) (solid black), and approximated solution in Eq. (1.28) (thin green). The dotted black line represent the secular motion.

Note that the three directions indicated by ξ can be decoupled because the potential is quadratic in each of the three Cartesian coordinates.

The Heisenberg equations for \hat{r}_ξ and \hat{p}_ξ read

$$\dot{\hat{r}}_\xi = \frac{1}{i\hbar} [\hat{r}_\xi, \hat{H}_\xi^{\text{trap}}] = \frac{\hat{p}_\xi}{M}, \quad \dot{\hat{p}}_\xi = \frac{1}{i\hbar} [\hat{p}_\xi, \hat{H}_\xi^{\text{trap}}] = -MW(t)\hat{r}_\xi \quad (1.31)$$

and can be combined to

$$\ddot{\hat{r}}_\xi + W_\xi(t)\hat{r}_\xi = 0. \quad (1.32)$$

The latter is equivalent to the Mathieu equation in Eq. (1.23) with the substitution of the operator \hat{r}_ξ with a function $u_\xi(t)$. Exploiting this fact, we look for solutions with initial conditions $u_\xi(0) = 1$ and $\dot{u}_\xi(0) = i\nu_\xi$. Such a solution is given by

$$u_\xi(t) = e^{i\frac{\beta_\xi}{2}\Omega_{\text{rf}}t} \sum_{n=-\infty}^{+\infty} C_{2n}^\xi e^{in\Omega_{\text{rf}}t}, \quad (1.33)$$

where the coefficients C_{2n}^ξ and β_ξ are calculated the same way as the classical case and the initial conditions result in

$$u(0) = \sum_{n=-\infty}^{+\infty} C_{2n}^\xi = 1, \quad \nu_\xi = \Omega_{\text{rf}} \sum_{n=-\infty}^{+\infty} C_{2n}^\xi \left(\frac{\beta_\xi}{2} + n \right) \quad (1.34)$$

with ν_ξ known as the reference harmonic oscillator frequency. The meaning of the latter becomes clear when we define the two following operators. The first is proportional to the Wronskian between the position operator $\hat{r}_\xi(t)$ and $u_\xi(t)$:

$$\begin{aligned}\hat{c}_{\xi,1}(t) &= i\sqrt{\frac{M}{2\hbar\nu_\xi}}\mathcal{W}\{\hat{r}_\xi(t), u_\xi(t)\} \\ &= i\sqrt{\frac{M}{2\hbar\nu_\xi}}[u_\xi(t)\dot{\hat{r}}_\xi(t) - \dot{u}_\xi(t)\hat{r}_\xi(t)] \\ &= \hat{c}_{\xi,1}(0) = \frac{1}{2M\hbar\nu_\xi}[M\nu_\xi\hat{r}_\xi(0) + i\hat{p}_\xi(0)],\end{aligned}\tag{1.35}$$

where the equality in the last line is a consequence of the fact that both $u_\xi(t)$ and $\hat{r}_\xi(t)$ are solutions of Eq. (1.32), and their Wronskian $\mathcal{W}\{u_\xi(t), u_\xi(-t)\}$ is a constant, due to the absence of a first derivative. The second is analogous, but with the linearly independent solution $u_\xi(-t)$:

$$\hat{c}_{\xi,2}(t) = \frac{1}{2M\hbar\nu_\xi}[M\nu_\xi\hat{r}_\xi(0) - i\hat{p}_\xi(0)].\tag{1.36}$$

Now, the operators $\hat{c}_{\xi,1}$ and $\hat{c}_{\xi,2}$ can be interpreted respectively as the creation and annihilation operators of an harmonic oscillator with frequency ν_ξ . This can be used to define $\hat{r}_\xi(t)$ and $\hat{p}_\xi(t)$ in terms of the two linearly independent solutions $u_\xi(t)$ and $u_\xi(-t)$. By using the identity $\mathcal{W}\{u_\xi(t), u_\xi(-t)\} = 2i\nu_\xi$, we get

$$\hat{r}_\xi(t) = \frac{\hat{r}_\xi(0)}{2}[u_\xi(t) + u_\xi(-t)] + \frac{\hat{p}_\xi(0)}{2iM\nu_\xi}[u_\xi(t) - u_\xi(-t)]\tag{1.37}$$

and

$$\hat{p}_\xi(t) = \frac{M\hat{r}_\xi(0)}{2}[\dot{u}_\xi(t) + \dot{u}_\xi(-t)] + \frac{\hat{p}_\xi(0)}{2i\nu_\xi}[\dot{u}_\xi(t) - \dot{u}_\xi(-t)].\tag{1.38}$$

We finally remark that the two solutions above are used in Ref. [74] and Ref. [L1] to compute the operator $\hat{\mathbf{r}}(t, \tau) \equiv \hat{U}(0, t)\hat{U}^\dagger(0, t - \tau)\hat{\mathbf{r}}\hat{U}(0, t - \tau)\hat{U}^\dagger(0, t)$, where \hat{U} is the time evolution operator for the ion in the Paul trap. This operator $\hat{\mathbf{r}}(t, \tau)$ is used to obtain the master equation for the trapped ion immersed in an ultracold gas. We refer to Sec. 2.1 for an overview of the derivation.

1.2.3 Excess micromotion

So far, we only considered the case of an ideal Paul trap. In experiments, however, the presence of stray electric fields and imperfections in the construction of the trap can cause a shift of the trap center as well as corrections to the frequency of the driving field.

These effects are taken into account with an additional driving term in Eq. (1.29). The Hamiltonian of the trapped ion becomes

$$\hat{H}_\xi^{\text{trap}} = \frac{\hat{p}_\xi^2}{2M} + \frac{M}{2} W_\xi(t) \hat{r}_\xi^2 - F_\xi(t) \hat{r}_\xi \quad \xi = x, y, z, \quad (1.39)$$

with

$$F_\xi(t) = eE_{\text{dc}}^\xi (1 - \delta_{\xi,z}) + eE_{\text{ac}} \sin\left(\Omega_{\text{rf}} t + \delta_{z,\xi} \pi/2\right) (1 - \delta_{\xi,y}). \quad (1.40)$$

Here, e is the electron charge while E_{dc} and E_{ac} are the components of the dc and ac spurious fields along the direction $\xi = x, y, z$.

In Ref. [114], it is shown that the time evolution of the ion's position operator is given by

$$\hat{r}_\xi(t) = \hat{r}_\xi^{\text{in}}(t) + \hat{r}_\xi^{\text{ex}}(t) \mathbb{I}, \quad (1.41)$$

where $\hat{r}_\xi^{\text{in}}(t)$ is the solution to the homogeneous Mathieu equation and indicates the ion motion in the ideal Paul trap, i.e. with *intrinsic* micromotion, and is given in Eq. (1.37). On the other hand, $\hat{r}_\xi^{\text{ex}}(t)$ is the solution to the classical inhomogeneous Mathieu equation with the source term $F_\xi(t)$, which provides the *excess* micromotion. This is obtained via the method of the variation of constant and reads

$$r_\xi^{\text{ex}}(t) = \int_0^t d\tau \frac{u_\xi(\tau) u_\xi(-\tau) - u_\xi(-\tau) u_\xi(\tau)}{\mathcal{W}\{u_\xi(\tau), u_\xi(-\tau)\}} \frac{F_\xi(\tau)}{M}, \quad (1.42)$$

where $\mathcal{W}\{u_\xi(\tau), u_\xi(-\tau)\}$ is the Wronskian of the two solutions to the Homogeneous equation [see Eq. (1.33)]. We do not report $r_\xi^{\text{ex}}(t)$ for brevity, but we remark that an operator $\hat{\mathbf{r}}^{\text{ex}}(t, \tau)$ can be derived as in the case of the ideal trap. This can be used in the derivation of the master equation for the ion in an ultracold bath, in order to evaluate how the excess micromotion affects the quantum dynamics of the ion.

Theoretical treatment

This chapter contains some of the most important theoretical results on which our work based. It is important to keep in mind that our interest in the study of hybrid atom-ion systems is centered on understanding the dynamics of the ion and how this is affected by the surrounding atoms. For this reason, the ion is treated as an open quantum system interacting with the ultracold atoms, which play the role of a bath.

In Sec. 2.1, we retrace the main steps of the theoretical derivation reported in Ref. [L1, L3], where a master equation approach is applied to the case of a trapped and free ion, respectively. In Sec. 2.2, we report some notions of the theory of quantum information and quantum parameter estimation, with the aim of explaining the thermometric protocol which is at the base of Ref. [L2].

2.1 Master equation for a single ion in a quantum gas

The master equation approach stands as a powerful framework in the field of quantum physics for describing and analyzing the dynamics of open quantum systems. It provides a mathematical toolset that enables us to comprehend the evolution of quantum systems interacting with their environment. By employing the master equation approach, we can effectively capture the effects of decoherence, dissipation, and environmental interactions on the quantum system of interest. In this section, we derive a master equation for an ionic impurity immersed in an ultracold atomic gas.

2.1.1 Redfield equation

We begin with a very brief derivation of the standard quantum optical master equation, aimed at setting the ground for the following discussion. We refer the interested reader to Ref. [115] for a more thorough treatment.

Let us consider a system¹ (S) coupled to a bath (B). The Hamiltonian in its general form can be written as the sum of three terms: $\hat{H} = \hat{H}_S + \hat{H}_B + \hat{H}_{SB}$, where the first two terms correspond to the Hamiltonian of the system and the bath, while H_{SB} takes into account their interaction. The explicit form of the Hamiltonian will be introduced later. Until that moment, the equations will be valid for any system and bath, provided that they satisfy the assumptions made during the derivation.

Now, we call $\hat{\chi}(t)$ the density matrix of the composite system and we define the reduced density matrix as

$$\hat{\rho}(t) = \text{Tr}_B\{\hat{\chi}(t)\}, \quad (2.1)$$

where Tr_B is the trace over the bath states. The objective of this entire section is to derive an equation for the reduced density matrix $\hat{\rho}$, where the information from the bath is incorporated solely as parameters. For this purpose, we start from the Schrödinger equation for $\hat{\chi}(t)$

$$\frac{d}{dt}\hat{\chi}(t) = \frac{1}{i\hbar}[\hat{H}, \hat{\chi}(t)] \quad (2.2)$$

and we transform it to the interaction picture by defining the explicitly time-dependent density matrix operator

$$\tilde{\chi}(t) = e^{i(H_S+H_B)t/\hbar} \hat{\chi}(t) e^{-i(H_S+H_B)t/\hbar}. \quad (2.3)$$

The resulting equation reads

$$\frac{d}{dt}\tilde{\chi}(t) = \frac{1}{i\hbar}[\tilde{H}_{SB}(t), \tilde{\chi}(t)] \quad (2.4)$$

¹In accordance with the literature, we use the term "system" to indicate the part exchanging energy with the bath. The combination of system and bath will be referred to as composite system.

where the definition of $\tilde{H}_{\text{SB}}(t)$ is analogous to Eq. (2.3), and its formal solution is

$$\tilde{\chi}(t) = \hat{\chi}(0) + \frac{1}{i\hbar} \int_0^\infty dt' \left[\tilde{H}_{\text{SR}}(t'), \tilde{\chi}(t') \right]. \quad (2.5)$$

Substituting Eq. (2.5) inside the commutator of Eq. (2.4) leads to the following integro-differential equation

$$\frac{d}{dt} \tilde{\chi}(t) = \frac{1}{i\hbar} \left[\tilde{H}_{\text{SB}}(t), \hat{\chi}(0) \right] - \frac{1}{\hbar^2} \int_0^t dt' \left[\tilde{H}_{\text{SB}}(t), \left[\tilde{H}_{\text{SB}}(t'), \tilde{\chi}(t') \right] \right] \quad (2.6)$$

which is equivalent to Eq. (2.2), but in a form which is more convenient for our purposes.

In order to proceed, some assumptions need to be made regarding the system-bath coupling and the bath correlation time. First, we assume that the coupling is turned on at $t = 0$. Therefore, no correlations are present between the system and the bath at the initial time and the total density matrix at $t = 0$ can be written as the following product

$$\hat{\chi}(0) = \hat{\rho}(0) \otimes \hat{B}_0 \quad (2.7)$$

B_0 being the initial density matrix of the bath. Then, we can trace over the bath states in Eq. (2.6), getting to the following master equation

$$\frac{d}{dt} \tilde{\rho}(t) = -\frac{1}{\hbar^2} \int_0^t dt' \text{Tr}_{\text{B}} \left\{ \left[\tilde{H}_{\text{SB}}(t), \left[\tilde{H}_{\text{SB}}(t'), \tilde{\chi}(t') \right] \right] \right\}. \quad (2.8)$$

Note that the term coming from $[\tilde{H}_{\text{SB}}(t), \hat{\chi}(0)]/(i\hbar)$ can be systematically excluded from the derivation thanks to Eq. (2.7) and by assuming $\text{Tr}_{\text{B}}\{\tilde{H}_{\text{SB}}\hat{B}_0\} = 0$. The latter condition is true when the bath operators in \hat{H}_{SB} have zero mean in the initial state of the bath, and can be always enforced by including $\text{Tr}_{\text{B}}\{\hat{H}_{\text{SB}}\hat{B}_0\}$ in the system Hamiltonian².

Now, we extend the validity of the condition stated in Eq. (2.7) to all times. To achieve this, we assume that the coupling between the system and the bath is weak, rendering the effects due to correlations negligible. Moreover, we consider the bath to be so large that its state is unaffected by the interaction with the system. Under these assumptions, we perform the so called Born approximation and write

$$\tilde{\chi}(t) = \tilde{\rho}(t) \otimes \hat{B}_0, \quad (2.9)$$

²This assumption justifies the derivation as it can be always guaranteed. However, the term $\text{Tr}_{\text{B}}\{\tilde{H}_{\text{SB}}(t), \hat{\chi}(0)\}$ can be zero for other reasons, as we will see in the following sections.

which simply leads to

$$\frac{d}{dt}\tilde{\rho}(t) = -\frac{1}{\hbar^2} \int_0^t dt' \text{Tr}_B \left\{ \left[\tilde{H}_{\text{SB}}(t), \left[\tilde{H}_{\text{SB}}(t'), \tilde{\rho}(t') \otimes \hat{B}_0 \right] \right] \right\}. \quad (2.10)$$

At this point, the state of the system at time t depends on its past history due to the presence of $\tilde{\rho}(t')$ on the right hand of the previous equation. In other words, the system is not Markovian and the master equation is still too complicated. To address this issue, we have to make the equation local in time resorting to the Markov approximation, which again relies on the largeness of the bath. In principle, the system would perturb the bath and be influenced by those same perturbations at later times. Nevertheless, for a very large bath at thermal equilibrium, any minor changes induced by the system are expected to decay rapidly, relative to the timescale of the system's dynamics. We can therefore replace $\tilde{\rho}(t')$ with $\tilde{\rho}(t)$ in Eq. (2.10), obtaining a master equation in the Born-Markov approximation

$$\frac{d}{dt}\tilde{\rho}(t) = -\frac{1}{\hbar^2} \int_0^t dt' \text{Tr}_B \left\{ \left[\tilde{H}_{\text{SB}}(t), \left[\tilde{H}_{\text{SB}}(t'), \tilde{\rho}(t) \otimes \hat{B}_0 \right] \right] \right\}. \quad (2.11)$$

which is known in the literature as the Redfield equation [116].

2.1.2 Hamiltonian description

We now proceed by making the Hamiltonian explicit for the case of an ionic impurity with mass M interacting with an ultracold gas of atoms with mass m , with the aim of obtaining a version of Eq. (2.11) which is suitable for numerical simulations. Let us start by assuming that the bath is a gas of bosons confined in a box with side L which is much larger than the other lengths involved in the system. Denoting by $g = 4\pi\hbar^2 a_{\text{bb}}^s/m$ the coupling strength of the contact potential between the atoms, where a_{bb}^s is the 3D atom-atom s -wave scattering length, we have

$$\hat{H}_B = \int_{\mathbb{R}^3} d\mathbf{r}_b \hat{\Psi}_b^\dagger(\mathbf{r}_b) \left[\frac{\hat{p}_b^2}{2m} + \frac{g}{2} \hat{\Psi}_b^\dagger(\mathbf{r}_b) \hat{\Psi}_b(\mathbf{r}_b) \right] \hat{\Psi}_b(\mathbf{r}_b), \quad (2.12)$$

and

$$\hat{H}_{\text{BS}} = \int_{\mathbb{R}^3} d\mathbf{r}_b \hat{\Psi}_b^\dagger(\mathbf{r}_b) V_{\text{ib}}(\mathbf{r}_b - \hat{\mathbf{r}}) \hat{\Psi}_b(\mathbf{r}_b), \quad (2.13)$$

where the subscript b indicates the bosons of the bath while $\hat{\mathbf{r}}$ is the position operator of the ion. Moreover, V_{ib} indicates the two-body interaction potential between the ion and the particles in the bath.

Below the critical temperature of Bose-Einstein condensation, the bosonic quantum field $\hat{\Psi}_b$ can be expanded around the zero-momentum mode

$$\hat{\Psi}_b(\mathbf{r}_b) = \sqrt{n_0} + \delta\hat{\Psi}_b(\mathbf{r}_b) \quad (2.14)$$

where $n_0 = N_0/L^3$ is the condensate density and N_0 is the number of particles in the condensate. The fluctuations are described by means of Bogolyubov theory

$$\delta\hat{\Psi}_b(\mathbf{r}_b) = L^{-3/2} \sum_{\mathbf{q}} \left(u_{\mathbf{q}} \hat{b}_{\mathbf{q}} e^{i\mathbf{q}\cdot\mathbf{r}_b} + v_{\mathbf{q}} \hat{b}_{\mathbf{q}}^\dagger e^{-i\mathbf{q}\cdot\mathbf{r}_b} \right) \quad (2.15)$$

where the operators $\hat{b}_{\mathbf{q}}^\dagger$ and $\hat{b}_{\mathbf{q}}$ create and annihilate a phonon with momentum \mathbf{q} , respectively, and obey the bosonic commutation relation $[\hat{b}_{\mathbf{q}}, \hat{b}_{\mathbf{q}'}^\dagger] = \delta_{\mathbf{q},\mathbf{q}'}$. The bath Hamiltonian can be rewritten as

$$\hat{H}_B = E_0 + \sum_{\mathbf{q}} \hbar\omega_{\mathbf{q}} \hat{b}_{\mathbf{q}}^\dagger \hat{b}_{\mathbf{q}} \quad (2.16)$$

where $E_0 = gN_0^2/(2L^3)$ is the ground state-energy and the phononic dispersion relation is given by

$$\varepsilon(\mathbf{q}) = \hbar\omega_{\mathbf{q}} = \sqrt{\left(\frac{\hbar^2 q^2}{2m}\right)^2 + (\hbar c_s q)^2} \quad (2.17)$$

with $c_s = \sqrt{gn_0/m}$ the speed of sound in the gas. Finally, the amplitude of the Bogolyubov modes is

$$u_{\mathbf{q}} = \sqrt{\frac{\hbar^2 q^2/(2m) + gn_0}{2\hbar\omega_{\mathbf{q}}}} + \frac{1}{2}, \quad v_{\mathbf{q}} = -\sqrt{\frac{\hbar^2 q^2/(2m) + gn_0}{2\hbar\omega_{\mathbf{q}}}} - \frac{1}{2}. \quad (2.18)$$

We refer the interested reader to Ref. [117] for more details.

We can now write the density operator as follows

$$\hat{\Psi}_b^\dagger(\mathbf{r}_b) \hat{\Psi}_b(\mathbf{r}_b) = n_0 + \Delta\hat{n}(\mathbf{r}_b) \quad (2.19)$$

and use Eq. (2.14) to obtain the following identity for the density fluctuation

$$\Delta\hat{n}(\mathbf{r}_b) = \delta\hat{n}(\mathbf{r}_b) + \delta^2\hat{n}(\mathbf{r}_b), \quad (2.20)$$

with

$$\delta\hat{n}(\mathbf{r}_b) = \sqrt{n_0}[\delta\hat{\Psi}_b(\mathbf{r}_b) + \delta\hat{\Psi}_b^\dagger(\mathbf{r}_b)], \quad \delta^2\hat{n}(\mathbf{r}_b) = \delta\hat{\Psi}_b^\dagger(\mathbf{r}_b)\delta\hat{\Psi}_b(\mathbf{r}_b). \quad (2.21)$$

The first term in Eq. (2.21) refers to the condensed part of the gas, as the presence of the factor $\sqrt{n_0}$ suggests. On the other hand, the contribution of the non-condensed part is taken into account by the second term. The latter becomes relevant when the temperature of the gas approaches the critical temperature of condensation from below and, of course,

in absence of condensation, where is the only one contributing. According to the definition of the field fluctuation in Eq. (2.15), we can write

$$\delta\hat{n}(\mathbf{r}_b) = \sqrt{\frac{n_0}{L^3}} \sum_{\mathbf{q}} \left[(u_{\mathbf{q}} + v_{\mathbf{q}}^*) \hat{b}_{\mathbf{q}} e^{i\mathbf{q}\cdot\mathbf{r}_b} + (u_{\mathbf{q}}^* + v_{\mathbf{q}}) \hat{b}_{\mathbf{q}}^\dagger e^{-i\mathbf{q}\cdot\mathbf{r}_b} \right] \quad (2.22)$$

and

$$\begin{aligned} \delta^2\hat{n}(\mathbf{r}_b) = \frac{1}{L^3} \sum_{\mathbf{q},\mathbf{q}'} & \left[u_{\mathbf{q}}^* \hat{b}_{\mathbf{q}}^\dagger u_{\mathbf{q}'} \hat{b}_{\mathbf{q}'} e^{-i(\mathbf{q}-\mathbf{q}')\cdot\mathbf{r}_b} + u_{\mathbf{q}}^* \hat{b}_{\mathbf{q}}^\dagger v_{\mathbf{q}'} \hat{b}_{\mathbf{q}'}^\dagger e^{-i(\mathbf{q}+\mathbf{q}')\cdot\mathbf{r}_b} \right. \\ & \left. + v_{\mathbf{q}}^* \hat{b}_{\mathbf{q}} u_{\mathbf{q}'} \hat{b}_{\mathbf{q}'} e^{i(\mathbf{q}+\mathbf{q}')\cdot\mathbf{r}_b} + v_{\mathbf{q}}^* \hat{b}_{\mathbf{q}} v_{\mathbf{q}'} \hat{b}_{\mathbf{q}'}^\dagger e^{i(\mathbf{q}-\mathbf{q}')\cdot\mathbf{r}_b} \right] \end{aligned} \quad (2.23)$$

We will refer to the terms in Eq. (2.23) resulting from the non-condensed part of the gas as quadratic terms, alluding to their dependence on the products between phonon operators.

In order to keep the derivation as general as possible, we define a new set of creation and annihilation operators $\hat{\Gamma}_{\mathbf{q}}^\dagger$ and $\hat{\Gamma}_{\mathbf{q}}$ which can be identified, depending on what the situation requires, with the phononic operators $\hat{b}_{\mathbf{q}}^\dagger$ and $\hat{b}_{\mathbf{q}}$ we used so far, or with the operators $\hat{f}_{\mathbf{q}}^\dagger$ and $\hat{f}_{\mathbf{q}}$ creating and annihilating a free fermion with energy $\varepsilon(\mathbf{q}) = \hbar^2 q^2 / (2m)$ and obeying the fermionic anti-commutation rule $\{\hat{f}_{\mathbf{q}}, \hat{f}_{\mathbf{q}'}^\dagger\} = \delta_{\mathbf{q},\mathbf{q}'}$. Hence, the system-bath interaction Hamiltonian becomes

$$\hat{H}_{\text{SB}} = \int_{\mathbb{R}^3} d\mathbf{r}_b V_{\text{ib}}(\mathbf{r}_b - \hat{\mathbf{r}}) \Delta\hat{n}(\mathbf{r}_b) \equiv \hat{H}_{\text{SB}}^{(1)} + \hat{H}_{\text{SB}}^{(2)} \quad (2.24)$$

with

$$\hat{H}_{\text{SB}}^{(1)} = \hbar \sum_{\mathbf{q}} (\hat{S}_{\mathbf{q}} \hat{\Gamma}_{\mathbf{q}} + \hat{S}_{\mathbf{q}}^\dagger \hat{\Gamma}_{\mathbf{q}}^\dagger) \quad (2.25a)$$

$$\hat{H}_{\text{SB}}^{(2)} = \hbar \sum_{\mathbf{q},\mathbf{q}'} (\hat{S}_{\mathbf{q},\mathbf{q}'}^{(u,u')} \hat{\Gamma}_{\mathbf{q}}^\dagger \hat{\Gamma}_{\mathbf{q}'} + \hat{S}_{\mathbf{q},\mathbf{q}'}^{(u,v')} \hat{\Gamma}_{\mathbf{q}}^\dagger \hat{\Gamma}_{\mathbf{q}'}^\dagger + \hat{S}_{\mathbf{q},\mathbf{q}'}^{(v,u')} \hat{\Gamma}_{\mathbf{q}} \hat{\Gamma}_{\mathbf{q}'} + \hat{S}_{\mathbf{q},\mathbf{q}'}^{(v,v')} \hat{\Gamma}_{\mathbf{q}} \hat{\Gamma}_{\mathbf{q}'}^\dagger), \quad (2.25b)$$

where we used the following definitions

$$\hat{S}_{\mathbf{q}} = \frac{\sqrt{n_0 L^3}}{\hbar} (u_{\mathbf{q}} + v_{\mathbf{q}}^*) e^{i\mathbf{q}\cdot\hat{\mathbf{r}}} c_{\mathbf{q}}, \quad \hat{S}_{\mathbf{q},\mathbf{q}'}^{(u,u')} = \frac{u_{\mathbf{q}}^* u_{\mathbf{q}'}}{\hbar} e^{i(\mathbf{q}'-\mathbf{q})\cdot\hat{\mathbf{r}}} c_{\mathbf{q}'-\mathbf{q}}. \quad (2.26)$$

and the coefficient $c_{\mathbf{q}}$ is related to the scattering amplitude $f(q)$ by

$$c_{\mathbf{q}} = \frac{1}{L^3} \int_{\mathbb{R}^3} d\mathbf{s} e^{i\mathbf{q}\cdot\mathbf{s}} V(\mathbf{s}) = -\frac{2\pi\hbar^2}{\mu L^3} f(q). \quad (2.27)$$

The definitions of the remaining $\hat{S}_{\mathbf{q},\mathbf{q}'}$ operators are left out for brevity³ and can be found in Ref. [L1]. Note that the term $\hat{H}_{\text{SB}}^{(1)}$ comes from the density fluctuation $\delta\hat{n}$ in Eq. (2.22) and takes into account the interaction of the ion with the Bose-Einstein condensed gas. This is referred to as the *Fröhlich* model Hamiltonian, borrowing the denomination from the theory of electron-phonon coupling in solid-state physics [118]. The term $\hat{H}_{\text{SB}}^{(2)}$, instead, corresponds to the quadratic terms in Eq. (2.23) and corresponds to the so-called *extended Fröhlich* model [119, 120]. In the case of a Fermi gas, the excitations are particles and the system-bath interaction reduces to

$$\hat{H}_{\text{SB}} = \hbar \sum_{\mathbf{q},\mathbf{q}'} \hat{S}_{\mathbf{q},\mathbf{q}'} \hat{\Gamma}_{\mathbf{q}}^\dagger \hat{\Gamma}_{\mathbf{q}'} \quad (2.28)$$

with $\hat{S}_{\mathbf{q},\mathbf{q}'} = e^{i(\mathbf{q}'-\mathbf{q})\cdot\hat{\mathbf{r}}} c_{\mathbf{q}'-\mathbf{q}}/\hbar$.

Finally, let us remark that the choice of the system Hamiltonian \hat{H}_{S} will be made explicit later in the derivation. Unless specified, the following arguments will be valid for both the Hamiltonian for the ion in the Paul trap defined in Eq. (1.29) as well as for that of a free ion.

2.1.3 Atom-ion master equation

The Hamiltonian functions described above maintain their structure when translated to the interaction picture, and they are easily obtained from their definitions in the Schrödinger picture with the substitutions of their operators with the following time-dependent operators

$$\tilde{S}_{\mathbf{q}}(t) = \hat{U}^\dagger(0,t) \hat{S}_{\mathbf{q}} \hat{U}(0,t), \quad \tilde{S}_{\mathbf{q},\mathbf{q}'}^{(u,u')}(t) = \hat{U}^\dagger(0,t) \hat{S}_{\mathbf{q},\mathbf{q}'}^{(u,u')} \hat{U}(0,t), \quad (2.29)$$

and

$$\tilde{\Gamma}_{\mathbf{q}}(t) = e^{i\hat{H}_{\text{B}}t/\hbar} \hat{\Gamma}_{\mathbf{q}} e^{-i\hat{H}_{\text{B}}t/\hbar} = \hat{\Gamma}_{\mathbf{q}} e^{i\omega_{\mathbf{q}}t}. \quad (2.30)$$

The evolution operator depends on the system Hamiltonian \hat{H}_{S}

$$\hat{U}(t_1, t_2) = \mathcal{T} \exp \left[-\frac{i}{\hbar} \int_{t_1}^{t_2} dt \hat{H}_{\text{S}}(t) \right], \quad (2.31)$$

where \mathcal{T} represents the time-ordered product. In the case of a time-independent system Hamiltonian, such as the one of the free ion, the evolution operator takes the simple form $\hat{U}(t_1, t_2) = \exp[-i\hat{H}_{\text{S}}(t_2 - t_1)/\hbar]$.

³The omitted definitions will not play any role in our derivation because they are all proportional to $v_{\mathbf{q}}$ [see Eq. (2.18)]. As we will see in Sec. 2.1.3, we are going to set $u_{\mathbf{q}} = 1$ and $v_{\mathbf{q}} = 0$, which corresponds to considering particle-like excitations only.

We can now substitute the system-bath Hamiltonian in the interaction picture inside the Redfield equation in Eq. (2.11) and calculate the partial trace over the bath degrees of freedom. On this purpose, we consider a thermal bath at temperature T described by the density matrix

$$\hat{B}_0 = \frac{e^{-\beta_T(\hat{H}_B - \mu_{\text{gas}}\hat{N})}}{\mathcal{Z}}, \quad \mathcal{Z} = \text{Tr}_B \{ e^{-\beta_T(\hat{H}_B - \mu_{\text{gas}}\hat{N})} \} \quad (2.32)$$

where $\beta_T = 1/k_B T$, μ_{gas} is the chemical potential of the gas and \hat{N} is the bath number operator. Let us recall that we decomposed the system-bath interaction into the sum of the Fröhlich Hamiltonian $\tilde{H}_{\text{SB}}^{(1)}(t)$ defined in Eq. (2.25a) and the quadratic Hamiltonian $\tilde{H}_{\text{SB}}^{(2)}(t)$ defined in Eq. (2.25b). Hence, the nested commutator in the Redfield equation gives a sum of all the possible combinations of the two terms. Let us consider the commutators containing only the Fröhlich Hamiltonian or only the quadratic Hamiltonian:

$$\text{Tr}_B \left\{ \left[\tilde{H}_{\text{SB}}^{(1)}(t), \left[\tilde{H}_{\text{SB}}^{(1)}(t'), \tilde{\rho}(t) \otimes \hat{B}_0 \right] \right] \right\}, \quad \text{Tr}_B \left\{ \left[\tilde{H}_{\text{SB}}^{(2)}(t), \left[\tilde{H}_{\text{SB}}^{(2)}(t'), \tilde{\rho}(t) \otimes \hat{B}_0 \right] \right] \right\}. \quad (2.33)$$

The term on the left only exists in the presence of Bose-Einstein condensation. It includes the thermal averages of the products of two bath operators, where the product of two creation or two annihilation operators average to zero, while the mixed terms are finite. For instance, we have

$$\text{Tr}_B \left\{ \hat{B}_0 \tilde{\Gamma}_{\mathbf{q}}(t) \tilde{\Gamma}_{\mathbf{q}'}^\dagger(t') \right\} \equiv \langle \tilde{\Gamma}_{\mathbf{q}}(t) \tilde{\Gamma}_{\mathbf{q}'}^\dagger(t') \rangle_{B_0} = e^{-i\omega_{\mathbf{q}}(t-t')} (n_{\mathbf{q}} + 1) \delta_{\mathbf{q},\mathbf{q}'}, \quad (2.34)$$

where $n_{\mathbf{q}} = \langle \hat{b}_{\mathbf{q}}^\dagger \hat{b}_{\mathbf{q}} \rangle = \{ \exp[\beta_T(\hbar\omega_{\mathbf{q}} - \mu_{\text{gas}})] - 1 \}^{-1}$ is the Bose-Einstein occupation number.

The nested commutator on the right of Eq. (2.33), on the other hand, contains products of four bath operators. Their thermal averages are computed with the help of Wick's theorem [121]. For the sake of completeness, we report the following example:

$$\begin{aligned} & \langle \tilde{\Gamma}_{\mathbf{q}}^\dagger(t) \tilde{\Gamma}_{\mathbf{q}'}(t) \tilde{\Gamma}_{\mathbf{k}}^\dagger(t') \tilde{\Gamma}_{\mathbf{k}'}(t') \rangle_{B_0} \\ &= e^{i(\omega_{\mathbf{q}} - \omega_{\mathbf{q}'})t + i(\omega_{\mathbf{k}} - \omega_{\mathbf{k}'})t'} [n_{\mathbf{q}} \delta_{\mathbf{q}',\mathbf{k}} \delta_{\mathbf{q},\mathbf{k}'} + n_{\mathbf{q}} n_{\mathbf{q}'} (\delta_{\mathbf{q},\mathbf{q}'} \delta_{\mathbf{k},\mathbf{k}'} + \delta_{\mathbf{q}',\mathbf{k}} \delta_{\mathbf{q},\mathbf{k}'})], \end{aligned} \quad (2.35)$$

and we refer to Appendix B of Ref. [L1] for the other terms. The remaining commutators mixing the Fröhlich and the quadratic Hamiltonian do not contribute to the Redfield equation. In fact, they only include products of three bath operators, which always give zero when averaged over the thermal bath.

Now, we insert the above results inside Eq. (2.11). The master equation for the ion density matrix is obtained by transforming back to the Schrödinger picture and defining

the new variable $\tau = t - t'$. With the aim of contextualizing future discussions, we report the contribution from the condensed Bose gas:

$$\begin{aligned} \frac{d}{dt}\hat{\rho}(t) = & -\frac{i}{\hbar}\left[\hat{H}_S(t), \hat{\rho}(t)\right] - \sum_{\mathbf{q}} \int_0^t d\tau \Omega_{\mathbf{q}} \left\{ (n_{\mathbf{q}} + 1) \left[\hat{Z}_{\mathbf{q}}, \hat{W}_{\mathbf{q}}(t, \tau) \hat{\rho}(t) \right] + \right. \\ & \left. + n_{\mathbf{q}} \left[\hat{\rho}(t) \hat{W}_{\mathbf{q}}(t, \tau), \hat{Z}_{\mathbf{q}} \right] + \text{H.c.} \right\}, \end{aligned} \quad (2.36)$$

where

$$\Omega_{\mathbf{q}}^2 = \frac{|u_{\mathbf{q}} + v_{\mathbf{q}}^*|^2}{\hbar^2} |c_{\mathbf{q}}|^2 n_0 L^3, \quad \hat{Z}_{\mathbf{q}} = e^{i\mathbf{q}\cdot\hat{\mathbf{r}}}, \quad \hat{W}_{\mathbf{q}} = e^{-i\omega_{\mathbf{q}}\tau} e^{-i\mathbf{q}\cdot\hat{\mathbf{r}}(t, \tau)}, \quad (2.37)$$

H.c. indicates the Hermitian conjugate, n_0 is the density of the condensate, and $\hat{\mathbf{r}}(t, \tau) \equiv \hat{U}(0, t) \hat{U}^\dagger(0, t - \tau) \hat{\mathbf{r}} \hat{U}(0, t - \tau) \hat{U}^\dagger(0, t)$ is related to the motion of the ion in absence of the gas and depends on the choice of \hat{H}_S . Up to this point, Eq. (2.36) is valid for any impurity in a Bose-Einstein condensate provided that the scattering amplitude in the definition of $c_{\mathbf{q}}$ can be computed. The complete equation with the contributions from the quadratic terms can be found in Eq. (41) of Ref. [L1].

To further simplify the master equation, we perform the *Lamb-Dicke* approximation. This involves expanding the exponentials in the commutators of Eq. (2.36) to second order in the product $\mathbf{q}\cdot\hat{\mathbf{r}}$. To ensure the validity of this approximation, the de Broglie wavelength of the gas $\lambda_{\text{dB}}(T) = \sqrt{2\pi\hbar^2/(mk_{\text{B}}T)}$ has to be much larger than the spacial extension of the ion along the three directions. In fact, typical changes in the atom momentum after an atom-ion collision are on the order of $1/\lambda_{\text{dB}}$. The first commutator inside the curly brackets of Eq. (2.36) reads

$$\begin{aligned} \left[\hat{Z}_{\mathbf{q}}, \hat{W}_{\mathbf{q}}(t, \tau) \hat{\rho}(t) \right] \simeq & e^{-i\omega_{\mathbf{q}}\tau} \left\{ i[\mathbf{q}\cdot\hat{\mathbf{r}}, \hat{\rho}(t)] + [\mathbf{q}\cdot\hat{\mathbf{r}}, \mathbf{q}\cdot\hat{\mathbf{r}}(t, \tau) \hat{\rho}(t)] - \right. \\ & \left. - \frac{1}{2} [(\mathbf{q}\cdot\hat{\mathbf{r}})^2, \hat{\rho}(t)] \right\}. \end{aligned} \quad (2.38)$$

Due to the symmetric summation over \mathbf{q} in the master equation, any term containing odd powers of q_ξ vanishes. Hence, terms like the first on the right hand side of Eq. (2.38) or any term coupling two different directions can be ruled out from the equation. Note that the same arguments cannot be applied to the case of a non homogeneous gas.

Finally, we apply the *particle-like* approximation to the equation for a bosonic bath. In case of a large energy difference between the bath and the ion, only particle-like excitations with dispersion relation $\omega_{\mathbf{q}} = \hbar q^2/(2m)$ couple to the ion motion. Therefore, we can assume the Bogolyubov amplitudes to satisfy $u_{\mathbf{q}} = 1$ and $v_{\mathbf{q}} = 0$. Such a simplification allows to only consider the first term in Eq. (2.25b), making the quadratic Hamiltonian for the Bose bath analogous to that for the Fermi bath in Eq. (2.28). The validity of the aforementioned approximations will be discussed separately for the trapped and free ion in the paragraphs dedicated to each of the two systems.

Before going ahead, let us recall that we are considering the gas to be confined in a box of volume L^3 . Therefore, the wave vector \mathbf{q} , assumes the quantized values $2\pi s_\xi/L$ with $s_\xi \in \mathbb{Z}$ along each direction. In the limit $L \rightarrow \infty$, those values become closely spaced and we can perform the substitution

$$\sum_{\mathbf{q}} \longrightarrow \frac{L^3}{(2\pi)^3} \int_{\mathbb{R}^3} d\mathbf{q}, \quad (2.39)$$

which is reasonable for a large bath.

Trapped ion Let us begin by discussing the validity of the particle-like and Lamb-Dicke approximations for the case of an ion in a Paul trap. The former is ensured by the choice of the trap parameters, as typical values result in a small speed of sound in the gas compared to the secular motion of the ion. For example, we consider the parameters for the x direction reported in Ref. [122]: $a_x = -0.001$, $q_x = 0.2$, $\Omega_{\text{rf}} = 2\pi \cdot 2 \text{ MHz}$, which results in a reference frequency $\nu_x \simeq 2\pi \cdot 169 \text{ kHz}$ for an ytterbium ion. The rescaled speed of sound for a sodium gas with $n_0 = 10^{14} \text{ cm}^{-3}$ in units of ν_x and $\ell_x = \sqrt{\hbar/(m\nu_x)}$ is $\bar{c}_s \simeq 0.009$. However, only phonons with energy comparable to $\hbar\nu_x$ couple to the ion motion. This leads to an atom velocity of $\bar{v}_x \simeq 1.4 \gg \bar{c}_s$, showing that the particle-like dispersion relation can be safely assumed. The applicability of the Lamb-Dicke approximations is also related to the trap parameters. In fact, the spatial extension of the ion can be estimated with the width of the ground state of the trap $l_\xi = \sqrt{\hbar/(M\nu_\xi)}$. For sodium atoms at $T = 200 \text{ nK}$, and the same parameters above, we get $l_x/\lambda_{\text{dB}} \simeq 0.023$.

On top of the two approximations justified above, we assume that the system varies in a timescale much larger than the timescale of the bath. This translates into the limit $t \rightarrow \infty$ in the time integral, and allows to use the following identity

$$\int_0^\infty d\tau e^{\pm i(\omega - \omega_0)\tau} = \pi\delta(\omega - \omega_0) \pm i \text{P} \left(\frac{1}{\omega - \omega_0} \right), \quad (2.40)$$

where δ denotes the Dirac delta, and P the Cauchy's principal value.

We can now proceed by identifying the system Hamiltonian with that of the parametric quantum harmonic oscillator in Eq. (1.29). Therefore, $\hat{r}_\xi(t, \tau)$ can be computed from Eq. (1.37) and Eq. (1.38), and reads

$$\hat{r}_\xi(t, \tau) = \sum_{s, s'} C_s^\xi C_{s'}^\xi \left\{ \hat{r}_\xi \left(\frac{\beta_\xi}{2} + s' \right) \frac{\Omega_{\text{rf}}}{\nu_\xi} \cos \left[\mathcal{I}_{s, s'}^\xi(t, \tau) \right] - \frac{\hat{p}_\xi}{M\nu_\xi} \sin \left[\mathcal{I}_{s, s'}^\xi(t, \tau) \right] \right\}, \quad (2.41)$$

with

$$\mathcal{I}_{s, s'}^\xi(t, \tau) = \Omega_{\text{rf}} \left[\left(\frac{\beta_\xi}{2} + s \right) \tau - (s - s')t \right]. \quad (2.42)$$

Using all the aforementioned identities and simplifications we can write the master equation in a compact form:

$$\begin{aligned} \frac{d}{dt}\hat{\rho}(t) = & -\frac{i}{\hbar}\left[\hat{H}_S(t) + \delta\hat{H}_S(t), \hat{\rho}(t)\right] - \Gamma \sum_{\xi=x,y,z} \left\{ \Lambda_{\xi}(t)[\hat{r}_{\xi}, \hat{\rho}(t)\hat{p}_{\xi}] - \right. \\ & \left. -\Lambda_{\xi}^*(t)[\hat{r}_{\xi}, \hat{p}_{\xi}\hat{\rho}(t)] - \Phi_{\xi}(t)[\hat{r}_{\xi}, \hat{\rho}(t)\hat{r}_{\xi}] + \Phi_{\xi}^*(t)[\hat{r}_{\xi}, \hat{r}_{\xi}\hat{\rho}(t)] \right\}, \end{aligned} \quad (2.43)$$

where $\Gamma = 2mn_0\pi\hbar/(3\mu^2)$, while $\Lambda_{\xi}(t)$ and $\Phi_{\xi}(t)$ are oscillating functions that depend on all the parameters involved in the description as well as on the gas statistics. The term proportional to Γ takes into account the action of the bath on the ion, whereas the first commutator represents the unitary evolution of the ion in the Paul trap in absence of the surrounding gas. The term $\delta\hat{H}_S$ is the so-called Lamb-Shift, and is a correction to the trap parameters corresponding to part of the terms coming from the Cauchy's principal value in Eq. (2.40). The Lamb-Shift is only considered for the Bose-Einstein condensed gas. We refer again to Ref. [L1] for the omitted definitions and other details on the derivation.

Free ion Here, we consider the scenario where an ion is created by ionizing one of the atoms of the gas. In this description, the ion is not confined by a trap and the system Hamiltonian is simply that of a free particle: $\hat{H}_S = \hat{p}^2/(2M)$. Therefore, we have $\hat{r}_{\xi}(t, \tau) = \hat{r}_{\xi} - (\hat{p}_{\xi}/M)\tau$.

In order to discuss the validity of the Lamb-Dicke approximation, let us focus on the ionization process described in Ref. [123]. There, a laser is focused with a beam waist w_0 much smaller than the atomic cloud. An ultrafast pulse of the laser with duration 215 fs allows a single atom to be ionized inside the condensate. This procedure can be interpreted as a continuous measurement, where the beam with Gaussian envelope $\exp(-2\mathbf{r}^2/w_0^2)$ is the probe field [124]. Under these conditions, the spacial extent of the initial state of the ion is estimated with the beam waist w_0 , and the condition for the Lamb-Dicke approximation to be valid is $\omega_0 \ll \lambda_{\text{dB}}$. Fixing the waist to the experimentally available value $w_0 = 1 \mu\text{m}$, we find that the gas temperature $T = 1 \text{ nK}$ satisfies the previous inequality. We refer to Ref. [L3] for a more detailed discussion, and for the case of ionization via a Rydberg state.

Since we limit the derivation to the case of a Bose-Einstein condensate, Eq. (2.36) contains all the terms we need. Using the $\hat{r}_{\xi}(t, \tau)$ above and performing the time integral, we get a master equation analogous to that for the trapped ion in Eq. (2.43). We refer the interested reader to Appendix C of Ref. [L3], where all the definitions are reported.

2.1.4 Solution strategies

Knowing the density matrix $\hat{\rho}(t)$ of the ion allows to calculate the expectation value of any observable \hat{O} with the relation $\langle \hat{O} \rangle = \text{Tr}\{\hat{O}\hat{\rho}(t)\}$. For this purpose, the master equations for the trapped ion in Eq. (2.43) and for the free ion (see Ref. [L3]), can be used to find a set of coupled differential equations for the elements of the ion density matrix. Note that, thanks to the Lamb-Dicke approximation, the three directions are decoupled and the 3D master equation corresponds to three separate equations. In principle, the dimension

of the basis set used to compute the matrix elements has to be infinite, meaning that a truncation is necessary to implement numerical simulations. However, this strategy turned out to be computationally very demanding, due to the large number of basis elements that are necessary to describe the evolution of the ion. Moreover, while for the trapped ion a natural choice is the basis of the harmonic oscillator with frequency ν_ξ [see Sec. 1.2.2 and Eq. (1.34)], it is not trivial to find a convenient basis set for the free ion⁴.

One way around the aforementioned problems consists of identifying the observables of interest, and using Eq. (2.43) or the equivalent for the free ion to find the differential equation for their expectation values by explicitly computing $\text{Tr}\{\hat{\mathcal{O}}\hat{\rho}(t)\}$. Of course, such a strategy comes with a loss of information, as the total density matrix remains unknown. Nevertheless, it allows the whole Hilbert space to be considered.

For the trapped ion, we are interested in its kinetic energy and we find that the equation for $\langle \hat{p}_\xi^2 \rangle$ forms a closed set of coupled differential equations with the remaining second order moments $\langle \hat{r}_\xi^2 \rangle$ and $\langle \hat{c}_\xi \rangle = \langle \hat{r}_\xi \hat{p}_\xi + \hat{p}_\xi \hat{r}_\xi \rangle$:

$$\begin{aligned} \frac{d}{dt} \langle \hat{r}_\xi^2 \rangle &= \frac{1}{M} \langle \hat{c}_\xi \rangle \\ \frac{d}{dt} \langle \hat{p}_\xi^2 \rangle &= \left\{ 2\hbar\Gamma \text{Im}[\Phi_\xi(t)] - MW'_\xi(t) \right\} \langle \hat{c}_\xi \rangle - \\ &\quad - 4\hbar\Gamma \text{Im}[\Lambda_\xi(t)] \langle \hat{p}_\xi^2 \rangle + 2\hbar^2\Gamma \text{Re}[\Phi_\xi(t)] \\ \frac{d}{dt} \langle \hat{c}_\xi \rangle &= 2 \left\{ 2\hbar\Gamma \text{Im}[\Phi_\xi(t)] - MW'_\xi(t) \right\} \langle \hat{r}_\xi^2 \rangle + \frac{2}{M} \langle \hat{p}_\xi^2 \rangle - \\ &\quad - 2\hbar\Gamma \text{Im}[\Lambda_\xi(t)] \langle \hat{c}_\xi \rangle + 2\hbar^2\Gamma \text{Re}[\Lambda_\xi(t)]. \end{aligned} \quad (2.44)$$

For the first order moments $\langle \hat{r}_\xi \rangle$ and $\langle \hat{p}_\xi \rangle$ we get

$$\begin{aligned} \frac{d}{dt} \langle \hat{r}_\xi \rangle &= \frac{1}{M} \langle \hat{p}_\xi \rangle \\ \frac{d}{dt} \langle \hat{p}_\xi \rangle &= \left\{ 2\hbar\Gamma \text{Im}[\Phi_\xi(t)] - MW'_\xi(t) \right\} \langle \hat{r}_\xi \rangle - 2\hbar\Gamma \text{Im}[\Lambda_\xi(t)] \langle \hat{p}_\xi \rangle. \end{aligned} \quad (2.45)$$

Analogous calculations bring to the equations for the first and second order moments of a free ion. We refer to Sec. III of Ref. [L3] for details.

⁴Although the choice of the basis should not affect the description, it becomes crucial when the simulations can only investigate a finite subspace of an infinite Hilbert space. In fact, a poor choice would result in the occupation of the states quickly dropping to zero, hence in a very large number of states required to preserve the trace of the density matrix

2.2 Temperature estimation with a two-level ion

The theory of quantum parameter estimation provides analytical tools to find the optimal measurement of a given quantity. This becomes essential whenever such a quantity is not directly accessible, due to theoretical reasons or experimental limitations. For instance, this is a common scenario in quantum mechanical systems, where relevant quantities do not always correspond to proper observables. In these situations, an indirect approach becomes necessary, where the value of the desired quantity is extrapolated from the measure of a different observable. In this section, we see how to exploit the decoherence dynamics of a charged two-level system coupled to a Fermi gas in order to optimize the measure of the gas temperature.

2.2.1 Decoherence dynamics

We consider a trapped ion with wave function $\chi(\mathbf{r})$ and two internal states $|0\rangle$ and $|1\rangle$. The ion is immersed in a homogeneous spin-polarized non-interacting Fermi gas with mean density \bar{n} . The density defines the following characteristic quantities of the gas: the Fermi wave vector $k_F = (6\pi\bar{n})^{1/3}$, energy and temperature $E_F = \hbar^2 k_F^2 / (2m) = k_B T_F$ and time $\tau_F = \hbar / E_F$, where k_B is the Boltzmann constant and m the mass of the atoms. We will henceforth refer to the gas as bath.

The objective of our description is to infer the temperature of the bath from the dynamics of the internal states of the ion, which will therefore serve as a probe. On this purpose, we write the total Hamiltonian as a sum of three terms: $\hat{H} = \hat{H}_P + \hat{H}_B + \hat{H}_I$. The Hamiltonian of the probe is

$$\hat{H}_P = E_0 |0\rangle \langle 0| + E_1 |1\rangle \langle 1|, \quad (2.46)$$

where we ignored the part describing the motion of the ion because we treat it as a static impurity.

The many-body bath Hamiltonian reads

$$\hat{H}_B = \int_{\mathbb{R}^3} d\mathbf{r} \hat{\Psi}^\dagger(\mathbf{r}) \left[-\frac{\hbar^2}{2m} \nabla^2 \right] \hat{\Psi}(\mathbf{r}) \quad (2.47)$$

where $\hat{\Psi}$ is the fermionic antisymmetric field operator satisfying the anticommutation relation $\{\hat{\Psi}(\mathbf{r}), \hat{\Psi}^\dagger(\mathbf{r}')\} = \delta(\mathbf{r} - \mathbf{r}')$.

Finally, the internal states interact asymptotically with the atoms in the bath via the polarization potential $-C_4/r^4$ introduced in Sec. 1.1.1. Due to its singularity, similarly to what we have done for the derivation of the atom-ion master equation, we use the regularization in Eq. 1.14. We refer to Sec. 1.1.3 for details. Hence, the interaction Hamiltonian describing the coupling of the ion with the bath is

$$\hat{H}_I = \sum_{s=0,1} \int_{\mathbb{R}^3} d\mathbf{r} \hat{\Psi}^\dagger(\mathbf{r}) V_{\text{reg}}^{(s)}(\mathbf{r}) \hat{\Psi}(\mathbf{r}) \otimes |s\rangle \langle s|. \quad (2.48)$$

Note that the regularized atom-ion potential relies on the internal state $s = 0, 1$. In fact, the use of external magnetic fields can be employed to tune the interaction parameters (e.g. the atom ion scattering length a_{ai} or the number of bound states) independently for the two spin states. Moreover, we remark that in the case of a neutral two-level system, the interaction of the state $|0\rangle$ with the bath can be set to zero by properly tuning the impurity-atom scattering length, as proposed in Ref. [125]. In our case, instead, the long-range tail of the polarization potential cannot be set to zero. As we will see in Sec. 2.2.3, this characteristic requires some precautions to be taken in the application of the thermometric protocol to the ionic probe.

The spin dynamics of the probe can be described by means of the the density matrix $\hat{\rho}_{\text{P}}(t) = (\mathbb{I} + \mathbf{v} \cdot \hat{\boldsymbol{\sigma}})/2$, where \mathbf{v} is the *Bloch vector* and $\hat{\boldsymbol{\sigma}} = (\hat{\sigma}_x, \hat{\sigma}_y, \hat{\sigma}_z)$ is the vector of the Pauli matrices. Considering the initial state of the probe to be an equal superposition of the two internal states, namely $|+\rangle = (|0\rangle + |1\rangle)/\sqrt{2}$ (modulo a global phase), the initial density matrix of the composite system is $\hat{\rho}(0) = |+\rangle\langle +| \otimes \hat{\rho}_{\text{B}}(T)$, where $\hat{\rho}_{\text{B}}(T)$ is the thermal state of the bath at temperature T . Under this assumption, the components of the Bloch vector are defined by⁵

$$\mathbf{v}(t) \equiv (v_x, v_y, v_z) = (\text{Re}[\nu(t)], \text{Im}[\nu(t)], 0), \quad (2.49)$$

where $\nu(t)$ is the so-called time-dependent *decoherence function*:

$$\nu(t) = \text{Tr}_{\text{B}} \left\{ e^{i\hat{H}_1 t/\hbar} e^{-i\hat{H}_0 t/\hbar} \hat{\rho}_{\text{B}}(T) \right\}. \quad (2.50)$$

Here, $\hat{H}_s = \langle s | \hat{H}_{\text{B}} + \hat{H}_{\text{I}} | s \rangle$ ($s = 0, 1$), and the trace is taken over the bath degrees of freedom. The z component of the Bloch vector being zero indicates that the populations of $|0\rangle$ and $|1\rangle$ are conserved in time and equal to $1/2$. In other words, the system undergoes *pure dephasing*, with the Bloch vector confined to the equatorial plane and the coherences evolving according to $\nu(t)$.

For a quadratic time-independent Hamiltonian, as it is in our case, the Levitov formula [126, 127] can be used to compute the decoherence function:

$$\nu(t) = \det \left\{ 1 - \hat{n} + \hat{n} e^{i\hat{h}_0 t/\hbar} e^{-i\hat{h}_1 t/\hbar} \right\}, \quad (2.51)$$

where $\hat{n} = \{\exp[\beta(\hat{h}_{\text{B}} - \mu)] + 1\}^{-1}$ is the Fermi distribution, μ is the chemical potential, $\beta = 1/(k_{\text{B}}T)$ and

$$\hat{h}_{\text{B}} = -\frac{\hbar^2}{2m}\nabla^2, \quad \hat{h}_s = \hat{h}_{\text{B}} + V_{\text{eff}}^{(s)}(\mathbf{r}) \quad (\text{with } s = 0, 1). \quad (2.52)$$

⁵To obtain Eq. (2.49), one has to start from the total density matrix of the composite system $\hat{\rho}(t) = \hat{U}(t)\hat{\rho}(0)\hat{U}^\dagger(t)$ with $\hat{U}(t) = \exp(-i\hat{H}t/\hbar)$, and compute the three components of the Bloch vector with $v_i = \text{Tr}\{\hat{\rho}(t)\hat{\sigma}_i\}$ ($i = x, y, z$), where the trace is taken over both the probe and the bath states.

The effective impurity-bath interaction is given by the convolution between the atom-ion potential and probability density $|\chi(\mathbf{r})|^2$ of the probe:

$$V_{\text{eff}}^{(s)}(\mathbf{r}) = \int_{\mathbb{R}^3} d\mathbf{r}' V_{\text{reg}}^{(s)}(\mathbf{r} - \mathbf{r}') |\chi(\mathbf{r})|^2. \quad (2.53)$$

In Ref. [L2] we investigate two scenarios: a delta-shaped distribution $|\chi(\mathbf{r})|^2 \propto \delta(r)$, corresponding to a point particle, and a Gaussian distribution with finite width σ , for which $|\chi(\mathbf{r})|^2 \propto \exp[-r^2/(2\sigma^2)]$, representing the spatial distribution of an ion in the ground state of a Paul trap or in an optical trap. We refer to Sec. IV of Ref. [L2] for details.

2.2.2 Quantum Cramer-Rao bound

Let us consider a Hermitian operator \hat{X} with eigenvalues x_s . We indicate with $p(x_s|T)$ the conditional probability to obtain x_s from a projective measure on the eigenspace of \hat{X} , given the gas temperature T . The classical *Fisher information* carried by \hat{X} about the gas temperature is defined by [128]

$$\mathcal{F}_T \equiv \mathcal{F}_T(\hat{X}) = - \sum_{s=\pm} p(x_s|T) \frac{\partial^2}{\partial T^2} \ln[p(x_s|T)], \quad (2.54)$$

where we used the fact that for a two-level system only two eigenvalues of \hat{X} are possible.

According to the theory of quantum parameter estimation [129–132], the quantum Cramer-Rao bound (QCRB), gives a bound from below to the attainable uncertainty ΔT for the estimation of the gas temperature after N independent measurements. The QCRB is valid in the limit $N \gg 1$ for any unbiased estimator [133] and reads

$$\Delta T^2 \geq \frac{\mathcal{F}_T}{N} \geq \frac{\mathcal{F}_T^{\mathcal{Q}}}{N}. \quad (2.55)$$

Given this, the Fisher information is related to its quantum counterpart $\mathcal{F}_T^{\mathcal{Q}}$ by the identity $\mathcal{F}_T^{\mathcal{Q}} = \max_{\hat{X}} \{\mathcal{F}_T(\hat{X})\}$. Moreover, we introduce the *quantum signal-to-noise ratio* (QSNR) \mathcal{Q} , defined by $\mathcal{Q}^2 = T^2 \mathcal{F}_T^{\mathcal{Q}}$. Using this definition in Eq. (2.55), we get the following inequality

$$\frac{\Delta T}{T} \geq \frac{1}{\mathcal{Q}\sqrt{N}}, \quad (2.56)$$

which shows that, for fixed N , the theoretical lower limit for the attainable temperature uncertainty is given by the QSNR.

For a two-level system, it can be demonstrated that $\mathcal{F}_T^{\mathcal{Q}} = \mathcal{F}_T(\hat{\Lambda}_T)$ [129], where $\hat{\Lambda}_T$ is the symmetric logarithmic derivative (SLD). In other words, the Fisher information

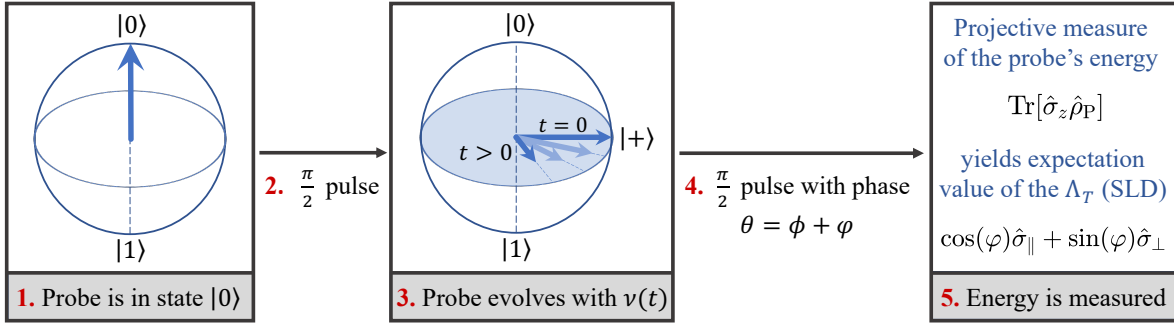


Figure 2.1: Scheme of the thermometric protocol.

carried by the projective measurement of the SLD is higher than or equal to that carried by the measurement of any other observable, and it's equal to the quantum Fisher information. Indicating the decoherence function as $\nu = |\nu|e^{i\phi}$, we have

$$\hat{\Lambda}_T \propto \cos(\varphi)\hat{\sigma}_{\parallel} + \sin(\varphi)\hat{\sigma}_{\perp}, \quad \tan(\varphi) = \frac{|\nu|(1-|\nu|)^2 \partial_T \phi}{\partial_T |\nu|}, \quad (2.57)$$

where $\hat{\sigma}_{\parallel} = \cos(\phi)\hat{\sigma}_x + \sin(\phi)\hat{\sigma}_y$ and $\hat{\sigma}_{\perp} = \cos(\phi)\hat{\sigma}_y - \sin(\phi)\hat{\sigma}_x$. Moreover, the quantum Fisher information for a two-level system can be also expressed in terms of $\nu(t)$. In polar coordinates, it is written as

$$\mathcal{F}_T^{\mathcal{Q}} = \frac{1}{1-|\nu|^2} \left(\frac{\partial |\nu|}{\partial T} \right)^2 + |\nu|^2 \left(\frac{\partial \phi}{\partial T} \right)^2 = \mathcal{F}_T^{\parallel} + \mathcal{F}_T^{\perp}, \quad (2.58)$$

where $\mathcal{F}_T^{\parallel}$ and \mathcal{F}_T^{\perp} denote the contribution parallel and perpendicular to the Bloch vector, respectively. More precisely, these two terms correspond to the Fisher information retained by the projective measure of the SLD in the basis of $\hat{\sigma}_{\parallel}$ and $\hat{\sigma}_{\perp}$. However, due to the dependence of $\hat{\sigma}_{\parallel,\perp}$ on both ϕ and φ , such a measure relies on the a priori knowledge of the gas temperature, i.e. of the unknown quantity of the problem. In Sec. 2.2.3, we will see how to address this problem with the thermometric protocol proposed in Ref. [125].

2.2.3 Thermometric protocol

We here discuss the protocol designed to infer the gas temperature from the decoherence dynamics of a two-level neutral or charged impurity. The protocol (see Fig. 2.1 for a scheme) is aimed at determining the expectation value of the SLD (see previous section), and it can be summarized in the following five steps:

1. the probe is prepared in the state $|0\rangle$, which does not interact with the bath. The initial density matrix of the composite system is therefore $\hat{\rho} = |0\rangle\langle 0| \otimes \hat{\rho}_B(T)$. As we already mentioned in Sec. 2.2.1, only a neutral impurity can be prepared in such a

way that one of the two states does not interact with the bath. We refer to Ref. [L2] for some strategies to overcome this issue. For instance, we can assume that the probe is initially neutral. Then, a two-photon process such as the one described in Ref. [64] can simultaneously ionize the probe and perform a $\pi/2$ pulse (see next point);

2. a $\pi/2$ pulse brings the probe to the superposition state $|+\rangle = (|0\rangle + |1\rangle)/\sqrt{2}$. We assume the pulse to be instantaneous and to be performed at $t = 0$;
3. at $t > 0$, the internal states of the probe evolve according to the decoherence function in Eq. (2.51). At this stage, the dephasing dynamics of the probe depends on the gas temperature via $\nu(t)$, which governs both the rotation in the equatorial plane of the Bloch vector and the reduction of its magnitude. Note that the evolution of the two internal states depend on the corresponding interaction with the bath;
4. after some time, a second $\pi/2$ pulse with relative phase θ is performed. After this pulse, the z component of the Bloch vector will no longer be zero, and its value will depend on the decoherence dynamics that occurred at the previous step;
5. the energy of the probe is projectively measured with $\text{Tr}\{\hat{\sigma}_z \hat{\rho}_P\}$, yielding a value proportional to $\cos(\theta)\langle\hat{\sigma}_x\rangle + \sin(\theta)\langle\hat{\sigma}_y\rangle$. According to the definition of the SLD in Eq. (2.57), one can determine $\langle\hat{\Lambda}_T\rangle$ by choosing $\theta = \phi + \varphi$. We note that measuring the energy is experimentally more feasible than performing measures in the eigenbasis of $\hat{\sigma}_{\parallel,\perp}$, although selecting ϕ and φ still requires a prior knowledge of the temperature. However, one can perform several measurements with different values of θ , and infer the value of the temperature by means of statistical analysis (see next paragraph).

Repeating the protocol above N times, yields a set $\{\xi_k\}_{k=1}^N$ of independent experimental values. Here, ξ_k is the outcome of the of the measurement of $\hat{\Lambda}_T$ on the k -th run, and corresponds to one of its two eigenvalues λ_{\pm} . Such a repetition will therefore produce N_+ measurements of λ_+ and N_- measurements of λ_- , with $N_+ + N_- = N$. Before estimating the temperature, one needs to determine the probability $p(\xi_k|T)$ of obtaining the outcome ξ_k at temperature T , which is still unknown. This is done by means of the expectation value of $\hat{\Lambda}_T$ [131]

$$p(\lambda_{\pm}|T) = \frac{1 \pm \langle\hat{\Lambda}_T\rangle}{2} = \frac{1 \pm f(\langle\hat{E}_T\rangle)}{2}, \quad f(\langle\hat{E}_T\rangle) = \frac{2\langle\hat{E}_T\rangle - E_{\max} - E_{\min}}{E_{\max} - E_{\min}}. \quad (2.59)$$

Now, a calibration of the thermometer is necessary. This can be accomplished for instance by measurements of $p(\lambda_{\pm}|T) = N_{\pm}/N$ for some known value of T and $N \gg 1$. After that, the unknown value of the temperature can be inferred from the set $\{\xi_k\}_{k=1}^N$ by means of a function \mathcal{T} , which in this context is referred to as estimator. A common choice for the latter is the maximum likelihood, defined as the value that maximizes the joint probability $\prod_k p(\xi_k|T)$ with respect to T . For more mathematical details, we refer to Ref. [134], where a similar procedure was applied for the estimation of the gradient of a magnetic field.

Main results of author's publications

In this chapter, we summarize the scientific contributions of the author's publications [L1–L3], reporting the motivation and the main outcomes of our studies.

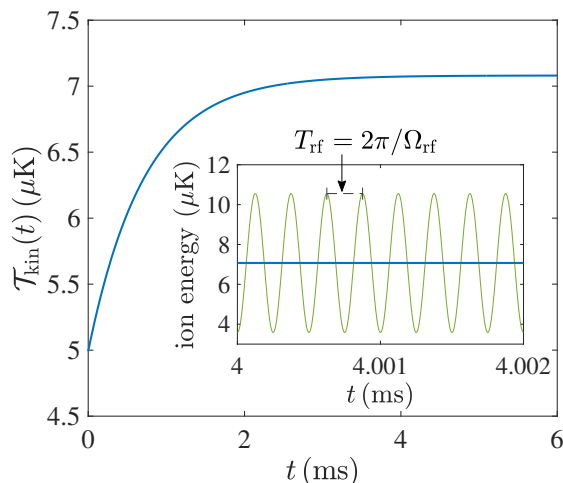


Figure 3.1: The time dependence of the ion's kinetic temperature is shown by the blue line. The green line in the inset represents the fast oscillating kinetic energy before the integral average over the micromotion, while the dashed gray line indicates the period of oscillation.

3.1 [L1] – Dynamics of a trapped ion in a quantum gas: effects of particle statistics

The goal of the study published in Ref. [L1] is to understand the non-equilibrium dynamics of a single ion confined in a Paul trap and immersed in a bath of ultracold Bosons or Fermions. For this purpose, we resort to the master equation approach outlined in Sec. 2.1. In particular, we recall that we derive a master equation in the Born-Markov and Lamb-Dicke approximations for the reduced density matrix of the ion, which is therefore treated as an open system. A similar approach was adopted in Ref. [135–137] for a neutral impurity and in Ref. [74] for an ion in a condensate, where the derivation of the master equation only included the contribution from the BEC, i.e. the Fröhlich Hamiltonian in Eq. (2.25a). In our work, the non condensed part of the Bose gas is also included via the quadratic terms of the extended Fröhlich Hamiltonian in Eq. (2.25b), and similar methods are employed to derive a master equation for the case of a Fermi gas. Moreover, the normalization of the ion trap parameters due to the coupling with the gas, i.e. the Lamb-Shift (LS), is also considered for the Bose gas. For these reasons, the final master equation reported in Eq. (2.43) can be regarded as the main analytical result of this study. As far as numerical simulations are concerned, we solve the coupled equations for the second order moments along the three directions [see Eq. (2.44)] in order to attain the ion's kinetic temperature, which is defined as [138]

$$\mathcal{T}_{\text{kin}}(t) = \frac{2}{3k_{\text{B}}} \langle \langle \hat{H}_{\text{kin}}(t) \rangle \rangle_{T_{\text{rf}}}, \quad \langle \langle \hat{H}_{\text{kin}}(t) \rangle \rangle_{T_{\text{rf}}} = \frac{1}{T_{\text{rf}}} \int_t^{t+T_{\text{rf}}} dt' \sum_{\xi=x,y,z} \frac{\langle \hat{p}_{\xi}^2(t') \rangle}{2M}. \quad (3.1)$$

Here, $\langle \hat{p}_{\xi}^2(t) \rangle$ is the time-dependent solution of the system of differential equations along the ξ direction and $T_{\text{rf}} = 2\pi/\Omega_{\text{rf}}$ is the period of the radiofrequency oscillation (see

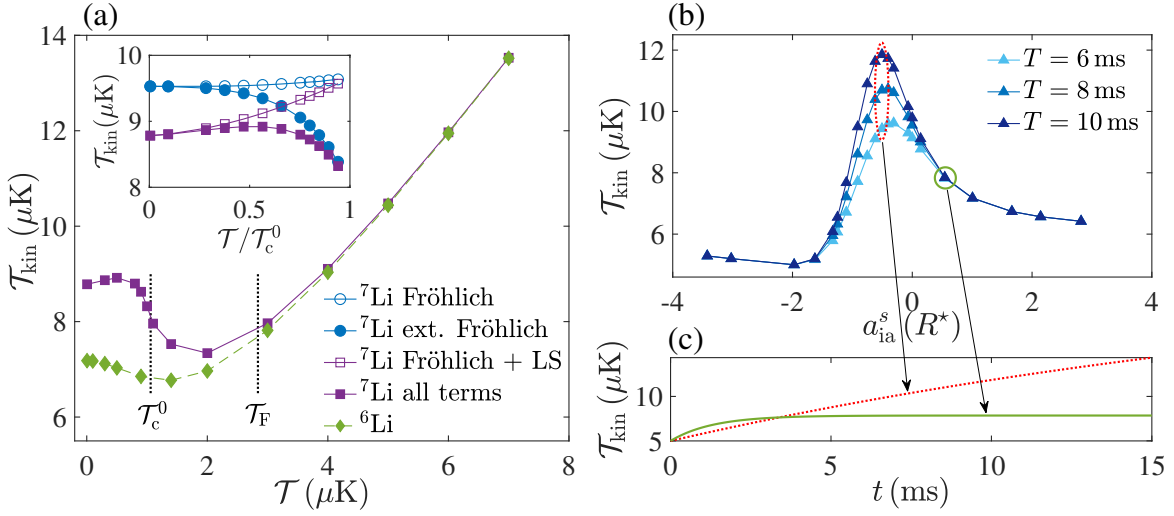


Figure 3.2: Temperature of ${}^{174}\text{Yb}^+$. **(a)** Final ion temperature as a function of the gas temperature for a total density $n_t = 10^{13} \text{ cm}^{-3}$. The regularized atom-ion potential is characterized by $b \simeq 0.078 R^*$ and $c \simeq 0.224 R^*$, corresponding to $a_{\text{ai}} \simeq R^*$. The s -wave threshold temperatures are $\mathcal{T}_s \simeq 256 \mu\text{K}$ for ${}^6\text{Li}$, $\mathcal{T}_s \simeq 164 \mu\text{K}$ for ${}^7\text{Li}$. *Main plot:* comparison between ${}^6\text{Li}$ (Fermion) and ${}^7\text{Li}$ (Boson). The vertical dotted lines represent the critical temperature of condensation of the Bose gas $\mathcal{T}_0^0 \simeq 1.06 \mu\text{K}$ and the Fermi temperature $\mathcal{T}_F \simeq 2.84 \mu\text{K}$; *inset:* different contributions to the bosonic case below \mathcal{T}_c^0 . **(b)** Ion temperature at different simulation times as a function of the atom-ion scattering length. The bath is ${}^6\text{Li}$ with fixed $n_t = 10^{13} \text{ cm}^{-3}$ and $\mathcal{T} = 0.1 \mu\text{K}$. **(c)** Time dependence of ion temperature for two selected values of the atom-ion scattering length. All the lines connecting the points are a mere guide to the eye. Figures adapted from Ref. [L1].

Fig. 3.1). Note that the inner angle brackets represent the expectation value of the operator, while the outer ones indicate the integral average over the rf-induced micromotion.

The main plot of Fig. 3.1 shows that the ion temperature increases due to the interaction with the gas and saturates to a finite value. Our simulations are mainly aimed at studying how this final value depends on the parameters of the system, such as the statistics of the gas (Bose or Fermi), the gas density and temperature and the atom-ion scattering length. The relevance of such a study is mainly given by the presence of several experiments involving a Paul-trapped ion in a bosonic [48, 51, 61, 139–141] or fermionic [24, 57] ultracold gas. Other theoretical works have studied the impact of micromotion on the atom-ion quantum dynamics. These include quantum mechanical calculations in 1D [142, 143] and semiclassical calculations in quasi-1D [144, 145]. Here, we consider a ${}^{174}\text{Yb}^+$ ion trapped in a linear Paul trap with parameters $a_{x,y} = -0.001$, $a_z = 0.002$, $q_x = -q_y = 0.2$, $q_z = 0$, $\Omega_{\text{rf}} = 2\pi \cdot 2 \text{ MHz}$, and immersed in a gas of ${}^6\text{Li}$ or ${}^7\text{Li}$ atoms. The main results are summarized in the next paragraphs.

General remarks First, we observe that for the considered parameters and a gas temperature between a few nano Kelvin and a few micro Kelvin, the ion temperature converges to values well below the threshold for the s -wave regime. With the same parameters and a bath of ${}^{23}\text{Na}$ atoms, however, the s -wave regime is not reached, confirming that a small

atom-ion mass ratio is preferable for this purpose¹. Moreover, we observe that below the Fermi temperature \mathcal{T}_F of the ${}^6\text{Li}$ gas, the latter guarantees lower ion temperatures compared to the ${}^7\text{Li}$ gas (see Fig. 3.2(a)). Being the atomic masses very similar in the two cases, we can attribute this behavior to the different quantum statistics. At higher temperatures, on the other hand, the difference between the fermionic and bosonic bath vanish and both reproduce the effect of a buffer gas.

For the bosonic gas below the critical temperature of condensation \mathcal{T}_c^0 , the impact of the different terms contributing to the master equation is evaluated. As shown in the inset of Fig. 3.2(a), both the quadratic terms (extended Fröhlich) and the Lamb-Shift (LS) allow for lower ion temperatures. However, whereas the former becomes relevant when \mathcal{T}_c^0 is approached and the non-condensed fraction of the gas increases, the latter contributes the most at lower temperatures, as it is related to the condensate.

Density dependence Comparing the results with $n_t = 10^{12} \text{ cm}^{-3}$ and $n_t = 10^{13} \text{ cm}^{-3}$, we see that the overall behavior is unaffected by the gas density. This can also be observed in the data corresponding to the Fröhlich contribution only (see empty circles in the inset of see Fig. 3.2(a)). There, the temperature of the gas affects the condensate density, but the ion temperature is practically constant. The only sensible differences in the complete curves (i.e. for the Fermi gas and for the Bose gas with all the contributions) can be spotted at very low temperatures. In that regime, the higher gas density gives slightly lower ion temperatures for both the Fermi and Bose gas. Furthermore, the impact of the Lamb-Shift is lower at lower density. In fact, the corrections to the trap parameters are proportional to the condensate density. All these differences, however, are negligible compared to the scale of the s -wave threshold and vanish at higher temperatures, where the behavior of the final ion temperature turns out to be influenced neither by the quantum statistics nor by the total gas density. Nevertheless, the density strongly affects the convergence time of the ion temperature. We find that decreasing the density by an order of magnitude increases the convergence time of roughly the same amount.

Scattering length dependence Finally, we fix the temperature of the ${}^6\text{Li}$ gas to $\mathcal{T} = 0.1 \mu\text{K}$ and we observe the dependence of the final ion temperature for different values of the scattering length in the interval from $a_{\text{ai}} \simeq -3.5 R^*$ to $a_{\text{ai}} \simeq 3 R^*$. Interestingly, we find the curve presents a non-trivial structure with a peak around the value $a_{\text{ai}} \simeq -0.5 R^*$, as shown in Fig. 3.2(b). Around that value, the convergence time is strongly enhanced, resulting in higher values of the ion temperature (see Fig. 3.2(c)). This behavior suggests the presence of instability that could be related to the occurrence of a resonance, as observed in Ref. [52]. We note, however that the master equation approach does not entail any information about the microscopic dynamics of atom-ion interactions. Nevertheless, the latter may emerge from the parameters of the regularized potential.

¹The threshold $E_s = k_B \mathcal{T}_s$ is obtained by imposing the collision energy E_{coll} to be much lower than the characteristic energy E^* of the atom-ion potential (see Sec. 1.1.2). Assuming an atom velocity much lower than the ion velocity, which is reasonable for an ultracold gas, we have $E_{\text{coll}} \approx \mu E_{\text{kin}}/M$, with E_{kin} the kinetic energy of the ion. Hence, we obtain $E_{\text{kin}} \ll E_s$ with $E_s = (1 + M/m)E^*$, showing that having $M \gg m$ gives a higher threshold.

3.2 [L2] – Quantum-limited thermometry of a Fermi gas with a charged spin particle

The objective of the study described in Ref. [L2] is to investigate the effectiveness of an ion-based sensor in accurately determining the temperature of an ultracold Fermi gas. To achieve this, our work extends the thermometric protocol proposed by Mitchison et al. [125] to the case of a charged impurity. Enhancing the precision of temperature estimation methods holds paramount importance for experiments where impurities are coupled to ultracold Fermi gases. This is particularly crucial when investigating non-equilibrium phenomena like Anderson’s orthogonality catastrophe [146, 147], the formation of polaronic states [148–152], or applications involving ionic impurities in Fermi gases [75, 77, 78]. These experiments necessitate minimally invasive strategies to locally monitor temperature and its associated uncertainty. It’s worth noting that ions have also been proposed as probes for measuring density-density correlations [153] and the energy distribution of a Fermi gas [154]. Moreover, we note that other strategies were adopted to indirectly measure the temperature of a Fermi gas. One example is in Ref. [155], where a Bose-Einstein condensate was used as a probe.

The protocol, outlined in Sec. 2.2 of this dissertation, is designed to infer the temperature of the gas from the measure of the symmetric logarithmic derivative (SLD), as this is the operator that maximizes the Fisher information. Thanks to this feature, the quantum Cramer-Rao bound can be used to identify the quantum signal-to-noise ratio (QSNR) \mathcal{Q} as an indicator of the maximum precision achievable. In our study, we assess the value of the QSNR by the definition $\mathcal{Q}^2 = T^2 \mathcal{F}_T^{\mathcal{Q}}$, where the quantum Fisher information $\mathcal{F}_T^{\mathcal{Q}}$ is computed via the decoherence function according to Eq. (2.58). We then investigate the dependence of \mathcal{Q} on several parameters of the system, such as the gas temperature, its density and the time of interaction between the probe and the gas. Unless stated differently, we consider the following configuration: the probe is a two-level system whose state $|0\rangle$ does not interact with the bath². The atom-ion regularized potential is characterized by $a \simeq -R^*$, $b \simeq 0.0023 R^*$ and $c \simeq 0.4878 R^*$ corresponding to zero bound states. Moreover we assume that the ion probe is located at $r = 0$ with density distribution $|\chi(\mathbf{r})|^2 = \delta(\mathbf{r})$, corresponding to the case where the impurity is tightly trapped or has infinite mass. Finally, we remark that the atom-bath interaction is quantified by the parameter $k_F a$, where k_F is the Fermi wave vector and a is the atom-ion s -wave scattering length.

Temperature and time dependence We begin by considering $k_F a = -0.5$ and $k_F a = -1.5$. Note that fixing the interaction parameter with a specific value of the scattering length is equivalent to fixing the density of the gas. We evaluate the dependence of \mathcal{Q} on the gas temperature in the interval between zero and the Fermi temperature T_F , and

²As mentioned in Sec. 2.2.3, this is experimentally not as trivial as in the case of a neutral probe. Because the protocol does not rely on the fact that the two levels are spin states, such a configuration can be achieved for example by designing a two-level system where one of the two states is far away from the gas. We refer to Sec. III of Ref. [L2] for a dedicated discussion.

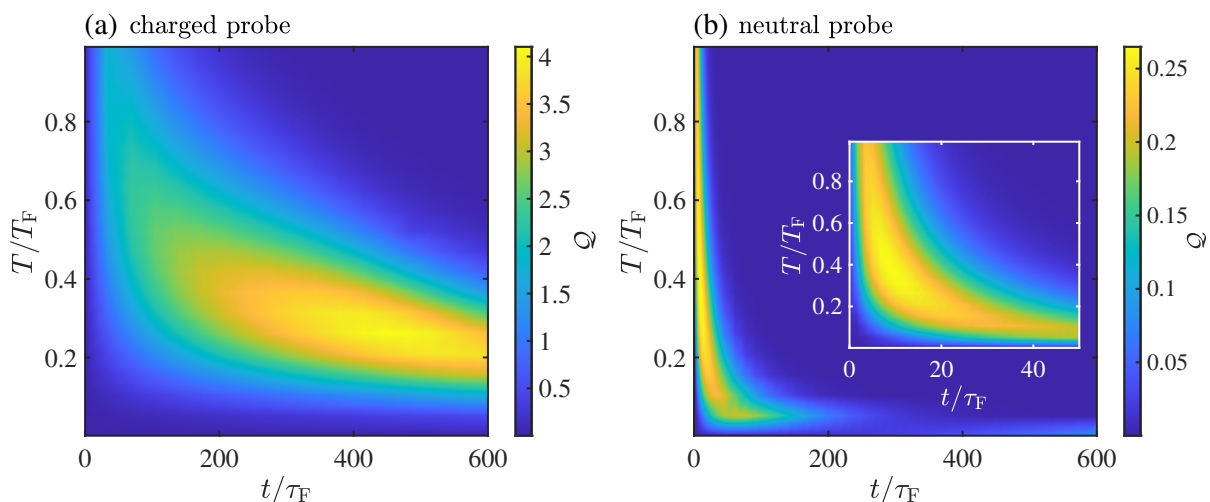


Figure 3.3: Temperature and time dependence of QSNR for fixed interaction parameter $k_F a = -1.5$. State $|0\rangle$ of the two-level probe does not interact with the bath. **(a)** Charged probe: state $|1\rangle$ interacts via V_{reg} with $a \simeq -R^*$. **(b)** Neutral probe: state $|1\rangle$ interacts via pseudopotential. Figure adapted from Ref. [L2].

on the interaction time, spanning from zero to a few hundreds times the Fermi time τ_F . Comparing the results with the case of a neutral particle (see Fig. 3.3), we observe that the temperature dependence is only barely affected by the long-range of the atom-ion potential. On the other hand, the region where Q reaches the highest values is shifted and extended to larger probing times for the charged impurity. This suggests that the atom-ion potential takes more time to bring the system in the regime where the dynamics is governed by temperature-sensitive excitations [156] and suppresses the decay of $|\nu|$. Most importantly, the maximum Q for $k_F a = -1.5$ is significantly enhanced by the atom-ion potential, showing that using a charged probe can result in a better performance of the thermometric protocol.

Finally, we consider an ion with Gaussian density distribution. The latter mimics the time-averaged distribution of an ion in a Paul trap or the ground state of a deep dipole trap. The width of the Gaussian is defined as $\sigma = \sqrt{\hbar/M\omega}$, with M the ion mass and ω the trap frequency. We fix $\sigma = 0.3 R^*$, corresponding to $\omega \simeq 2\pi \cdot 133$ kHz for a $^{174}\text{Yb}^+$ ion. Studying the time dependence of Q for fixed temperature, we observe that a finite width can enhance the sensitivity at shorter times. This can be relevant in experiments, where the onset of undesired effects such as spin relaxation [157] or three body recombination [56, 139, 158] can be prevented by a proper choice of the trap frequency that allows to reduce the probing time without affecting the sensitivity.

Interaction dependence of maximal QSNR The value of $Q_{\text{max}} = \max_t \{Q(t)\}$ is studied at fixed temperature $T = 0.2 T_F$ and for different values of the interaction parameter $k_F a$ with fixed $a \simeq -R^*$. For a single interacting state, we identify three separate regions (see Fig. 3.4(a)): for $k_F a \lesssim -4$, corresponding to a mean interparticle distance $\bar{d} \lesssim -R^*$, the collisions between the atoms in the bath and the short-range repulsive core of V_{reg} are more frequent, resulting in a faster decay of the decoherence function.

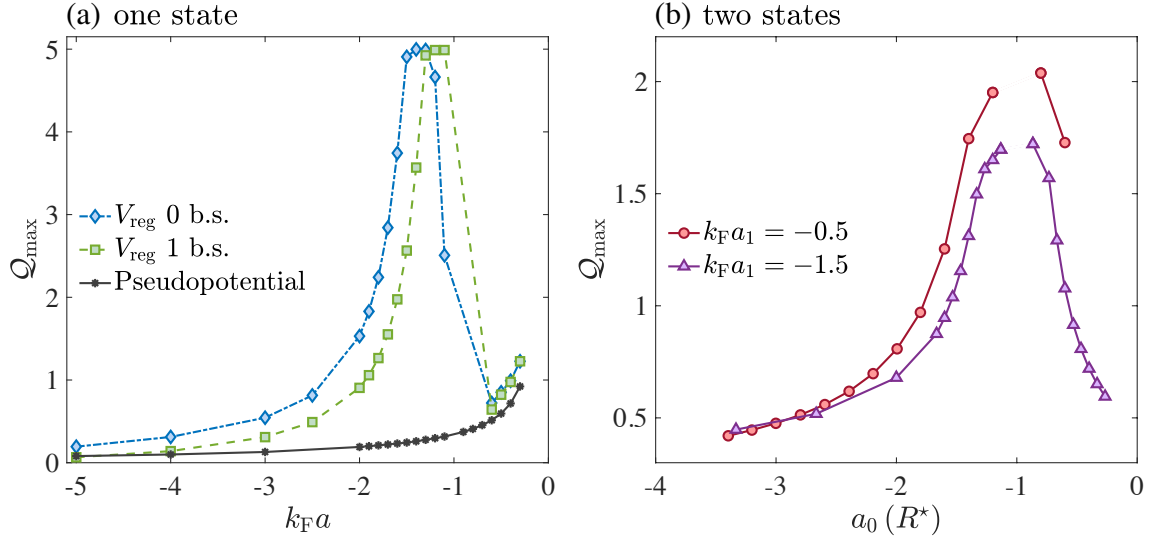


Figure 3.4: Value of $Q_{\max} = \max_t \{Q(t)\}$ with fixed temperature $T = 0.2 T_F$. **(a)** state $|0\rangle$ is non-interacting, state $|1\rangle$ interacts via the indicated potentials. The regularized potentials with zero or one bound state have fixed $a \simeq -R^*$; **(b)** state $|1\rangle$ interacts via V_{reg} with fixed $a_1 \simeq -R^*$, while the scattering length a_0 corresponding to state $|0\rangle$ is varied. The discontinuity of the line indicates that the thermometer does not work when $a_1 = a_0$ (see text). All the lines are a mere guide to de eye. Figures adapted from Ref. [L2].

Note that for fixed a , the mean density \bar{n} is fixed and $\bar{d} = \bar{n}^{-1/3} \propto 1/k_F$. Both for the pseudopotential and V_{reg} , the value of Q_{\max} gets lower as the value of $|k_F a|$ increases. Similarly, the charged and neutral probe give comparable results in the region where $k_F a \gtrsim -0.5$, corresponding to $\bar{d} \gtrsim 8 R^*$. Here, the rate of collisions is lower and the decoherence function decays slowly compared to τ_F , allowing the ion to probe the gas for longer times and resulting in an increasing Q_{\max} . Finally, in the intermediate region, the balance between the interactions with the repulsive core and the attractive part of the regularized potential results in a suppressed decay of the decoherence function. In this regime, the values of Q_{\max} present a peak which is not observed with the neutral particle. We attribute this strong enhancement of the maximal thermometric precision to the the atom-ion potential, which is able to probe a larger part of the temperature-dependent perturbations thanks to its long-range tail. We also remark that no qualitative difference is observed when other potentials with one or two bound states are considered.

In the case of two interacting states, the same non-monotonous behavior attributed to the long-range potential is observed. The plots in Fig. 3.4(b) show that the peak is centered around the value $a_0 = a_1 \simeq -R^*$. Note, however that when the two scattering lengths coincide, the dynamics of the two states is identical and the thermometric protocol cannot work. Comparing the maximal values of Q in Fig. 3.4(a) and Fig. 3.4(b), suggests that a scheme with one interacting state allows to attain a better thermometric precision. Nevertheless, even with two interacting states, a proper choice of the parameters can strongly enhance the sensitivity of the ion probe.

3.3 [L3] – Cooling dynamics of a free ion in a Bose-Einstein condensate

In Ref. [L3], we derive a master equation in the Born-Markov and Lamb-Dicke approximation for an untrapped ion, hence referred to as free, moving inside a Bose-Einstein condensate with an initial finite momentum. The derivation is summarized in Sec. 2.1 and follows the same steps of that in Ref. [L1] for the trapped ion. Our work is motivated by the recent progress in experiments involving untrapped ions in condensates [66, 123] and by the possibility to control the ion motion with optical traps [20, 159]. We remark that the research on mobile charged impurities in ultracold gases is at an earlier stage compared to its neutral counterpart, where substantial advancements have been made in the study of polarons within Fermi [149, 151, 160, 161] and Bose environments [162–164]. This can be attributed to the inherent experimental challenges presented by atom-ion systems, such as the difficulty in reaching the s -wave regime.

Here, we focus on the experiment reported by T. Kroker *et al.* in Ref. [123], where an ultrafast laser pulse ionizes some of the atoms in a ^{87}Rb BEC, hence creating ions with finite kinetic energy inside the condensate. We therefore consider the homonuclear system $^{87}\text{Rb}^+ / ^{87}\text{Rb}$. Moreover, according to the values estimated in the experiment, the condensate density is chosen between $\sim 10^{13} \text{ cm}^{-3}$ and $\sim 10^{14} \text{ cm}^{-3}$, whereas the value of the initial kinetic energy of the ion is on the order of 10^{-7} eV , corresponding to $E_{\text{kin}}/k_{\text{B}} \sim 1 \text{ mK}^3$. Before reporting the results, a few remarks are in order. First, the bath is treated as an infinite non-interacting BEC, and the derivation is limited to the contribution from the Fröhlich Hamiltonian [see Eq. (2.25a)]. Second, the atom-ion interaction is modeled by the regularized polarization potential in Eq. (1.14) with $b \simeq 0.078 R^*$ and $c \simeq 0.224 R^*$, corresponding to $a_{\text{ai}} \simeq R^*$. Finally, the Lamb-Dicke approximation allows the decoupling of the three directions. Hence, without loss of generality, we can assume the initial momentum of the ion to be entirely directed along x and restrict our analysis to that direction. We refer to the last paragraph of Sec. 2.1.3 for a brief discussion on the validity of the Lamb-Dicke approximation and to Ref. [L3] for more details.

Cooling dynamics We define the ion temperature along x as $T_{\text{kin}}^x = \langle \hat{p}_x^2 \rangle / (2Mk_{\text{B}})$ and we start by studying its time evolution for different values of the initial momentum k_0 and condensate density n_0 for a fixed gas temperature $T_{\text{gas}} = 1 \text{ nK}$. Such a low value is chosen to guarantee the validity of the Lamb-Dicke approximation. However, no dependence on the gas temperature is noticed for a fixed condensate density. In Fig. 3.5(a) we observe that for $n_0 = 2 \cdot 10^{14} \text{ cm}^{-3}$, the ion temperature decays to $\sim 2 \mu\text{K}$ in a time on the order of the microsecond. The decay time is barely affected by its initial value, meaning that a higher initial temperature corresponds to a more efficient cooling. On the other hand, the cooling rate is sensibly affected by the gas density. This behavior is characterized by defining the full duration at half maximum (FDHM) as the time required by the temperature to reach half of its initial value (see inset of Fig. 3.5(b)). In our description,

³Note that the value reported in the experiment is on the order of a few microelectronvolts, but it can be reduced by an order of magnitude.

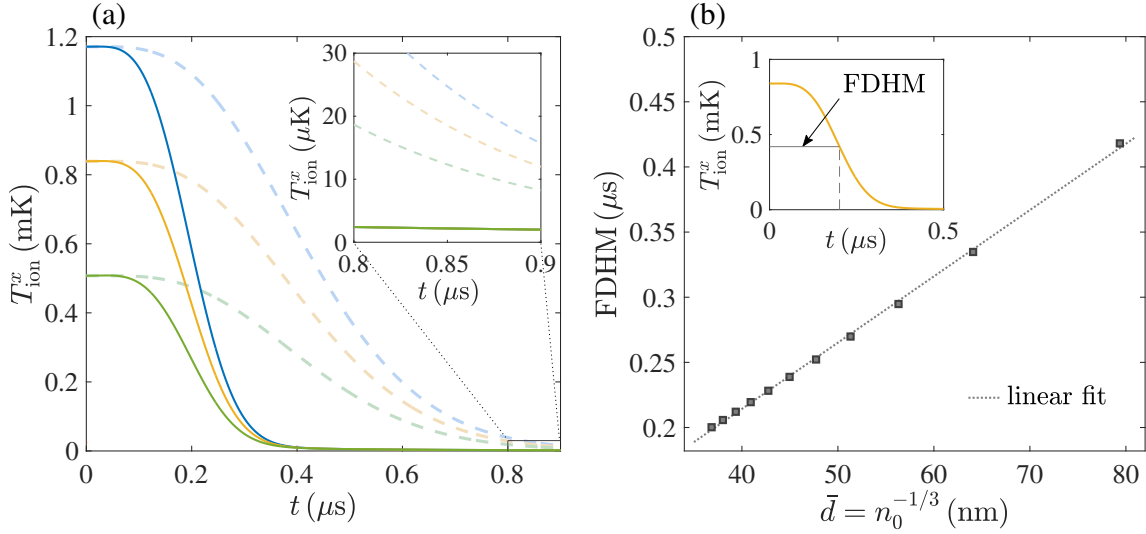


Figure 3.5: (a) Time dependence of ion temperature T_{ion}^x for $n_0 = 2 \cdot 10^{14} \text{ cm}^{-3}$ (dark solid lines) and $n_0 = 2 \cdot 10^{13} \text{ cm}^{-3}$ (light dashed lines). The initial values correspond to $T_{\text{ion}}^x = 1.17 \text{ mK}$ (blue), $T_{\text{ion}}^x = 0.84 \text{ mK}$ (orange) and $T_{\text{ion}}^x = 0.51 \text{ mK}$ (green). The inset shows a magnification of the region between $8 \mu\text{s}$ and $9 \mu\text{s}$. (b) *Main plot:* FDHM (full duration at half maximum) as a function of mean particle separation in the gas for $T_{\text{ion}}^x(t = t_0) \simeq 1 \text{ mK}$. The dotted line represents a linear fit; *inset:* definition of FDHM. Figures are adapted from Ref. [L3].

the FDHM has a linear dependence on the mean particle separation $\bar{d} = n_0^{-1/3}$ of the condensate, as shown in Fig. 3.5(b) for a fixed initial temperature $T_{\text{ion}}^x(t = t_0) \simeq 1 \text{ mK}$. Although one could expect a linear dependence on the condensate density, we recall that the Lamb-Dicke approximation decouples the three directions. As a consequence, despite treating the system in three dimensions, the results correspond to the simulations along the x -direction only. The ion dynamics is therefore characterized by the mean distance between the bosons, which accounts for the rate of atom-ion collisions in one direction. In particular, we observe that a lower particle distance corresponds to a lower FDHM, i.e. a more efficient cooling.

Pinning dynamics Let us now consider the expectation value of position and velocity the ion⁴. Interestingly, the dynamics of the ion at short times indicates polaronic behavior. Namely, the ion is dressed by phononic excitations and moves freely within the bath. At larger times, the onset of nonlinear effects like phonon-phonon interactions brings the ion to rest: we refer to this behavior as pinning dynamics. Focusing on the results for a density $n_0 = 2 \cdot 10^{14} \text{ cm}^{-3}$, we find that the ion velocity drops to $\sim 10^{-10} \text{ m s}^{-1}$ in the same timescale of the cooling dynamics described in the previous paragraph, as shown by the

⁴Note that the value of $\langle \hat{p}_x \rangle$ and that of $\langle \hat{p}_x^2 \rangle$ are not necessarily related in a quantum system. One example is the ion in the center of an ideal Paul trap described in Ref. [L1] and in Sec. 3.1 of this dissertation. In that case, we find that the squared momentum is finite, while the linear momentum is constantly zero.

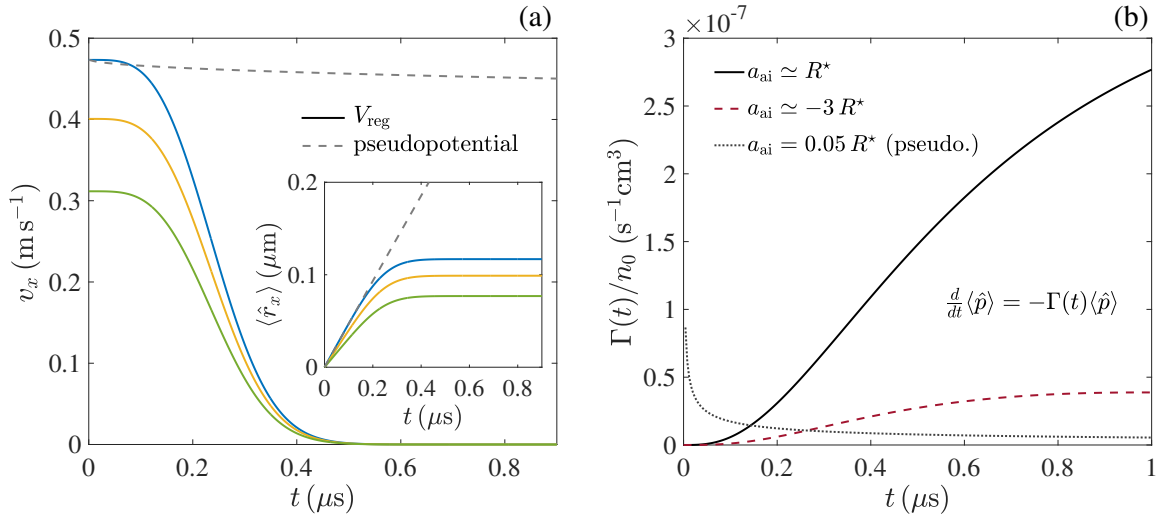


Figure 3.6: (a) *Main plot:* time dependence of ion velocity $v_x = \langle \hat{p}_x \rangle / M$ for different initial conditions and fixed condensate density $n_0 = 2 \cdot 10^{14} \text{ cm}^{-3}$. Solid lines correspond to a regularized atom-ion potential with $a_{\text{ai}} \simeq R^*$, while the dashed line corresponds to a neutral impurity interacting with the atoms with a zero-range pseudopotential with scattering length $a = 0.05 R^*$. The initial velocities are $v_x = 0.47 \text{ m s}^{-1}$ (blue), $v_x = 0.40 \text{ m s}^{-1}$ (orange) and $v_x = 0.31 \text{ m s}^{-1}$ (green); *inset:* time dependence of ion position. (b) Time-dependent friction in units of the condensate density n_0 as a function of time for two different atom-ion scattering lengths (solid and dashed) and for a neutral impurity (dotted). Figures adapted from Ref. [L3].

solid lines Fig. 3.6(a). Consequently, the position of the ion converges to a finite value. Similarly to what observed for the ion temperature, the decay time of the velocity is barely affected by its initial value at $t = t_0$, and the final positions are reached at approximately the same time for all the initial conditions (see solid lines in the inset of Fig. 3.6(a)). We compare these results with those obtained by considering a neutral impurity (dashed lines in Fig. 3.6(a)). The impurity-bath interaction in the neutral case is represented by a zero-range pseudopotential. For a meaningful comparison, we choose the scattering length to be on the order of the typical range of the van der Waals potential, i.e. $\sim 0.05 R^*$. The neutral impurity does not come to rest on the timescale in which the pinning of the ion is observed, confirming that the long-range character of the polarization potential plays a key role in describing atom-ion interactions.

Furthermore, we note that the equation for the expectation value of the ion momentum can be compared to the equation describing the damped motion of a classical particle:

$$\frac{d}{dt} \langle \hat{p}_x \rangle = -\Gamma \langle \hat{p}_x \rangle. \quad (3.2)$$

In our case, the friction $\Gamma \equiv \Gamma(t)$ is a time dependent function that we compute numerically and contains the information on the pinning dynamics of the ion. In Fig. 3.6(b), we observe that the friction for the ionic impurity (solid and dashed lines) is almost zero at short times, in agreement with the aforementioned polaron-like behavior. At longer

times, the value of Γ increases, corresponding to the pinning of the ion. We attribute this behavior to the dephasing of the phononic modes due to the interaction of the bath with the ion. However, the master equation approach does not allow to investigate the cause of this phenomenon, which therefore requires a dedicated study. Finally, we observe that the friction coefficient for the neutral impurity (dotted line in Fig. 3.6(b)) has a completely different time evolution. The decrease of its value at longer times can be associated to the formation of a Bose polaron, corresponding to a regime where the impurity gets dressed by phononic excitations while it moves through the condensate. The qualitative difference between the friction coefficient in the neutral and ionic case highlights, once again, the impact of the long-range character of the atom-ion potential.

In conclusion, our study predicts the cooling and pinning of the ion. Moreover, a remarkable robustness of the results is observed against the parameters involved. We refer to Sec. V of Ref. [L3] for a discussion on the possible experimental validation of our findings.

Conclusions and outlook

Throughout the course of project that culminated in this dissertation, we focused on understanding the quantum dynamics of ions immersed in baths of ultracold atomic gases. More specifically, we addressed our efforts towards the study of how the properties of the bath influence the behavior of the ionic impurity. In doing this, we have always been driven by the continuous advances on the experimental side, which require the support of adequate theoretical studies as well as new hints for possible applications of ultracold hybrid atom-ion systems.

In this dissertation, we presented a master equation description for the said systems that does not rely on the computation of the entire density matrix of the impurity. More precisely, although the total master equations that we derived do describe the time evolution of the ion's density matrix, we employed them to analytically calculate the equations for the expectation value of relevant observables. In the scenarios we had explored, we were mainly interested in evaluating the first order (position and momentum) and second order momenta (squared momentum, squared position and covariance) of the ion. Remarkably, the corresponding equations form two closed sets for each direction, substantially mitigating the computational demand. This shows that our strategy stands as a powerful and versatile tool for investigating the out-of-equilibrium quantum dynamics of ions in ultracold gases.

Based on ongoing experiments, we considered two noteworthy cases: a single ion in an ideal quadrupole trap (also known as Paul trap or radiofrequency trap) and an untrapped ion released inside the bath with finite initial momentum. For the trapped ion, we were able to consider a fermionic environment as well as the contribution of the non-condensed part of the gas in a bosonic bath and the correction to the trap parameters due to the condensate. We remark that similar 3D investigations preceding our study, such as the one reported by Krych and Idziaszek [74], only considered a bath represented by a BEC. With our comprehensive description, we captured the effect of the radiofrequency-induced micromotion, studying how its impact is affected by the parameters involved. Most notably, we observed that at gas temperatures comparable to the critical temperature of Bose-Einstein condensation, the quantum nature of the bath emerges. In this regime, the difference between a bosonic or fermionic environment is sensible, with the latter allowing for lower ion temperatures. As far as the untrapped ion is concerned, the master equation only takes into account the contribution of the BEC. Nonetheless, our description of such a system in a full quantum picture is unprecedented in the literature, where most of the studies relied on a semiclassical representation of the ion. We predict a remarkably effective reduction of the ion temperature and velocity inside the condensate.

Albeit versatile and powerful, the master equation approach is accompanied by its own weaknesses. For instance, the bath is treated as an homogeneous non-interacting gas. As natural continuation of our work, it would be interesting to include the perturbations on the bath density due to the presence of the ion. This improvement, could allow to study the formation of many-body bound states such as those predicted in Ref. [69–71]. Moreover, the master equation is based on several major approximations, namely the Born, Markov and Lamb-Dicke. In future works, one might try to relax some of those approximation. In particular, avoiding the Lamb-Dicke approximation would enable an actual three dimensional description of the system. The attempts we made so far to compute the next orders in the Lamb-Dicke expansion, however, led to overly intricate calculations. An alternative would be to adopt the strategy proposed in Ref. [137]. There, the dynamics can be simulated by a stochastic Schrödinger equation similarly to the Monte Carlo wave-function method [165, 166], giving access to the full 3D dynamics.

In addition to the master equation analysis, we reported in this dissertation our study on the possible application of an ion as a thermometry sensor for an ultracold Fermi gas. In the work in question, we considered the interferometric protocol proposed by Mitchison, Fogarty, Guarnieri, Campbell, Busch, and Gould [125] for a static neutral spin system, and we adapted it to the case of a charged one. By studying the decoherence dynamics of the spin states, we evaluated how the parameters involved in the description affect the quantum signal-to-noise ratio (QSNR) associated to the temperature estimation. This quantity is related to the maximal precision achievable according to the theory of quantum parameter estimation. Moreover, we discussed the possible application of the procedure based on typical experiments.

We numerically investigated two different scenarios: only one internal state or both internal states interacting with the Fermi gas. Our results show that, in both cases, the atom-ion interaction parameter can be tuned to a range where the quantum signal-to-noise ratio is strongly enhanced. In particular, this behavior is more pronounced when a single interacting state is considered. Outside from this range, on the other hand, the QSNR assumes values comparable to the case of the neutral impurity. These observations suggest that, with the appropriate choice of setup and parameters, the long-range character of the atom-ion potential can improve the sensitivity of the two-level probe in the estimation of the gas temperature.



As the main drawback in the application of the aforementioned protocol to the charged impurity, we identified the effect of few-body processes, such as three-body recombination or spin relaxation. These could happen in experiments during the probing time, leading to bad thermometric performances. A possible strategy to suppress their onset, is represented by coupling the atomic cloud to a Rydberg state [167, 168]. This would enhance the atomic polarizability, allowing to put the ion at some distance from the gas. Alternatively, the Rydberg dressing can be exploited to manipulate the atom-ion interaction, creating a short-range barrier to prevent the atoms from getting too close to the ion.

In light of what discussed above, an interesting perspective for future work is the investigation of different setups aimed at mitigating undesired effects and further improving the precision. For instance, designing new protocols based e.g. on the motional states of the probe or relying on two entangled ions could help on this regard.

To conclude this dissertation, let us spend few words regarding ongoing projects and other studies that we are planning to undertake in the near future.

Current simulations are investigating the effect of coupling a quantum gate to an ultracold gas. The setup that we consider consists of a one-dimensional chain of three ions whose motion can be decomposed into normal modes of oscillation. A two-qubit gate is made with the two external ions by subjecting them to a spin-dependent force, while the central ion is immersed in a bath of ultracold atoms. The dissipative dynamics is captured by deriving a master equation in analogy to our previous works. Our aim is to describe how the behavior of the gate is affected by the gas and, in particular, whether the latter can counteract the heating term due to the coupling of the ion chain with an external bath at room temperature. In addition, we are planning to exploit the descriptions of multiple ions as a vibrating chain to study the dynamics of two ions both immersed in the ultracold gas. This would allow to understand how the interaction between the two ions is mediated by the surrounding bath. Finally, we mention that among our next goal is the development of a novel method for describing the dynamical properties of ions in ultracold gases. The approach is based on a combination of path integral and functional determinant methods for fermionic systems and allows to obtain the time evolution of the impurity without relying on the Born and Markov approximation.

Publications

Dynamics of a trapped ion in a quantum gas: Effects of particle statisticsLorenzo Oghittu , Melf Johannsen, and Antonio Negretti *Zentrum für Optische Quantentechnologien, Universität Hamburg, Luruper Chaussee 149, 22761 Hamburg, Germany*Rene Gerritsma *Van der Waals Zeeman Institute, Institute of Physics, University of Amsterdam, Science Park 904, 1098 XH Amsterdam, The Netherlands*

(Received 7 September 2021; accepted 2 November 2021; published 17 November 2021)

We study the quantum dynamics of an ion confined in a radio-frequency trap in interaction with either a Bose or spin-polarized Fermi gas. To this end, we derive quantum optical master equations in the limit of weak coupling and the Lamb-Dicke approximations. For the bosonic bath, we also include the so-called “Lamb-shift” correction to the ion trap due to the coupling to the quantum gas as well as the extended Fröhlich interaction within the Bogolyubov approximation that have been not considered in previous studies. We calculate the ion kinetic energy for various atom-ion scattering lengths as well as gas temperatures by considering the intrinsic micromotion and we analyze the damping of the ion motion in the gas as a function of the gas temperature. We find that the ion’s dynamics depends on the quantum statistics of the gas and that a fermionic bath enables to attain lower ionic energies.

DOI: [10.1103/PhysRevA.104.053314](https://doi.org/10.1103/PhysRevA.104.053314)**I. INTRODUCTION**

The interest in studying both experimentally and theoretically quantum mixtures of ions and ultracold gases is increasing rapidly. Indeed, such a compound system offers various fascinating perspectives both on fundamental quantum few- and many-body physics research and on technological applications that the two systems separately cannot afford, for instance, the exploration of novel polaronic states [1–3] and quantum simulation of the electron-phonon coupling [4–6]. For an extensive overview on atom-ion physics research, we refer to [7–9]. Experimentally, a considerable effort has been undertaken in the last few years in order to cool the atom-ion compound system down to the quantum regime, namely, when only *s*-wave atom-ion collisions take place. To this end, three experimental approaches have been pursued so far: ionization of a highly excited Rydberg atom in a Bose-Einstein condensate [10,11]; an ion confined in a radio-frequency (rf) trap interacting with an optically trapped atomic gas [12,13]; sympathetic cooling of ions and atoms in optical dipole traps [14,15]. In the former approach, the ion is not trapped after ionization and a controlled momentum kick via external electric fields is imparted in order to investigate charge transport in a bosonic medium [16,17]. The second relies on the well-established laser cooling and manipulation techniques of trapped ions, which are confined by means of a combination of time-dependent and time-independent electric fields. The exquisite control of the ion motion enables to prepare various nonclassical states [18,19] and, in principle, to infer on environment properties by reading out the ion quantum state. The time-dependent fields, however, can seriously jeopardize the attainment of the ultracold atom-ion collisional regime, a notorious issue named micromotion. Finally, the

third approach is somehow a hybrid of the former two, as it reduces drastically the impact of ion micromotion in Paul traps and, at least in principle, it enables to control the ion motion optically. At the same time, however, since the optical trap is not as deep as the rf trap, unavoidable stray fields can reduce the ion lifetime in the trap [20,21]. Moreover, an intense laser light can induce undesired chemical reactions between the ion and the particles of the gas.

Here, we focus our attention on the second approach and investigate the cooling dynamics of a trapped ion immersed in either a bosonic or fermionic environment. Albeit the *s*-wave regime in hybrid traps has been attained with only fermionic atoms so far [12,22], several ongoing experiments involve bosonic ensembles [14,23–28]. Up until now, however, a few theoretical studies have been undertaken in order to assess the impact of ion micromotion on the atom-ion quantum dynamics: a quantum mechanical calculation in one dimension (1D) [29,30], a semiclassical investigation of confinement-induced resonances in quasi-1D [31,32], and a three-dimensional (3D) master-equation analysis [33]. Apart from the latter, all others concerned a single trapped atom and ion, and therefore only the emerging two-body physics has been investigated. In Ref. [33], however, the Fröhlich model was assumed, while the Lamb shift and, specifically for the bosonic case, the contribution of the noncondensed fraction were not considered. Here, by Lamb shift we refer to the renormalization of the ion trap parameters due to the coupling to the quantum gas. In condensed matter and for a free impurity such a shift is named polaron shift, whereas in this work we use the quantum optics terminology. The aforementioned studies confirmed that the impact of the ion micromotion can be mitigated by choosing a small atom-ion mass ratio. With this study, we first aim at developing a formalism for mobile quantum

impurities based on an open quantum system approach, which does not rely on the (linear) Fröhlich impurity-bath interaction model and rotating-wave approximation. Moreover, we want to understand the role of the gas quantum statistics on the ion-cooling dynamics and whether atom-ion pairs different than Li/Yb⁺ can reach the *s*-wave limit. As far as the first objective is concerned, we find that the corrections causing the Lamb shift yield additional dissipative contributions in the master equation, as a consequence of the nonapplicability of the rotating-wave approximation. Furthermore, the quantum statistics of the ultracold gas affects significantly the ion dynamics. While for temperatures larger than the Fermi temperature T_F and the critical temperature of condensation T_c^0 the ion dynamics reproduces essentially the one corresponding to the interaction with a buffer gas, at low temperature the fermionic and bosonic nature of the gas is observable in a distinct gas temperature dependence of the ion energy. Both for the fermionic and bosonic gas we observe a minimum in the ion energy for a temperature T_{\min} close to T_c^0 . Below T_{\min} the ion energy increases again, but only marginally for fermions. On the other hand, for a bosonic gas the ion-energy dependence on the gas temperature T exhibits a more rich structure. Indeed, after the enhancement of the ion energy for $T_c^0 < T < T_{\min}$, below T_c^0 it presents a maximum due to the interplay between the condensate contribution and that of the normal part of the gas. Moreover, the damping rate of the ion motion exhibits the same dependence on the gas temperature as the condensate fraction for $T < T_c^0$. In addition, we elucidate the role of the long-range character of the atom-ion polarization potential on the ion quantum dynamics by comparing our findings with those of the pseudopotential. Contrary to neutral impurities, the nonequilibrium dynamics of the ion in the quantum gas is nonuniversal, that is, it cannot be uniquely characterized by the impurity-gas scattering length like for neutral impurities. Since there is no clear separation of length scales in the many-body problem at typical gas densities, the tail of the atom-ion interaction plays a crucial role in the ion dynamics and the effective range corrections cannot be neglected.

The paper is organized as follows: In Sec. II we introduce the atom-ion potential, while in Sec. III the system plus bath description is outlined, which is kept on purpose quite general. A master equation including the contribution of the noncondensed fraction is obtained in a way that is valid for both neutral and charged impurities. In Sec. IV we focus on the trapped ion case and make use of the well-known Lamb-Dicke approximation, which enables us to further simplify the description of the ion dynamics. We continue with Sec. V by providing the equations of motion of observables of interest, while in Sec. VI we present our results. In Sec. VII we draw our conclusions and provide an outlook for future work.

II. ATOM-ION INTERACTION POTENTIAL

In this section we discuss briefly the interaction between an atom and an ion and how we model it for the master-equation calculation.

Polarization potential. The interaction between an atom and an ion in free space is described asymptotically by

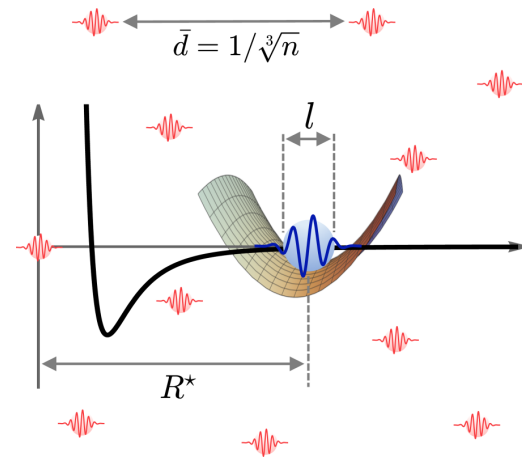


FIG. 1. Schematic view of the open quantum system with the main length scales. The width l of the Paul trap potential (represented by the saddle) corresponds to the size of the ion in the ground state (large blue wave) and is (much) smaller than the two other lengths: the average distance \bar{d} among the gas particles (small red waves), which is defined by atomic density n ; the characteristic length R^* of the atom-ion potential (black thick line).

($r \equiv |\mathbf{r}|$)

$$V_{\text{ai}}(\mathbf{r}) = -\frac{C_4}{r^4} \quad (1)$$

with $C_4 = \frac{\alpha e^2}{2} \frac{1}{4\pi\epsilon_0}$ (in SI units) [34], where α is the static polarizability of the atom, e is the elementary electronic charge, and ϵ_0 the vacuum permittivity. Here, r denotes the separation between the atom and the ion. The potential is characterized by the length $R^* = (2\mu C_4/\hbar^2)^{1/2}$ and energy $E^* = \hbar^2/[2\mu(R^*)^2]$ scales, with $\mu = mM/(m+M)$ the reduced mass, m the atom mass, and M the ion mass.

Length scales. In our setting there are several relevant length scales (see Fig. 1). First, the aforementioned R^* , which is typically in the range of hundreds of nanometers and gives, as a rule of thumb, the order of magnitude of the 3D zero-energy *s*-wave atom-ion scattering length (see also Refs. [35,36]). For instance, for the atom-ion pair ⁷Li/¹⁷⁴Yb⁺ we have $R^* \simeq 75.15$ nm, for ²³Na/¹⁷⁴Yb⁺ $R^* \simeq 129.85$ nm, and for ⁸⁷Rb/¹⁷⁴Yb⁺ $R^* \simeq 307.23$ nm. Second, the atom-atom (background) scattering length a_{aa}^s which is typically on the order of a few nanometers. Third, for a condensate, we have the healing length, which is defined as $\xi = (8\pi n a_{\text{aa}}^s)^{-1/2}$ with n being the gas density. For a typical gas density $n = 10^{14}/\text{cm}^3$ we have, e.g., $\xi \simeq 273.61$ nm for ⁸⁷Rb, and $\xi \simeq 380.38$ nm for ²³Na. Instead, for a Fermi gas, the inverse of the Fermi wave vector $\lambda_F = 2\pi/k_F = (3\pi^2 n)^{-1/3}$ gives another length scale. For $n = 10^{14}/\text{cm}^3$, we have $\lambda_F \simeq 437.56$ nm. Fourth, the mean path length \bar{d} that at the aforementioned typical gas density is about 215.44 nm. Hence, all lengths are comparable and therefore there is no separation of length scales as in the neutral counterpart. As a consequence, nonuniversal behavior in the ion static and dynamical properties is expected (see, for instance, Refs. [37–39] for a static ion analysis). Thus, either very low atomic densities are considered,

where a universal behavior is expected, or else the long-range tail of the atom-ion interaction strongly matters.

Finally, the last relevant length for a trapped ion system is the ion trap length l , which corresponds to the ion ground-state size. This length is about a few tens of nm for $^{174}\text{Yb}^+$, as we discuss in Sec. IV. While l is rather small compared to R^* for heavy atoms, for lithium it is roughly half of the corresponding R^* . This means that scattering of an atom and an ion should not be analyzed in free space, as we do in the next paragraph, as the confinement affects the atom-ion collision as for neutrals in waveguides. Here, however, we neglect effects like confinement-induced resonances as a dedicated study of such a phenomenology is required.

Quantum regime condition. It is important to note that the energy E^* sets the onset of s -wave atom-ion collisions, namely, for energies smaller than E^* the quantum regime can be attained [40]. Indeed, E^* corresponds to the height of the centrifugal barrier for the $\ell = 1$ partial wave from threshold (see, e.g., Fig. 1 of Ref. [9]). Assuming that the kinetic energy of the atom is negligible, since it is ultracold compared to the ion, the collisional energy in the relative atom-ion coordinate frame is given by [41,42]

$$E_{\text{coll}} = k_{\text{B}} \mathcal{T}_{\text{coll}} \simeq \frac{\mu}{M} E_{\text{kin}} \quad (2)$$

with $E_{\text{kin}} = k_{\text{B}} \mathcal{T}_{\text{kin}}$ the ion's average kinetic energy in the laboratory frame of reference and k_{B} being the Boltzmann constant [43]. Hence, in order to enter the quantum regime of s -wave collisions, the ion's kinetic energy must be smaller than E^* , that is,

$$E_{\text{kin}} \ll E_s = \frac{M}{\mu} E^* = \left(1 + \frac{M}{m}\right) E^*. \quad (3)$$

In case of a light atom and a heavy ion we have $\mu \simeq m$ so that $M/\mu \gg 1$, and thus a significant gain in the upper limit for s -wave collisions is obtained. For example, for $^7\text{Li}/^{174}\text{Yb}^+$ we have $E_s/k_{\text{B}} \simeq 164.26 \mu\text{K}$ and for $^{23}\text{Na}/^{174}\text{Yb}^+$ we find $E_s/k_{\text{B}} \simeq 6.07 \mu\text{K}$. This shows that there is a rather broad range of temperatures and that these are at least an order of magnitude smaller than those of ultracold neutral collisions (on the mK scale).

Regularized potential. Given the fact that the potential (1) is singular and that later in the master equation we need to compute the Fourier transform of the atom-ion potential, we introduce the regularization [33]

$$V_{\text{ai}}^r(\mathbf{r}) = -C_4 \frac{r^2 - c^2}{r^2 + c^2} \frac{1}{(b^2 + r^2)^2}. \quad (4)$$

Here, b and c are tunable parameters that have units of a length and control the energy spectrum of the potential as well as the atom-ion scattering length. The Fourier transform of (4) is linked to the scattering amplitude in the first-order Born approximation, which is defined as

$$f(q) = -\frac{\mu}{2\pi\hbar^2} \int_{\mathbb{R}^3} d\mathbf{r} e^{i\mathbf{q}\cdot\mathbf{r}} V_{\text{ai}}^r(\mathbf{r}). \quad (5)$$

By using spherical coordinates and by integrating out the angular part, we obtain

$$\begin{aligned} f(q) &= -\frac{2\mu}{q\hbar^2} \int_{\mathbb{R}^+} dr r \sin(qr) V_{\text{ai}}^r(r) \\ &= \frac{c^2\pi(R^*)^2}{(b^2 - c^2)^2 q} \left\{ e^{-bq} \left[1 + \frac{(b^4 - c^4)q}{4bc^2} \right] - e^{-cq} \right\}, \end{aligned} \quad (6)$$

where we used the fact that $(R^*)^2 = 2\mu C_4/\hbar^2$. The determination of b and c is discussed in Appendix A.

III. IMPURITY MASTER EQUATION

In this section we provide an open system description of an impurity in a quantum gas of either bosons or fermions by following the approach of Ref. [44], where the impurity is described in first quantization, whereas the quantum bath in the second one. We focus mainly on the bosonic case, for which we apply Bogolyubov theory, but we consider also the quadratic terms of the bosonic field operators, which result in an extended Fröhlich interaction Hamiltonian. The inclusion of this interaction has been proven to be crucial in the description of the many-body response function of Rydberg [45] and Bose polarons in vicinity of a Feshbach resonance [46]. The fermionic case is considered only for a normal gas, i.e., not superfluid BCS theory, and it is obtained as a special case of the master equation for a bosonic bath for gas temperatures above the critical temperature of condensation. We note that in the literature a master-equation treatment of an impurity in a degenerate Bose gas has already been undertaken [33,47–49], but (i) only the (linear) Fröhlich interaction has been considered and (ii) the Lamb shift has not been taken into account. Moreover and specifically for the ionic impurity, the fermionic bath has been not investigated in Ref. [33].

A. System plus bath Hamiltonian

The total Hamiltonian of the system, the atomic impurity in interaction with a bosonic bath, is given by $\hat{H} = \hat{H}_S + \hat{H}_B + \hat{H}_{BS}$, where \hat{H}_S is the impurity time-dependent Hamiltonian [50]

$$\hat{H}_B = \int_{\mathbb{R}^3} d\mathbf{r}_b \hat{\Psi}_b^\dagger(\mathbf{r}_b) \left[\frac{\hat{\mathbf{p}}_b^2}{2m} + \frac{g}{2} \hat{\Psi}_b^\dagger(\mathbf{r}_b) \hat{\Psi}_b(\mathbf{r}_b) \right] \hat{\Psi}_b(\mathbf{r}_b) \quad (7)$$

and

$$\hat{H}_{BS} = \int_{\mathbb{R}^3} d\mathbf{r}_b \hat{\Psi}_b^\dagger(\mathbf{r}_b) V_{\text{ib}}(\mathbf{r}_b - \hat{\mathbf{r}}) \hat{\Psi}_b(\mathbf{r}_b). \quad (8)$$

Here, V_{ib} denotes the interaction between the impurity and a particle of the bath. Besides, we assume that the bath is confined in a box of length L [51] and that the interaction between the bosons is given by a contact potential with coupling constant $g = 4\pi\hbar^2 a_{\text{bb}}^s/m$ and a_{bb}^s the 3D s -wave atom-atom scattering length, while for the fermions we assume a spin-polarized gas with no intraparticle interaction. Let us note that at this stage the models describing the bosonic and fermionic baths are different, i.e., the former is interacting while the latter is not. Nonetheless, and specifically for the ion in a Paul trap, it turns out that the interaction among bosons is much smaller than other energies involved, so that we can safely neglect it (see Sec. IV for details). Hence, the differences we

observe in the ionic dynamics in the two baths are owed to their quantum statistics and not to the interaction. For the sake of completeness, however, we keep here the derivation of the master equation as general as possible.

The bosonic quantum field is expanded as

$$\hat{\Psi}_b(\mathbf{r}_b) = \sqrt{n_0} + \delta\hat{\Psi}_b(\mathbf{r}_b), \quad (9)$$

where $n_0 = N_0/L^3$ is the density of the condensate, i.e., the zero-momentum component, while N_0 is the atom number. Fluctuations around the condensate mode are described in terms of Bogolyubov modes

$$\delta\hat{\Psi}_b(\mathbf{r}_b) = L^{-3/2} \sum_{\mathbf{q}} u_{\mathbf{q}} \hat{b}_{\mathbf{q}} e^{i\mathbf{q}\cdot\mathbf{r}_b} + v_{\mathbf{q}} \hat{b}_{\mathbf{q}}^\dagger e^{-i\mathbf{q}\cdot\mathbf{r}_b}, \quad (10)$$

where $[\hat{b}_{\mathbf{q}}, \hat{b}_{\mathbf{q}'}^\dagger] = \delta_{\mathbf{q},\mathbf{q}'}$. Using this expression in Eq. (7), we arrive at

$$\hat{H}_B = E_0 + \sum_{\mathbf{q}} \hbar\omega_{\mathbf{q}} \hat{b}_{\mathbf{q}}^\dagger \hat{b}_{\mathbf{q}}. \quad (11)$$

Here, $E_0 = gN_0^2/(2L^3)$ is the ground-state energy of the condensate and $\mu_G = \partial_{N_0} E_0 = gn_0$ is the chemical potential at zero temperature. The corresponding dispersion relation is given by [52]

$$\varepsilon(\mathbf{q}) = \hbar\omega_{\mathbf{q}} = \sqrt{\left(\frac{\hbar^2 q^2}{2m}\right)^2 + (\hbar c_s q)^2} \quad (12)$$

with $c_s = (gn_0/m)^{1/2}$ being the speed of sound, and the Bogolyubov amplitudes $u_{\mathbf{q}}$ and $v_{\mathbf{q}}$ are given in Ref. [52]. Given this, the atomic density operator is

$$\hat{\Psi}_b^\dagger(\mathbf{r}_b) \hat{\Psi}_b(\mathbf{r}_b) = n_0 + \Delta\hat{n}(\mathbf{r}_b). \quad (13)$$

The first term provides a constant energy term in Eq. (8) for a homogeneous gas, as we consider here, and it can be neglected since it shifts merely the energy minimum. The second term is given by

$$\begin{aligned} \Delta\hat{n}(\mathbf{r}_b) &= \hat{\Psi}_b^\dagger(\mathbf{r}_b) \hat{\Psi}_b(\mathbf{r}_b) - n_0 \\ &= \sqrt{n_0} [\delta\hat{\Psi}_b(\mathbf{r}_b) + \delta\hat{\Psi}_b^\dagger(\mathbf{r}_b)] + \delta\hat{\Psi}_b^\dagger(\mathbf{r}_b) \delta\hat{\Psi}_b(\mathbf{r}_b) \\ &= \delta\hat{n}(\mathbf{r}_b) + \delta^2\hat{n}(\mathbf{r}_b) \end{aligned} \quad (14)$$

with $\delta\hat{n}(\mathbf{r}_b) = \sqrt{n_0} [\delta\hat{\Psi}_b(\mathbf{r}_b) + \delta\hat{\Psi}_b^\dagger(\mathbf{r}_b)]$. Hence, we have

$$\delta\hat{n}(\mathbf{r}_b) = \sqrt{\frac{n_0}{L^3}} \sum_{\mathbf{q}} (u_{\mathbf{q}} + v_{\mathbf{q}}^*) \hat{b}_{\mathbf{q}} e^{i\mathbf{q}\cdot\mathbf{r}_b} + (u_{\mathbf{q}}^* + v_{\mathbf{q}}) \hat{b}_{\mathbf{q}}^\dagger e^{-i\mathbf{q}\cdot\mathbf{r}_b} \quad (15)$$

and

$$\begin{aligned} \delta^2\hat{n}(\mathbf{r}_b) &= L^{-3} \sum_{\mathbf{q},\mathbf{q}'} [u_{\mathbf{q}}^* u_{\mathbf{q}'} e^{-i(\mathbf{q}+\mathbf{q}')\cdot\mathbf{r}_b} \hat{b}_{\mathbf{q}}^\dagger \hat{b}_{\mathbf{q}'} \\ &\quad + u_{\mathbf{q}}^* v_{\mathbf{q}'} e^{-i(\mathbf{q}+\mathbf{q}')\cdot\mathbf{r}_b} \hat{b}_{\mathbf{q}}^\dagger \hat{b}_{\mathbf{q}'}^\dagger + v_{\mathbf{q}}^* u_{\mathbf{q}'} e^{i(\mathbf{q}+\mathbf{q}')\cdot\mathbf{r}_b} \hat{b}_{\mathbf{q}} \hat{b}_{\mathbf{q}'} \\ &\quad + v_{\mathbf{q}}^* v_{\mathbf{q}'} e^{i(\mathbf{q}+\mathbf{q}')\cdot\mathbf{r}_b} \hat{b}_{\mathbf{q}} \hat{b}_{\mathbf{q}'}^\dagger]. \end{aligned} \quad (16)$$

Given this, the system-bath Hamiltonian becomes

$$\begin{aligned} \hat{H}_{BS} &= \int_{\mathbb{R}^3} d\mathbf{r}_b V_{\text{ib}}(\mathbf{r}_b - \hat{\mathbf{r}}) \Delta\hat{n}(\mathbf{r}_b) \\ &= \hbar \sum_{\mathbf{q}} (\hat{S}_{\mathbf{q}} \hat{\Gamma}_{\mathbf{q}} + \hat{S}_{\mathbf{q}}^\dagger \hat{\Gamma}_{\mathbf{q}}^\dagger) + \hbar \sum_{\mathbf{q},\mathbf{q}'} (\hat{S}_{\mathbf{q},\mathbf{q}'}^{(u,u')} \hat{\Gamma}_{\mathbf{q}}^\dagger \hat{\Gamma}_{\mathbf{q}'} \\ &\quad + \hat{S}_{\mathbf{q},\mathbf{q}'}^{(u,v')} \hat{\Gamma}_{\mathbf{q}}^\dagger \hat{\Gamma}_{\mathbf{q}'}^\dagger + \hat{S}_{\mathbf{q},\mathbf{q}'}^{(v,u')} \hat{\Gamma}_{\mathbf{q}} \hat{\Gamma}_{\mathbf{q}'} + \hat{S}_{\mathbf{q},\mathbf{q}'}^{(v,v')} \hat{\Gamma}_{\mathbf{q}} \hat{\Gamma}_{\mathbf{q}'}^\dagger) \\ &= \hat{H}_{BS}^{(1)} + \hat{H}_{BS}^{(2)}, \end{aligned} \quad (17)$$

where we used the notation of Ref. [44]: $\hat{\Gamma}_{\mathbf{q}} \equiv \hat{b}_{\mathbf{q}}$, and

$$\begin{aligned} \hat{S}_{\mathbf{q}} &= \frac{\sqrt{nL^3}}{\hbar} (u_{\mathbf{q}} + v_{\mathbf{q}}^*) e^{i\mathbf{q}\cdot\hat{\mathbf{r}}} c_{\mathbf{q}}, \\ \hat{S}_{\mathbf{q},\mathbf{q}'}^{(u,u')} &= \frac{u_{\mathbf{q}}^* u_{\mathbf{q}'}}{\hbar} e^{i(\mathbf{q}'-\mathbf{q})\cdot\hat{\mathbf{r}}} c_{\mathbf{q}'-\mathbf{q}}, \\ \hat{S}_{\mathbf{q},\mathbf{q}'}^{(u,v')} &= \frac{u_{\mathbf{q}}^* v_{\mathbf{q}'}}{\hbar} e^{-i(\mathbf{q}'+\mathbf{q})\cdot\hat{\mathbf{r}}} c_{\mathbf{q}'+\mathbf{q}}, \\ \hat{S}_{\mathbf{q},\mathbf{q}'}^{(v,u')} &= \frac{v_{\mathbf{q}}^* u_{\mathbf{q}'}}{\hbar} e^{i(\mathbf{q}'+\mathbf{q})\cdot\hat{\mathbf{r}}} c_{\mathbf{q}'+\mathbf{q}}, \\ \hat{S}_{\mathbf{q},\mathbf{q}'}^{(v,v')} &= \frac{v_{\mathbf{q}}^* v_{\mathbf{q}'}}{\hbar} e^{-i(\mathbf{q}'-\mathbf{q})\cdot\hat{\mathbf{r}}} c_{\mathbf{q}'-\mathbf{q}}, \\ c_{\mathbf{q}} &= \frac{1}{L^3} \int_{\mathbb{R}^3} d\mathbf{y} e^{i\mathbf{q}\cdot\mathbf{y}} V_{\text{ib}}(\mathbf{y}). \end{aligned} \quad (18)$$

In addition, $\hat{H}_{BS}^{(1)}$ is the first sum over \mathbf{q} in Eq. (17) and it denotes the so-called Fröhlich model Hamiltonian in the context of the electron-phonon coupling in solid state [53], while $\hat{H}_{BS}^{(2)}$ refers to the double sum over \mathbf{q}, \mathbf{q}' , which describes the so-called extended Fröhlich model [45,54]. Specifically for the ionic impurity, the coefficient $c_{\mathbf{q}}$ is linked to the scattering amplitude (5) as

$$c_{\mathbf{q}} = -\frac{2\pi\hbar^2}{\mu L^3} f(q). \quad (19)$$

Apart from the Bogolyubov approximation, the expression (17) is exact for a bosonic bath. For a normal Fermi gas, the interaction Hamiltonian reduces to

$$\hat{H}_{BS} = \hbar \sum_{\mathbf{q},\mathbf{q}'} \hat{S}_{\mathbf{q},\mathbf{q}'} \hat{\Gamma}_{\mathbf{q}}^\dagger \hat{\Gamma}_{\mathbf{q}'} \quad (20)$$

with $\hat{S}_{\mathbf{q},\mathbf{q}'} = e^{i(\mathbf{q}'-\mathbf{q})\cdot\hat{\mathbf{r}}} c_{\mathbf{q}'-\mathbf{q}}/\hbar$ and $\hat{\Gamma}_{\mathbf{q}}^\dagger \equiv \hat{c}_{\mathbf{q}}^\dagger$ ($\hat{\Gamma}_{\mathbf{q}} \equiv \hat{c}_{\mathbf{q}}$) being the creation (annihilation) operator of a free fermion of momentum \mathbf{q} with $\{\hat{c}_{\mathbf{q}}, \hat{c}_{\mathbf{q}'}^\dagger\} = \delta_{\mathbf{q},\mathbf{q}'}$.

If the impurity-bath interaction is described by the pseudopotential, as for neutral impurities, we have [55]

$$V_{\text{ib}}(\mathbf{r}) = g_{\text{ib}} \delta(\mathbf{r}), \quad (21)$$

where $g_{\text{ib}} = 2\pi\hbar^2 a_{\text{ib}}^s/\mu$ with a_{ib}^s being the 3D s -wave impurity-bath scattering length. Thus, Eq. (19) becomes

$$c_{\mathbf{q}} = \frac{2\pi\hbar^2}{\mu L^3} a_{\text{ib}}^s. \quad (22)$$

Specifically for the atom-ion case, we see that $f(q) \rightarrow -a_{\text{ib}}^s$. Thus, if we would replace the atom-ion interaction (4) by Eq. (21), in all subsequent equations one has simply to replace

TABLE I. Top: Critical temperature for condensation \mathcal{T}_c^0 of a noninteracting gas for three bosonic species and densities. Bottom: Fermi temperature \mathcal{T}_F for two fermionic species and three densities. Temperature values are given in units of nK.

Boson	$n_t = 10^{12} \text{ cm}^{-3}$	10^{13} cm^{-3}	10^{14} cm^{-3}
^7Li	229	1063	4934
^{23}Na	70	324	1506
^{87}Rb	18	86	398
Fermion	$n_t = 10^{12} \text{ cm}^{-3}$	10^{13} cm^{-3}	10^{14} cm^{-3}
^6Li	613	2844	13 198
^{40}K	92	428	1987

the scattering amplitude in the first-Born approximation with the scattering length a_{ib}^s .

B. Validity requirements and chemical potential

Let us comment on the validity of the Bogolyubov approximation, which implies that both the quantum and thermal depletion must be small [56]. As we shall discuss in Sec. IV, we are mostly interested in the high-temperature regime, that is, $k_B \mathcal{T} \gg g n_t$, which means that the intraparticle interactions are essentially negligible. Here, n_t is the total gas density that in the zero-temperature limit corresponds to the condensate density n_0 . In this regime, the Bogolyubov approximation is valid only if $n_t \lambda_{\text{dB}}(\mathcal{T})^3 \gg \zeta(3/2)$. Here, $\lambda_{\text{dB}}(\mathcal{T}) = [2\pi \hbar^2 / (m k_B \mathcal{T})]^{1/2}$ denotes the thermal de Broglie wavelength, $\zeta(x)$ is the Riemann zeta function. The last inequality can be also rewritten as $\mathcal{T} \ll \mathcal{T}_c^0 = \frac{2\pi \hbar^2 n_t^{2/3}}{m k_B [\zeta(3/2)]^{2/3}}$, where \mathcal{T}_c^0 is the critical temperature of condensation of a noninteracting and untrapped Bose gas. Thus, in order to perform the Bogolyubov approximation, all conditions have to be fulfilled simultaneously, namely, the noncondensed fraction $n_t (\mathcal{T} / \mathcal{T}_c^0)^{3/2} \ll 1$. Here, $n_t = n_0 + n_n$ is the total density of the gas with n_n being the normal (i.e., noncondensed) component, from which we retrieve the condensate density as

$$n_0 = n_t - n_n = n_t [1 - (\mathcal{T} / \mathcal{T}_c^0)^{3/2}]. \quad (23)$$

In Table I we provide some values of the critical temperature of condensation at typical quantum gas densities.

Afterwards, it will be important to compute the chemical potential for a noninteracting and homogeneous Bose and Fermi gas at temperature \mathcal{T} . To this end, let us remind that the chemical potential for the bosons reads as [57]

$$\mu_G = \begin{cases} 0, & \text{if } \mathcal{T} \leq \mathcal{T}_c^0, \\ \text{root of } n_t \lambda_{\text{dB}}^3 = g_{3/2}(z), & \text{if } \mathcal{T} > \mathcal{T}_c^0. \end{cases} \quad (24)$$

Here, $z = e^{\mu_G / k_B \mathcal{T}}$ is the so-called fugacity and $g_{3/2}(z) = \sum_{l=1}^{\infty} z^l l^{-3/2}$. We note that the chemical potential for $\mathcal{T} > \mathcal{T}_c^0$ is negative or else $g_{3/2}(z)$ does not converge.

For the fermions, the chemical potential is obtained by solving numerically the equation of state [57]

$$n_t \lambda_{\text{dB}}^3 = f_{3/2}(z), \quad (25)$$

where $f_{3/2}(z) = \sum_{l=1}^{\infty} (-1)^{l+1} z^l l^{-3/2}$. At $\mathcal{T} = 0$, the chemical potential corresponds to the Fermi energy E_F :

$$\mu_G \equiv E_F = \frac{\hbar^2}{2m} (6\pi^2 n_t)^{2/3}. \quad (26)$$

We note that for $\mathcal{T} > \mathcal{T}_F$, μ_G is negative, similarly to the bosonic case, where $\mathcal{T}_F = E_F / k_B$ is the Fermi temperature. In the high-temperature limit $\mathcal{T} \gg \mathcal{T}_c^0$, \mathcal{T}_F , the chemical potential of both the bosons and the fermions is well described by that of the Boltzmann gas

$$\mu_G = k_B \mathcal{T} \ln(n_t \lambda_{\text{dB}}^3). \quad (27)$$

C. Markovian master equation

In this section we describe the relevant steps of the derivation of the master equation for the bosons, while for the fermionic bath we simply provide the final result since the derivation is analogous.

We start from the full system-bath density matrix $\hat{\chi}(t)$, which obeys the von Neumann equation

$$\frac{d}{dt} \hat{\chi}(t) = -\frac{i}{\hbar} [\hat{H}, \hat{\chi}]. \quad (28)$$

Writing the density operator in the interaction picture as

$$\tilde{\chi}(t) = \hat{U}^\dagger(0, t) e^{i\hat{H}_B t / \hbar} \hat{\chi}(t) e^{-i\hat{H}_B t / \hbar} \hat{U}(0, t), \quad (29)$$

where

$$\hat{U}(t_1, t_2) = \mathbb{T} \exp \left[-\frac{i}{\hbar} \int_{t_1}^{t_2} dt \hat{H}_S(t) \right] \quad (30)$$

with \mathbb{T} the time-ordered evolution operator, we have

$$\frac{d}{dt} \tilde{\chi}(t) = -\frac{i}{\hbar} [\tilde{H}_{BS}(t), \tilde{\chi}(t)]. \quad (31)$$

Here, \tilde{H}_{BS} is the interaction Hamiltonian in the interaction picture, which is defined similarly to Eq. (29). The formal solution of Eq. (31) is

$$\tilde{\chi}(t) = \tilde{\chi}(0) - \frac{i}{\hbar} \int_0^t dt' [\tilde{H}_{BS}(t'), \tilde{\chi}(t')] \quad (32)$$

and substituting it into the commutator (31) we obtain

$$\begin{aligned} \frac{d}{dt} \tilde{\chi}(t) = & -\frac{i}{\hbar} [\tilde{H}_{BS}(t), \tilde{\chi}(0)] \\ & - \frac{1}{\hbar^2} \int_0^t dt' [\tilde{H}_{BS}(t), [\tilde{H}_{BS}(t'), \tilde{\chi}(t')]]. \end{aligned} \quad (33)$$

Thus, we assume that initially, at $t = 0$, the system and the bath are uncorrelated, namely, $\hat{\chi}(0) = \tilde{\chi}(0) = \hat{\rho}(0) \otimes \hat{B}_0$, where \hat{B}_0 is the initial bath density matrix. This is a reasonable assumption if the impurity and the bath are initially well separated such that no interaction occurs. By tracing over the bath degrees of freedom in Eq. (33) we arrive to the equation [58]

$$\frac{d}{dt} \tilde{\rho}(t) = -\frac{1}{\hbar^2} \int_0^t dt' \text{Tr}_B \{ [\tilde{H}_{BS}(t), [\tilde{H}_{BS}(t'), \tilde{\chi}(t')]] \}. \quad (34)$$

The next step consists in performing the so-called Born approximation, namely, we assume that the impurity-bath

coupling is weak and that the bath is so large that $\tilde{\chi}(t') \simeq \tilde{\rho}(t') \otimes \hat{B}_0 \forall t'$ holds. Thus, Eq. (34) becomes

$$\frac{d}{dt} \tilde{\rho}(t) = -\frac{1}{\hbar^2} \int_0^t dt' \text{Tr}_B \{ [\tilde{H}_{BS}(t), [\tilde{H}_{BS}(t'), \tilde{\rho}(t') \otimes \hat{B}_0]] \}. \quad (35)$$

In order to further simplify this equation, we make the Markov approximation, namely, we replace $\tilde{\rho}(t')$ by $\tilde{\rho}(t)$ in order to obtain a time-local master equation

$$\frac{d}{dt} \tilde{\rho}(t) = -\frac{1}{\hbar^2} \int_0^t dt' \text{Tr}_B \{ [\tilde{H}_{BS}(t), [\tilde{H}_{BS}(t'), \tilde{\rho}(t) \otimes \hat{B}_0]] \}. \quad (36)$$

This equation is known in the literature as the Redfield equation [59]. The Hamiltonian $\tilde{H}_{BS}(t)$ keeps the original structure of the Schrödinger picture, but with time-dependent system and bath operators:

$$\begin{aligned} \hat{S}_{\mathbf{q}}(t) &= \hat{U}^\dagger(0, t) \hat{S}_{\mathbf{q}} \hat{U}(0, t), \\ \hat{\Gamma}_{\mathbf{q}}(t) &= e^{i\hat{H}_B t/\hbar} \hat{\Gamma}_{\mathbf{q}} e^{-i\hat{H}_B t/\hbar} = e^{-\frac{i}{\hbar} \varepsilon(\mathbf{q}) t} \hat{\Gamma}_{\mathbf{q}}, \\ \hat{S}_{\mathbf{q}, \mathbf{q}'}^{(u, u')}(t) &= \hat{U}^\dagger(0, t) \hat{S}_{\mathbf{q}, \mathbf{q}'}^{(u, u')} \hat{U}(0, t). \end{aligned} \quad (37)$$

Next, we need to perform the partial trace over the bath degrees of freedom, namely, we need to assess

$$\begin{aligned} &\text{Tr}_B \{ [\tilde{H}_{BS}(t), [\tilde{H}_{BS}(t'), \tilde{\rho}(t) \otimes \hat{B}_0]] \} \\ &= \text{Tr}_B \{ [\tilde{H}_{BS}^{(1)}(t), [\tilde{H}_{BS}^{(1)}(t'), \tilde{\rho}(t) \otimes \hat{B}_0]] \} \\ &\quad + \text{Tr}_B \{ [\tilde{H}_{BS}^{(2)}(t), [\tilde{H}_{BS}^{(2)}(t'), \tilde{\rho}(t) \otimes \hat{B}_0]] \} \end{aligned}$$

$$\begin{aligned} &+ \text{Tr}_B \{ [\tilde{H}_{BS}^{(2)}(t), [\tilde{H}_{BS}^{(1)}(t'), \tilde{\rho}(t) \otimes \hat{B}_0]] \} \\ &+ \text{Tr}_B \{ [\tilde{H}_{BS}^{(1)}(t), [\tilde{H}_{BS}^{(2)}(t'), \tilde{\rho}(t) \otimes \hat{B}_0]] \}. \end{aligned} \quad (38)$$

Thus, we consider the bath's thermal density matrix

$$\hat{B}_0 = \frac{e^{-\beta(\hat{H}_B - \mu_G \hat{N})}}{\mathcal{Z}}, \quad \mathcal{Z} = \text{Tr}_B \{ e^{-\beta(\hat{H}_B - \mu_G \hat{N})} \}, \quad (39)$$

where \hat{N} is the bath number operator. The mixed terms in the third and fourth lines of Eq. (38) are zero since they contain an odd number of bath operators. Thus, only the terms of the second (i.e., with $\tilde{H}_{BS}^{(1)}(t)$ only) and the last line (i.e., with $\tilde{H}_{BS}^{(2)}(t)$ only) of Eq. (38) remain.

First, we consider the thermal average of the double commutator involving $\tilde{H}_{BS}^{(1)}(t)$, which includes the averages of two bath operators only, for example, $\langle \tilde{\Gamma}_{\mathbf{q}}(t) \tilde{\Gamma}_{\mathbf{q}'}(t') \rangle_{B_0} = \text{Tr}_B \{ \hat{B}_0 \tilde{\Gamma}_{\mathbf{q}}(t) \tilde{\Gamma}_{\mathbf{q}'}(t') \}$. On the other hand, $\langle \tilde{\Gamma}_{\mathbf{q}}^\dagger(t) \tilde{\Gamma}_{\mathbf{q}'}(t') \rangle_{B_0} = \langle \tilde{\Gamma}_{\mathbf{q}}^\dagger(t) \tilde{\Gamma}_{\mathbf{q}'}^\dagger(t') \rangle_{B_0} = 0$, while

$$\langle \tilde{\Gamma}_{\mathbf{q}}(t) \tilde{\Gamma}_{\mathbf{q}'}^\dagger(t') \rangle_{B_0} = e^{-\frac{i}{\hbar} \varepsilon(\mathbf{q})(t-t')} (n_{\mathbf{q}} + 1) \delta_{\mathbf{q}, \mathbf{q}'}. \quad (40)$$

Here, $n_{\mathbf{q}} = \langle \hat{b}_{\mathbf{q}}^\dagger \hat{b}_{\mathbf{q}} \rangle = [e^{\beta \tau [\varepsilon(\mathbf{q}) - \mu_G]} - 1]^{-1}$ is the Bose-Einstein occupation number and $\beta \tau = 1/(k_B \mathcal{T})$.

The average of the double commutator with only $\tilde{H}_{BS}^{(2)}(t)$ has terms that vanish when the number of raising and lowering bath operators is not the same, while the nonzero contributions are given in Appendix B. Putting all together into Eq. (36) and performing the change of variable $\tau = t - t'$, and finally transforming back to the Schrödinger picture, we arrive at the following final master equation:

$$\begin{aligned} \frac{d}{dt} \hat{\rho}(t) &= -\frac{i}{\hbar} [\hat{H}_S, \hat{\rho}] - \sum_{\mathbf{q}} \int_0^t d\tau \Omega_{\mathbf{q}}^2 \{ (n_{\mathbf{q}} + 1) [\hat{Z}_{\mathbf{q}}, \hat{W}_{\mathbf{q}}(t, \tau) \hat{\rho}(t)] + n_{\mathbf{q}} [\hat{\rho}(t) \hat{W}_{\mathbf{q}}(t, \tau), \hat{Z}_{\mathbf{q}}] + \text{H.c.} \} \\ &\quad - \sum_{\mathbf{q}, \mathbf{q}'} \int_0^t d\tau \{ n_{\mathbf{q}} (n_{\mathbf{q}'} + 1) [\hat{Z}_{\mathbf{q}-\mathbf{q}}, \hat{W}_{\mathbf{q}-\mathbf{q}}(t, \tau) \hat{\rho}(t)] \Omega_{u, u'}^{u, u'}(\mathbf{q}' - \mathbf{q}) + 2n_{\mathbf{q}} (n_{\mathbf{q}'} + 1) [\hat{Z}_{\mathbf{q}-\mathbf{q}}, \hat{W}_{\mathbf{q}-\mathbf{q}}(t, \tau) \hat{\rho}(t)] \Omega_{u, u'}^{v, v'}(\mathbf{q}' - \mathbf{q}) \\ &\quad \times ((1 + n_{\mathbf{q}} + n_{\mathbf{q}'} + n_{\mathbf{q}} n_{\mathbf{q}'}) [\hat{Z}_{\mathbf{q}+\mathbf{q}}, \hat{W}_{\mathbf{q}+\mathbf{q}}(t, \tau) \hat{\rho}(t)] + n_{\mathbf{q}} n_{\mathbf{q}'} [\hat{Z}_{\mathbf{q}+\mathbf{q}}, \hat{\rho}(t) \hat{W}_{\mathbf{q}+\mathbf{q}}(t, \tau)]) (\Omega_{v, u'}^{u, v'}(\mathbf{q}' + \mathbf{q}) + \tilde{\Omega}_{v, u'}^{u, v'}(\mathbf{q}' + \mathbf{q})) \\ &\quad \times n_{\mathbf{q}'} (n_{\mathbf{q}} + 1) [\hat{Z}_{\mathbf{q}-\mathbf{q}}, \hat{W}_{\mathbf{q}-\mathbf{q}}(t, \tau) \hat{\rho}(t)] \Omega_{v, v'}^{v, v'}(\mathbf{q} - \mathbf{q}') + \text{H.c.} \}. \end{aligned} \quad (41)$$

Here, we have defined the operators

$$\begin{aligned} \hat{Z}_{\mathbf{q}} &= e^{i\mathbf{q} \cdot \hat{\mathbf{r}}}, \quad \hat{W}_{\mathbf{q}}(t, \tau) = e^{-\frac{i}{\hbar} \varepsilon(\mathbf{q}) \tau} e^{-i\mathbf{q} \cdot \hat{\mathbf{r}}(t, \tau)}, \\ \hat{W}_{\mathbf{q}-\mathbf{q}'}(t, \tau) &= e^{-\frac{i}{\hbar} [\varepsilon(\mathbf{q}') - \varepsilon(\mathbf{q})] \tau} e^{-i(\mathbf{q}' - \mathbf{q}) \cdot \hat{\mathbf{r}}(t, \tau)}, \\ \hat{W}_{\mathbf{q}+\mathbf{q}'}(t, \tau) &= e^{-\frac{i}{\hbar} [\varepsilon(\mathbf{q}) + \varepsilon(\mathbf{q}')] \tau} e^{-i(\mathbf{q} + \mathbf{q}') \cdot \hat{\mathbf{r}}(t, \tau)}, \end{aligned} \quad (42)$$

and the coefficients

$$\begin{aligned} \Omega_{\mathbf{q}}^2 &= \frac{|u_{\mathbf{q}} + v_{\mathbf{q}}^*|^2}{\hbar^2} |c_{\mathbf{q}}|^2 n_0 L^3, \\ \Omega_{u, u'}^{u, u'}(\mathbf{q}' - \mathbf{q}) &= \frac{|u_{\mathbf{q}}|^2 |u_{\mathbf{q}'}|^2}{\hbar^2} |c_{\mathbf{q}' - \mathbf{q}}|^2, \\ \Omega_{v, v'}^{v, v'}(\mathbf{q}' - \mathbf{q}) &= \frac{|v_{\mathbf{q}}|^2 |v_{\mathbf{q}'}|^2}{\hbar^2} |c_{\mathbf{q}' - \mathbf{q}}|^2, \end{aligned}$$

$$\Omega_{u, u'}^{v, v'}(\mathbf{q}' - \mathbf{q}) = \frac{u_{\mathbf{q}}^* v_{\mathbf{q}} u_{\mathbf{q}'} v_{\mathbf{q}'}}{\hbar^2} |c_{\mathbf{q}' - \mathbf{q}}|^2, \quad (43)$$

$$\Omega_{v, u'}^{u, v'}(\mathbf{q}' + \mathbf{q}) = \frac{u_{\mathbf{q}}^* v_{\mathbf{q}} u_{\mathbf{q}'} v_{\mathbf{q}'}}{\hbar^2} |c_{\mathbf{q}' + \mathbf{q}}|^2,$$

$$\tilde{\Omega}_{v, u'}^{u, v'}(\mathbf{q}' + \mathbf{q}) = \frac{|v_{\mathbf{q}}|^2 |u_{\mathbf{q}'}|^2}{\hbar^2} |c_{\mathbf{q}' + \mathbf{q}}|^2,$$

whereas

$$\hat{\mathbf{r}}(t, \tau) = \hat{U}(0, t) \hat{U}^\dagger(0, t - \tau) \hat{\mathbf{r}} \hat{U}(0, t - \tau) \hat{U}^\dagger(0, t). \quad (44)$$

This relation describes the impurity position evolution in absence of the gas. Equation (41) is not yet a Markovian master equation, even though the time development of the system density matrix relies only on the density matrix at time t . Indeed, the impurity density matrix in Eq. (41) still depends

on the specific choice for the system preparation at $t = 0$ via the impurity's trajectory in $W_{\mathbf{q}-\mathbf{q}}(t, \tau)$ or, in a more precise mathematical language, it is not yet a dynamical semigroup [59]. Hence, to render (41) a Markovian master equation, we let the upper limit of the integral go to infinity, which is permissible if the integrand disappears sufficiently fast for $\tau \gg \tau_R = \hbar/(k_B T)$. This is justifiable if the timescale of the system τ_S over which the system density matrix $\hat{\rho}(t)$ varies appreciably, is much larger than the timescale of the bath τ_R . In other words, we require the bath correlation functions to decay much faster than τ_S [59]. Hence, the Markov approximation is justified when the bath correlation functions, e.g., $\langle \tilde{\Gamma}_{\mathbf{q}}(t) \tilde{\Gamma}_{\mathbf{k}}(t') \rangle_{B_0} = \text{Tr}_B \{ \tilde{B}_0 \tilde{\Gamma}_{\mathbf{q}}(t) \tilde{\Gamma}_{\mathbf{k}}(t') \}$, are proportional to $\delta(t - t')$. Instead, the Born approximation is fulfilled if the dissipative damping rate is smaller than the relevant system's transition frequencies. We shall come back to this point later in the paper. Note that with the upper limit of the integral going to infinity, the first line of Eq. (41) is equal to Eq. (23) of Ref. [33]. However, while in the latter the time integral in the definition of $W_{\mathbf{k}, \mathbf{k}'}(t)$ is included, we prefer here to write it explicitly.

Finally, we underline that up until now Eq. (41) is valid for any impurity in a condensate (not only for an ion), provided that the Fourier transform (19) can be computed. Indeed, the solution to Eq. (44) depends on the impurity dynamics only and the Hamiltonian $\hat{H}_S(t)$ can also represent the free evolution of a not trapped ion in a BEC or an impurity atom in an optical lattice. For a normal Fermi gas, however, the master equation (41) reduces to the double sum only, namely, the sum over \mathbf{q} in the first line disappears. Moreover, only one term of the double sum contributes, as we have single-particle energy states and not Bogolyubov modes. In practice, one sets in Eq. (41) the Bogolyubov amplitudes $u \equiv 1$ and $v \equiv 0$ and replaces $n_{\mathbf{q}'} + 1$ by $1 - n_{\mathbf{q}'}$ because of the anticommutation relations of the fermionic field operators. Here, $n_{\mathbf{q}} = [e^{\beta \tau (\varepsilon(\mathbf{q}) - \mu_G)} + 1]^{-1}$ is the Fermi-Dirac occupation number with μ_G being the chemical potential obtained from solving Eq. (25).

IV. TRAPPED ION MASTER EQUATION

The Markovian master equation (41) can be further simplified for an ion in a radio-frequency trap because of the separation of energy and length scales between the atomic ensemble and the trapped ion system. Indeed, we are going to make two further approximations:

- (a) the particlelike approximation;
- (b) the Lamb-Dicke approximation.

The former concerns the bosonic energy dispersion (12). Because of the large energy difference between the bosonic bath and the ion system, only particlelike excitations couple to the ion motion. This implies that the Bogolyubov dispersion relation (12) is essentially quadratic in the wave vector q . For a linear Paul trap, for instance, we have (see Appendix C 1 for details) the following: $a_{x,y} = -0.001$, $a_z = 0.002$, $q_x = 0.2$, $q_y = -0.2$, $q_z = 0$, and $\Omega_{rf} = 2\pi \times 2$ MHz, as obtained from the trap design of Ref. [60]. These parameters yield the following reference trap frequencies for an ytterbium ion (see Appendix C 2): $\nu_x \simeq 2\pi \times 169$ kHz, $\nu_y \simeq 2\pi \times 112$ kHz, $\nu_z \simeq 2\pi \times 45$ kHz (the z axis is the longitudinal direction,

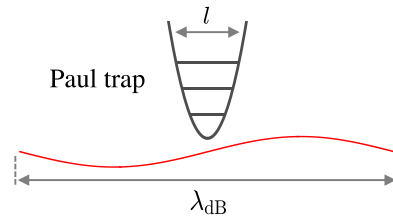


FIG. 2. Schematic representation of the Lamb-Dicke approximation: the size l of the ion trap (corresponding to the size of the ion in its ground state) is much smaller than the de Broglie wavelength λ_{dB} of the atoms in the gas.

where a system with two or more ions would form a linear crystal). For the sake of convenience, we rescale the dispersion relation (12) as

$$\frac{\omega_{\mathbf{q}}}{v_{\xi}} = \sqrt{\left(\frac{\bar{q}^2}{2}\right)^2 + (\bar{c}_s \bar{q})^2}, \quad \xi = x, y, z \quad (45)$$

where $\bar{q} = \ell_{\xi} q$ with $\ell_{\xi} = \sqrt{\hbar/(m v_{\xi})}$, and $\bar{c}_s = 4\pi(a_{\text{aa}}^s/\ell_{\xi})n\ell_{\xi}^3$. For sodium atoms with a density $n_0 = 10^{14}$ cm^{-3} we have $\bar{c}_s \simeq 0.009$ ($\xi \equiv x$), $\bar{c}_s \simeq 0.014$ ($\xi \equiv y$), and $\bar{c}_s \simeq 0.034$ ($\xi \equiv z$). The bosons speed of sound ($c_s = \bar{c}_s \ell_{\xi} v_{\xi}$) is therefore quite small compared to the ion motion in the secular trap such that only phonons of quite low $\bar{q} \sim \bar{c}_s$ (i.e., large wavelength) yield an appreciable difference in the dispersion relation compared to the free particle energy $\bar{q}^2/2$. On the other hand, only phonons in the condensate of comparable energy as $\hbar v_{\xi}$ will couple to the ion motion, so that we can safely assume a particlelike dispersion relation $\varepsilon(\mathbf{q}) = \hbar^2 q^2/(2m)$, and set $u_{\mathbf{q}} \simeq 1$, $v_{\mathbf{q}} \simeq 0$, namely, the bosonic bath can be treated as a noninteracting Bose gas. This corresponds to an atom velocity of $\sqrt{2\hbar v_{\xi}/m}$ in the ξ th direction. For example, $v_x \simeq 0.077$ m/s or, in rescaled units, $\bar{v}_x \simeq 1.414$, which is much larger than \bar{c}_s , and therefore the atom is moving at supersonic velocities. To such an atomic velocity it is associated the wavelength $\lambda_x \simeq 226.63$ nm. As a consequence of the energy separation, several terms of the quadratic corrections of the atom-ion interaction in Eq. (41) can be safely discarded.

On the other hand, the approximation (b) implies that the typical wavelength of the bosons or of the fermions, i.e., the thermal de Broglie wavelength $\lambda_{dB}(T)$, is much larger than the ξ th width of the ion ground state $l_{\xi} = \sqrt{\hbar/(M v_{\xi})}$ (see Fig. 2). Let us still consider the example of bosonic sodium atoms at a temperature of $T = 200$ nK. Thus, we have $\lambda_{dB}(T) \simeq 814.18$ nm, while for a trapped ytterbium ion the width of the ground state in the secular trap is $l_z \simeq 36.05$ nm. This yields a ratio $l_z/\lambda_{dB}(T) \simeq 0.044$ (similarly for the other directions). Even if we consider the previously estimated supersonic atom velocity, we get $l_{\xi}/\lambda_{\xi} \simeq 0.045$ for lithium atoms, $l_{\xi}/\lambda_{\xi} \simeq 0.082$ for sodium atoms, and $l_{\xi}/\lambda_{\xi} \simeq 0.159$ for rubidium atoms. Hence, the ion spreading is quite localized compared to that of the bath's particle, and therefore the Lamb-Dicke approximation holds very well in the regime we are interested in.

A. Simplified master equation

Under the applicability conditions of the Lamb-Dicke approximation, we can legitimately expand the exponential functions appearing in Eq. (41) up to second order in $\mathbf{q} \cdot \hat{\mathbf{r}}$.

For instance, the commutator reduces to

$$\begin{aligned} & [\hat{Z}_{\mathbf{q}}, \hat{W}_{\mathbf{q}}(t, \tau) \hat{\rho}(t)] \\ & \simeq e^{-\frac{i}{\hbar} \varepsilon(\mathbf{q}) \tau} \{ i[\mathbf{q} \cdot \hat{\mathbf{r}}, \hat{\rho}(t)] + [\mathbf{q} \cdot \hat{\mathbf{r}}, \mathbf{q} \cdot \hat{\mathbf{r}}(t, \tau) \hat{\rho}(t)] \\ & \quad - \frac{1}{2} [(\mathbf{q} \cdot \hat{\mathbf{r}})^2, \hat{\rho}(t)] \}. \end{aligned} \quad (46)$$

Here, the operators $\hat{W}_{\mathbf{q}}(t, \tau) \equiv \hat{W}_{\mathbf{q}}(t, t - \tau)$ and $\hat{\mathbf{r}}(t, \tau) \equiv \hat{\mathbf{r}}(t - \tau)$ [see also Eq. (44)]. Given this, the three directions are decoupled from each other because odd powers of the wave vectors \mathbf{q} vanish, as a consequence of the symmetric summation in the master equation, that is, since the bath is homogeneously confined. Therefore, Eq. (41) can be rewritten as follows:

$$\begin{aligned} \frac{d}{dt} \hat{\rho}(t) = & -\frac{i}{\hbar} [\hat{H}_S, \hat{\rho}] - \sum_{\mathbf{q}, \xi} \int_0^\infty d\tau \Omega_{\mathbf{q}}^2 q_\xi^2 \left\{ i \sin\left(\frac{\varepsilon(\mathbf{q})\tau}{\hbar}\right) [\hat{r}_\xi^2, \hat{\rho}(t)] + e^{-\frac{i\varepsilon(\mathbf{q})\tau}{\hbar}} [\hat{r}_\xi, \hat{r}_\xi(t, \tau) \hat{\rho}(t)] - e^{\frac{i\varepsilon(\mathbf{q})\tau}{\hbar}} [\hat{r}_\xi, \hat{\rho}(t) \hat{r}_\xi(t, \tau)] \right. \\ & + 2n_{\mathbf{q}} \cos\left(\frac{\varepsilon(\mathbf{q})\tau}{\hbar}\right) ([\hat{r}_\xi, \hat{r}_\xi(t, \tau) \hat{\rho}(t)] - [\hat{r}_\xi, \hat{\rho}(t) \hat{r}_\xi(t, \tau)]) \left. \right\} - \sum_{\mathbf{q}, \mathbf{q}'} \sum_{\xi} \int_0^\infty d\tau n_{\mathbf{q}} (n_{\mathbf{q}'} + 1) (q'_\xi - q_\xi)^2 \Omega_{\mathbf{q}, \mathbf{q}'}^{u, u'} (\mathbf{q}' - \mathbf{q}) \\ & \times \left\{ i \sin\left(\frac{\varepsilon(\mathbf{q}') - \varepsilon(\mathbf{q})}{\hbar} \tau\right) [\hat{r}_\xi^2, \hat{\rho}(t)] + e^{-\frac{i[\varepsilon(\mathbf{q}') - \varepsilon(\mathbf{q})]\tau}{\hbar}} [\hat{r}_\xi, \hat{r}_\xi(t, \tau) \hat{\rho}(t)] - e^{\frac{i[\varepsilon(\mathbf{q}') - \varepsilon(\mathbf{q})]\tau}{\hbar}} [\hat{r}_\xi, \hat{\rho}(t) \hat{r}_\xi(t, \tau)] \right\} \end{aligned} \quad (47)$$

with $\xi = x, y, z$. The first sum over \mathbf{q} in the first two lines of Eq. (47) refers to the Frölich model, while the double sum in the last two lines refers to the extended Frölich model (17), that is, $\hat{H}_{RS}^{(2)}$. Because of the particlelike approximation, however, only the term $\Omega_{u, u'}^{u, u'}$ remains, while for the fermions no Frölich interaction appears.

In order to make further progress, we need to explicitly use the solution of the ion dynamics in the Paul trap in the absence of the gas. The full solution $\hat{r}_\xi(t)$ is provided with various details in Ref. [33], which is given by

$$\begin{aligned} \hat{r}_\xi(t, \tau) = & \sum_{s, s'} C_s^\xi C_{s'}^\xi \left[\hat{r}_\xi \left(\frac{\beta_\xi}{2} + s' \right) \frac{\Omega_{rf}}{v_\xi} \cos[\mathcal{I}_{s, s'}^\xi(t, \tau)] \right. \\ & \left. - \frac{\hat{p}_\xi}{v_\xi M} \sin[\mathcal{I}_{s, s'}^\xi(t, \tau)] \right] \end{aligned} \quad (48)$$

for $\xi = x, y, z$, $[\hat{\mathbf{r}}, \hat{\mathbf{p}}] = i\hbar$ ($\hat{\mathbf{p}}$ is the ion momentum operator), and

$$\mathcal{I}_{s, s'}^\xi(t, \tau) = \Omega_{rf} \left[\left(\frac{\beta_\xi}{2} + s \right) \tau - (s - s')t \right]. \quad (49)$$

The coefficients C_s^ξ , the trap parameters β_ξ , and the frequencies v_ξ are introduced in Appendix C 1.

Since we consider a gas confined in a box of volume L^3 , the wave vector \mathbf{q} assumes quantized values: $2\pi s_\xi / L$ with $s_\xi \in \mathbb{Z}$ (periodic boundary conditions) and $\xi = x, y, z$. Hence, in the limit $L \rightarrow +\infty$ the allowed values of \mathbf{q} in momentum space become closely spaced, and since their density is $ds = L^3 / (2\pi)^3 d\mathbf{q}$, we make the replacement

$$\sum_{\mathbf{q}} \rightarrow \frac{L^3}{(2\pi)^3} \int_{\mathbb{R}^3} d\mathbf{q}. \quad (50)$$

Such a continuum limit approximation is reasonable for a large bath. Furthermore, we use the identity [44]

$$\int_0^\infty d\tau e^{-i(\omega - \omega_0)\tau} = \pi \delta(\omega - \omega_0) - i\text{P}\left(\frac{1}{\omega - \omega_0}\right), \quad (51)$$

where P denotes the Cauchy principal value (CPV), whose action on a test function $\varphi(\omega)$ is

$$\text{P}\left(\frac{1}{\omega}\right)(\varphi) = \lim_{\epsilon \rightarrow 0^+} \int_{\mathbb{R}/[-\epsilon, \epsilon]} d\omega \frac{\varphi(\omega)}{\omega}. \quad (52)$$

Now, we apply these results and we focus first our attention on the Frölich contribution to the master equation, namely, the incoherent term in Eq. (47) involving the summation over \mathbf{q} . Besides, at the moment, we neglect the contribution due to the CPV and look at the δ contributions only. Thus, $\omega \equiv \varepsilon(\mathbf{q})/\hbar$, while $\omega_0 \equiv 0$ or $\omega_0 \equiv \Omega_{rf}(\beta_\xi/2 + s)$ in Eq. (51). When $\omega_0 \equiv 0$, however, the contribution of the term coming from the sine function in the first line of Eq. (47) vanishes, as it can be verified by performing the integration (50) in spherical coordinates. On the other hand, when $\omega_0 \equiv \Omega_{rf}(\beta_\xi/2 + s)$ and after having moved to spherical coordinates, we first write the Dirac's delta as

$$\delta(\omega - \omega_0) = \frac{m}{\hbar q} \delta(q - q_{s, \xi}) \quad (53)$$

with $q = |\mathbf{q}|$, and [61]

$$q_{s, \xi} = \sqrt{\frac{2m\Omega_{rf}}{\hbar} \left| \frac{\beta_\xi}{2} + s \right|}. \quad (54)$$

Hence, the integration in momentum space yields

$$\int_{\mathbb{R}^3} d\mathbf{q} \frac{f^2(q) q_\xi^2}{q} \delta(q - q_{s, \xi}) = \frac{4}{3} \pi q_{s, \xi}^3 f^2(q_{s, \xi}) \quad (55)$$

with f being the scattering amplitude (6) evaluated in $q = q_{s, \xi}$.

As far as the contribution of the extended Fröhlich model is concerned, namely, the terms due to the double summation over \mathbf{q} and \mathbf{q}' in Eq. (47), we proceed in a very similar manner with the exception that we now have to assess a double integration in momentum space. In Appendix D 1 we provide details of this calculation. On the other hand, in order to assess the contribution due the Lamb shift we have to compute the integral (52), whose details are outlined in Appendix D 2. We note, however, that we performed such a Lamb-shift calculation only for the linear terms of Eq. (47) since the contribution of the extended Fröhlich model is much smaller, and therefore it can be neglected.

Under the above outlined approximations, we arrive at

$$\begin{aligned} \frac{d}{dt}\hat{\rho}(t) = & -\frac{i}{\hbar}[\hat{H}_S + \delta\hat{H}_S, \hat{\rho}] - \Gamma \sum_{\xi=x,y,z} \{\Lambda_\xi[\hat{r}_\xi, \hat{\rho}(t)\hat{p}_\xi] \\ & - \Lambda_\xi^*[\hat{r}_\xi, \hat{p}_\xi\hat{\rho}(t)] - \Phi_\xi[\hat{r}_\xi, \hat{\rho}(t)\hat{r}_\xi] + \Phi_\xi^*[\hat{r}_\xi, \hat{r}_\xi\hat{\rho}(t)]\}. \end{aligned} \quad (56)$$

Here, $\Gamma = \frac{2}{3} \frac{mn_0\pi\hbar}{\mu^2}$ and $\delta\hat{H}_S$ is the correction to the free-ion Hamiltonian due to the interaction to the quantum gas (i.e., the Lamb shift), which is given by

$$\delta\hat{H}_S = (1 - \phi) \frac{M}{2} \sum_{\xi=x,y,z} \delta W_\xi(t) \hat{r}_\xi^2 \quad (57)$$

with $\phi = 0$ for the bosons and $\phi = 1$ for the fermions,

$$\delta W_\xi(t) = \frac{\Omega_{rf}^2}{4} [\delta a_\xi - 2\delta q_\xi \cos(\Omega_{rf}t) - 2\delta q'_\xi g_\xi(t)], \quad (58)$$

and

$$\begin{aligned} g_\xi(t) &= \sum_{s,s' \notin S_i} F_{s,s'}^\xi \cos[(s-s')\Omega_{rf}t] [\mathcal{J}'_+(q_{s,\xi}) - \mathcal{J}'_-(q_{s,\xi})], \\ \delta a_\xi &= -Q\mathcal{J}'_-(0) + Q \sum_s \{F_{s,s}^\xi [\mathcal{J}'_-(q_{s,\xi}) - \mathcal{J}'_+(q_{s,\xi})]\}, \\ \delta q_\xi &= \frac{Q}{2} \sum_{|s-s'|=1} \{F_{s,s'}^\xi [\mathcal{J}'_+(q_{s,\xi}) - \mathcal{J}'_-(q_{s,\xi})]\}, \end{aligned} \quad (59)$$

where $\mathcal{J}'_\pm(q_{s,\xi})$ are defined in Eqs. (D32) and (D33), $\delta q'_\xi = Q/2$, and

$$\begin{aligned} S_i &= \{(s, s') : |s-s'| = 0 \text{ or } 1\}, \\ F_{s,s'}^\xi &= C_s^\xi C_{s'}^\xi \left(\frac{\beta_\xi}{2} + s' \right) \frac{\Omega_{rf}}{2\nu_\xi}, \quad S_{s,s'}^\xi = i \frac{C_s^\xi C_{s'}^\xi}{M\nu_\xi^2}, \\ Q &= \frac{32}{3} \frac{m}{M} \frac{\hbar^2 n_0}{\mu^2 \Omega_{rf}^2}. \end{aligned} \quad (60)$$

We see that the coupling to the quantum gas renormalizes the geometric Paul trap parameters as $a_\xi \mapsto a_\xi + \delta a_\xi$ and $q_\xi \mapsto q_\xi + \delta q_\xi$ [see also Eq. (C14)] and it yields additional time-dependent driving terms [i.e., $g_\xi(t)$]. Moreover, we introduced the functions $\Phi_\xi(t) = \Phi_\xi^\delta(t) + (1 - \phi)\Phi_\xi^P(t)$, $\Lambda_\xi(t) = \Lambda_\xi^\delta(t) + (1 - \phi)\Lambda_\xi^P(t)$, where

$$\begin{aligned} \Phi_\xi^\delta(t) &= \sum_{s,s'} F_{s,s'}^\xi \left\{ |q_{s,\xi}|^3 f(q_{s,\xi})^2 (1 - \phi) \left[\cos[(s-s')\Omega_{rf}t] (1 + 2n_{q_{s,\xi}}) + i \sin[(s-s')\Omega_{rf}t] \operatorname{sgn}\left(\frac{\beta_\xi}{2} + s\right) \right] \right. \\ &\quad \left. + \eta_{s,\xi}^- e^{-i(s-s')\Omega_{rf}t} + \eta_{s,\xi}^+ e^{i(s-s')\Omega_{rf}t} \right\}, \end{aligned} \quad (61)$$

$$\begin{aligned} \Lambda_\xi^\delta(t) &= \sum_{s,s'} S_{s,s'}^\xi \left\{ |q_{s,\xi}|^3 f(q_{s,\xi})^2 (1 - \phi) \left[i \sin[(s-s')\Omega_{rf}t] (1 + 2n_{q_{s,\xi}}) + \cos[(s-s')\Omega_{rf}t] \operatorname{sgn}\left(\frac{\beta_\xi}{2} + s\right) \right] \right. \\ &\quad \left. - \eta_{s,\xi}^+ e^{-i(s-s')\Omega_{rf}t} + \eta_{s,\xi}^- e^{i(s-s')\Omega_{rf}t} \right\} \end{aligned} \quad (62)$$

with

$$\eta_{s,\xi}^\pm = \frac{m}{16\pi^2 \hbar^2 \beta_T n_0} (\mathcal{F}_{s,\xi}^{(1),\pm} + (-1)^\phi \mathcal{F}_{s,\xi}^{(2)}). \quad (63)$$

Here, $\mathcal{F}_{s,\xi}^{(1),\pm}$ and $\mathcal{F}_{s,\xi}^{(2)}$ are defined in Eqs. (D21) and (D28), respectively, and

$$\begin{aligned} \Phi_\xi^P(t) &= \frac{2}{\pi} \sum_{s,s'} F_{s,s'}^\xi \sin[(s-s')\Omega_{rf}t] \{ \mathcal{J}'_+(q_{s,\xi}) + \mathcal{J}'_-(q_{s,\xi}) + 2[\mathcal{J}_+^{n_q}(q_{s,\xi}) + \mathcal{J}_-^{n_q}(q_{s,\xi})] \} \{ 2\Theta[\operatorname{sgn}(\beta_\xi/2 + s)] - 1 \}, \\ \Lambda_\xi^P(t) &= i \frac{2}{\pi} \sum_{s,s'} S_{s,s'}^\xi \{ (1 - 2\Theta[\operatorname{sgn}(\beta_\xi/2 + s)]) \{ \mathcal{J}'_+(q_{s,\xi}) + \mathcal{J}'_-(q_{s,\xi}) + 2[\mathcal{J}_+^{n_q}(q_{s,\xi}) + \mathcal{J}_-^{n_q}(q_{s,\xi})] \} \cos[(s-s')\Omega_{rf}t] \\ &\quad - i \sin[(s-s')\Omega_{rf}t] [\mathcal{J}'_-(q_{s,\xi}) - \mathcal{J}'_+(q_{s,\xi})] \}. \end{aligned} \quad (64)$$

The labels δ and P indicate the origin of the contribution, namely, with δ from the Dirac's delta in Eq. (51), whereas

with P from the Cauchy principal value, i.e., the Lamb shift. On the other hand, the terms involving the functions $\mathcal{F}_{s,\xi}^{(1,2)}$

stem from the extended Fröhlich model. Besides, the integrals $\mathcal{J}_{\pm}^{n_s}(q_{s,\xi})$ are defined in Eq. (D34) and they stem from the first term in the second line of Eq. (47), i.e., the one involving the cosine function. Interestingly, this term does not contribute to the renormalization of the Paul trap parameters (59), as the sum of each single exponential function, when the cosine is written as a linear combination of exponentials, vanishes for the part that concerns the unitary dynamics. Furthermore, because of the Lamb-Dicke approximation we made, we note that the three directions are decoupled. Thus, Eq. (56) can be split into three components, each representing a direction of the ion motion. In other words, we have a master equation per each direction.

A few remarks, however, are in order. First, we note that even the contribution stemming from the CPV yields incoherent terms, as indicated by the functions $\Phi_{\xi}^P(t)$ and $\Lambda_{\xi}^P(t)$. Second, the contribution stemming from the Dirac's delta yields coherent (i.e., unitary) dynamics as well since the functions $\Phi_{\xi}(t)$ and $\Lambda_{\xi}(t)$ are complex. This is because we did not perform the rotating-wave approximation (RWA), that is, we did not neglect the nonsecular terms with $\omega \neq \Omega_{rf}(\beta_{\xi}/2 + s)$, which is typically applied in quantum optics. Given the fact that the most relevant Paul trap coefficients C_s^{ξ} for a linear geometry are those with $s = 0, \pm 1$, the contributions in $\Phi_{\xi}^P(t)$ and $\Lambda_{\xi}^P(t)$ with $\sin[(s - s')\Omega_{rf}t]$ are in general small, and therefore one could in principle apply the RWA also in this context. Nonetheless, we find that the term in $\Lambda_{\xi}^P(t)$ involving $\cos[(s - s')\Omega_{rf}t]$ has a non-negligible contribution. This means that an application of the RWA would underestimate the overall dissipative dynamics. A similar reasoning applies for the coherent dynamics stemming from the imaginary contributions of the $\Phi_{\xi}^{\delta}(t)$ and $\Lambda_{\xi}^{\delta}(t)$ functions. This is also the reason why we cannot transform Eq. (56) in Lindblad form (see also Appendix F), as an essential requisite is the RWA [59]. We note that, up until now, these effects have been not taken into account in investigations in the context of impurity physics for settings similar to ours [33,47,48,62].

V. ION ENERGY AND FIRST-ORDER MOMENTS

The energy of the ion at time t is given by the expectation value of the ion Hamiltonian (C15):

$$\langle \hat{H}_I^{\text{trap}}(t) \rangle = \langle \hat{H}_I^{\text{kin}}(t) \rangle + \frac{M}{2} W_{\xi}'(t) \langle \hat{r}_{\xi}^2 \rangle, \quad (65)$$

where $W_{\xi}'(t) = W_{\xi}(t) + \delta W_{\xi}(t)$, with $W_{\xi}(t)$ given by

$$W_{\xi}(t) = \frac{\Omega_{rf}^2}{4} [a_{\xi} - 2q_{\xi} \cos(\Omega_{rf}t)], \quad (66)$$

$\delta W_{\xi}(t)$ defined in Eq. (58) and

$$\langle \hat{H}_I^{\text{kin}}(t) \rangle = \sum_{\xi=x,y,z} \frac{\langle \hat{p}_{\xi}^2 \rangle}{2M}. \quad (67)$$

In order to calculate it, we have to determine the expectation values $\langle \hat{p}_{\xi}^2(t) \rangle = \text{Tr}\{\hat{\rho}_{\xi}^2 \hat{p}_{\xi}(t)\}$ and $\langle \hat{r}_{\xi}^2(t) \rangle = \text{Tr}\{\hat{\rho}_{\xi}^2 \hat{r}_{\xi}(t)\} \forall \xi = x, y, z$ with $\hat{\rho}_{\xi}(t)$ being the ion density matrix corresponding to the ξ th direction, whose equation of motion is obtained by considering only the pertinent direction in the sum

appearing in Eq. (56). Instead of solving the full master equation, however, it is computationally less expensive to solve the corresponding differential equations for the expectation values of the square of the position and momentum, which are coupled to the covariance $\langle \hat{c}_{\xi} \rangle = \langle (\hat{r}_{\xi} \hat{p}_{\xi} + \hat{p}_{\xi} \hat{r}_{\xi})(t) \rangle$. Therefore, by using the definition of the expectation value of an observable $\langle \hat{O} \rangle = \text{Tr}\{\hat{O} \hat{\rho}(t)\}$, and the master equation (56), one arrives at the set of coupled differential equations:

$$\begin{aligned} \frac{d}{dt} \langle \hat{r}_{\xi}^2 \rangle &= \frac{\langle \hat{c}_{\xi} \rangle}{M}, \\ \frac{d}{dt} \langle \hat{p}_{\xi}^2 \rangle &= \{2\hbar\Gamma \text{Im}[\Phi_{\xi}(t)] - MW_{\xi}'(t)\} \langle \hat{c}_{\xi} \rangle \\ &\quad - 4\hbar\Gamma \text{Im}[\Lambda_{\xi}(t)] \langle \hat{p}_{\xi}^2 \rangle + 2\hbar^2\Gamma \text{Re}[\Phi_{\xi}(t)], \\ \frac{d}{dt} \langle \hat{c}_{\xi} \rangle &= 2\{2\hbar\Gamma \text{Im}[\Phi_{\xi}(t)] - MW_{\xi}'(t)\} \langle \hat{r}_{\xi}^2 \rangle + 2 \frac{\langle \hat{p}_{\xi}^2 \rangle}{M} \\ &\quad - 2\hbar\Gamma \text{Im}[\Lambda_{\xi}(t)] \langle \hat{c}_{\xi} \rangle + 2\hbar^2\Gamma \text{Re}[\Lambda_{\xi}(t)]. \end{aligned} \quad (68)$$

In the limit for which the Lamb shift and the extended Fröhlich model are not considered, the equations of motion (58) of Ref. [33] are retrieved. We note that the set of equations (68) holds for both the bosonic and fermionic baths, but with different Φ_{ξ} and Λ_{ξ} functions.

The radio-frequency fields set the smallest timescale in the open quantum system. It is therefore useful to evaluate the time-averaged energy over a rf period, namely,

$$\langle \langle \hat{H}_I^{\text{kin}}(t) \rangle \rangle_{T_{\text{rf}}} = \frac{1}{T_{\text{rf}}} \int_t^{t+T_{\text{rf}}} dt' \langle \hat{H}_I^{\text{kin}}(t') \rangle, \quad (69)$$

where $T_{\text{rf}} = 2\pi/\Omega_{\text{rf}}$. Here, the notation $\langle \langle \dots \rangle \rangle_{T_{\text{rf}}}$ denotes the time average over T_{rf} . In this way we average out the fast oscillations due to the rf field and the final ion energy at thermal equilibrium with the atomic gas can be assessed.

Finally, we provide equations of motion of the first-order moments of the ion position and momentum operators. Exactly with the same procedure that we outlined previously for Eq. (68), the coupled differential equations for the first-order moments read as

$$\begin{aligned} \frac{d}{dt} \langle \hat{r}_{\xi} \rangle &= \frac{\langle \hat{p}_{\xi} \rangle}{M}, \\ \frac{d}{dt} \langle \hat{p}_{\xi} \rangle &= \{2\hbar\Gamma \text{Im}[\Phi_{\xi}(t)] - MW_{\xi}'(t)\} \langle \hat{r}_{\xi} \rangle \\ &\quad - 2\hbar\Gamma \text{Im}[\Lambda_{\xi}(t)] \langle \hat{p}_{\xi} \rangle. \end{aligned} \quad (70)$$

The first equation of motion of $\langle \hat{r}_{\xi} \rangle$ is simply the definition of the ion momentum in the ξ direction, while the second one provides the average force acting on the ion. The latter is, on the one side, due to the ion trap, i.e., the term proportional to $W_{\xi}'(t)$, and, on the other side, to the atom-ion interaction, namely, the term proportional to $\text{Im}[\Phi_{\xi}(t)]$. Moreover, the term proportional to $\text{Im}[\Lambda_{\xi}(t)]$ relies on the ion momentum, that is, it corresponds to a velocity-dependent force, which results in a damped ion motion because of the presence of the gas, unless the initial conditions for $\langle \hat{r}_{\xi} \rangle$ and $\langle \hat{p}_{\xi} \rangle$ vanish. It is interesting to note that the form of the equations of motion (70) resembles that of $\langle \hat{r}_{\xi}^2 \rangle$ and $\langle \hat{p}_{\xi}^2 \rangle$, where $\langle \hat{c}_{\xi} \rangle$ is replaced by $\langle \hat{p}_{\xi} \rangle$ or $\langle \hat{r}_{\xi} \rangle$ and $\langle \hat{p}_{\xi}^2 \rangle$ by $\langle \hat{p}_{\xi} \rangle$, but Eq. (70) does not have source terms.

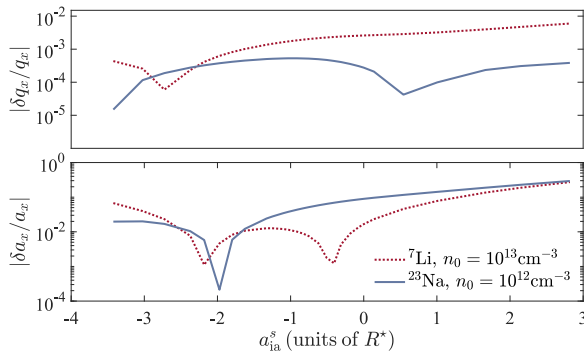


FIG. 3. Corrections to the Paul trap parameters along the x direction for sodium and lithium atoms for two densities as a function of the atom-ion scattering length. Top panel: relative correction to the q parameter. Bottom panel: relative correction to the a parameter.

VI. NUMERICAL RESULTS

Before we present and discuss our numerical findings, we note that hereafter they are based on the parameters b and c computed as explained in Appendix A. Moreover, the bare Paul trap parameters are chosen as $a_{x,y} = -0.001$, $a_z = 0.002$, $q_x = -q_y = 0.2$, $q_z = 0$, and $\Omega_{\text{rf}} = 2\pi \times 2$ MHz. Such parameters correspond to a linear trap geometry, whose frequencies are $\nu_x \simeq 2\pi \times 169$ kHz, $\nu_y \simeq 2\pi \times 112$ kHz, $\nu_z \simeq 2\pi \times 45$ kHz (a ^{174}Yb ion is always assumed). Thus, we have $\beta_{x,y} \simeq 0.1389$ and $\beta_z \simeq 0.0447$. Details on the choice of the initial density matrix are provided in Appendix C 2.

A. Renormalized Paul trap parameters

To begin with, we analyze the impact of the coupling to the quantum gas on the ion dynamics by considering the renormalized trap a and q parameters. The absolute amount of change of those parameters from their bare values, i.e., without the gas, provides us a rule of thumb to assess how strong can be the coupling, that is, how large can be the atomic density such that the master equation can yield a faithful description of the ion dynamics. The modification of those parameters relies on the particular atom-ion species via the mass ratio as well as on the condensate density.

In Fig. 3 we show the corrections to the Paul trap parameters δa_ξ and δq_ξ relatively to their bare values as a function of the atom-ion scattering length for $n_0 = 10^{12}/\text{cm}^3$ and $n_0 = 10^{13}/\text{cm}^3$ for sodium and lithium, respectively, along the transverse direction $\xi \equiv x$. Note that for lower densities the values of δa_ξ and δq_ξ are reduced by $n_0/(10^{12}/\text{cm}^3)$ for sodium and by $n_0/(10^{13}/\text{cm}^3)$ for lithium due to their definition. As it can be seen, the q parameter, namely, that of the driving rf field, is very weakly affected by the coupling to the gas (top panel). The a parameter, instead, assumes larger values, especially for positive scattering lengths (bottom panel). Furthermore, we see that the heavier the atom, the larger is the impact on the trap (for equal densities), as expected (in the figure the result for lithium has to be divided by 10 to be compared with that of sodium). These results show that, while for lithium densities up to $n_0 = 10^{13}/\text{cm}^3$ can be considered

(ideally the ratio should be smaller than unity), it is better not to exceed $n_0 = 10^{12}/\text{cm}^3$ for sodium atoms because of the strong modification to the a parameter.

B. Ion in a lithium gas

In Fig. 4 we show the averaged ion kinetic energy expressed as a temperature $\mathcal{T}_{\text{kin}} = 2\langle\langle\hat{H}_I^{\text{kin}}(T)\rangle\rangle_{T_{\text{rf}}}/3k_B$ at the final time T , namely, when the ion has thermalized with the quantum gas, where the averaged energy is given by Eq. (69). The definition of the kinetic temperature \mathcal{T}_{kin} includes the secular motion and the micromotion of the ion and the factor $\frac{2}{3}$ is due to the equipartition theorem [42]. We note that the value of the thermalization time T relies on various system parameters, especially on the atomic density. For a fixed scattering length, decreasing the density by an order of magnitude implies an increase of the thermalization time by roughly the same amount. As a consequence and for $\mathcal{T} < \mathcal{T}_c^0$, T strongly depends on the gas temperature since the latter determines the density of the condensed fraction, i.e., n_0 . A first estimation of the thermalization time for each plot is found by looking at \mathcal{T}_{kin} as a function of time for a single value of the temperature (see, e.g., the bottom panel of Fig. 7). Then, the values of \mathcal{T}_{kin} at all temperatures are computed at the estimated time and at several larger times up to the one at which the difference between the curves becomes negligible.

General remarks. Let us first focus on the bosonic case below \mathcal{T}_c^0 . As we can see from the insets of Fig. 4, the behavior of the ion kinetic energy is the result of the interplay among the different contributions. The empty blue circles correspond to the Fröhlich model, i.e., they show the contribution of the condensed part of the gas only. The final temperature of the ion is basically independent of the gas temperature in this approximation. This result is consistent with the fact that the density barely affects the final energy of the ion. Indeed, in the Fröhlich model the dependence of the equations on the gas temperature is almost entirely carried by the condensate density n_0 , as the temperature-dependent factor $n_{q_s,\xi}$ in the definitions of $\Phi(t)$ and $\Lambda(t)$ is always much lower than unity. This behavior has to be traced back to the nature of the condensate, in which all the particles occupy the same single-particle state. For this reason, the cooling effect of the condensate does not change when its temperature changes, as the latter only affects the fraction of condensed particles. A similar reasoning can be applied to the Lamb shift, whose contribution can be observed in the purple empty squares of Fig. 4. The additional cooling effect is stronger at temperatures much lower than \mathcal{T}_c^0 . This phenomenon is related to the condensate density n_0 increasing when the temperature is decreased, which implies a stronger coupling to the gas, and it is in agreement with what discussed in Sec. VI A about the dependence of the δa_ξ and δq_ξ parameters on n_0 . On the other hand, the contribution of the extended Fröhlich model shows the opposite trend. As it can be seen from the full blue circles of the aforementioned insets, when \mathcal{T} approaches the critical temperature the contribution of the interaction with the normal part of the gas bends the ion temperature downward. The extended Fröhlich model, which is the only one contributing at $\mathcal{T} > \mathcal{T}_c^0$ in the bosonic case and at every gas temperature \mathcal{T} for the fermions, is responsible for a minimum

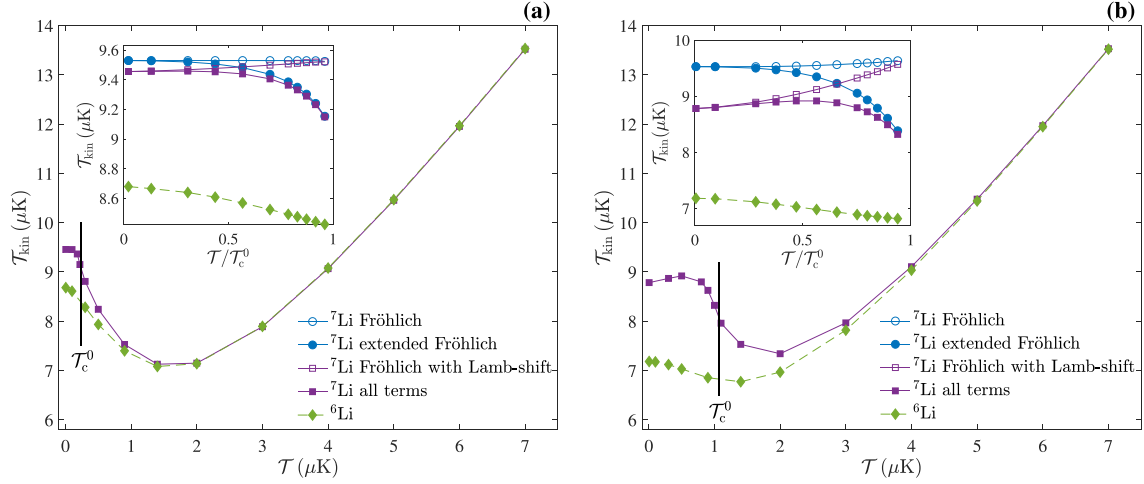


FIG. 4. Ion temperature obtained from the averaged energy (69) for $b \simeq 0.0780 R^*$, $c \simeq 0.2239 R^*$, which correspond to $a_{\text{ia}}^s \simeq R^*$. The square and circle symbols refer to the bosons, while the diamonds to the fermions. The black vertical line indicates the position of the critical temperature of condensation T_c^0 , while the Fermi temperature is not indicated. (a) $n_t = 10^{12} \text{ cm}^{-3}$, $T = 50 \text{ ms}$, $T_F = 0.61 \text{ } \mu\text{K}$. (b) $n_t = 10^{13} \text{ cm}^{-3}$, $T = 6 \text{ ms}$, $T_F = 2.48 \text{ } \mu\text{K}$.

in the final ion temperature, i.e., kinetic energy. In order to understand its nature, we studied the temperature dependence of some characteristic quantities involved in the equations such as $\eta_{s,\xi}^\pm$ [see Eq. (63)]. For simplicity, let us now focus on the fermionic case, where no other contributions have to be considered. In this case, all the temperature dependence relies on $\eta_{s,\xi}^\pm$, which monotonically increases with T for all s and $\xi = x, y, z$ (not shown). Moreover, by looking at the kinetic energy along the three directions at $t = T$ (also not shown), i.e., when thermalization is achieved, we found that the temperature dependence along $\xi = x$ and y presents the same minimum of T_{kin} while along $\xi = z$ it is monotonic. We can therefore attribute the emergence of the minimum to the presence of the trap and, in particular, to the interference between terms with different s due to the radio-frequency-induced micromotion. Finally, in Fig. 5 we observe that when the regularized polarization potential is substituted with the pseudopotential, the depth of the minimum is strongly decreased for $n_t = 10^{12} \text{ cm}^{-3}$ (orange data), and even barely visible at $n_t = 10^{13} \text{ cm}^{-3}$ (light blue data). We thus conclude that the long-range character of the atom-ion potential renders the occurrence of the minimum in the kinetic energy more pronounced.

Density dependence. While the overall behavior is not substantially affected by the value of the density, there are some differences that are worthy of remark. First, for large densities, the ion temperature in the case of ${}^6\text{Li}$ (green diamonds in Fig. 4) is slightly lower at very low T . This difference, though, is not substantial and is definitely negligible compared to the scale of s -wave energy threshold. Another difference concerns the contribution of the Lamb shift (purple squares), which is enhanced at large densities, thus confirming what we discussed in Sec. VIA and in the previous paragraph. Both of these differences, though, are only visible at very low temperatures. At high temperatures, neither the density nor the statistics of the gas influence the result in a sensible way, apart

from the time required for thermalization that, as anticipated, increases linearly with the decrease of the density.

Damping rates. We investigated the temperature dependence of the damping rates γ_x of $\langle \hat{r}_x \rangle$. In Fig. 6 they are shown for ${}^6\text{Li}$ and ${}^7\text{Li}$ with a density $n_t = 10^{13} \text{ cm}^{-3}$. Before commenting on the result, let us briefly explain the procedure we followed in order to calculate the values of γ_x . We started from a nonzero initial condition for $\langle \hat{r}_x \rangle$. Its value is not particularly important because the damping rates do not rely on it anyway. By solving the system in Eq. (70), we obtain $\langle \hat{r}_x(t) \rangle$, whose behavior is a damped oscillation with zero average value. We

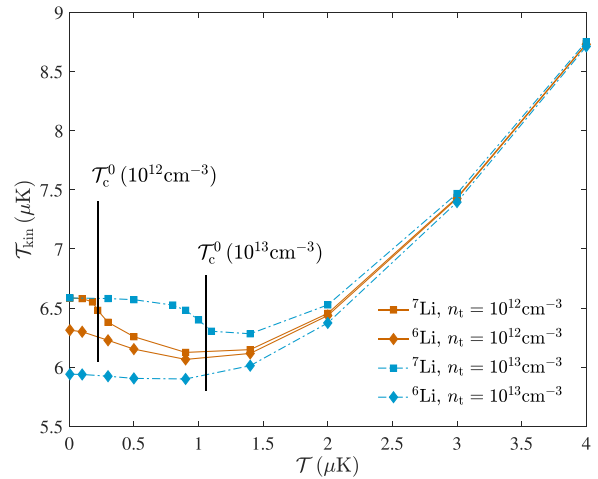


FIG. 5. Ion temperature obtained from the averaged energy (69) with the pseudopotential and $a_{\text{ia}}^s = R^*$. The dotted-dashed light blue lines correspond to $n_t = 10^{13} \text{ cm}^{-3}$, while the solid orange ones to $n_t = 10^{12} \text{ cm}^{-3}$. The simulation time is $T = 10$ and 100 ms , respectively.

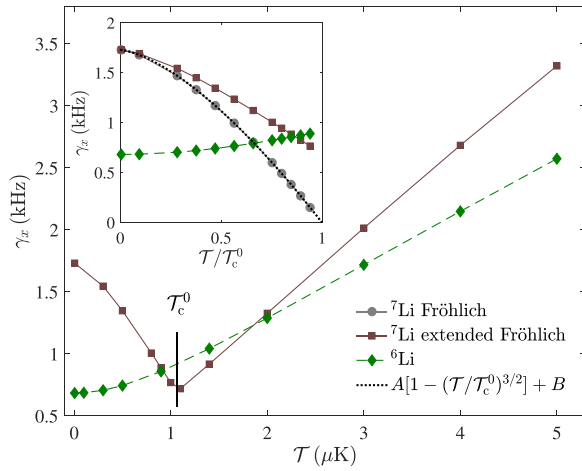


FIG. 6. Damping rates of $\langle \hat{r}_\xi \rangle$ as a function of the gas temperature with a total density $n_t = 10^{13} \text{ cm}^{-3}$. The dotted line in the inset represents a fit with the condensate density dependence on the ratio $\mathcal{T}/\mathcal{T}_c^0$.

calculated the curve enveloping the oscillation and we fitted it with the exponential function $\alpha_x e^{-\gamma_x t}$ (the same procedure was applied to all other directions with similar findings). Interestingly, the temperature dependence of the coefficients γ_ξ does not reproduce that of \mathcal{T}_{kin} . In the case of ${}^6\text{Li}$ (fermion), the curve is monotonic and so it is for ${}^7\text{Li}$ (boson) above \mathcal{T}_c^0 . In the bosonic case, when the gas temperature is reduced below \mathcal{T}_c^0 , the damping rates increase with the density of the condensate. The gray circles in the inset of Fig. 6 show that in the Fröhlich model there is a one-to-one correspondence between the damping rates and the condensate density. The extended Fröhlich model (brown squares) enhances the damping rates when the contribution of the normal part of the gas becomes stronger. This relation between the condensate density and the values of γ_ξ strongly underlines the difference between bosonic and fermionic baths at low temperatures. Moreover, it could be exploited in experiments, where the condensate fraction may be extracted from the measurement of the damping rates.

Scattering length dependence. Figure 7 shows the dependence of the ion energy on the atom-ion scattering length at $\mathcal{T} = 100 \text{ nK}$ in the case of ${}^6\text{Li}$. As it can be seen in the top panel, for some values of the scattering length convergence is already achieved at $T = 6 \text{ ms}$. When the value of a_{ia}^s approaches roughly $-0.5R^*$, the thermalization time strongly increases, as shown in the bottom panel (red dotted line). Such (numerical) observation suggests an instability that could be related to the occurrence of a resonance, as experimentally observed recently [15]. Indeed, although the master equation does not entail information about two-particle bound states, the behavior of the final energy could still give some hint about the microscopic dynamics, the latter emerging through the parameters of the atom-ion potential. As a reference, the gray dashed line shows the values of the converged ion temperature in the case of the pseudopotential approximation, where the only parameter involved is the scattering length.

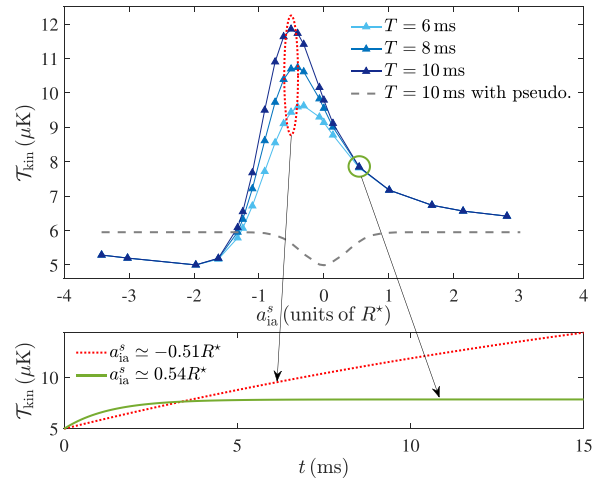


FIG. 7. Top panel: ion temperature vs the atom-ion scattering length for ${}^6\text{Li}$ for $n_t = 10^{13} \text{ cm}^{-3}$ and a gas temperature $\mathcal{T} = 0.1 \mu\text{K}$. Bottom panel: ion temperature vs time for two different scattering lengths.

The curve is symmetric because $f(k) \propto -a_{\text{ia}}$ and the latter enters only via $|f(k)|^2$. Hence, the long-ranged character of the polarization potential together with the fact that there is no separation of length scales in the impurity system crucially affects the ion dynamical properties.

Let us conclude by mentioning that recently the polaronic properties of a free ion in a condensate have been investigated [2]. There, quite different polaronic states have been identified on the basis that the atom-ion polarization potential supports either one bound state or none. Without a two-body bound state, a polaron resembling that of a neutral impurity, albeit with a larger effective mass, has been found. Here, we have also investigated the scenario for which the potential does not support any bound state. In this case, however, we found for a broad range of negative atom-ion scattering lengths that the ion does not thermalize, that is, its dynamics is very unstable in the Paul trap. Thereby, even though in the framework of the master equation we cannot make quantitative predictions on the dynamical formation of many-body bound states such as its size, the presence of two-body bound states and the inclusion of the extended Fröhlich model in the master-equation description is of paramount importance for stabilizing the ion dynamics in the rf trap.

C. Ion in a sodium gas

We have also investigated the ion dynamics in a heavier bosonic ensemble. In Fig. 8 we illustrate the result of this analysis. With the linear Paul trap that we have assumed so far, the ion energy as a function of the gas temperature is shown by the purple squares. As it can be seen, the ion energy is always above the s -wave threshold and therefore no ultracold atom-ion collisions can be expected. Nonetheless, by reducing the rf by an order of magnitude, that is, $\Omega_{\text{rf}} = 2\pi \times 200 \text{ kHz}$, and by reducing the q parameter by one-half, i.e., $q_x = -q_y = 0.1$, which result in the trap frequencies $\nu_x \simeq 2\pi \times 7 \text{ kHz}$,

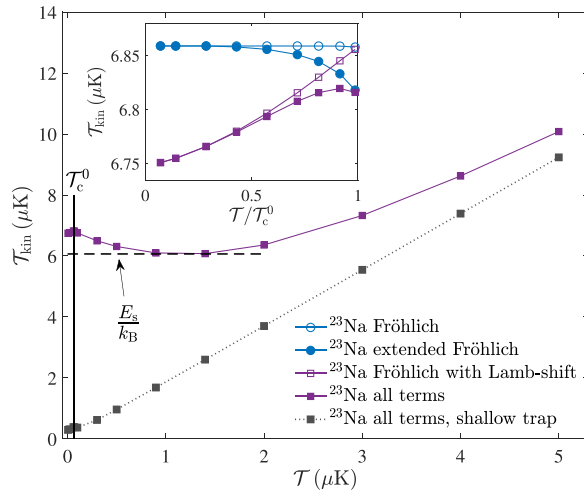


FIG. 8. Ion temperature obtained from the averaged energy (69) for $b \simeq 0.0780 R^*$, $c \simeq 0.2239 R^*$, which correspond to $a_{\text{ia}}^s \simeq R^*$, and a total density $n_i = 10^{12} \text{ cm}^{-3}$. The gray squares with dotted line correspond to the shallow trap (see text for parameters). The black vertical lines indicate the position of the critical temperature of condensation \mathcal{T}_c^0 , while the dashed horizontal one to the s -wave threshold.

$\nu_y \simeq 2\pi \times 6 \text{ kHz}$, $\nu_z \simeq 2\pi \times 4 \text{ kHz}$ and $\beta_{x,y} \simeq 0.0634$, $\beta_z \simeq 0.0447$, we find that at low gas temperatures (i.e., $\lesssim 400 \text{ nK}$) the s -wave limit can be beaten, as shown by the gray squares with dotted line in Fig. 8. The resulting trap frequencies indicate an almost isotropic ion trap. It has to be noticed, however, that with such a shallow Paul trap it will be experimentally challenging to suppress excess micromotion and to keep under control the ion heating due to the background electric noise.

VII. SUMMARY OF THE MAIN RESULTS AND CONCLUSIONS

We have investigated the quantum nonequilibrium dynamics of an ion in an rf trap superimposed to a quantum gas of either bosons or fermions. To this end, in Sec. IV, we developed a quantum master equation by including the contribution of the Lamb shift and the extended Fröhlich model, that is, the noncondensate fraction. The final master equation can be found in Eq. (56), where the definitions of the corresponding functions discern the case of the fermionic and bosonic baths. The equations of motion for the second and first moments are calculated in Sec. V directly from the master equation and are given in Eqs. (68) and (70), respectively. These systems of equations were numerically solved resulting in the findings exposed in Sec. VI. We also note that the master equation (41) is also an important result of our study, as it can be the starting point for other investigations, such as a free ion in a Bose-Einstein condensate. We found significant differences in the ion dynamics between the bosonic and fermionic baths at low temperatures ($\mathcal{T} \lesssim \mathcal{T}_c^0$), where the quantum nature of the gas emerges. As shown in Fig. 4, in this regime, a fermionic environment seems to ensure better cooling of the ion compared to the bosonic one, while at higher temperatures

the difference gets less and less pronounced and it vanishes when $\mathcal{T} \gg \mathcal{T}_c^0$. Similarly, the nature of the gas affects the damping of the ion below \mathcal{T}_c^0 (see Fig. 6): the temperature dependence of the damping rates in the bosonic case is strongly characterized by the presence of the condensate and reflects the arising of its density. Moreover, we observed that the thermalization time strongly increases for values of the scattering length around $-0.5R^*$ (see Fig. 7) and thermalization may not even be achievable if the potential does not support any bound state. The former might be related to the occurrence of a resonance as recently found experimentally [15] and it will be a subject of future investigations. Furthermore, as illustrated in Fig. 8, we found that a proper choice of the ion trap parameters enables to cool the ion motion in a sodium gas to the quantum regime, which affords prospects to quantum simulate impurity physics with large atom-ion mass ratios. Finally, with the developed theoretical methods it will be interesting to investigate how the gas quantum statistics affects the Fock-state distribution of the ion motion, the coherence of ionic motional superpositions, and to develop interferometric protocols for measuring the gas temperature by reading out the thermal phonon distribution.

ACKNOWLEDGMENTS

This work is supported by the project “NE 1711/3-1” of the Deutsche Forschungsgemeinschaft. We acknowledge H. Fürst, Z. Idziaszek, and K. Jachymski for discussions. R.G. was supported by the Dutch Research Council (Vrije Program No. 680.92.18.05).

APPENDIX A: PARAMETERS OF THE REGULARIZED POTENTIAL

To determine the parameters b and c of the regularized potential (4), we follow the approach of Ref. [33]. Here, however, we provide details that were not discussed in that reference.

Since we have two free parameters, we need two physical conditions to determine them. To this aim, we impose the following:

(a) The scattering length amplitude in first-order Born approximation (6) is exactly equal to minus the atom-ion scattering length at zero energy.

(b) The potential (4) supports one bound state only.

The condition (b) is motivated by that fact that the energy separation between bound states of the atom-ion polarization potential (1) is rather large (order of hundreds of E^*), thus rendering very unlikely the population of deeper bound states at typical atomic gas densities.

In the zero-energy limit the three-dimensional s -wave ion-atom scattering length is indeed defined as

$$a_{\text{ia}}^s = -\lim_{q \rightarrow 0} f_s(q) \quad (\text{A1})$$

with $f_s(q)$ being the full s -wave scattering amplitude at energy $\hbar^2 q^2 / (2\mu)$, where $q = |\mathbf{k} - \mathbf{k}'|$ is the magnitude of the momentum transfer in the relative frame of reference. Hence, the first aforementioned condition (a) reads as

$$a_{\text{ia}}^s = -f(0). \quad (\text{A2})$$

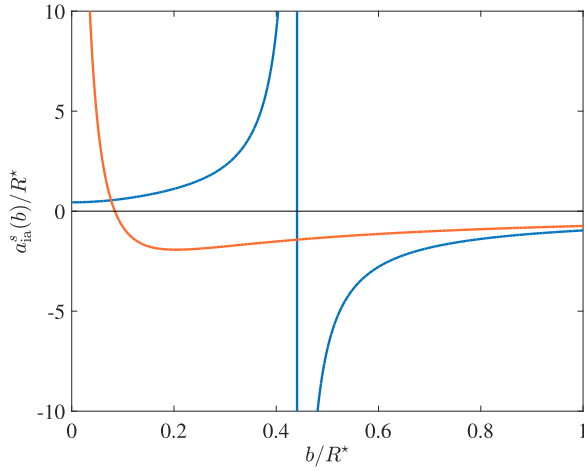


FIG. 9. . Atom-ion scattering length (blue line) computed via Eq. (A6) and minus the scattering amplitude (orange line) at zero energy (A3) as a function of the b parameter of the regularized atom-ion interaction (4). Here, we have chosen $c = 0.2039R^*$. The two lines intersect at $b \simeq 0.0770R^*$, which yields a scattering length $a_{\text{ia}}^s \simeq 0.5385R^*$.

In the zero-energy limit $q \rightarrow 0$, and therefore, by expanding the exponential functions in the last line of Eq. (6) to first order, we obtain

$$f(0) = \pi(R^*)^2 \frac{(b^2 + 2bc - c^2)}{4b(b+c)^2}. \quad (\text{A3})$$

Note that the scattering amplitude has the units of a length, which is consistent with the definition (A1).

The fulfillment of the second condition (b) is attained by determining the s -wave scattering length as a function of either b or c by solving the scattering problem at zero energy. To this aim, we solve numerically the radial time-independent Schrödinger equation

$$\left[-\frac{\hbar^2}{2\mu} \frac{d^2}{dr^2} + V_{\text{ai}}^r(r) \right] \psi(r) = 0, \quad r \in [0, +\infty) \quad (\text{A4})$$

which in the E^* and R^* units reduces to

$$\left[\frac{d^2}{dr^2} + \frac{r^2 - c^2}{r^2 + c^2} \frac{1}{(b^2 + r^2)^2} \right] \psi(r) = 0. \quad (\text{A5})$$

This differential equation is solved with boundary conditions $\psi(0) = 0$ and $\psi'(0) = \epsilon$, where ϵ is a small number (e.g., 0.1). We note, however, that the result does not rely on the particular numerical value of ϵ , as we have verified numerically. Thus, we fix the value of the parameter c (in units of R^*) and we solve iteratively Eq. (A5) for different values of the parameter b by evaluating the corresponding scattering length, which becomes a function of b . We do the same for the scattering amplitude (A3) and thus search for the value of b where $a_{\text{ia}}^s(b)$ and $-f(b)$ do cross, particularly where the first zero-energy resonance occurs, which indicates that we have one bound state only (see Fig. 9).

Let us now briefly explain some details about the numerical calculation of the scattering length. First, we note that the solution to Eq. (A5) behaves like $r - a_{\text{ia}}^s(b)$ at large distances, where the atom-ion interaction vanishes. Hence, we have

$$a_{\text{ia}}^s(b) = \lim_{r \rightarrow +\infty} \left[r - \frac{\psi(r)}{\psi'(r)} \right]. \quad (\text{A6})$$

Numerically, we have noticed that a large grid size has to be chosen (a few thousands of R^*) such that the term on the right-hand side of the limit (A6) converges to a constant value, i.e., it is r independent. An example of such a calculation is given in Fig. 9.

For instance, by fixing $c = 0.2239R^*$, we find $b \simeq 0.078R^*$, which yields $a_{\text{ia}}^s \simeq 1.0054R^*$. Finally, let us remark that such a strategy relies crucially on the first Born approximation. Other strategies can be adopted in order to relax the latter (see, e.g., Refs. [35,36]). We chose, however, the method outlined above for consistency since we make use of the first Born scattering amplitude in the derivation of the master equation, as a consequence of the perturbative description of the open system.

APPENDIX B: THERMAL AVERAGES

The thermal averages of the double commutator (38) that yield nonzero contributions are

$$\begin{aligned} \langle \tilde{\Gamma}_{\mathbf{q}}^\dagger(t) \tilde{\Gamma}_{\mathbf{q}'}^\dagger(t) \tilde{\Gamma}_{\mathbf{k}}^\dagger(t') \tilde{\Gamma}_{\mathbf{k}'}^\dagger(t') \rangle_{B_0} &= e^{\frac{i}{\hbar} \{ [\varepsilon(\mathbf{q}) - \varepsilon(\mathbf{q}')]t + [\varepsilon(\mathbf{k}) - \varepsilon(\mathbf{k}')]t' \}} [n_{\mathbf{q}} \delta_{\mathbf{q},\mathbf{k}} \delta_{\mathbf{q},\mathbf{k}'} + n_{\mathbf{q}} n_{\mathbf{q}'} (\delta_{\mathbf{q}',\mathbf{q}} \delta_{\mathbf{k},\mathbf{k}'} + \delta_{\mathbf{q},\mathbf{k}} \delta_{\mathbf{q},\mathbf{k}'}), \\ \langle \tilde{\Gamma}_{\mathbf{q}}^\dagger(t) \tilde{\Gamma}_{\mathbf{q}'}^\dagger(t) \tilde{\Gamma}_{\mathbf{k}}^\dagger(t') \tilde{\Gamma}_{\mathbf{k}'}^\dagger(t') \rangle_{B_0} &= e^{\frac{i}{\hbar} \{ [\varepsilon(\mathbf{q}) - \varepsilon(\mathbf{q}')]t + [\varepsilon(\mathbf{k}') - \varepsilon(\mathbf{k})]t' \}} n_{\mathbf{q}} (1 + n_{\mathbf{k}'} (\delta_{\mathbf{q}',\mathbf{q}} \delta_{\mathbf{k},\mathbf{k}'} + \delta_{\mathbf{q},\mathbf{k}'} \delta_{\mathbf{q},\mathbf{k}}), \\ \langle \tilde{\Gamma}_{\mathbf{q}}^\dagger(t) \tilde{\Gamma}_{\mathbf{q}'}^\dagger(t) \tilde{\Gamma}_{\mathbf{k}}^\dagger(t') \tilde{\Gamma}_{\mathbf{k}'}^\dagger(t') \rangle_{B_0} &= e^{\frac{i}{\hbar} \{ [\varepsilon(\mathbf{q}) + \varepsilon(\mathbf{q}')]t - [\varepsilon(\mathbf{k}') + \varepsilon(\mathbf{k})]t' \}} n_{\mathbf{q}} n_{\mathbf{q}'} (\delta_{\mathbf{q}',\mathbf{k}} \delta_{\mathbf{q},\mathbf{k}'} + \delta_{\mathbf{q},\mathbf{k}'} \delta_{\mathbf{q},\mathbf{k}}), \\ \langle \tilde{\Gamma}_{\mathbf{q}}^\dagger(t) \tilde{\Gamma}_{\mathbf{q}'}^\dagger(t) \tilde{\Gamma}_{\mathbf{k}}^\dagger(t') \tilde{\Gamma}_{\mathbf{k}'}^\dagger(t') \rangle_{B_0} &= e^{\frac{i}{\hbar} \{ [\varepsilon(\mathbf{k}) + \varepsilon(\mathbf{k}')]t' - [\varepsilon(\mathbf{q}') + \varepsilon(\mathbf{q})]t \}} (1 + n_{\mathbf{q}} + n_{\mathbf{q}'} + n_{\mathbf{k}} n_{\mathbf{k}'} (\delta_{\mathbf{q}',\mathbf{k}} \delta_{\mathbf{q},\mathbf{k}'} + \delta_{\mathbf{q},\mathbf{k}'} \delta_{\mathbf{q},\mathbf{k}}), \\ \langle \tilde{\Gamma}_{\mathbf{q}}^\dagger(t) \tilde{\Gamma}_{\mathbf{q}'}^\dagger(t) \tilde{\Gamma}_{\mathbf{k}}^\dagger(t') \tilde{\Gamma}_{\mathbf{k}'}^\dagger(t') \rangle_{B_0} &= e^{\frac{i}{\hbar} \{ [\varepsilon(\mathbf{q}') - \varepsilon(\mathbf{q})]t + [\varepsilon(\mathbf{k}) - \varepsilon(\mathbf{k}')]t' \}} [n_{\mathbf{q}} \delta_{\mathbf{q},\mathbf{k}} \delta_{\mathbf{q},\mathbf{k}'} + n_{\mathbf{k}} \delta_{\mathbf{q},\mathbf{q}'} \delta_{\mathbf{k},\mathbf{k}'} + n_{\mathbf{q}'} n_{\mathbf{k}} (\delta_{\mathbf{q}',\mathbf{q}} \delta_{\mathbf{k},\mathbf{k}'} + \delta_{\mathbf{q},\mathbf{k}'} \delta_{\mathbf{q},\mathbf{k}}), \\ \langle \tilde{\Gamma}_{\mathbf{q}}^\dagger(t) \tilde{\Gamma}_{\mathbf{q}'}^\dagger(t) \tilde{\Gamma}_{\mathbf{k}}^\dagger(t') \tilde{\Gamma}_{\mathbf{k}'}^\dagger(t') \rangle_{B_0} &= e^{\frac{i}{\hbar} \{ [\varepsilon(\mathbf{q}') - \varepsilon(\mathbf{q})]t + [\varepsilon(\mathbf{k}') - \varepsilon(\mathbf{k})]t' \}} [n_{\mathbf{k}} \delta_{\mathbf{q},\mathbf{k}'} \delta_{\mathbf{q},\mathbf{k}} + (1 + n_{\mathbf{k}} + n_{\mathbf{q}}) \delta_{\mathbf{q},\mathbf{q}'} \delta_{\mathbf{k},\mathbf{k}'} + n_{\mathbf{q}'} n_{\mathbf{k}'} (\delta_{\mathbf{q}',\mathbf{q}} \delta_{\mathbf{k},\mathbf{k}'} + \delta_{\mathbf{q},\mathbf{k}'} \delta_{\mathbf{q},\mathbf{k}})]. \end{aligned} \quad (\text{B1})$$

For these identities we used the relation (4.7) of Ref. [63].

APPENDIX C: ION MOTION IN A PAUL TRAP

Here, we provide details on the analytical solution of the ion motion in a Paul trap using the notation of [18]. The goal is to provide the relevant steps of its derivation such that the interested reader can implement them in numerics quickly and efficiently.

1. Classical solution of a charge in a Paul trap

Let us consider a particle of mass M and charge $Z|e|$ in the quadruple field

$$\Phi(x, y, z, t) = \frac{U}{2}(\alpha x^2 + \beta y^2 + \gamma z^2) + \frac{\tilde{U}}{2} \cos(\Omega_{rf}t)(\alpha' x^2 + \beta' y^2 + \gamma' z^2). \quad (C1)$$

For a linear Paul trap we have $0 < \gamma = -(\alpha + \beta)$, $\alpha' = -\beta'$, and $\gamma' = 0$ and Poisson equation, $\nabla^2 \Phi = 0$, is fulfilled. The Newton equation of motion along the x direction is given by (similarly for the other directions)

$$\ddot{x}(t) = -\frac{|e|Z}{m} \frac{\partial \Phi}{\partial x} = -\frac{|e|Z}{m} [U\alpha + \tilde{U}\alpha' \cos(\Omega_{rf}t)]x.$$

By introducing the dimensionless variable $\tau = \Omega_{rf}t/2$, the corresponding rescaled equation reads as

$$\ddot{x}(\tau) + [a_x - 2q_x \cos(2\tau)]x = 0, \quad (C2)$$

where the newly introduced parameters are defined as $a_x = 4|e|Z\alpha U/(M\Omega_{rf}^2)$ and $q_x = -2|e|Z\alpha'\tilde{U}/(M\Omega_{rf}^2)$. Note that for a linear Paul trap we have $q_y = -q_x \equiv q$ and $q_z = 0$, where $a_y = a_x = -a_z/2 \equiv a$. The above outlined equation is solved by using the following ansatz:

$$x(\tau) = A_x e^{i\beta_x \tau} \sum_{n=-\infty}^{\infty} C_{2n}^x e^{i2n\tau} + B_x e^{-i\beta_x \tau} \sum_{n=-\infty}^{\infty} C_{2n}^x e^{-i2n\tau}, \quad (C3)$$

where A_x, B_x are constants that depend on the initial conditions, while the parameter β_x and coefficients C_{2n}^x have to

be determined recursively. Here, we use the same notation of Ref. [18], but we note that the coefficients C_{2n}^x could have been named C_n^x , as we actually do in Eq. (48). To this end, we insert the ansatz into Eq. (C2) and we obtain

$$C_{2n+2}^x - D_{2n}^x C_{2n}^x + C_{2n-2}^x = 0, \quad D_{2n}^x = \frac{a_x - (\beta_x + 2n)^2}{q_x}. \quad (C4)$$

Iterative application of the above identities yield the continued fraction solutions

$$\frac{C_{2n}^x}{C_{2n+2}^x} = \frac{1}{D_{2n}^x - \frac{1}{D_{2n-2}^x - \frac{1}{D_{2n-4}^x - \dots}}}, \quad \frac{C_{2n}^x}{C_{2n-2}^x} = \frac{1}{D_{2n}^x - \frac{1}{D_{2n+2}^x - \frac{1}{D_{2n+4}^x - \dots}}}. \quad (C5)$$

With these expressions and Eq. (C4), we obtain

$$D_{2n}^x = \frac{1}{D_{2n-2}^x - \frac{1}{D_{2n-4}^x - \dots}} + \frac{1}{D_{2n+2}^x - \frac{1}{D_{2n+4}^x - \dots}}. \quad (C6)$$

Since $D_0^x = (a_x - \beta_x^2)/q_x$ and D_{2n}^x above, we have

$$\beta_x^2 = a_x - q_x \left[\frac{1}{D_{-2}^x - \frac{1}{D_{-4}^x - \dots}} + \frac{1}{D_2^x - \frac{1}{D_4^x - \dots}} \right]. \quad (C7)$$

Note that the expression in the brackets [...] of Eq. (C7) still depends on β_x, a_x , and q_x . Nonetheless, given a_x and q_x , Eq. (C7) can be solved with respect to β_x after a few iterations of the continued fraction.

For the numerical assessment of the coefficients C_{2n}^x we proceed as follows: First, we set the maximum of the n index to some positive integer N_F and $C_0^x = 1$ such that $C_{\pm 2n}^x = 0 \forall n > N_F$. Second, using the previously obtained value of β_x and the formula (C4), we solve an inhomogeneous linear system of equations given by

$$\begin{pmatrix} D_{2N_F}^x & -1 & 0 & 0 & 0 & \dots & \dots & \dots & \dots & \dots & \dots & \dots & \dots \\ -1 & D_{2(N_F-1)}^x & -1 & 0 & 0 & \dots & \dots & \dots & \dots & \dots & \dots & \dots & \dots \\ 0 & -1 & D_{2(N_F-2)}^x & -1 & 0 & \dots & \dots & \dots & \dots & \dots & \dots & \dots & \dots \\ \vdots & \vdots & \vdots & \vdots & \vdots & \vdots & \vdots & \vdots & \vdots & \vdots & \vdots & \vdots & \vdots \\ \vdots & \dots & \dots & \dots & 0 & -1 & D_2^x & 0 & 0 & \dots & \dots & \dots & \dots \\ \vdots & \dots & \dots & \dots & 0 & 0 & 0 & D_{-2}^x & -1 & 0 & \dots & \dots & \dots \\ \vdots & \vdots & \vdots & \vdots & \vdots & \vdots & \vdots & \vdots & \vdots & \vdots & \vdots & \vdots & \vdots \\ \vdots & \dots & \dots & \dots & \dots & \dots & \dots & \dots & \dots & \dots & 0 & -1 & D_{-2N_F}^x \end{pmatrix} \begin{pmatrix} C_{2N_F}^x \\ C_{2(N_F-1)}^x \\ C_{2(N_F-2)}^x \\ \vdots \\ C_2^x \\ C_{-2}^x \\ \vdots \\ C_{-2N_F}^x \end{pmatrix} = \begin{pmatrix} 0 \\ 0 \\ 0 \\ \vdots \\ 1 \\ 1 \\ \vdots \\ 0 \end{pmatrix}. \quad (C8)$$

The total number of numerically calculated coefficients is therefore $2N_F$. Moreover, the normalization condition

$$\sum_{n=-\infty}^{\infty} C_{2n}^x \simeq \sum_{n=-N_F}^{N_F} C_{2n}^x = 1 \quad (\text{C9})$$

has to be satisfied, from which we obtain the final normalized coefficients $c_{2n}^x = C_{2n}^x / \sum_{j=-N_F}^{N_F} C_{2j}^x$. In this way we can then immediately evaluate the reference harmonic oscillator frequency

$$v_x = \Omega_{\text{rf}} \sum_{n=-N_F}^{N_F} c_{2n}^x \left(\frac{\beta_x}{2} + n \right). \quad (\text{C10})$$

Exactly the same procedure applies to the determination of the coefficients $C_{2n}^{y,z}$, $c_{2n}^{y,z}$ and frequencies $v_{y,z}$. We note that the coefficients appearing in the ion solution (48) are precisely the coefficients $c_{2n}^{x,y,z}$.

Finally, the classical trajectory is obtained as $x(\tau = 0) = A_x + B_x \equiv x_0$ and

$$\dot{x}(\tau = 0) = i(A_x - B_x) \left[\beta_x + 2 \sum_{n=-N_F}^{N_F} n c_{2n}^x \right] \equiv \frac{p_0}{M}.$$

From these equalities we obtain

$$A_x = \frac{x_0}{2} - i \frac{p_0}{2M} \left[\beta_x + 2 \sum_{n=-N_F}^{N_F} n c_{2n}^x \right]^{-1}, \quad (\text{C11})$$

$$B_x = \frac{x_0}{2} + i \frac{p_0}{2M} \left[\beta_x + 2 \sum_{n=-N_F}^{N_F} n c_{2n}^x \right]^{-1}. \quad (\text{C12})$$

In the limit $a_x < |q_x|^2 \ll 1$ and for $p_0 = 0$, an approximated solution is given by

$$x_{\text{apx}}(\tau) = \frac{2x_0}{2 - q_x} \cos(\beta_x \tau) \left[1 - \frac{q_x}{2} \cos(2\tau) \right]. \quad (\text{C13})$$

This solution can be compared with the numerically obtained one from Eq. (C3). In Fig. 10 an example is shown, where we compare the solutions $x_{\text{apx}}(\tau)$ (thin black line), Eq. (C3) (blue slighter thicker line than the black line), and the numerically solved Eq. (C2) (thick yellow line).

2. Quantum Hamiltonian

As it can be verified, Eq. (C2) reproduces the motion of a parametric harmonic oscillator with squared frequency

$$W_{\xi}(t) = \frac{\Omega_{\text{rf}}^2}{4} [a_{\xi} - 2q_{\xi} \cos(\Omega_{\text{rf}} t)]. \quad (\text{C14})$$

As it can be shown formally with the Heisenberg equations of motion for \hat{r}_{ξ} and \hat{p}_{ξ} [18], the following Hamiltonian in one spatial direction

$$\hat{H}_I^{\text{trap}} = \frac{\hat{p}_{\xi}^2}{2M} + \frac{M}{2} W_{\xi}(t) \hat{r}_{\xi}^2, \quad \xi = x, y, z \quad (\text{C15})$$

reproduces exactly the same equation of motion (C2) for the operators \hat{r}_{ξ} . Thus, Eq. (C15) is the quantized version of the classical Hamiltonian for an ion in a Paul trap, where we have promoted the ion position and momentum variables to

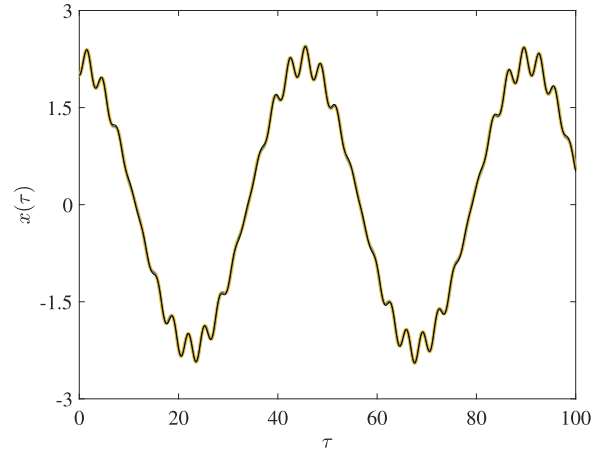


FIG. 10. Comparison of the numerically exact solution obtained by solving the Newton equation of motion (C2), the analytical solution (C3), and the approximated one (C13). We have chosen the following parameters: $a_x = 0$, $q_x = 0.28$, and $N_F = 20$.

operators. Aside from this, we note that the spatial directions are uncoupled because of the form of the quadrupole field (C1).

The eigenfunctions of \hat{H}_I^{trap} are given by

$$\psi_n(r_{\xi}, t) = \left(\frac{M v_{\xi}}{\pi \hbar} \right)^{\frac{1}{4}} \frac{e^{-i n v_{\xi} t + i \frac{M}{2n} \frac{u_{\xi}(t)}{u_{\xi}(0)} r_{\xi}^2}}{\sqrt{2^n n! u_{\xi}(t)}} \times H_n \left(\sqrt{\frac{M v_{\xi}}{\hbar |u_{\xi}(t)|^2}} r_{\xi} \right), \quad (\text{C16})$$

where

$$u_{\xi}(t) = e^{i \beta_{\xi} \Omega_{\text{rf}} t / 2} \sum_{n=-\infty}^{\infty} C_{2n}^{\xi} e^{i n \Omega_{\text{rf}} t}, \quad (\text{C17})$$

with $u_{\xi}(0) = \sum_{n=-\infty}^{\infty} C_{2n}^{\xi} = 1$, $\dot{u}_{\xi}(0) = i v_{\xi}$, and v_{ξ} given by Eq. (C10).

Finally, as initial condition of the ion density matrix for the solution of the master equation we have chosen

$$\hat{\rho}_{\xi} = |\psi_0(t = T_{\text{rf}})\rangle \langle \psi_0(t = T_{\text{rf}})|, \quad \forall \xi = x, y, z \quad (\text{C18})$$

since by starting from $|\psi_0(t = 0)\rangle \langle \psi_0(t = 0)|$ and by computing the expectation value (65), one can numerically verify that the minimum of the ion energy occurs at the time $t = 2\pi / \Omega_{\text{rf}}$. This is the energy minimum we assumed in our analyses and Eq. (C18) as initial condition. With that initial matrix we have computed the initial conditions for the moments of Sec. V.

APPENDIX D: ION MASTER EQUATION DETAILS

In this Appendix, we provide a few technical details on the calculation of the double integral as a consequence of the double summation in momentum space in Eq. (47). The derivations are detailed for a bosonic bath only, while for a fermionic one we simply provide the final result, as they are very similar. Additionally, we provide details of the analytical

calculation of the Cauchy principal value within the Fröhlich model that yields the Lamb shift.

1. Double integration in momentum space

In Eq. (47) we have to evaluate terms of the kind

$$\sum_{\mathbf{q}, \mathbf{q}'} n_{\mathbf{q}} (n_{\mathbf{q}'} + 1) (q_{\xi}' - q_{\xi})^2 |c_{\mathbf{q}' - \mathbf{q}}|^2 \delta(\omega_{\mathbf{q}'} - \omega_{\mathbf{q}} \pm \omega_{s, \xi}), \quad (\text{D1})$$

where $\omega_{s, \xi} = \Omega_{\text{rf}}(\beta_{\xi}/2 + s)$ and $\omega_{\mathbf{q}} \equiv \varepsilon(\mathbf{q})/\hbar$. To this end, we first perform the center-of-mass and relative coordinate transformation

$$\mathbf{k} = \mathbf{q}' - \mathbf{q}, \quad \mathbf{K} = \frac{\mathbf{q}' + \mathbf{q}}{2}, \quad (\text{D2})$$

with

$$\mathbf{q}' = \mathbf{K} + \frac{\mathbf{k}}{2}, \quad \mathbf{q} = \mathbf{K} - \frac{\mathbf{k}}{2}, \quad (\text{D3})$$

and therefore we have

$$\omega_{\mathbf{q}'} - \omega_{\mathbf{q}} = \frac{\hbar}{2m} [(\mathbf{q}')^2 - \mathbf{q}^2] = \frac{\hbar}{m} (\mathbf{k} \cdot \mathbf{K}). \quad (\text{D4})$$

Given this, we can rewrite Eq. (D1) as

$$\sum_{\mathbf{k}, \mathbf{K}} n_{\mathbf{k}, \mathbf{K}}^{-} (n_{\mathbf{k}, \mathbf{K}}^{+} + 1) k_{\xi}^2 |c_{\mathbf{k}}|^2 \delta\left(\frac{\hbar}{m} \mathbf{k} \cdot \mathbf{K} \pm \omega_{s, \xi}\right), \quad (\text{D5})$$

where

$$n_{\mathbf{k}, \mathbf{K}}^{-} = \frac{1}{\exp\{\beta_{\mathcal{T}}[\frac{\hbar^2}{2m}(\mathbf{K}^2 + \frac{\mathbf{k}^2}{4} - \mathbf{k} \cdot \mathbf{K}) - \mu_G]\} - 1},$$

$$n_{\mathbf{k}, \mathbf{K}}^{+} = \frac{1}{\exp\{\beta_{\mathcal{T}}[\frac{\hbar^2}{2m}(\mathbf{K}^2 + \frac{\mathbf{k}^2}{4} + \mathbf{k} \cdot \mathbf{K}) - \mu_G]\} - 1}. \quad (\text{D6})$$

We remind that μ_G is the bosons' chemical potential and $\beta_{\mathcal{T}} = (k_B \mathcal{T})^{-1}$. Thus, we perform the continuum limit

$$\sum_{\mathbf{k}, \mathbf{K}} \rightarrow \frac{L^6}{(2\pi)^6} \int_{\mathbb{R}^3} d\mathbf{k} \int_{\mathbb{R}^3} d\mathbf{K}, \quad (\text{D7})$$

which transforms the double sum in Eq. (D5) in the following two double integrals:

$$\mathcal{I}_1 + \mathcal{I}_2 = \int_{\mathbb{R}^3} d\mathbf{k} \int_{\mathbb{R}^3} d\mathbf{K} n_{\mathbf{k}, \mathbf{K}}^{-} k_{\xi}^2 |c_{\mathbf{k}}|^2 \delta\left(\frac{\hbar}{m} \mathbf{k} \cdot \mathbf{K} \pm \omega_{s, \xi}\right)$$

$$+ \int_{\mathbb{R}^3} d\mathbf{k} \int_{\mathbb{R}^3} d\mathbf{K} n_{\mathbf{k}, \mathbf{K}}^{-} n_{\mathbf{k}, \mathbf{K}}^{+} k_{\xi}^2 |c_{\mathbf{k}}|^2 \delta\left(\frac{\hbar}{m} \mathbf{k} \cdot \mathbf{K} \pm \omega_{s, \xi}\right). \quad (\text{D8})$$

Here, we have neglected the common factor $(\frac{L}{2\pi})^6$. In order to solve them, we first move to spherical coordinates

$$k_x = k \sin(\theta_k) \cos(\varphi_k),$$

$$k_y = k \sin(\theta_k) \sin(\varphi_k),$$

$$k_z = k \cos(\theta_k). \quad (\text{D9})$$

Thus, the corresponding volume element is given by $d\mathbf{k} = dk d\theta_k d\varphi_k k^2 \sin(\theta_k)$ with $k \equiv |\mathbf{k}|$. While a similar change of variables applies to the center-of-mass variable \mathbf{K} as well, but with subscript K for the angular variables, we note that we choose the “ z axis” of the vector \mathbf{K} along the relative variable

\mathbf{k} . In such a way the scalar product appearing in the Dirac's delta can be written as

$$\mathbf{k} \cdot \mathbf{K} = kK \cos(\theta_K). \quad (\text{D10})$$

Given this, the first integral becomes

$$\mathcal{I}_1 = 2\pi^2 (1 + \delta_{z, \xi}) \int_0^{\infty} dk k^4 \int_0^{\pi} d\theta_k g_{\xi}^2(\theta_k) \sin(\theta_k) |c_{\mathbf{k}}|^2$$

$$\times \int_0^{\infty} dK K^2 \int_0^{\pi} d\theta_K \sin(\theta_K) n_{\mathbf{k}, \mathbf{K}}^{-}$$

$$\times \delta\left(\frac{\hbar}{m} kK \cos(\theta_K) \pm \omega_{s, \xi}\right), \quad (\text{D11})$$

where we have performed the integrations of the variables φ_k and φ_K since only k_{ξ} relies on φ_k , while none of the functions in the integrand depend on φ_K . Aside from this, because of k_{ξ} we have introduced the angle function $g_{\xi}(\theta_k) = \delta_{z, \xi} \cos(\theta_k) + (1 - \delta_{z, \xi}) \sin(\theta_k)$ with $\delta_{z, \xi}$ being the Kronecker delta. Since neither $|c_{\mathbf{k}}|^2$ nor $n_{\mathbf{k}, \mathbf{K}}^{-}$ rely on θ_k , we can easily perform the integration

$$\int_0^{\pi} d\theta_k g_{\xi}^2(\theta_k) \sin(\theta_k) = \frac{2}{3} [\delta_{z, \xi} + 2(1 - \delta_{z, \xi})]. \quad (\text{D12})$$

Our next step is to integrate out the variable K . Towards this end, we first rewrite the Dirac's delta as

$$\delta\left(\frac{\hbar}{m} kK \cos(\theta_K) \pm \omega_{s, \xi}\right)$$

$$= \frac{m}{\hbar k |\cos(\theta_K)|}$$

$$\times \delta(K \pm K_{s, \xi}(\theta_K, k)) \delta_{0, 1 \pm \text{sgn}(\omega_{s, \xi} \cos(\theta_K))}, \quad (\text{D13})$$

where $\text{sgn}(\dots)$ is the sign function. The last Kronecker delta ensures that $K_{s, \xi}(\theta_K, k) = \frac{m\omega_{s, \xi}}{\hbar k \cos(\theta_K)} \geq 0$ in the minus case and $K_{s, \xi}(\theta_K, k) \leq 0$ in the plus case since $K \in \mathbb{R}^+$ and the integral over K would be zero otherwise, and so would be \mathcal{I}_1 . Hence, we obtain

$$\mathcal{I}_1 = \frac{8}{3} \pi^2 \left(\frac{m}{\hbar}\right)^3 \omega_{s, \xi}^2 \int_0^{\infty} dk k |c_{\mathbf{k}}|^2$$

$$\times \int_0^{\pi} d\theta_K \frac{\tan(\theta_K) n_{\mathbf{k}, \mp \mathbf{K}_{s, \xi}(\theta_K, k)}^{-}}{\cos(\theta_K) |\cos(\theta_K)|} \delta_{0, 1 \pm \text{sgn}(\omega_{s, \xi} \cos(\theta_K))}. \quad (\text{D14})$$

Finally, we perform the angular integral

$$\int_0^{\pi} d\theta_K \frac{\tan(\theta_K) n_{\mathbf{k}, \mp \mathbf{K}_{s, \xi}(\theta_K, k)}^{-}}{\cos(\theta_K) |\cos(\theta_K)|} \delta_{0, 1 \pm \text{sgn}(\omega_{s, \xi} \cos(\theta_K))}$$

$$= \int_{-1}^1 du \frac{n_{\mathbf{k}, \mp \mathbf{K}_{s, \xi}(u, k)}^{-}}{u^2 |u|} \delta_{0, 1 \pm \text{sgn}(\omega_{s, \xi} u)}, \quad (\text{D15})$$

where we performed the change of variable $u = \cos(\theta_K)$. Hence,

$$n_{\mathbf{k}, \mathbf{K}_{s, \xi}(u, k)}^{-} = \frac{1}{e^{\frac{\beta \hbar \omega_{s, \xi}}{2(k\ell_{s, \xi})^2} \left[\frac{1}{u^2} + \frac{(k\ell_{s, \xi})^4}{4} \pm (k\ell_{s, \xi})^2 \right]} - \beta \mu_G} - 1} \quad (\text{D16})$$

with $\ell_{s,\xi}^2 = \frac{\hbar}{m\omega_{s,\xi}}$ and (D15) can be rewritten as

$$\mathcal{J} = \int_0^1 du \frac{n_{\mathbf{k},\mathbf{K}_{s,\xi}}^-(u,k)}{u^3} = \int_0^1 \frac{du}{u^3 (e^{\frac{\alpha_0}{u^2} + \alpha_{\pm}} - 1)}, \quad (\text{D17})$$

where

$$\alpha_0 = \frac{\beta_{\mathcal{T}} \hbar \omega_{s,\xi}}{2(k\ell_{s,\xi})^2},$$

$$\alpha_{\pm} = \alpha_0 \left[\frac{(k\ell_{s,\xi})^4}{4} \pm (k\ell_{s,\xi})^2 \right] - \beta_{\mathcal{T}} \mu_G. \quad (\text{D18})$$

In order to solve \mathcal{J} , we perform the change of variable:

$$z = \frac{\alpha_0}{u^2} + \alpha_{\pm} \implies du = -\frac{\sqrt{\alpha_0}}{2} \frac{dz}{(z - \alpha_{\pm})^{3/2}}. \quad (\text{D19})$$

In such a way \mathcal{J} is rewritten as

$$\mathcal{J} = \frac{1}{2\alpha_0} \int_{\alpha_0 + \alpha_{\pm}}^{+\infty} \frac{dz}{e^z - 1} = \frac{\alpha_0 + \alpha_{\pm} - \ln(e^{\alpha_0 + \alpha_{\pm}} - 1)}{2\alpha_0},$$

which holds as long as $\alpha_0 > 0$, as it is indeed the case. Hence, the integral (D14) is given by

$$\left(\frac{L}{2\pi}\right)^6 \mathcal{I}_1^{\pm} = \frac{1}{6} \left(\frac{m}{\pi\mu}\right)^2 \frac{\hbar}{\beta_{\mathcal{T}}} \mathcal{F}_{s,\xi}^{(1),\pm} \quad (\text{D20})$$

with

$$\mathcal{F}_{s,\xi}^{(1),\pm} = \int_0^{\infty} dk k^3 \frac{\alpha_0(k) + \alpha_{\pm}(k) - \ln(e^{\alpha_0(k) + \alpha_{\pm}(k)} - 1)}{|f(k)|^{-2}}. \quad (\text{D21})$$

The integral over k in Eq. (D21) is computed numerically. We note that $\alpha_0(k) \sim k^{-2}$ and therefore the exponential diverges for $k \rightarrow 0$, which is not the case for $\alpha_{\pm}(k) \sim k^2$ that tends to zero. Because of the logarithm, however, the exponent of the exponential function compensates the $\alpha_0(k)$ on the left-hand side of the logarithm so that the overall behavior of the integrand is zero when $k \rightarrow 0$. Instead, when $k \rightarrow \infty$, we have $\alpha_0(k) \rightarrow 0$, while $\alpha_{\pm}(k)$ diverges. For the same argument as before, the function of the integrand numerator tends to zero. Therefore, the integral converges, even if $|f(k)|^2 = 1$. For the

fermionic bath, we get the expression

$$\mathcal{F}_{s,\xi}^{(1),\pm} = \int_0^{\infty} dk k^3 \frac{\ln(1 + e^{\alpha_0(k) + \alpha_{\pm}(k)}) - \alpha_0(k) - \alpha_{\pm}(k)}{|f(k)|^{-2}}. \quad (\text{D22})$$

The result is very similar to the bosonic case, but one has to remember that the chemical potentials are different, especially for temperature below the Fermi temperature and the critical temperature for condensation.

The integral \mathcal{I}_2 is almost the same, but \mathcal{J} in Eq. (D17) is defined now as

$$\mathcal{J} = \int_0^1 du \frac{n_{\mathbf{k},\mathbf{K}_{s,\xi}}^-(u,k) n_{\mathbf{k},\mathbf{K}_{s,\xi}}^+(u,k)}{u^3}$$

$$= \int_0^1 \frac{du}{u^3 (e^{\frac{\alpha_0}{u^2} + \alpha_-} - 1) (e^{\frac{\alpha_0}{u^2} + \alpha_+} - 1)}. \quad (\text{D23})$$

To solve it, we first perform the change of variable (D19), which yields

$$\mathcal{J} = \frac{1}{2\alpha_0} \int_{\alpha_0 + \alpha_-}^{+\infty} \frac{dz}{(e^z - 1)(e^{z + \alpha_+ - \alpha_-} - 1)}. \quad (\text{D24})$$

Thus, we perform the additional change of variable $y = e^z$ with $dz = dy/y$, and we obtain

$$\mathcal{J} = \frac{1}{2\alpha_0 e^{\alpha_+ - \alpha_-}} \int_a^{+\infty} \frac{dy}{y(y-1)(y-b)}, \quad (\text{D25})$$

with $a = e^{\alpha_0 + \alpha_-}$ and $b = e^{\alpha_- - \alpha_+}$. The integral in Eq. (D25) can be solved analytically, which finally gives

$$\mathcal{J} = \frac{\ln(e^{\alpha_0 + \alpha_-} - e^{\alpha_- - \alpha_+}) - \alpha_0 - \alpha_-}{2\alpha_0(1 - e^{\alpha_- - \alpha_+})}$$

$$- \frac{e^{\alpha_- - \alpha_+} \text{Re}\{\text{arctanh}(1 - 2e^{\alpha_0 + \alpha_-})\}}{\alpha_0(1 - e^{\alpha_- - \alpha_+})}. \quad (\text{D26})$$

Hence, \mathcal{I}_2 preserves the structure of \mathcal{I}_1 , that is,

$$\left(\frac{L}{2\pi}\right)^6 \mathcal{I}_2 = \frac{1}{6} \left(\frac{m}{\pi\mu}\right)^2 \frac{\hbar}{\beta_{\mathcal{T}}} \mathcal{F}_{s,\xi}^{(2)}, \quad (\text{D27})$$

where the radial integration in momentum space is given by

$$\mathcal{F}_{s,\xi}^{(2)} = \int_0^{\infty} dk k^3 |f(k)|^2 \left[\frac{\ln(e^{\alpha_0 + \alpha_-} - e^{\alpha_- - \alpha_+}) - \alpha_0 - \alpha_- - 2e^{\alpha_- - \alpha_+} \text{Re}\{\text{arctanh}(1 - 2e^{\alpha_0 + \alpha_-})\}}{1 - e^{\alpha_- - \alpha_+}} \right]. \quad (\text{D28})$$

For the fermions we obtain a similar expression

$$\mathcal{F}_{s,\xi}^{(2)} = \int_0^{\infty} dk k^3 |f(k)|^2 \left[\frac{e^{\alpha_- - \alpha_+} \ln(1 + e^{\alpha_0 + \alpha_-}) - \ln(e^{\alpha_- - \alpha_+} + e^{\alpha_0 + \alpha_-})}{e^{\alpha_- - \alpha_+} - 1} - \alpha_0(k) - \alpha_-(k) \right]. \quad (\text{D29})$$

We note that in the numerical assessment of $\mathcal{F}_{s,\xi}^{(2)}$ we found that both for the bosons and the fermions the integral is essentially zero, as a consequence of the large numerical values taken by the exponents. For high densities and high temperatures, however, $\mathcal{F}_{s,\xi}^{(2)}$ is not negligible anymore.

2. Cauchy principal value calculation

We need to compute the Cauchy principal value

$$\mathcal{I} = \text{P} \int_{\mathbb{R}^3} d\mathbf{q} \frac{f^2(q) q_{\xi} q_{\xi'}}{\omega_0 - \omega}, \quad \xi, \xi' = 1, 2, 3 \quad (\text{D30})$$

where $\omega_0 \equiv |\Omega_{rf}(\beta_\xi/2 + s)|$, $\omega \equiv \varepsilon(\mathbf{q})/\hbar$, and $f(q)$ given by Eq. (6). Henceforth, we neglected the imaginary unit i in Eq. (51). The above integral can be rewritten as $[q_{s,\xi}$ is defined in Eq. (54)]

$$\begin{aligned} \mathcal{I}_-(q_{s,\xi}) &= \frac{2m}{\hbar} \mathbb{P} \int_{\mathbb{R}^3} d\mathbf{q} \frac{f^2(q)q_\xi q_{\xi'}}{|q_{s,\xi}^2| - q^2} \\ &= \frac{2m}{\hbar} \mathbb{P} \int_0^\infty dq q^2 \int_0^\pi d\theta \sin(\theta) \int_0^{2\pi} d\varphi \frac{f^2(q)q_\xi q_{\xi'}}{|q_{s,\xi}^2| - q^2}, \end{aligned} \quad (\text{D31})$$

where we transformed the wave vector in spherical coordinates (D9). The only angular dependence in the integrand comes from $q_\xi q_{\xi'}$, as the other functions rely on q only. Given this, one can verify that the angular integral of $q_\xi q_{\xi'}$ always vanishes for $\xi \neq \xi'$. Thus, we just need to compute the CPV for each direction separately. The angular part of the integration is the same for all directions, namely, it yields $4\pi/3$. Thus, we need to assess the integral

$$\mathcal{I}_-(q_{s,\xi}) = \frac{8m\pi}{3\hbar} \mathbb{P} \int_0^\infty dq \frac{f^2(q)q^4}{|q_{s,\xi}^2| - q^2} = \frac{8m\pi}{3\hbar} \mathcal{J}'_-(q_{s,\xi}). \quad (\text{D32})$$

In case the denominator of the integrand has a plus sign, we have an integration without any singularity:

$$\mathcal{I}_+(q_{s,\xi}) = -\frac{2m}{\hbar} \int_{\mathbb{R}^3} d\mathbf{q} \frac{f^2(q)q_\xi^2}{|q_{s,\xi}^2| + q^2} = -\frac{8m\pi}{3\hbar} \mathcal{J}'_+(q_{s,\xi}). \quad (\text{D33})$$

This integration can be in principle carried out analytically, but we refrain to provide an expression since it is quite in-

volved and it includes Meijer G functions. A similar argument holds for the integrals involving the bosonic occupation number, that is,

$$\begin{aligned} \mathcal{I}_\pm^{n_q}(q_{s,\xi}) &= \mp \frac{2m}{\hbar} \int_{\mathbb{R}^3} d\mathbf{q} \frac{f^2(q)q_\xi^2}{|q_{s,\xi}^2| \pm q^2} \frac{1}{e^{[\beta\tau(\varepsilon(\mathbf{q})-\mu_G)]} - 1} \\ &= \mp \frac{8m\pi}{3\hbar} \mathcal{J}_\pm^{n_q}(q_{s,\xi}). \end{aligned} \quad (\text{D34})$$

To compute them, we performed a numerical integration with *Mathematica*.

APPENDIX E: RESCALED EQUATIONS OF MOTION

In our numerical simulations we solve the differential equations (68) in rescaled units, namely, we rescaled the time and space variables with respect to v_ξ and $l_\xi = \sqrt{\hbar/(Mv_\xi)}$, respectively, that is, with respect to the reference harmonic oscillator frequency and length scale. Hence, we have $\bar{r}_\xi^2 = ((r_\xi)/l_\xi)^2$, $\bar{p}_\xi^2 = [(p_\xi)/(l_\xi v_\xi M)]^2 = (l_\xi/\hbar)^2 (p_\xi^2)$, and $\bar{c}_\xi = c_\xi/(l_\xi^2 v_\xi M) = c_\xi/\hbar$, where we introduced a bar for indicating the dimensionless quantities. Given this, Eqs. (68) in rescaled units read as

$$\begin{aligned} \frac{d}{d\tau} \bar{r}_\xi^2 &= \bar{c}_\xi, \\ \frac{d}{d\tau} \bar{p}_\xi^2 &= \{\bar{\Gamma}_\xi \text{Im}[\bar{\Phi}_\xi(\tau)] - \bar{W}'_\xi(\tau)\} \bar{c}_\xi - 2\bar{\Gamma}_\xi \text{Im}[\bar{\Lambda}_\xi(\tau)] \bar{p}_\xi^2 \\ &\quad + \bar{\Gamma}_\xi \text{Re}[\bar{\Phi}_\xi(\tau)], \\ \frac{d}{d\tau} \bar{c}_\xi &= 2\{\bar{\Gamma}_\xi \text{Im}[\bar{\Phi}_\xi(\tau)] - \bar{W}'_\xi(\tau)\} \bar{r}_\xi^2 + 2\bar{p}_\xi^2 \\ &\quad - \bar{\Gamma}_\xi \{\text{Im}[\bar{\Lambda}_\xi(\tau)] \bar{c}_\xi - \text{Re}[\bar{\Lambda}_\xi(\tau)]\} \end{aligned} \quad (\text{E1})$$

with $\tau = v_\xi t$, $\bar{\Omega}_{rf}^\xi = \Omega_{rf}/v_\xi$, and

$$\begin{aligned} \bar{\Gamma}_\xi &= \frac{2\pi}{3} \frac{m}{M} \left(\frac{M}{\mu}\right)^2 (n_0 l_\xi^3), \\ \bar{W}'_\xi(\tau) &= \frac{\bar{W}_\xi(\tau) + \delta \bar{W}_\xi(\tau)}{v_\xi^2} = \left(\frac{\bar{\Omega}_{rf}^\xi}{2}\right)^2 [a_\xi + \delta \bar{a}_\xi - 2(q_\xi + \delta \bar{q}_\xi) \cos(\bar{\Omega}_{rf}^\xi \tau) - 2\delta \bar{q}'_\xi \bar{g}_\xi(\tau)], \\ \bar{g}_\xi(\tau) &= \sum_{s,s' \notin \mathcal{S}_i} F_{s,s'}^\xi \cos[(s-s')\bar{\Omega}_{rf}^\xi \tau] [\bar{\mathcal{J}}'_+(q_{s,\xi}) - \bar{\mathcal{J}}'_-(q_{s,\xi})], \\ \bar{Q}_\xi &= \frac{Q}{l_\xi} = \frac{32}{3} \frac{m}{M} \left(\frac{M}{\mu}\right)^2 \frac{(n_0 l_\xi^3)}{(\bar{\Omega}_{rf}^\xi)^2} \end{aligned} \quad (\text{E2})$$

and $\bar{\mathcal{J}}'_\pm(q_{s,\xi}) = \mathcal{J}'_\pm(q_{s,\xi})l_\xi$. Here, for the sake of simple notation, we just refer to the bosonic case. Moreover, the rescaled Φ and Λ functions read as

$$\begin{aligned} \bar{\Lambda}_\xi(\tau) &= i \sum_{s,s'} C_s^\xi C_{s'}^\xi \{ |\bar{q}_{s,\xi}|^3 \bar{f}(\bar{q}_{s,\xi})^2 (1-\phi) [i \sin[(s-s')\bar{\Omega}_{rf}^\xi \tau] (1+2n_{\bar{q}_{s,\xi}}) + \cos[(s-s')\bar{\Omega}_{rf}^\xi \tau] \text{sgn}(\beta_\xi/2 + s)] \\ &\quad - \bar{\eta}_{s,\xi}^+ e^{-i(s-s')\bar{\Omega}_{rf}^\xi \tau} + \bar{\eta}_{s,\xi}^- e^{i(s-s')\bar{\Omega}_{rf}^\xi \tau} \} - \frac{2}{\pi} \bar{\Omega}_{rf}^\xi \sum_{s,s'} C_s^\xi C_{s'}^\xi \{ \cos[(s-s')\bar{\Omega}_{rf}^\xi \tau] [1 - 2\Theta[\text{sgn}(\beta_\xi/2 + s)]] \\ &\quad \times [\bar{\mathcal{J}}'_-(q_{s,\xi}) + \bar{\mathcal{J}}'_+(q_{s,\xi}) + 2[\bar{\mathcal{J}}_+^{n_q}(q_{s,\xi}) + \bar{\mathcal{J}}_+^{n_q}(q_{s,\xi})]] - i \sin[(s-s')\bar{\Omega}_{rf}^\xi \tau] [\bar{\mathcal{J}}'_-(q_{s,\xi}) - \bar{\mathcal{J}}'_+(q_{s,\xi})] \}, \end{aligned} \quad (\text{E3})$$

$$\begin{aligned}
\bar{\Phi}_\xi(\tau) = & \bar{\Omega}_{rf} \sum_{s,s'} C_s^\xi C_{s'}^\xi (\beta_\xi/2 + s') \{ |\bar{q}_{s,\xi}|^3 \bar{f}(\bar{q}_{s,\xi})^2 (1 - \phi) [\cos[(s - s')\bar{\Omega}_{rf}\tau] (1 + 2n_{\bar{q}_{s,\xi}}) \\
& + i \sin[(s - s')\bar{\Omega}_{rf}\tau] \text{sgn}(\beta_\xi/2 + s)] + \bar{\eta}_{s,\xi}^- e^{-i(s-s')\bar{\Omega}_{rf}\tau} + \bar{\eta}_{s,\xi}^+ e^{i(s-s')\bar{\Omega}_{rf}\tau} \} \\
& - \frac{2}{\pi} \bar{\Omega}_{rf} \sum_{s,s'} C_s^\xi C_{s'}^\xi (\beta_\xi/2 + s') \sin[(s - s')\bar{\Omega}_{rf}\tau] [2\Theta[\text{sgn}(\beta_\xi/2 + s)] - 1] [\bar{\mathcal{J}}_-'(\bar{q}_{s,\xi}) + \bar{\mathcal{J}}_+'(\bar{q}_{s,\xi}) \\
& + 2[\bar{\mathcal{J}}_-^{nq}(\bar{q}_{s,\xi}) + \bar{\mathcal{J}}_+^{nq}(\bar{q}_{s,\xi})]], \tag{E4}
\end{aligned}$$

where $\bar{f}(\bar{q}_{s,\xi}) = f(q_{s,\xi})/l_\xi$, $\bar{\beta}_T^\xi = \beta_T \hbar v_\xi$, $\bar{\mathcal{J}}_\pm^{nq}(\bar{q}_{s,\xi}) = \mathcal{J}_\pm^{nq}(q_{s,\xi})l_\xi$, and

$$\begin{aligned}
\bar{\eta}_{s,\xi}^\pm &= \frac{1}{16\pi^2} \frac{m}{M} \frac{\bar{\mathcal{F}}_{s,\xi}^{(1),\pm} + (-1)^\phi \bar{\mathcal{F}}_{s,\xi}^{(2)}}{(n_0 l_\xi^3) \bar{\beta}_T^\xi}, \\
\bar{q}_{s,\xi} &= l_\xi q_{s,\xi} = \sqrt{\frac{2m\Omega_{rf}}{Mv_\xi} \left| \frac{\beta_\xi}{2} + s \right|}. \tag{E5}
\end{aligned}$$

For the numerical assessment of the integrals involved in the functions $\bar{\mathcal{F}}_{s,\xi}^{(1,2)} = \bar{\mathcal{F}}_{s,\xi}^{(1,2)}/l_\xi^2$, we note that they have the units of a wave vector. Given this, we replace the integral variable by $k \mapsto \bar{k}_\xi = kl_\xi$ in Eqs. (D21) and (D28) and we define the rescaled parameters in Eq. (D18) as

$$\begin{aligned}
\alpha_0(\bar{k}_\xi) &= \frac{m}{M} \frac{\varpi_{s,\xi}^2}{2} \frac{\bar{\beta}_T^\xi}{\bar{k}_\xi^2}, \\
\alpha_\pm(\bar{k}_\xi) &= \frac{\bar{\beta}_T^\xi \varpi_{s,\xi}}{2} \left[\frac{\bar{k}_\xi^2}{4} \frac{M}{m} \frac{1}{\varpi_{s,\xi}} \pm 1 \right] - \bar{\beta}_T^\xi \bar{\mu}_G^\xi, \\
\varpi_{s,\xi} &= \frac{\Omega_{rf}}{v_\xi} \left(\frac{\beta_\xi}{2} + s \right), \quad \bar{\mu}_G^\xi = \frac{\mu_G}{\hbar v_\xi}. \tag{E6}
\end{aligned}$$

Finally, let us comment on the rescaling of the scattering amplitude $f(q)$. The expression given in Eq. (6) assumes that the regularization parameters b, c are given in units of R^* , as it is more convenient to work with that unit length when solving the Schrödinger equation (A4). Thus, if everything is in that unit length, that is, also the q wave vector, then the scattering amplitude is in R^* units as well. As a consequence, if we wish to have it in l_ξ units, we have to multiply $f(q)$ by R^*/l_ξ . Hence, when we have to assess the scattering amplitude in the $\bar{\Lambda}$ and $\bar{\Phi}$ functions, we need first to provide $q_{s,\xi}$ in R^* units as well as b and c , and then multiply the obtained result by R^*/l_ξ . The wave vector $q_{s,\xi}$ in R^* units is given by

$$q_{s,\xi}^* = R^* q_{s,\xi} = \frac{R^*}{l_\xi} \bar{q}_{s,\xi}, \tag{E7}$$

where $\bar{q}_{s,\xi}$ is defined in Eq. (E5). The situation is slightly different when the integrations involved in the functions $\bar{\mathcal{F}}_{s,\xi}^{(1,2)}$, $\bar{\mathcal{J}}_\pm^{nq}(q_{s,\xi})$, and $\bar{\mathcal{J}}_\pm^{nq}(\bar{q}_{s,\xi})$ are considered. We can rescale the integrands in R^* units, as the scattering amplitude (6), and then we rescale the result in l_ξ units. Alternatively, we first rescale the scattering amplitude in units of l_ξ , thus, we perform the integrations in l_ξ units. We have chosen the second option, as the regularization parameters b, c have been obtained in R^* units. In this case the scattering amplitude in l_ξ units is given

by

$$\bar{f}(\bar{q}) = \frac{\bar{c}^2 \pi (R^*)^2 l_\xi^{-2}}{(\bar{b}^2 - \bar{c}^2)^2 \bar{q}} \left\{ e^{-\bar{b}\bar{q}} \left[1 + \frac{(\bar{b}^4 - \bar{c}^4)\bar{q}}{4\bar{b}\bar{c}^2} \right] - e^{-\bar{c}\bar{q}} \right\}, \tag{E8}$$

where we have introduced the factor $(R^*/l_\xi)^2$. The regularization parameters \bar{b}, \bar{c} are in l_ξ units, which can be obtained from the b, c in R^* units using the relations

$$\bar{b} = b \frac{R^*}{l_\xi}, \quad \bar{c} = c \frac{R^*}{l_\xi}. \tag{E9}$$

A similar reasoning applies for the integral (D32). Indeed, using the definitions (E9) and (D32), one has to replace R^* in Eq. (D32) by $(R^*/l_\xi)^4$. Furthermore, the free-particle dispersion relation is rescaled as $\bar{\varepsilon}(\mathbf{q}) = \varepsilon(\mathbf{q})/(\hbar v_\xi) = M\bar{q}^2/(2m)$.

APPENDIX F: LINDBLAD FORM OF THE MASTER EQUATION

The ion master equation (56) cannot be transformed in a Lindblad-type Markovian master equation, as a crucial assumption to obtain such a form is the rotating-wave approximation. Using the definitions for the position and momentum operators for each spatial direction $\xi = x, y, z$,

$$\hat{r}_\xi = \sqrt{\frac{\hbar}{2Mv_\xi}} (\hat{a}_\xi^\dagger + \hat{a}_\xi), \quad \hat{p}_\xi = i\sqrt{\frac{M\hbar v_\xi}{2}} (\hat{a}_\xi^\dagger - \hat{a}_\xi), \tag{F1}$$

we can rewrite Eq. (56) as

$$\begin{aligned}
\dot{\hat{\rho}}_\xi = & -\frac{i}{\hbar} [\hat{H}_S^\xi + \delta\hat{H}_S^\xi + \hat{H}_S^\xi, \hat{\rho}_\xi] + \gamma_\xi^a \hat{\mathcal{D}}[a_\xi] \hat{\rho}_\xi + \gamma_\xi^a \hat{\mathcal{D}}[a_\xi^\dagger] \hat{\rho}_\xi \\
& + \gamma_\xi^+ \hat{G}_+[a_\xi, \hat{a}_\xi^\dagger] \hat{\rho}_\xi - \frac{i}{\hbar} \gamma_\xi^- \hat{G}_-[a_\xi, \hat{a}_\xi^\dagger] \hat{\rho}_\xi. \tag{F2}
\end{aligned}$$

Here, we have introduced the operators

$$\begin{aligned}
\hat{H}_S^\xi &= \hbar \Delta_\xi \left[\hat{a}_\xi^\dagger \hat{a}_\xi + \frac{(\hat{a}_\xi^\dagger)^2 + \hat{a}_\xi^2}{2} \right] \\
&+ i\hbar \Delta_\xi' [(\hat{a}_\xi^\dagger)^2 - \hat{a}_\xi^2], \\
\hat{\mathcal{D}}[a_\xi] \hat{\rho}_\xi &= \hat{a}_\xi \hat{\rho}_\xi \hat{a}_\xi^\dagger - \frac{\hat{a}_\xi^\dagger \hat{a}_\xi \hat{\rho}_\xi + \hat{\rho}_\xi \hat{a}_\xi^\dagger \hat{a}_\xi}{2}, \\
\hat{G}_\pm[a_\xi, \hat{a}_\xi^\dagger] \hat{\rho}_\xi &= \hat{a}_\xi^\dagger \hat{\rho}_\xi \hat{a}_\xi^\dagger \pm \hat{a}_\xi \hat{\rho}_\xi \hat{a}_\xi \\
&- \frac{[(\hat{a}_\xi^\dagger)^2 \pm \hat{a}_\xi^2] \hat{\rho}_\xi + \hat{\rho}_\xi [(\hat{a}_\xi^\dagger)^2 \pm \hat{a}_\xi^2]}{2}, \tag{F3}
\end{aligned}$$

and the damping rates as well as energy shifts

$$\begin{aligned}\gamma_{\xi}^a &= \hbar\Gamma \left[\frac{\text{Re}(\Phi)}{Mv_{\xi}} + \text{Im}(\Lambda) \right], & \gamma_{\xi}^{a\dagger} &= \hbar\Gamma \left[\frac{\text{Re}(\Phi)}{Mv_{\xi}} - \text{Im}(\Lambda) \right], \\ \gamma_{\xi}^+ &= \frac{\hbar\Gamma \text{Re}(\Phi)}{Mv_{\xi}}, & \gamma_{\xi}^- &= \hbar^2\Gamma \text{Re}(\Lambda), \\ \Delta &= -\frac{\hbar\Gamma \text{Im}(\Phi)}{Mv_{\xi}}, & \Delta' &= \frac{\hbar\Gamma \text{Im}(\Lambda)}{2}.\end{aligned}\quad (\text{F4})$$

The first line of Eq. (F2) has the structure of the usual Lindblad master equation with damping rates $\gamma_{\xi}^a, \gamma_{\xi}^{a\dagger}$ and damping operators \hat{a}_{ξ} and \hat{a}_{ξ}^{\dagger} , respectively. The second line of Eq. (F2), however, cannot be recasted in either a unitary term like the commutator in the first line or in a dissipative term as the second and third terms of the first line of Eq. (F2). Those two last terms originate from the fact that we did not apply the rotating-wave approximation. The additional Hamiltonian term \hat{H}_{ξ}^{\dagger} is also a consequence of this fact. Now, looking at the structure of the Φ [Eq. (61)] and Λ functions [Eqs. (62) and (64)] and at the fact that we consider a linear Paul trap for which the most relevant coefficients C_n^{ξ} are those for $n = 0, \pm 1$, we see that while $\text{Re}(\Phi^{\text{P}}) = \Phi^{\text{P}}$ has a negligible effect, $\text{Re}(\Phi^{\delta})$ provides a non-negligible effect such that it renders γ_{ξ}^+ nonzero. A similar argument holds for γ_{ξ}^- for which $\text{Re}(\Lambda^{\text{P}})$ yields a significant contribution, but not $\text{Re}(\Lambda^{\delta})$. On the other hand, $\text{Im}(\Phi^{\delta})$ is almost negligible so that $\Delta \simeq 0$, but $\text{Im}(\Lambda^{\delta})$ produces a non-negligible contribution, while $\text{Im}(\Lambda^{\text{P}})$ is negligible, so that Δ' provides an important contribution to the ion dynamics.

In conclusion, the ion master equation like the ones for a neutral impurity in a condensate [47,48,62] cannot be recasted in Lindblad form, unless the counter-rotating terms are neglected. In the future, however, it would be interesting to explore another approach that has been recently proposed [64]. Here, it is shown that one does not need to apply the rotating-wave approximation and, by using another strategy to apply the Markov approximation, it is possible to derive a different Markovian quantum master equation in Lindblad form, but with time-dependent decay operators. The advantage of this approach is that the master equation can be equivalently simulated by a stochastic Schrödinger equation, similarly to the well-known Monte Carlo wave-function approach [65,66]. The reduction from a density matrix to a ket state description, albeit averaging over many quantum trajectories, could be especially useful for simulating the impurity dynamics fully in three dimensions.

APPENDIX G: SELF-CONSISTENCY OF THE MASTER EQUATION

As we already pointed out, the dissipative damping rate must be smaller than the thermal energy and the typical system's transition frequencies. In this case, the dissipative rate in the ξ th direction is proportional to [see also Eq. (F4)]

$$\gamma_{\xi} \sim \Gamma \sum_s |q_{s,\xi}|^3 f(q_{s,\xi})^2 n_{q_{s,\xi}} |F_{s,s}^{\xi}|, \quad (\text{G1})$$

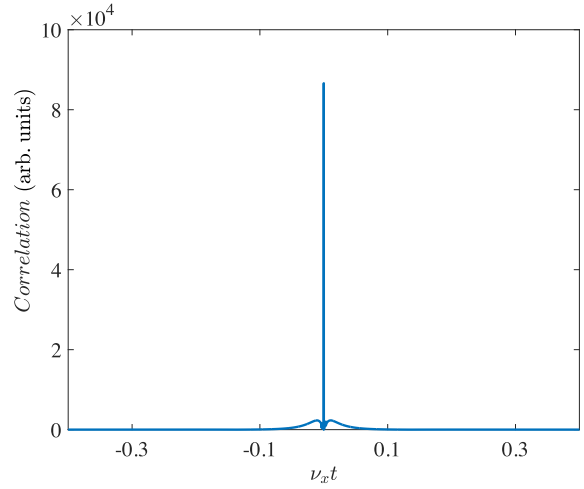


FIG. 11. Example of bath correlation function as evaluated by Eq. (G2) for the x direction.

where we have neglected the contribution of the terms for which $s \neq s'$ since these, on average, vanish due to the fast rf oscillations. The dissipative rate has to satisfy the two conditions $\hbar\gamma_{\xi}/(k_B\mathcal{T}) \ll 1$ and $\gamma_{\xi}/v_{\xi} \ll 1$. For instance, for the $^{23}\text{Na}/^{174}\text{Yb}^+$ pair with a gas temperature of $\mathcal{T} = 200$ nK and trap parameters $a = -0.001$, $q = 0.2$, and $\Omega_{rf} = 2\pi \cdot 2$ MHz we obtain the trap frequencies $\nu_x = 2\pi \cdot 112$ kHz, $\nu_y = 2\pi \cdot 169$ kHz, $\nu_z = 2\pi \cdot 45$ kHz, $k_B\mathcal{T}/\hbar = 2\pi \cdot 4$ kHz, for which the dissipative rate fulfils the above outlined requirements rather well, i.e., the ratios are smaller than 3×10^{-4} for an atomic peak density 10^{14} cm^{-3} . These conclusions can be further corroborated by an evaluation of the bath correlation functions. For example, starting from Eq. (47) and by performing the replacement (50), the first correlation function due to the single sum over \mathbf{q} in the curly brackets is given by



$$\begin{aligned}& \sum_{\mathbf{q}} \Omega_{\mathbf{q}}^2 \sin[\varepsilon(\mathbf{q})\tau/\hbar] q_j q_s \\ & \propto \int_0^{\infty} d\bar{q} \bar{q}^2 \left\{ e^{-\bar{b}\bar{q}} \left[1 + \frac{(\bar{b}^4 - \bar{c}^4)\bar{q}}{4\bar{b}\bar{c}^2} \right] \right. \\ & \quad \left. - e^{-\bar{c}\bar{q}} \right\} \sin(\Xi\bar{q}^2\bar{\tau}),\end{aligned}\quad (\text{G2})$$

where $\Xi = \mu E^*/(m\hbar v_{\xi})$, $\bar{\tau} = v_{\xi}\tau$, and the regularization parameters b, c as well as the wave vector q have been rescaled with respect to R^* and $1/R^*$, respectively. An example of such a correlation function is given in Fig. 11 for the spatial direction x . As it can be seen, the function decays rapidly to zero, i.e., for times larger than, approximately, $0.15/v_x$ it vanishes. Hence, the Markov approximation in our setting is satisfied reasonably well.

- [1] W. Casteels, J. Tempere, and J. Devreese, Polaronic properties of an ion in a bose-einstein condensate in the strong-coupling limit, *J. Low Temp. Phys.* **162**, 266 (2011).
- [2] G. E. Astrakharchik, L. A. P. Ardila, R. Schmidt, K. Jachymski, and A. Negretti, Ionic polaron in a bose-einstein condensate, *Commun. Phys.* **4**, 94 (2021).
- [3] E. R. Christensen, A. Camacho-Guardian, and G. M. Bruun, Charged Polarons and Molecules in a Bose-Einstein Condensate, *Phys. Rev. Lett.* **126**, 243001 (2021).
- [4] U. Bissbort, D. Cocks, A. Negretti, Z. Idziaszek, T. Calarco, F. Schmidt-Kaler, W. Hofstetter, and R. Gerritsma, Emulating Solid-State Physics with a Hybrid System of Ultracold ions and Atoms, *Phys. Rev. Lett.* **111**, 080501 (2013).
- [5] A. B. Michelsen, M. Valiente, N. T. Zinner, and A. Negretti, Ion-induced interactions in a tomonaga-luttinger liquid, *Phys. Rev. B* **100**, 205427 (2019).
- [6] K. Jachymski and A. Negretti, Quantum simulation of extended polaron models using compound atom-ion systems, *Phys. Rev. Research* **2**, 033326 (2020).
- [7] M. Tomza, K. Jachymski, R. Gerritsma, A. Negretti, T. Calarco, Z. Idziaszek, and P. S. Julienne, Cold hybrid ion-atom systems, *Rev. Mod. Phys.* **91**, 035001 (2019).
- [8] R. Côté, Chapter two-ultracold hybrid atom-ion systems, *Adv. At. Mol. Opt. Phys.* **65**, 67 (2016).
- [9] A. Härter and J. Hecker Denschlag, Cold atom-ion experiments in hybrid traps, *Contemp. Phys.* **55**, 33 (2014).
- [10] K. S. Kleinbach, F. Engel, T. Dieterle, R. Löw, T. Pfau, and F. Meinert, Ionic Impurity in a Bose-Einstein Condensate at Submicrokelvin Temperatures, *Phys. Rev. Lett.* **120**, 193401 (2018).
- [11] F. Engel, T. Dieterle, T. Schmid, C. Tomschitz, C. Veit, N. Zuber, R. Löw, T. Pfau, and F. Meinert, Observation of Rydberg Blockade Induced by a Single ion, *Phys. Rev. Lett.* **121**, 193401 (2018).
- [12] T. Feldker, H. Furst, H. Hirzler, N. V. Ewald, M. Mazzanti, D. Wiater, M. Tomza, and R. Gerritsma, Buffer gas cooling of a trapped ion to the quantum regime, *Nat. Phys.* **16**, 413 (2020).
- [13] H. Hirzler, T. Feldker, H. Furst, N. V. Ewald, E. Trimby, R. S. Lous, J. D. Arias Espinoza, M. Mazzanti, J. Joger, and R. Gerritsma, Experimental setup for studying an ultracold mixture of trapped Yb^{+6}Li , *Phys. Rev. A* **102**, 033109 (2020).
- [14] J. Schmidt, P. Weckesser, F. Thielemann, T. Schaetz, and L. Karpa, Optical Traps for Sympathetic Cooling of ions with Ultracold Neutral Atoms, *Phys. Rev. Lett.* **124**, 053402 (2020).
- [15] P. Weckesser, F. Thielemann, D. Wiater, A. Wojciechowska, L. Karpa, K. Jachymski, M. Tomza, T. Walker, and T. Schaetz, Observation of feshbach resonances between a single ion and ultracold atoms, [arXiv:2105.09382](https://arxiv.org/abs/2105.09382).
- [16] T. Dieterle, M. Berngruber, C. Hölzl, R. Löw, K. Jachymski, T. Pfau, and F. Meinert, Transport of a Single Cold ion Immersed in a Bose-Einstein Condensate, *Phys. Rev. Lett.* **126**, 033401 (2021).
- [17] T. Dieterle, M. Berngruber, C. Hölzl, R. Löw, K. Jachymski, T. Pfau, and F. Meinert, Inelastic collision dynamics of a single cold ion immersed in a bose-einstein condensate, *Phys. Rev. A* **102**, 041301(R) (2020).
- [18] D. Leibfried, R. Blatt, C. Monroe, and D. Wineland, Quantum dynamics of single trapped ions, *Rev. Mod. Phys.* **75**, 281 (2003).
- [19] C. Schneider, D. Porras, and T. Schaetz, Experimental quantum simulations of many-body physics with trapped ions, *Rep. Prog. Phys.* **75**, 024401 (2012).
- [20] C. Schneider, M. Enderlein, T. Huber, S. Dürr, and T. Schaetz, Influence of static electric fields on an optical ion trap, *Phys. Rev. A* **85**, 013422 (2012).
- [21] A. Lambrecht, J. Schmidt, P. Weckesser, M. Debatin, L. Karpa, and T. Schaetz, Long lifetimes in optical ion traps, *Nat. Photonics* **11**, 704 (2017).
- [22] H. Hirzler, R. S. Lous, E. Trimby, J. Pérez-Ríos, A. Safavi-Naini, and R. Gerritsma, Observation of chemical reactions between a trapped ion and ultracold feshbach dimers, [arXiv:2110.14475](https://arxiv.org/abs/2110.14475).
- [23] K. Ravi, S. Lee, A. Sharma, G. Werth, and S. Rangwala, Cooling and stabilization by collisions in a mixed ion-atom system, *Nat. Commun.* **3**, 1126 (2012).
- [24] P. Eberle, A. D. Dörfler, C. Von Planta, K. Ravi, and S. Willitsch, A dynamic ion-atom hybrid trap for high-resolution cold-collision studies, *ChemPhysChem* **17**, 3769 (2016).
- [25] A. Krüchow, A. Mohammadi, A. Härter, J. H. Denschlag, J. Pérez-Ríos, and C. H. Greene, Energy Scaling of Cold Atom-Atom-Ion Three-Body Recombination, *Phys. Rev. Lett.* **116**, 193201 (2016).
- [26] Z. Meir, T. Sikorsky, R. Ben-Shlomi, N. Akerman, Y. Dallal, and R. Ozeri, Dynamics of a Ground-State Cooled ion Colliding with Ultracold Atoms, *Phys. Rev. Lett.* **117**, 243401 (2016).
- [27] S. Dutta, R. Sawant, and S. A. Rangwala, Collisional Cooling of Light ions by Cotrapped Heavy Atoms, *Phys. Rev. Lett.* **118**, 113401 (2017).
- [28] P. Wessels, B. Ruff, T. Kroker, A. Kazansky, N. Kabachnik, K. Sengstock, M. Drescher, and J. Simonet, Absolute strong-field ionization probabilities of ultracold rubidium atoms, *Commun. Phys.* **1**, 32 (2018).
- [29] H. N. Le, A. Kalev, M. D. Barrett, and B.-G. Englert, Micromotion in trapped atom-ion systems, *Phys. Rev. A* **85**, 052718 (2012).
- [30] J. Joger, A. Negretti, and R. Gerritsma, Quantum dynamics of an atomic double-well system interacting with a trapped ion, *Phys. Rev. A* **89**, 063621 (2014).
- [31] V. S. Melezhik, Z. Idziaszek, and A. Negretti, Impact of ion motion on atom-ion confinement-induced resonances in hybrid traps, *Phys. Rev. A* **100**, 063406 (2019).
- [32] V. S. Melezhik, Improving efficiency of sympathetic cooling in atom-ion and atom-atom confined collisions, *Phys. Rev. A* **103**, 053109 (2021).
- [33] M. Krych and Z. Idziaszek, Description of ion motion in a paul trap immersed in a cold atomic gas, *Phys. Rev. A* **91**, 023430 (2015).
- [34] We note that for lithium additive and nonadditive interaction coefficients for the three-body Li-Li-Li^+ system have been recently computed [67].
- [35] Z. Idziaszek, T. Calarco, and P. Zoller, Controlled collisions of a single atom and an ion guided by movable trapping potentials, *Phys. Rev. A* **76**, 033409 (2007).
- [36] Z. Idziaszek, A. Simoni, T. Calarco, and P. S. Julienne, Multichannel quantum-defect theory for ultracold atom-ion collisions, *New J. Phys.* **13**, 083005 (2011).
- [37] J. Goold, H. Doerk, Z. Idziaszek, T. Calarco, and T. Busch, Ion-induced density bubble in a strongly correlated one-dimensional gas, *Phys. Rev. A* **81**, 041601(R) (2010).

- [38] J. M. Schurer, P. Schmelcher, and A. Negretti, Ground-state properties of ultracold trapped bosons with an immersed ionic impurity, *Phys. Rev. A* **90**, 033601 (2014).
- [39] J. M. Schurer, A. Negretti, and P. Schmelcher, Capture dynamics of ultracold atoms in the presence of an impurity ion, *New J. Phys.* **17**, 083024 (2015).
- [40] We note that this is a necessary condition, but not yet a sufficient one, as trap-shaped induced resonances can still occur.
- [41] R. Saito, S. Haze, M. Sasakawa, R. Nakai, M. Raoult, H. Da Silva, O. Dulieu, and T. Mukaiyama, Characterization of charge-exchange collisions between ultracold ${}^6\text{Li}$ atoms and ${}^{40}\text{Ca}^+$ ions, *Phys. Rev. A* **95**, 032709 (2017).
- [42] H. A. Furst, N. V. Ewald, T. Secker, J. Joger, T. Feldker, and R. Gerritsma, Prospects of reaching the quantum regime in li-yb + mixtures, *J. Phys. B: At., Mol. Opt. Phys.* **51**, 195001 (2018).
- [43] The relation (2) is obtained easily as follows. Since what matters is the relative atom-ion kinetic energy, the collision energy is thus given by $E_{\text{coll}} = \mu v_{\text{rel}}^2/2 = \mu(\mathbf{v}_a - \mathbf{v}_i)^2/2 = \mu/2(v_i^2 + v_a^2 - 2\mathbf{v}_a \cdot \mathbf{v}_i)$. Here, $v_i \equiv |\mathbf{v}_i|$ ($v_a \equiv |\mathbf{v}_a|$) denotes the magnitude of the ion (atom) velocity. Now, if $v_i \gg v_a$, that is, the atoms are very slow (i.e., ultracold) compared to the ion micro-motion, then $E_{\text{coll}} \simeq \mu v_i^2/2 = \mu E_{\text{kin}}/M$ with $E_{\text{kin}} = M v_i^2/2$.
- [44] H. J. Carmichael, *Statistical Methods in Quantum Optics 1*, Texts and Monographs in Physics (Springer, Berlin, 1999), pp. xxii+361, master equations and Fokker-Planck equations.
- [45] R. Schmidt, J. D. Whalen, R. Ding, F. Camargo, G. Woehl, S. Yoshida, J. Burgdorfer, F. B. Dunning, E. Demler, H. R. Sadeghpour, and T. C. Killian, Theory of excitation of rydberg polarons in an atomic quantum gas, *Phys. Rev. A* **97**, 022707 (2018).
- [46] Y. E. Shchadilova, R. Schmidt, F. Grusdt, and E. Demler, Quantum Dynamics of Ultracold Bose Polarons, *Phys. Rev. Lett.* **117**, 113002 (2016).
- [47] A. J. Daley, P. O. Fedichev, and P. Zoller, Single-atom cooling by superfluid immersion: A nondestructive method for qubits, *Phys. Rev. A* **69**, 022306 (2004).
- [48] R. G. Lena and A. J. Daley, Dissipative dynamics and cooling rates of trapped impurity atoms immersed in a reservoir gas, *Phys. Rev. A* **101**, 033612 (2020).
- [49] M. T. Mitchison, T. H. Johnson, and D. Jaksch, Probing the dynamic structure factor of a neutral fermi superfluid along the bcs-bec crossover using atomic impurity qubits, *Phys. Rev. A* **94**, 063618 (2016).
- [50] For the specific case of the trapped ion, $\hat{H}_S \equiv \hat{H}_I^{\text{trap}}$ with \hat{H}_I^{trap} given in Appendix C 2.
- [51] L is assumed to be much larger than other length scale involved in the system description.
- [52] E. M. Lifshitz and L. P. Pitaevski, *Course of Theoretical Physics*, Vol. 10, Pergamon International Library of Science, Technology, Engineering and Social Studies (Pergamon, Oxford, 1981), pp. xi+452, translated from the Russian by J. B. Sykes and R. N. Franklin.
- [53] G. D. Mahan, *Many-Particle Physics* (Kluwer Academi, New York, 2000).
- [54] S. P. Rath and R. Schmidt, Field-theoretical study of the bose polaron, *Phys. Rev. A* **88**, 053632 (2013).
- [55] Here we neglect the differential operator $\partial_r(r\cdot)_{|r=0}$ since its application to a plane wave has unity effect.
- [56] Y. Castin, Bose-Einstein condensates in atomic gases: Simple theoretical results, in *Coherent Atomic Matter Waves*, edited by R. Kaiser, C. Westbrook, and F. David (Springer, Berlin, 2001), pp. 1–136.
- [57] K. Huang, *Statistical Mechanics*, 2nd ed. (Wiley, New York, 1987), pp. xiv+493.
- [58] Here, $\text{Tr}_R[\tilde{\chi}(t)] = \tilde{\rho}(t)$ and we eliminated the term $\text{Tr}_B\{[\hat{H}_{BS}(t), \tilde{\chi}(0)]\}$ by assuming $\text{Tr}_B\{\hat{H}_{BS}(t)\hat{B}_0\} = 0$ (see Ref. [44] for details).
- [59] H.-P. Breuer and F. Petruccione, *The Theory of Open Quantum Systems* (Oxford University Press, New York, 2002), pp. xxii+625.
- [60] J. Joger, H. Furst, N. Ewald, T. Feldker, M. Tomza, and R. Gerritsma, Observation of collisions between cold li atoms and yb $^+$ ions, *Phys. Rev. A* **96**, 030703(R) (2017).
- [61] We note that the definition of $q_{s,\xi}$ is a mere definition originated by the fact that $q_{s,\xi}^2 = 2m\Omega_{rf}(\beta_\xi/2 + s)/\hbar$ has been introduced when manipulating the exponential and trigonometric functions in the master equation (47). Importantly, $q_{s,\xi}^2$ can assume negative or positive values, upon the sign of $\beta_\xi/2 + s$.
- [62] K. K. Nielsen, L. A. P. Ardila, G. M. Bruun, and T. Pohl, Critical slowdown of non-equilibrium polaron dynamics, *New J. Phys.* **21**, 043014 (2019).
- [63] T. Evans and D. Steer, Wick’s theorem at finite temperature, *Nucl. Phys. B* **474**, 481 (1996).
- [64] F. Nathan and M. S. Rudner, Universal lindblad equation for open quantum systems, *Phys. Rev. B* **102**, 115109 (2020).
- [65] J. Dalibard, Y. Castin, and K. Molmer, Wave-Function Approach to Dissipative Processes in Quantum Optics, *Phys. Rev. Lett.* **68**, 580 (1992).
- [66] K. Molmer, Y. Castin, and J. Dalibard, Monte carlo wave-function method in quantum optics, *J. Opt. Soc. Am. B* **10**, 524 (1993).
- [67] P.-G. Yan, L.-Y. Tang, Z.-C. Yan, and J. F. Babb, Long-range interaction of $\text{Li}(2^2s) - \text{Li}(2^2s) - \text{Li}^+(1^1s)$, *Phys. Rev. A* **101**, 032702 (2020).

Quantum-limited thermometry of a Fermi gas with a charged spin particle

Lorenzo Oghittu  and Antonio Negretti 

Zentrum für Optische Quantentechnologien, Fachbereich Physik, Luruper Chaussee 149, D-22761 Hamburg, Germany



(Received 23 February 2022; accepted 29 March 2022; published 25 April 2022)

We investigate the sensitivity of an ion sensor in determining the temperature of an atomic Fermi gas. Our study extends to charged impurities the proposal by M. T. Mitchison *et al.* [*Phys. Rev. Lett.* **125**, 080402 (2020)], where atomic neutral impurities were used as an *in situ* thermometer of the quantum gas. We find that the long-range character of the atom-ion interaction enhances the thermometer's sensitivity for certain system parameters. In addition, we investigate the impact of the ion quantum motional state on the sensitivity by assuming that it is confined in a harmonic trap. We observe that the temperature sensitivity of the ion is noticeably influenced by its spatial extension, making the latter a versatile tool to be manipulated for improving the thermometer performance. We finally discuss our findings in the context of current experimental atom-ion mixtures.

DOI: [10.1103/PhysRevResearch.4.023069](https://doi.org/10.1103/PhysRevResearch.4.023069)

I. INTRODUCTION

Quantum impurities in a bath such as that provided by ultracold atomic gases is currently a very active field of research owed to the advances and prospects offered by atomic physics laboratories. Indeed, these systems enable with their degree of controllability to investigate various out-of-equilibrium phenomena such as Anderson orthogonality catastrophe [1,2] and the formation of polaronic states [3,4], to mention a few. The former is fundamental for understanding phenomena in the solid-state realm like the Kondo effect [5] and transport of heavy impurities in a Fermi liquid [6], while mediated interactions are important for pairing formation [7–9]. In particular, in recent years, the study of Fermi polarons with neutral impurities in bulk systems has been quite vigorous both experimentally [10–13] and theoretically [14–16]. Albeit not yet mature as the neutral counterpart, an important experimental effort has been undertaken to immerse charged impurities such as ions in quantum gases [17–19]. Sympathetic cooling of ions in a Fermi gas with calcium ions has been experimentally investigated [20], which culminated with the approach of the *s*-wave regime of atom-ion collisions [21,22]. In addition to the aforementioned out-of-equilibrium phenomena, ions in a 1D fermionic bath have been proposed to study induced interactions in a Li-Yb⁺ mixture [23] (see also Ref. [24] for neutral ytterbium impurities), Peierls instability [25], and bipolaron states with low effective mass [26]. Such interesting many-body quantum physics, however, requires a Fermi gas to reach very low temperatures, i.e., on the order of a few percentage of the Fermi temperature. It is therefore crucial to devise experimental schemes to attain those temperatures as well as to determine accurately its uncertainty.

Recently, M. T. Mitchison *et al.* [27] have proposed an interferometric method to probe locally the temperature of a Fermi gas by means of a neutral spin impurity. The method relies on the fact that the Pauli exclusion principle slows the decay of coherence of the spin impurity allowing for enhanced signal-to-noise ratios. Therefore, by tracking the dynamics of the spin impurity and, importantly, without requiring its thermalization, it is possible to estimate the temperature with high accuracy. Here, we extend the method to an ionic impurity probe, whose impurity-gas interaction is longer-ranged compared to the neutral case. We find that the r^{-4} tail of the atom-ion polarization potential has a profound impact on the thermometer sensitivity, quantified by the quantum signal-to-noise ratio \mathcal{Q} , and that for some system parameters, it reaches a larger performance than a neutral probe. We investigate \mathcal{Q} in reliance of the density of the gas, the number of two-body bound states, and finite-width of the ion spatial density, i.e., confinement. The latter is shown to enable to obtain higher signal-to-noise ratios and at shorter times. Let us also note that ions have been already used as probes of the density profile of a condensate [28,29] as well as to trace molecule gases [30] and proposed for measuring density-density correlations [31] and the local single-particle energy distribution of a degenerate Fermi gas [32].

The paper is organized as follows: in Sec. II we describe our system, while in Sec. III, the Cramer-Rao bound together with the interferometric protocol for sensing the gas temperature is summarized. This summary, which is based on the ideas of Ref. [27] together with a few remarks from our side, is provided for the sake of completeness. The results are exposed and discussed in Sec. IV, whereas the experimental applicability of the extended method to the ionic probe is discussed in Sec. V. Finally, in Sec. VI, we recapitulate our findings and provide an outlook for future work.

II. SYSTEM

We consider the system displayed pictorially in Fig. 1. A (trapped) ion (or more), whose wave function is denoted by

Published by the American Physical Society under the terms of the Creative Commons Attribution 4.0 International license. Further distribution of this work must maintain attribution to the author(s) and the published article's title, journal citation, and DOI.

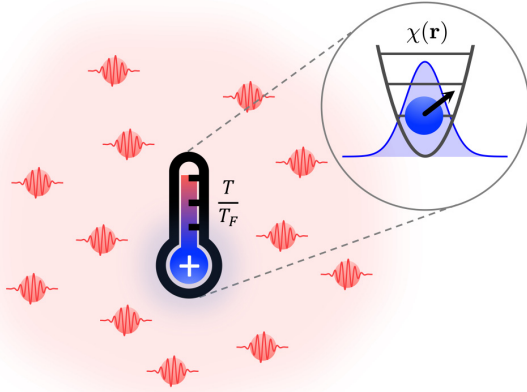


FIG. 1. Schematic of the system: a positively charged ion, immersed in a Fermi gas (red wavy particles), acts as a thermometer for measuring the gas temperature ratio T/T_F . As it is shown in the inset, such an ion is harmonically trapped with Gaussian spatial density $|\chi(\mathbf{r})|^2$ (blue shadowed area), i.e., it is prepared in the ground state, and has a spin degree of freedom denoted pictorially by an arrow.

$\chi(\mathbf{r})$, has two internal states $|0\rangle$ and $|1\rangle$. The ion is immersed in a homogeneous spin-polarized noninteracting Fermi gas (henceforth also referred to as bath) of mean density \bar{n} . The gas density defines the following bath characteristics: the Fermi wave vector $k_F = (6\pi\bar{n})^{1/3}$, the energy (or temperature) $E_F = \hbar^2 k_F^2 / 2m = k_B T_F$, and the time $\tau_F = \hbar / E_F$. Here, k_B is the Boltzmann constant and m the mass of the atom. In the case of a neutral impurity probe [27], one can assume that the impurity internal state $|0\rangle$ does not interact with the bath, while the state $|1\rangle$ interacts via a short-range impurity-bath pseudopotential. This is legitimate, because one can tune the impurity-bath interaction such that the scattering length vanishes, thereby resulting effectively in a vanished potential.¹ In the present setting, however, the electric field of the ion polarizes the neighbourhood independently of the atom-ion scattering length such that the r^{-4} tail of the spin-independent polarization potential cannot be set to zero in our model. In other words, this tail is always present, unless the gas density is so low that the interaction can be replaced by a pseudopotential, thus falling back again into the neutral probe scenario. Controlling the atom-ion scattering length and therefore the ion internal state means that we manipulate the short-range part of the potential only (e.g., the number of bound states). Given this, both ion internal states interact (asymptotically) with the bath via the two-body polarization potential

$$V(\mathbf{r}) = -\frac{C_4}{r^4} \quad (1)$$

with $C_4 = \alpha e^2 / 8\pi \epsilon_0$ (in SI units). Here, α is the (static) polarizability of the atom, e is the elementary electronic charge

¹This is permitted because of the separation of length scales involved in the system, that is, the range of the impurity-bath interaction is much smaller than any other length scale.

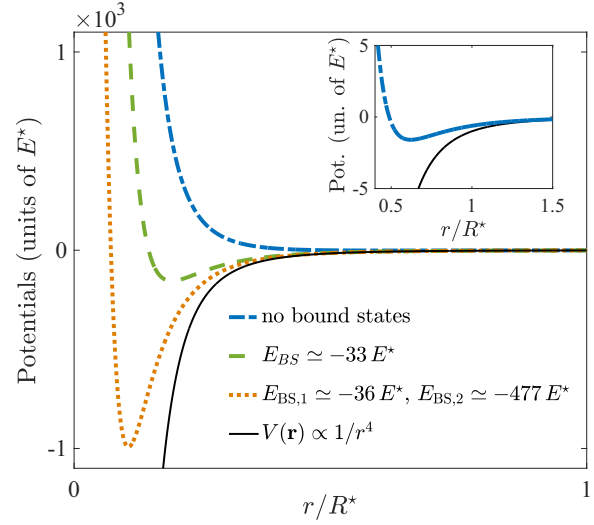


FIG. 2. Regularized atom-ion polarization potentials $V_{\text{reg}}(r)$ corresponding to $a \simeq -R^*$ with three different bound state properties: no bound states in blue dot-dashed, one bound state in green dashed, and two bound states in orange dotted (see legend for bound state energies). Two-body polarization potential (1) in thin black solid. The inset illustrates the r^{-4} tail of the potential without bound states.

(i.e., only singly ionized atoms) and ϵ_0 the vacuum permittivity. We note that recently Feshbach resonances in hybrid atom-ion systems have been observed [22], thus providing the perspective to control (magnetically) the interspecies interactions.

The potential (1) introduces two more length and energy scales: $R^* = (2\mu_{\text{red}} C_4 / \hbar^2)^{1/2}$ and $E^* = \hbar^2 / [2\mu_{\text{red}} (R^*)^2]$ with $\mu_{\text{red}} = mM / (m + M)$ being the reduced atom-ion mass and M is the ion mass. Due to the singularity of Eq. (1) at short range and for the sake of a simpler analytical treatment, we use the regularization [33,34]

$$V_{\text{reg}}^{(s)}(\mathbf{r}) = -C_4 \frac{r^2 - c^2}{r^2 + c^2} \frac{1}{(r^2 + b^2)^2}. \quad (2)$$

An example of the spatial dependence of this potential is shown in Fig. 2. By tuning the parameters b and c one can control the sign and strength of the three-dimensional s -wave atom-ion scattering length a as well as the number of bound states, which can be attained by preparing the ion in specific electronic configurations, i.e., spin state $|s\rangle$, and by controlling external magnetic fields. Towards this end, we employ the strategy already used in Ref. [34], namely, we impose that the scattering length equals in magnitude the scattering amplitude of the regularized potential in Born approximation and that the potential supports a fixed number of bound states (one or two). For the case without bound states, we just seek for parameters that generate a potential without bound states, but that yield a certain value of the scattering length.

For the purpose of thermometry, we are interested mainly in the dynamics of the ion's internal degrees of freedom, since these two states are utilized to read out the gas temperature and its uncertainty, while the motional degrees of freedom

affect the ion-gas interaction, as we shall see later. Hence, the ionic probe internal state Hamiltonian reads as²

$$\hat{H}_P = E_0|0\rangle\langle 0| + E_1|1\rangle\langle 1|. \quad (3)$$

On the other hand, the many-body Hamiltonian of the bath is given by

$$\hat{H}_B = \int_{\mathbb{R}^3} d\mathbf{r} \hat{\Psi}^\dagger(\mathbf{r}) \left[-\frac{\hbar^2}{2m} \nabla^2 + V_{\text{ext}}(\mathbf{r}) \right] \hat{\Psi}(\mathbf{r}), \quad (4)$$

where $V_{\text{ext}}(\mathbf{r})$ denotes the external trap potential, $\hat{\Psi}$ is the fermionic antisymmetric field operator satisfying the anti-commutation rule $\{\hat{\Psi}(\mathbf{r}), \hat{\Psi}^\dagger(\mathbf{r}')\} = \delta(\mathbf{r} - \mathbf{r}')$. The (many-body) interaction between the ion and the quantum gas is described by the Hamiltonian

$$\hat{H}_I = \sum_{s=0,1} \int_{\mathbb{R}^3} d\mathbf{r} \hat{\Psi}^\dagger(\mathbf{r}) V_{\text{reg}}^{(s)}(\mathbf{r}) \hat{\Psi}(\mathbf{r}) \otimes |s\rangle\langle s|, \quad (5)$$

where $V_{\text{reg}}^{(s)}$ relies on the ion internal state via the short-range physics we discussed earlier, namely, by tuning the atom-ion scattering length with different choices of the parameters b and c . Moreover, we note that $[\hat{H}_P, \hat{H}_I] = 0$.

The ion spin dynamics can be described by a single time-dependent function, as we show in some detail in Appendix A. Specifically, the ion Bloch vector \mathbf{v} , whose density matrix is $\hat{\rho}_P = \frac{1}{2}(\mathbb{I} + \mathbf{v} \cdot \hat{\boldsymbol{\sigma}})$, is given by³

$$\mathbf{v}(t) \equiv (v_x, v_y, v_z) = (\text{Re}[v(t)], \text{Im}[v(t)], 0), \quad (6)$$

where the so-called time-dependent decoherence function is defined as

$$v(t) = \text{Tr}_B [e^{i\hat{H}_I t/\hbar} e^{-i\hat{H}_0 t/\hbar} \hat{\rho}_B(T)] \quad (7)$$

with $\hat{H}_s = \langle s | \hat{H}_B + \hat{H}_I | s \rangle$, $s = 0, 1$, $\hat{\rho}_B(T)$ the thermal state at temperature T of the bath, and $\hat{\boldsymbol{\sigma}} = (\hat{\sigma}_x, \hat{\sigma}_y, \hat{\sigma}_z)$ the vector of Pauli matrices. We note that since the z component of the Bloch vector is zero [see Eq. (6)], the populations of the states $|0\rangle$ and $|1\rangle$ are conserved in time and equal to $1/2$, while the coherences evolve accordingly to Eq. (7) (pure dephasing). Notwithstanding, when $\pi/2$ pulses are applied to ion internal state prior and after the impurity and the bath interact, as we shall discuss in the interferometric protocol of Sec. III, $v_z(t)$ relies on $v(t)$.

By means of the well-known Levitov formula [35,36], the decoherence function can be computed exactly via the

²We note that we do not include the motional part of the ion, i.e., its (spin-independent) Hamiltonian in the trap, as we consider it as a static impurity, namely, a mere scattering center for the bath. Even in the nonstatic approximation, however, this Hamiltonian, being spin-independent, would simply add a global phase that can be removed by moving the system description in the interaction picture. We can thus safely ignore it.

³Here, we implicitly assume that the ion internal state lies in the equatorial plane as shown in Fig. 3 (see protocol in Sec. III). Let us also note that the populations of the eigenstates of $\hat{\sigma}_x$ are conserved as a consequence of $[\hat{H}_P, \hat{H}_I] = 0$.

formula⁴

$$v(t) = \det[1 - \hat{n} + \hat{n} e^{i\hat{H}_0 t/\hbar} e^{-i\hat{H}_I t/\hbar}], \quad (8)$$

where $\hat{n} = (e^{\beta(\hat{H}_B - \mu)} + 1)^{-1}$ is the Fermi distribution, μ denotes the chemical potential, $\beta = (k_B T)^{-1}$, and

$$\begin{aligned} \hat{h}_B &= -\frac{\hbar^2}{2m} \nabla^2 + V_{\text{ext}}(\mathbf{r}), \\ \hat{h}_\alpha &= \hat{h}_B + V_{\text{eff}}^{(s)}(\mathbf{r}) \text{ with } s = 0, 1. \end{aligned} \quad (9)$$

In our setting, the Fermi gas is homogeneous and as a consequence $V_{\text{ext}} = 0$. The effective impurity-gas interaction is given by

$$V_{\text{eff}}^{(s)}(\mathbf{r}) = \int d\mathbf{r}' V_{\text{reg}}^{(s)}(\mathbf{r} - \mathbf{r}') |\chi(\mathbf{r}')|^2. \quad (10)$$

Here, the reliance of $V_{\text{reg}}^{(s)}$ on the ion internal state $|s\rangle$ highlights the fact that we can associate to it two scattering lengths for different pairs (b, c) . As it can be seen, the ion motional state $\chi(\mathbf{r}')$ determines the shape of the effective interaction (see also Fig. 9 in Sec. IV B). In the following sections we shall consider two different forms of the ionic probe's probability density $|\chi(\mathbf{r})|^2$. Firstly, we shall treat the ion as a static point particle and set $|\chi(\mathbf{r})|^2 = \delta(\mathbf{r})$ or, in spherical coordinates

$$|\chi(\mathbf{r})|^2 = \frac{1}{4\pi r^2} \delta(r). \quad (11)$$

Secondly, we shall replace the point-like distribution of Eq. (11) with a finite-width Gaussian, that is, $\delta(r) \mapsto \Delta_\sigma(r) = \exp[-r^2/(2\sigma^2)]/\sqrt{2\pi\sigma^2}$. In the limit $\sigma \rightarrow 0$, we retrieve Eq. (11) for which $V_{\text{eff}}^{(s)}(\mathbf{r}) = V_{\text{reg}}^{(s)}(\mathbf{r})$. We make use of a Gaussian spatial density as it represents the ground state of an ion in a Paul trap [37] (i.e., secular approximation) as well as the one in an optical trap [38].

III. THERMOMETRY WITH A SPIN IMPURITY

In this section, we recap the key aspects of the interferometric protocol proposed in Ref. [27]. For more details, however, we refer to that paper.

Quantum Cramer-Rao bound. In order to motivate the protocol discussed below, it is necessary to resort to the theory of quantum parameter estimation [39–42]. Let us start by invoking the so-called quantum Cramer-Rao bound (QCRB). This provides a bound (from below) on the attainable uncertainty ΔT for the estimation of the temperature of the gas after N independent realizations, i.e., measurements, according to $\Delta T^2 \geq 1/N \mathcal{F}_T \geq 1/N \mathcal{F}_T^Q$, which is valid for any unbiased estimator [43]. Note, however, that the first inequality, i.e. $\Delta T^2 \geq 1/(N \mathcal{F}_T)$, is reached for $N \gg 1$ within the maximum likelihood estimation procedure [44]. Here, \mathcal{F}_T is the (classical) Fisher information [44]

$$\mathcal{F}_T \equiv \mathcal{F}_T(\hat{X}) = - \sum_{s=\pm} p(x_s|T) \frac{\partial^2}{\partial T^2} \ln[p(x_s|T)] \quad (12)$$

⁴We note that the Levitov formula can be applied to quadratic and time-independent Hamiltonians only.

with \hat{X} being any hermitian operator (i.e., observable), whereas $p(x_s|T)$ is the conditional probability to obtain from a measurement the outcome x_s , i.e., an eigenvalue of \hat{X} , given the gas temperature T . Let us underscore that the probability $p(x_s|T)$ results from measurements described by projections (or more generally by positive operator-valued measurement operators) on the corresponding eigenspaces of \hat{X} . Furthermore, since we consider a two-level system, not more than two outcomes, i.e., eigenvalues of \hat{X} , are possible. Given this, \mathcal{F}_T is related to its quantum counterpart \mathcal{F}_T^Q by the identity $\mathcal{F}_T^Q = \max_{\hat{X}} \mathcal{F}_T(\hat{X})$ with $\mathcal{F}_T(\hat{X})$ as in Eq. (12).⁵ It turns out that $\mathcal{F}_T^Q = \mathcal{F}_T(\hat{\Lambda}_T)$ with $\hat{\Lambda}_T$ being the symmetric logarithmic derivative operator (SLD) [39]

$$\hat{\Lambda}_T \propto \cos(\varphi)\hat{\sigma}_{\parallel} + \sin(\varphi)\hat{\sigma}_{\perp}, \quad \tan(\varphi) = \frac{|\nu|(1-|\nu|)^2\partial_T\phi}{\partial_T|\nu|}. \quad (13)$$

Here, $\hat{\sigma}_{\parallel} = \cos(\phi)\hat{\sigma}_x + \sin(\phi)\hat{\sigma}_y$, $\hat{\sigma}_{\perp} = \cos(\phi)\hat{\sigma}_y - \sin(\phi)\hat{\sigma}_x$ and $\nu = |\nu|e^{i\phi}$. In other words, the Fisher information retained in the projective measure of $\hat{\Lambda}_T$ on a two-level system is higher or equal than in the measurement of any other observable, and it equals the quantum Fisher information. It is for this reason that the protocol outlined below aims at measuring the observable represented by the symmetric logarithmic derivative and inferring the temperature and its uncertainty from it.

Before explaining the protocol, let us briefly discuss the estimation of the relative error on the measure of T . The quantum signal-to-noise ratio (QSNR) \mathcal{Q} is defined via the quantum Fisher information by $\mathcal{Q}^2 = T^2\mathcal{F}_T^Q$ and satisfies the following inequality:

$$\frac{\Delta T}{T} \geq \frac{1}{\mathcal{Q}\sqrt{N}}, \quad (14)$$

which gives a lower limit of the attainable temperature uncertainty.

In the case of a two-level system, \mathcal{F}_T^Q can be expressed in terms of the decoherence function $\nu(t)$ [45]. In polar coordinates, it reads

$$\mathcal{F}_T^Q = \frac{1}{1-|\nu|^2} \left(\frac{\partial|\nu|}{\partial T} \right)^2 + |\nu|^2 \left(\frac{\partial\phi}{\partial T} \right)^2 = \mathcal{F}_T^{\parallel} + \mathcal{F}_T^{\perp}. \quad (15)$$

Here, $\mathcal{F}_T^{\parallel}$ and \mathcal{F}_T^{\perp} denote the contributions parallel and perpendicular to the Bloch vector, namely, they correspond to the measurement of $\hat{\sigma}_{\parallel}$ and $\hat{\sigma}_{\perp}$, respectively. More precisely, it means that if we would perform a projective measurement of

⁵Here, the notation is rather compact. More precisely, we mean the following: first, one needs to diagonalize the operator \hat{X} , whose eigenvectors are $|x_s\rangle$. Thus the projection operators $\hat{P}_s = |x_s\rangle\langle x_s|$ are defined. This is carried out for any observable \hat{X} . The Fisher information is then defined as a function of the set $\{\hat{P}_s\}$. Thus the maximum over such a set for any \hat{X} is sought. We note that one could also look for the optimal probe state, $\hat{\rho}_p$, for a certain measurement, and therefore ask how the probe has to be prepared to attain the minimal uncertainty. Here, however, the state of the probe is determined by the interaction with the gas.

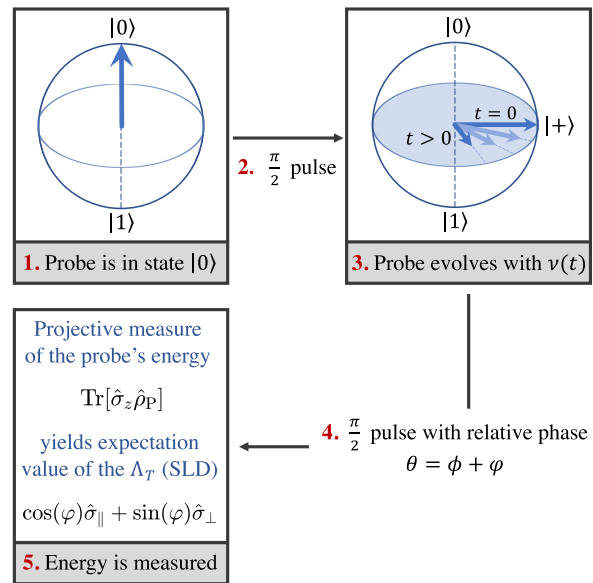


FIG. 3. Schematic of the interferometric protocol with its five steps that allow to determine the expectation value of the SLD. The SLD is the estimator of the temperature that maximizes the quantum Fisher information.

the SLD in the eigenbasis of either $\hat{\sigma}_{\parallel}$ or $\hat{\sigma}_{\perp}$ we would obtain a Fisher information via the respective conditional probabilities $p(\Lambda_s^{\parallel,\perp}|T)$ of measuring the outcome $\Lambda_s^{\parallel,\perp}$ in one of the two eigenbasis given by either $\mathcal{F}_T^{\parallel}$ or \mathcal{F}_T^{\perp} . We note, however, that measuring the probe in those two eigenbasis implies that the gas temperature has to be known *a priori*, since the eigenvectors of $\hat{\sigma}_{\parallel}$ and $\hat{\sigma}_{\perp}$ depend on both angles ϕ and φ . In other words, one would need to set the measurement apparatus upon the gas temperature itself, which is our unknown. We shall come back to this point in the following paragraph.

Protocol. Let us describe briefly the main steps of the protocol sketched in Fig. 3 in order to determine the expectation value of the SLD-operator. The atomic probe is initially prepared in the state $|0\rangle$. Therefore the initial total density matrix is defined as: $\hat{\rho} = |0\rangle\langle 0| \otimes \hat{\rho}_B(T)$. After a $\pi/2$ -pulse, which takes the impurity-probe to the state $|+\rangle = (|0\rangle + |1\rangle)/\sqrt{2}$, the system evolves for a time t according to Eq. (6) with decoherence function given by Eq. (8). Then, a second $\pi/2$ -pulse is performed with a certain phase θ and the energy is projectively measured. This kind of measurement yields an expectation value of the energy proportional to $\cos(\theta)\langle\hat{\sigma}_x\rangle + \sin(\theta)\langle\hat{\sigma}_y\rangle$. Accordingly to Eq. (13) as well as the definitions of $\hat{\sigma}_{\parallel}$ and $\hat{\sigma}_{\perp}$, one can determine $\langle\hat{\Lambda}_T\rangle$ by choosing $\theta = \phi + \varphi$. We repeat this procedure until the desired precision is reached. The number N of independent repetitions realizes a measurement of the gas temperature with an error bounded from below by the right-hand-side of Eq. (14). In Appendix A, we provide some details on the aforementioned sequence of pulses.

A few comments are in order now. First, measuring the energy is an experimentally more feasible task than performing a measurement in the eigenbasis of $\hat{\sigma}_{\parallel}$ and $\hat{\sigma}_{\perp}$, which in addition rely on the unknown T . Second, the procedure

outlined above is referred to estimation from the first moment in parameter estimation theory. Indeed, we estimate the gas temperature by measuring the expectation value of the SLD, i.e., the energy. Of course, the value of the phase θ depends on the gas temperature, but one would perform several repetitions of the procedure by varying θ in the Ramsey interferometer sequence. By assessing the Fisher information (12) for various θ , its maximum is reached for the actual gas temperature, i.e., our best estimation of T . Third, the corresponding uncertainty is given by $\Delta T = \Delta E (\partial \langle E \rangle / \partial T)^{-1}$ with ΔE^2 being the variance of the energy. It can be shown that $\Delta T = 1/\sqrt{\mathcal{F}_T}$ [44]. The standard deviation on the mean of the estimation is then given by $\Delta T/\sqrt{N}$, that is, the right-hand side of Eq. (14). A crucial element of this discussion, however, is the determination of the conditional probability $p(\lambda_s|T)$ with λ_s being the eigenvalues of $\hat{\Lambda}_T$ and $s = \pm$. We shall come back to this point in Sec. V.

Finally, let us discuss the preparation of the initial product state $\hat{\rho} = |0\rangle\langle 0| \otimes \hat{\rho}_B(T)$ that it is an assumption of the interferometric protocol, which is not so easily realizable as for a neutral impurity by tuning the impurity-bath interaction to zero, as we discussed at the beginning of Sec. II. Towards this aim, we propose three solutions, the third one of which is outlined in more detail in the next paragraph. In the first solution, we assume that the impurity is initially neutral and prepared in the internal state $|0\rangle$, whose interaction with the bath is tuned to zero by means of Feshbach resonances like in the original proposal of Ref. [27]. Then, with a two-photon process as the one utilized in Ref. [46], the ion is created and instantaneously (with respect to the system dynamics) its internal state is brought in the equatorial plane of the Bloch sphere and interactions with the gas take place upon the ion internal state. An alternative second solution relies on the utilization of Rydberg dressing of the atomic bath as suggested in Ref. [47]. More precisely, the ion is located at μm distances from the bath in order to ensure no interaction between it and the bath. Thus the atoms in the bath are slightly coupled to Rydberg state in order to enhance the spatial range of the atom-ion interaction via the increase of the atomic polarizability of the bath. At this stage, the equal superposition state of the ion internal states can be prepared. This solution, however, loses the *in situ* character of the protocol, since the ion is positioned at a certain distance from the gas.

Setup for a single internal state. We propose another solution for preparing the initial state $\hat{\rho} = |0\rangle\langle 0| \otimes \hat{\rho}_B(T)$ that is particularly suitable if we aim at using only one ion internal state interacting with the gas. This solution mimics the case of the neutral impurity, where the interaction with the internal state $|0\rangle$ and the fermions is tuned to zero. Indeed, as we shall see in Sec. IV, the use of a single internal state enables to attain an even higher sensitivity of the thermometer.

Specifically, the previously discussed interferometric protocol cannot be employed exactly in the same way, since the two-level system is reduced to a single internal state. To overcome this, we suggest to map the two-level system into the setup displayed in Fig. 4, where the states $|0\rangle$, $|1\rangle$ are replaced by the left and right wave functions $\psi_L(x)$ and $\psi_R(x)$ of the ion in a double-well potential. Only the right well is immersed in the gas, letting the ion in state $\psi_L(x)$ to evolve freely without interaction with the gas. When the barrier is

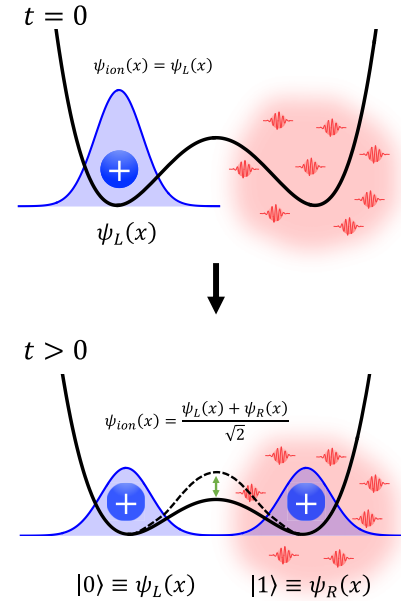


FIG. 4. Setup for a single internal state. Initially the ion is prepared in one of the two internal states, but the two-level system of the interferometric protocol is now represented by the ground states $\psi_L(x)$ and $\psi_R(x)$ of a double well potential. At $t = 0$, the ion is prepared in the left well such that it does not interact in the bath. At $t > 0$, the barrier is lowered such that tunneling takes place and the ion is prepared in an equal superposition state of the left and right states. In this way, the ion's wave-function component in the $\psi_R(x)$ state interacts with the bath and probing of its temperature can take place.

lowered, due to the tunneling effect, the ion occupies the right well and at a precise time its state is described by an equal superposition of $\psi_L(x)$ and $\psi_R(x)$, thus mimicking a $\pi/2$ -pulse. Immediately after that time, the barrier is raised again in order to suppress tunneling and let the ion to probe the Fermi gas. When the QSNR maximum is attained, as we shall discuss in Sec. IV, a second $\pi/2$ pulse is applied, namely, the barrier is lowered again to allow tunneling and thus to move the ion back to the left well. In such a way, the previous interferometric protocol can be still applied, albeit with different type of measurements.

Let us remark that Ramsey interferometry with motional states of an atom in an optical lattice has been experimentally realized [48] (also with the ground and first excited state of a quasi-1D condensate [49]). Additionally, the dynamics of Coulomb crystals in a double well potential has been theoretically investigated [50,51], while state-dependent optical potentials for trapped ions have been recently demonstrated in the laboratory [52]. The latter paves the way to engineer state-dependent potentials such as those created by microwave fields in atom chips [53,54]. These studies together with the possibility to employ optimal control methods [55] for steering the impurity dynamics appropriately corroborate the feasibility of the suggested scheme.

Decoherence and precision. To broadly understand how the thermometric precision can be affected by the parameters, we summarize some aspects of the decoherence dynamics. At short times, the decay of $|\nu|$ is due to collective excitations of the Fermi sea and the decoherence dynamics is essentially unaffected by the temperature. At large times, the dynamics is governed by low-energy excitations with temperature-dependent distribution and $|\nu|$ decays exponentially with rates depending on T [15]. It is intuitively clear that the probing time should be large enough in order to probe the gas temperature. According to Eq. (15), however, high precision is achieved for large values of the derivative of $|\nu|$ with respect to T . Nonetheless, being the decay exponential at large times, it implies that long probing times decrease the quantum signal-to-noise ratio. For the same reason, a choice of the parameters that enhances the decoherence in the temperature-independent regime would result in less precise measurements. On this regard, we shall see in Sec. IV A how the effective interaction (10) affects the dependence on $k_F a$ of the maximum of Q over time.

IV. RESULTS

To begin with, let us first provide a few pieces of information on the results we are going to discuss that will be helpful for the subsequent analyses. Our investigations will mostly focus on the case for which the ion is prepared only in one of the two internal states, since we aim at demonstrating the impact of the long-ranged atom-ion potential on the thermometer sensitivity (in Sec. III an alternative interferometric protocol is suggested). In order to apply the protocol discussed in Sec. III, however, we shall provide our findings corresponding to the scenario for which the ionic impurity is prepared in a superposition of the two internal states as well, where both states interact with the gas. Hence, unless explicitly indicated, the interaction parameter $k_F a$ refers to the case with the single interacting state $|s\rangle$ with $s = 0$ or 1 and the atom-ion scattering length is assumed to be $a \simeq -R^*$.⁶ We shall explore different scenarios of the regularized atom-ion polarization potential (also shown in Fig. 2), for which the absence or presence of one or more bound states is assumed. This will enable us to investigate the impact of bound states on the dynamics of the probe and, most importantly, on the precision of the temperature estimation. Let us remark that the choice of a negative scattering length motivates the scenario without bound states. In fact, a negative scattering length implies that the corresponding state is deeply bound and that it has a rather small size. Hence, if recombination timescales are long enough, it is unlikely that such states are populated. We note that in a different context than ours, precisely in this regime of interactions and time scales phenomena such as attractive polarons have been predicted [56]. We shall turn back to this matter in Sec. V.

As far as the interaction parameter $k_F a$ is concerned, we note that, differently from the neutral impurity case where the s -wave scattering length is the only parameter character-

TABLE I. Most relevant physical quantities for some atom-ion species: $k_F = 0.5/R^*$ (top row) and $k_F = 1.5/R^*$ (bottom row).

Atom - ion (R^* (nm))	Mean density (cm^{-3})	τ_F (μs)	T_F (μK)
${}^6\text{Li}-{}^{174}\text{Yb}^+$ (69.77)	6.2×10^{12}	3.7	2.07
	1.7×10^{14}	0.41	18.64
${}^{40}\text{K}-{}^{174}\text{Yb}^+$ (219.24)	2.0×10^{11}	240	0.032
	5.4×10^{12}	26	0.29
${}^{40}\text{K}-{}^{40}\text{Ca}^+$ (171.92)	4.15×10^{11}	145	0.053
	1.1×10^{13}	16	0.47

izing the two-body interaction, for the long-ranged atom-ion polarization potential the reliance of $k_F a$ on the scattering length is less trivial. Indeed, its typical length scale R^* is comparable to the mean interparticle distance and the system properties depend not only on a and the effective range of the two-body potential, but also rely on the presence of the long-range tail of the interaction. Hence, while in the neutral case a specific choice of the product $k_F a$ can be obtained for a fixed gas density by a single value of the scattering length, in the atom-ion scenario the same value of the scattering length can result in different two-body potentials leading to different system properties.

In Table I, we report the Fermi time and temperature for different atom-ion pairs for two values of the interaction parameter $k_F = 0.5/R^*$ and $1.5/R^*$, from which we obtain the corresponding gas densities.⁷

A. Static ion approximation

We shall first consider the case with zero bound states (dot-dashed line in Fig. 2). This will allow us for a direct comparison with the pseudopotential for neutral atoms and thus highlight the effect of the long-range character of the polarization potential more clearly. For the same reason, we shall first consider the case for which the ion probe is localized at $r = 0$ with $|\chi(\mathbf{r})|^2 = \delta(\mathbf{r})$. Note that this is how the static ion approximation has to be intended and it is achieved either by confining the ion in a very tight trap or by considering the mass of the ion to be much larger than the mass of the atoms in the gas, i.e., infinite mass limit. To compare directly with the neutral impurity case, our analysis begins with the case where only one of the two internal states interacts with the bath. The parameters for this regularized potential are $b \simeq 0.0023 R^*$ and $c \simeq 0.4878 R^*$ that correspond to $a \simeq -R^*$.⁸ We finally

⁷As it can be seen, there is a rather large variation of the two time and energy scales for three exemplary atom-ion pairs. In particular, the Fermi temperature for the pair ${}^6\text{Li}-{}^{174}\text{Yb}^+$ is the largest, reflecting the fact that a lighter atom with a heavy ion are also easier to cool down to the s -wave collisional regime, while for the pair ${}^{40}\text{K}-{}^{174}\text{Yb}^+$ with the largest R^* (due to the larger atomic polarizability) it is more challenging to attain the quantum degeneracy. Furthermore, larger gas densities reduce the coherence time τ_F which has the smallest value for lighter atoms, that is, for the atom-ion pair ${}^6\text{Li}-{}^{174}\text{Yb}^+$.

⁸In presence of two-body bound states, the parameters of the regularized atom-ion polarization potential assume the following values: $b \simeq 0.07018 R^*$ and $c \simeq 0.1455 R^*$ for one supported bound state, whereas $b \simeq 0.09 R^*$ and $c \simeq 0.0718 R^*$ for two bound states.

⁶The choice of a negative scattering length is motivated by recent experimental investigations [21,22].

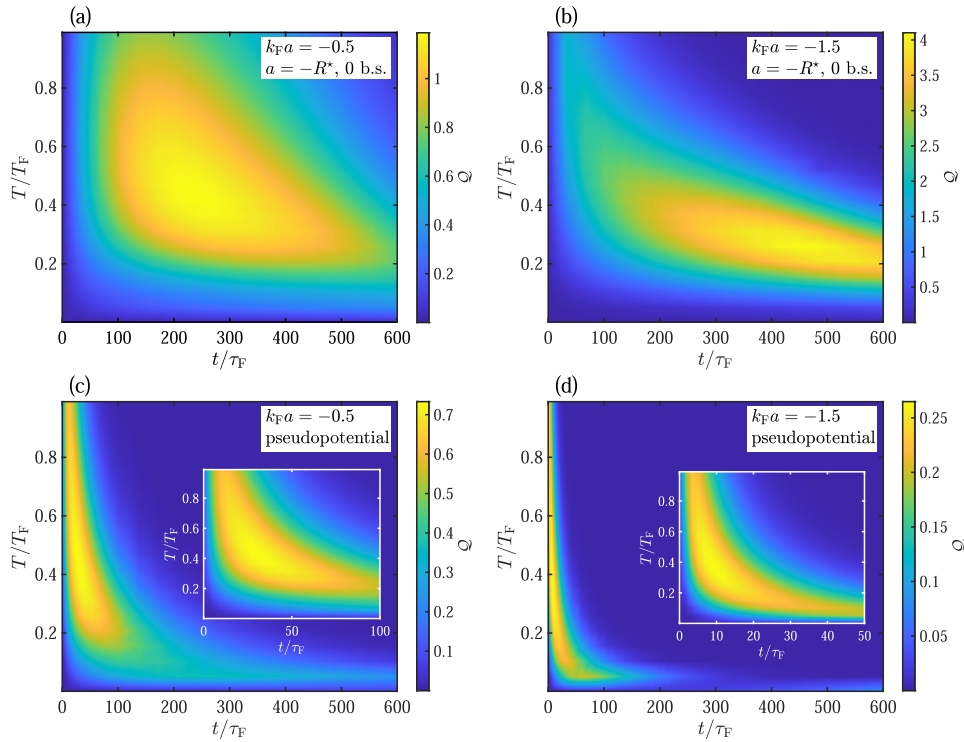


FIG. 5. Quantum signal-to-noise ratio for $k_F a = -0.5$ and -1.5 in the static impurity approximation. (a) and (b) for an ion with an atom-ion polarization potential without bound states, whereas (c) and (d) for a neutral impurity with impurity-bath interaction given by the pseudopotential.

remark that the QSNR is calculated via the relation $\mathcal{Q}^2 = T^2 \mathcal{F}_T^{\mathcal{Q}}$, where the quantum Fisher information is obtained from Eq. (15).

Temperature and time dependence of QSNR. We consider $k_F a = -0.5$ and -1.5 in the case with one internal state and we start by analyzing the temperature and time dependence of the quantum signal-to-noise ratio. These two choices result in values of the mean density and Fermi time of typical quantum gas experiments (see also Table I). As we can observe in Fig. 5, the temperature dependence is only slightly affected by the two different types of potentials (atom-ion polarization interaction vs. pseudopotential) for both of the two values of the interaction parameter. Indeed, the yellow (i.e., bright) region corresponding to the maximum of \mathcal{Q} appears roughly in the same range of the Fermi temperature ratio [~ 0.4 , see panels (a) and (b) versus panels (c) and (d)]. The time dependence of \mathcal{Q} for the two $k_F a$, however, is significantly modified: the region of highest precision, i.e., higher \mathcal{Q} , it is extended to longer probing times for a charged impurity [panels (a) and (b)], while it occurs at earlier times and for a smaller time window for the case of a neutral impurity [panels (c) and (d)]. This behavior suggests that V_{reg} suppresses the decay of $|\nu|$, as it also clearly showed in Fig. 6. Moreover, the shift of the yellow region to longer times also suggests that the potential takes more time to bring the system in the regime where the dynamics is governed by particlelike excitation, which are more sensitive to the gas temperature. Concerning that point,

Fig. 6 shows clearly that the long time behavior of the decoherence function is more affected by the gas temperature as well as that the larger the temperature, the stronger the effect

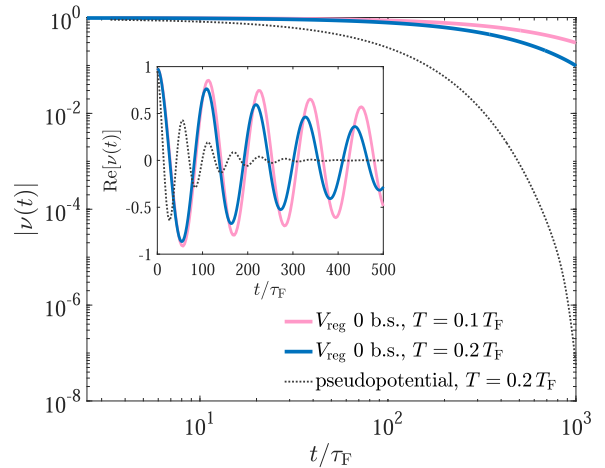


FIG. 6. Decoherence function for $k_F a = -0.5$ for a static impurity. Solid line for the atom-ion polarization potential without bound states and two different temperatures (see legend), while the dotted line for the pseudopotential. In the main panel, the time dependence of $|\nu(t)|$ is shown, while in the inset its real part is displayed.

on the decoherence function. As a consequence, it results in a better temperature probe at long times.

Finally, Fig. 5 shows that the use of an ion probe is more favorable in some circumstances. Indeed, in the case of low densities [panels (a) and (c)], i.e., small $|k_F|$, a limited gain in the thermometer sensitivity can be obtained, but for longer interrogation times. On the other hand, at large values of $|k_F a|$ [panels (b) and (d)], that is, high gas densities, i.e. large $|k_F|$ for the polarization potential, the use of an ion instead of a neutral impurity particle significantly enhances \mathcal{Q} (up to 5 times more at the maximum), and therefore the temperature sensor accuracy, in a large part of the considered time range. Hence, such findings demonstrate that using ionic impurities for sensing the temperature of a Fermi gas result in a superior thermometer performance.

Interaction dependence of the maximal QSNR at fixed T.— At fixed $T = 0.2 T_F$, Fig. 7(a) shows that the monotonous behavior of $\mathcal{Q}_{\max} = \max_t \{Q(t)\}$ in the case of the neutral impurity (grey asterisks) is not reproduced with the ion, where instead a peak appears (blue diamonds). In order to understand the onset of the latter, one can observe that the two potentials give a similar dependence on $k_F a$ in the extremal regions of the considered range of Fig. 7 (i.e., small and large magnitudes of $|k_F a|$). Indeed, the dependence on $k_F a$ can be mapped to a dependence on the mean interparticle distance of the bath particles $\bar{d} = (\bar{n})^{-1/3} \propto 1/|k_F a|$.⁹ When \bar{d} is sufficiently large, i.e., $\bar{d} \gtrsim 8 R^*$ corresponding to $k_F a \gtrsim -0.5$ and small densities, the two potentials give similar results. In this regime, the rate of collisions affecting the ionic probe is small and the decoherence function $\nu(t)$ decays slowly compared to τ_F (see also Fig. 6). This allows the ion to probe the bath for a longer time, thus resulting in increasing \mathcal{Q}_{\max} values for decreasing values of $|k_F a|$. On the contrary at large densities, i.e., $\bar{d} \lesssim R^*$ and $k_F a \lesssim -4$, the rate of collisions between the particles of the bath and the strongly repulsive core of the potential is higher. Both with the regularized pseudopotential and V_{reg} , when $|k_F a|$ increases, the decoherence function $\nu(t)$ decays more rapidly (not shown) and the values reached by \mathcal{Q}_{\max} are lower.¹⁰ When the probe is an ion, an intermediate regime can be identified where the balance between interactions with the repulsive core and the attractive well of V_{reg} strongly suppresses the decay of $\nu(t)$, and therefore allowing to attain much higher values of the quantum signal-to-noise ratio. Besides this, we attribute the enhanced precision to the accumulated phase given by the long-range polarization

⁹Here, the overbar indicates that the length has been rescaled with respect to a .

¹⁰Let us underscore that the interaction parameter $|k_F a|$ has to be interpreted differently for the neutral and charged impurity. Indeed, for the ionic impurity, we keep fixed the scattering length, while we vary the wave vector k_F , i.e., the gas density. Conversely, when the impurity is neutral, although the value of $|k_F a|$ can in principle correspond to any of the possible combinations of the two terms, one has to consider a fixed gas density, and hence k_F , and a varying scattering length. Otherwise, at large magnitudes of the interaction parameter, the applicability of the pseudopotential would be invalidated, as \bar{d} would be comparable or even smaller than the effective range of the van der Waals interaction.

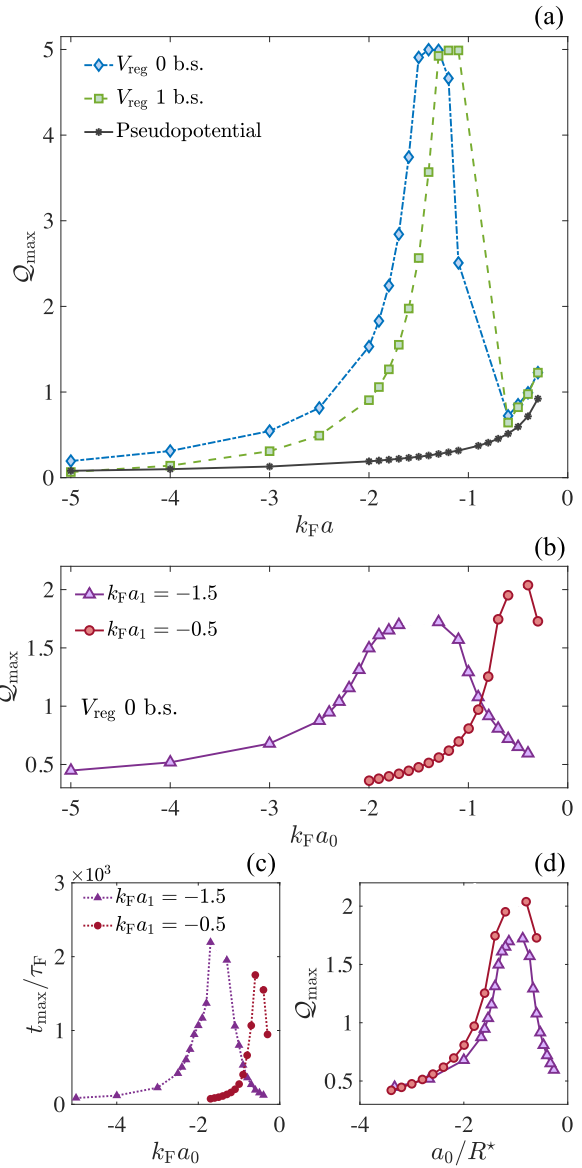


FIG. 7. (a) $\mathcal{Q}_{\max} \equiv \mathcal{Q}(t_{\max})$ for different values of $k_F a$ at $T = 0.2 T_F$ and for an internal ion state only (e.g., the state $|1\rangle$). (b) \mathcal{Q}_{\max} for different values of $k_F a_0$ (i.e., state $|0\rangle$) at $T = 0.2 T_F$ and fixed $k_F a_1 = -1.5 R^*$ (purple triangles) and $k_F a_1 = -0.5 R^*$ (red circles), i.e., state $|1\rangle$. (c) Values of t_{\max} corresponding to (b). (d) Same data of (b) plotted against a_0 . All the lines are merely a guide to the eye. Their discontinuity in (b)–(d) indicates that the thermometer does not work when $k_F a_0 = k_F a_1$ (see text).

potential, i.e., the relative phase proportional to the integral of the atom-ion potential over the density perturbations of the bath because of the presence of the impurity. Since the atom-ion potential is long-range, it will collect more of those perturbations. However, as in the case of low densities, a large \mathcal{Q} requires a long probing time which could affect the effectiveness of the protocol. Note that the attractive region of

the potential with no bound states is not visible in Fig. 2 (blue dot-dashed line), because it is considerably more shallow than the other two cases. Similar results are obtained when the atom-ion polarization potential supports one bound state [green squares in Fig. 7(a)] or two bound states (not shown) with the only difference that a slight shift of the maximum of Q_{\max} occurs. This indicates that the phenomenon does not rely on the number of bound states, but it is rather a peculiarity of the long-range character of the two-body interaction. As already mentioned, the most relevant case for the application of the protocol explained in Sec. III is the one where the two internal states interact with the gas, whose result is displayed in Figs. 7(b)–7(d). To understand the plots, it is necessary to quickly explain the meaning of the interaction parameters $k_F a_1$ and $k_F a_0$. The choice of the value $k_F a_1 = -1.5 R^*$ or $k_F a_1 = -0.5 R^*$ (purple triangles and red circles, respectively), with $a_1 \simeq -R^*$ the scattering length relative to the state $|1\rangle$, fixes the density of the bath. Consequently, the variation of $k_F a_0$ corresponds to the tuning of the atom-ion scattering length a_0 of the state $|0\rangle$. In this way, different values of the interaction parameter $k_F a_0$ are obtained without changing the density of the bath. Note that the thermometer does not work when $k_F a_0 = k_F a_1$, since the two potentials are identical and therefore the induced dephasing dynamics is the same. This is can be also recognized in Eq. (B3) and it is indicated in the panels (b)–(d) of Fig. 7 by the discontinuity of the connecting line. The plot in Fig. 7(b) shows that the nonmonotonous behavior that we attribute to the long-range of the potential is preserved and that a proper choice of the parameters can lead to a higher sensitivity. Other than the enhancement of the sensitivity, a shift in the position of the peaks is observed, depending on the value of $k_F a_1$. This is better understood by observing the QSNR as a function of the scattering length a_0 instead of the interaction parameter $k_F a_0$. As shown in Fig. 7(d), the dependence of the QSNR on a_0 is similar for the two cases and the peak appears around $a_0 = -R^*$. Finally, we note that the time at which each Q_{\max} occurs [see Fig. 7(c)] is slightly longer than the case of the single internal state. The latter is not shown, but it does not exceed $10^3 \tau_F$ for the values in Fig. 7(a). This difference can be attributed to the cancellation between the accumulated phases in the elements of the matrix from which the decoherence function is calculated [see Eqs. (7) and (B3)]. On the other hand, the peaks of Q_{\max} are smaller than the single internal state case, but still larger than the neutral impurity probe. We attribute this reduction of sensitivity to the previous argument of the accumulated phases around the density perturbations, that is, the two states compensate partially each other.

B. Finite ion density distribution

We now investigate the impact of a spatial density distribution of the ion as that obtained when the ion is confined in a trap of finite width. In particular, we choose a Gaussian distribution, as it approximates the time-averaged distribution of the ion subject to micromotion in the ground state of a Paul trap (secular approximation) or the ground state in a deep optical dipole trap. The width of the Gaussian distribution is defined as $\sigma = \sqrt{\hbar/M\omega}$ with M the ion mass and ω the frequency of the trap. A trap width of $\sigma = 0.3 R^*$

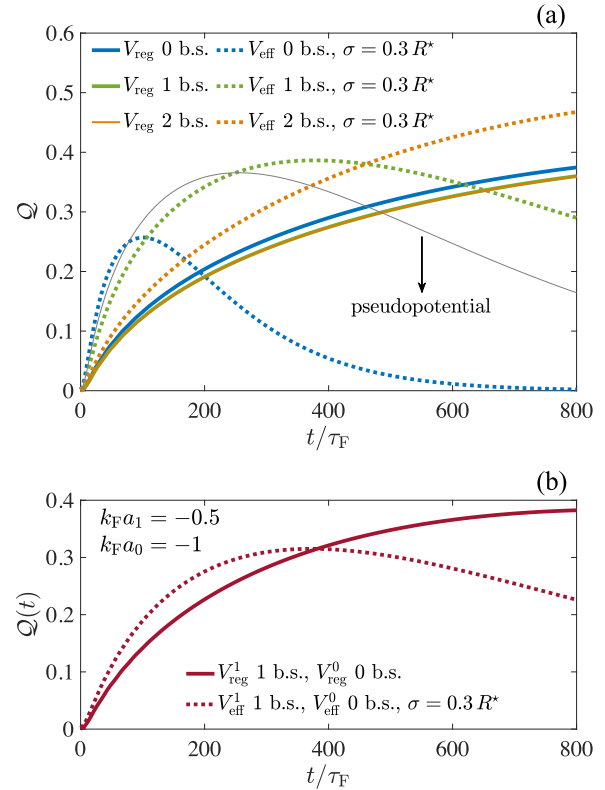


FIG. 8. Quantum signal-to-noise ratio as a function of the probing time for $T = 0.05 T_F$. (a) Single state with $k_F a = -0.5$. (b) Two states with $k_F a_1 = -0.5$ and -1 . Solid lines represent the localized impurity case; dotted lines correspond to the impurity with Gaussian spatial density.

corresponds to a trap frequency $\omega/(2\pi) \simeq 133$ kHz for $^{174}\text{Yb}^+$ and $\omega/(2\pi) \simeq 95$ kHz for $^{40}\text{Ca}^+$ (see also Table I). In Fig. 8, we show exemplary the time evolution of the quantum signal-to-noise ratio for the case of $T = 0.05 T_F$. The thick solid lines in Fig. 8(a) show the result for one single internal state with $k_F a = -0.5$ in the static ion approximation with zero (blue line), one (green line) and two (orange line) bound states. The latter two are essentially superimposed to each other (almost indistinguishable in the plot). As it can be seen, apart from a slight difference between the case of zero bound states and those with a finite number of bound states, the QSNR does not exhibit any reliance on the number of bound states when the ionic probe's distribution is delta-shaped. Moreover, Q assumes large values only at long times, where the impact of detrimental effects such as three-body recombination or reduced trap lifetime, especially for optical-based trap technology, are more likely. On the other hand, when the Gaussian distribution of the probe is considered, the convolution between the latter and the regularized potential results in an effective potential V_{eff} [see also Eq. (10)]. Such an effective potential has different characteristics compared to V_{reg} and it substantially modifies the dynamics of Q . Indeed, as it is also visible in Fig. 9, the attractive region becomes more shallow

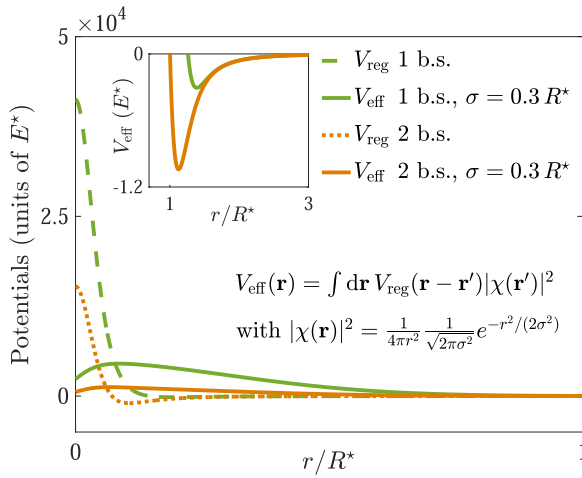


FIG. 9. Regularized atom-ion potentials with one (green line) and two (orange line) bound states together with their corresponding effective potentials (see also Sec. II). The inset shows the attractive region of the effective potentials. Note that the case without bound states is not shown, because both the energy and the atom-ion separation are of a rather different scale compared to those shown in the picture. Specifically, one has to consider much larger separations and no additional novel feature would have been manifested.

and the repulsive core gets flattened and broadened. Interestingly, a reliance on the number of bound states is manifested (see dotted lines in Fig. 8), especially for zero and one bound states, where a maximum at short times is displayed, which enables to attain higher sensitivities of the ionic temperature sensor at shorter times and thus to reduce the impact of undesired effects. On the other hand, the situation with two bound states resembles the case of the static ion limit, albeit attaining larger \mathcal{Q} values at longer times (see orange dotted line). This shows that the deeply bound states have a marginal impact on the sensor performance. A similar behavior is shown in Fig. 8(b) where two internal states are considered. In this case, the interaction parameters are fixed to $k_F a_0 = -1$ and -0.5 , and the regularized potentials support zero and one bound states for $|0\rangle$ and $|1\rangle$, respectively. For times shorter than $t \simeq 400 \tau_F$, a finite spatial density (dotted line) results in slightly higher values of the QSNR with respect to the case with the static ion (solid line). Although the difference is not remarkable, Fig. 8(b) confirms that, in general, the ion finite spatial density allows to improve the sensitivity at shorter times, even though the sensor performance is worse compared to the single internal state. Hence, our analysis indicates that the trap frequency ω can be used as a “knob” to enhance the signal-to-noise ratio at short times, which is particularly relevant in view of spin relaxation [57].

We finally remark that other strategies to determine the temperature of an ultracold Fermi gas were proposed. In particular, Lous *et al.* showed in Ref. [58] that a temperature $T \simeq 0.06 T_F$ of a ${}^6\text{Li}$ gas can be estimated with a 10% error by using a Bose-Einstein condensate of ${}^{41}\text{K}$ atoms as a probe. The strategy is based on the thermalization between the two atomic species and on the estimation of the condensate

fraction. Their aim, however, was to propose an experimental technique to determine the lowest possible temperature of the fermionic gas specifically for their setup. Here, on the other hand, we provide a theoretical estimation of the interrogation time, i.e., when the maximum achievable QSNR is attained, and the number of measurements that are needed to obtain a comparable error. For instance, a precision $\Delta T/T = 0.1$ of a measured temperature $T = 0.05 T_F$ can be obtained with $N \approx 625$ repetitions on a time of the order of a few milliseconds ($\sim 1000 \tau_F$) for an atom-ion pair ${}^6\text{Li}-{}^{174}\text{Yb}^+$, where the number of repetitions N can be reduced by employing more ions as sensors at the same time. We underscore again, however, that the experimental achievement of such a measurement relies on the capability of performing the protocol outlined in Sec. III.

V. DISCUSSION

The results we exposed in the previous section show that an impurity ion, whose interaction with the bath is described by the long-range atom-ion polarization potential, yields a higher quantum signal-to-noise ratio than a neutral impurity in an experimentally accessible parameter regime. Nonetheless, a few remarks on the interferometric protocol as well as on interparticle collisions are in order.

Interferometric protocol. The protocol outlined in Sec. III aims at determining the symmetric logarithmic derivative via the projective measurement of the energy. To this end, one performs a series of independent experimental runs by collecting data as $\{\xi_k\}_{k=1}^N$ with ξ_k being the outcome of the measurement of $\hat{\Lambda}_T$, namely, λ_{\pm} , of the k th run. Being the measurement projective, one will collect N_+ (N_-) outcomes for λ_+ (λ_-) such that $N = N_+ + N_-$. The determination of such an expectation value, however, requires the ability to determine $|\nu\rangle$ and ϕ together with their derivatives with respect to T with the aim of choosing $\theta = \phi + \varphi$. By tracking $\nu(t)$, one can fix the “optimal” probing time at which \mathcal{Q} is maximal, and therefore quantify what is the actual uncertainty on the estimated gas temperature. Nonetheless, to determine these quantities a prior knowledge of the temperature of the gas is needed. This means that, before the actual temperature estimation begins, one needs first to determine the probability of obtaining ξ_k in an experimental run, that is, $p(\xi_k|T)$, which is no less than the conditioned probability on the actual value, yet unknown, of the gas temperature to be determined. How to estimate the probability $p(\lambda_{\pm}|T)$? This is accomplished by means of the expectation value of $\hat{\Lambda}_T$ (or the energy) as [41]

$$p(\lambda_{\pm}|T) = \frac{1 \pm \langle \hat{\Lambda}_T \rangle}{2} = \frac{1 \pm f(\langle \hat{E}_T \rangle)}{2}, \quad (16)$$

where

$$f(\langle \hat{E}_T \rangle) = \frac{2\langle \hat{E}_T \rangle - E_{\max} - E_{\min}}{E_{\max} - E_{\min}}. \quad (17)$$

Here, we used the fact that the expectation value of $\hat{\Lambda}_T$ has support in the interval $[-1, 1]$, while the energy expectation value has been normalized accordingly. Of course, one needs first to perform a calibration of the ionic thermometer. This can be accomplished either with a theoretical model of the probabilities, as the one based on $\langle \hat{\Lambda}_T \rangle$ given by Eq. (13), or by measurements of the energy spectrum as $p(\lambda_{\pm}|T) = N_{\pm}/N$

for some known values of T and $N \gg 1$. The latter can be extracted independently by looking at specific properties of the gas (e.g., wings of the spatial distribution of the gas in the time-of-flight measurement). After this calibration stage, the inference about the value of the unknown gas temperature is drawn from the data $\{\xi_k\}_{k=1}^N$ by means of a certain function \mathcal{T} of the acquired measurement data, which in the context of the theory of parameter estimation it is called estimator. A commonly used one is the maximum likelihood estimator, which is defined as the value of \mathcal{T} that maximizes the joint probability distribution $L(T) = \prod_k p(\xi_k|T)$ with respect to T . The sequence of N experimental runs is performed several times and yields an estimate of the unknown gas temperature T , namely, it is expected that its statistical mean, $\mathbf{E}[\mathcal{T}] := T_{\text{est}}$, is $T_{\text{est}} \simeq T$. Since the outcomes of the measurements fluctuate from a data set to another one, i.e., for fixed N the variables N_{\pm} are stochastic as well as the likelihood $L(T)$, the estimator \mathcal{T} of the unknown gas temperature has an uncertainty. Given the fact that the protocol gives access to the measurements set by the SLD that maximizes the Fisher information, the uncertainty is then given by the Cramer-Rao bound, that is, the right-hand side of Eq. (14). For a more precise mathematical formalism of the estimation of an unknown parameter, we refer to Ref. [59]. Albeit it concerns the estimation of the gradient of a magnetic field, the formalism applies to our context in the precise same way.

Finally, let us note that the decoherence function $\nu(t)$ can be determined by means of many-body Ramsey interferometry [2], which has been successfully implemented for the experimental observation of Fermi [11] and Bose [60,61] polarons.

Few-body processes. The times required to attain the highest values of \mathcal{Q} could lead in experiments to undesired chemical reactions, which are not only not considered in the theory presented in this work, but, importantly, they would affect the state of the bath and thus resulting in a bad temperature sensor. In particular, three-body recombination is the main process owed to the presence of deeply bound states. Estimation of the decay rate γ based on classical trajectory theory [62–64] predicts a rate on the order of a few Hz for gas densities on the order of 10^{12} cm^{-3} up to a few kHz for 10^{14} cm^{-3} , therefore from seconds to sub-millisecond timescales. The numbers quoted in table I for the Fermi time and the QSNR of Fig. 8 show that we are reasonable good within the predicted decays. We note, however, that since the ion interacts with a spin-polarized fermionic bath, the quantum statistic of the gas helps in this regard, as no more than one atom can populate a two-body bound state.¹¹ Furthermore, given the fact that very deep bound states are less likely populated, one can conclude that the fermionic statistic of the gas does not allow to populate more than the most loosely bound state of the polarization potential, thus losing eventually a single atom of the bath per ion. This would be not the case if the bath would be bosonic for which mesoscopic molecular ions can be formed [56,65–67].

¹¹We note, however, that when a fermion of the bath is brought to populate a two-body bound state via a three-body collision, there is a finite probability that the released energy may lead to a spin flip, i.e., a spin impurity in the bath might be created.

Another important collisional process to be taken into account is spin relaxation. As it has been shown in the experiment of Ref. [57], the ion spin can decohere rather quickly because of spin-exchange and spin-nonconserving interactions. In particular, the spin-orbit coupling provides a major role in the relaxation dynamics of the ion internal state [68]. Specifically, it has been observed in a ^{87}Rb bath that after a few Langevin collision times t_L the probability of finding a Yb^+ in the initial spin configuration is close to 15%.¹² For a $^6\text{Li} - ^{174}\text{Yb}^+$ compound system with a gas density of $6.2 \times 10^{12} \text{ cm}^{-3}$ we find $t_L/\tau_F \simeq 13$ for $k_F R^* = -0.5$. This can be indeed a major obstacle to the successful realization of the ion thermometer. A solution is discussed in the next paragraph. In addition to this, we mention that for low-dimensional atom-ion systems such as quasi-one dimensional the impact of spin relaxation can be limited, as the spin-orbit coupling is reduced, while confinement-induced resonances can provide a tool to control atom-ion interactions [69].

An alternative strategy that can be employed to avoid undesired few-body processes is given by Rydberg dressing [47,70], where the atomic cloud is slightly coupled to a Rydberg-state. In such a way, the atomic polarizability is enhanced and the ion can be placed to some distance (on a micrometer scale) from the bath, thus without the need to immerse the ion in the latter [47]. This strategy is not only suitable to reduce the impact of micromotion when ions are confined in a Paul trap, but also to reduce the aforementioned spin relaxation effect. If we want to keep the *in situ* character of the protocol, however, we can still immerse the ion in the Rydberg-dressed atomic bath, but by means of a properly laser-engineered potential of the form [70]

$$V_d(\mathbf{r}) = \frac{A R_w^4}{r^4 + R_w^4} - \frac{C_4}{r^4}. \quad (18)$$

Here, A and R_w are laser-controlled parameters. With such an engineered atom-ion interaction it is possible to create a repulsive barrier [the first term in Eq. (18)] around the ion to avoid the atoms to get too close to it. Note that recent experiments have shown that long-range and laser-controlled interactions can be realized [71–73] and an ion-induced Rydberg excitation blockade can be realized [46]. The two-photon scheme utilized in the latter can be exploited also to initialize the thermometer, i.e., to create the ion impurity in the atomic cloud in the internal state $|0\rangle$. Finally, we note that the aforementioned Rydberg-dressing strategy modifies the short-range interaction in the scale of a few tens of nanometers without affecting the potential at micrometer distances. For this reason, it can also help to suppress the eventuality of charge-exchange collisions that may occur at long times [74].

VI. CONCLUSIONS

Based on an interferometric protocol for the *in situ* estimation of the temperature of a Fermi gas with immersed neutral atomic impurities [27], we investigated the performance of the scheme when ions are utilized as thermometers.

¹²The Langevin time is defined as $t_L = 1/\gamma_L$ with $\gamma_L = 2\pi n_g \sqrt{C_4/\mu_{\text{red}}}$ being the energy-independent rate with n_g the gas density.

We have found that the long-ranged character of the atom-ion polarization potential substantially modifies the quantum signal-to-noise ratio and that it enhances the sensor performance, especially when a single interacting internal state is used. We have investigated mainly two scenarios, namely, a static ion and an ion ground-state cooled in a finite trap, for various impurity-gas interactions and different number of bound states of the two-body atom-ion potential. We compared our findings with the case of a static neutral impurity, as originally proposed in Ref. [27], whose impurity-bath interaction is described by a zero-range pseudopotential. In Sec. III, we provided an alternative scheme that enables to use a single internal state, and therefore to reach higher values of \mathcal{Q} in shorter times ($< 10^3 \tau_F$). The latter point is important to limit the impact of ion spin relaxation. In Sec. IV A, we studied the temperature and time dependence of the QSNR for $k_F a = -0.5$ [see Fig. 5(a)] and $k_F a = -1.5$ [see Fig. 5(b)] finding that in order to attain a higher sensor sensitivity the probing time has to be larger compared to the case of a neutral impurity [see Figs. 5(c) and 5(d)]. We have shown in Fig. 7(a) that the dependence of the maximum of the quantum signal-to-noise ratio \mathcal{Q} on $k_F a$ (i.e., on the gas density) at fixed T is strongly modified by the long-range potential and it presents a peak. The effect of this finding, however, is reduced when both internal states are used for sensing the gas temperature [see Fig. 7(b)], since the accumulated phases of the states compensate each other partially. In Sec. IV B, we analyzed the impact of a Gaussian spatial density of the ion at low gas temperatures, i.e., $T = 0.05 T_F$ and $k_F a = -0.5$, and found that a finite width of the ion trap can enhance the sensitivity of the thermometer as well as reduces the probing time with respect to the case of a delta-shaped spatial density, i.e., static ion approximation (see also Fig. 8). Finally, in Sec. V, we discussed the implementation of the interferometric protocol based on the most recent experimental observations involving hybrid atom-ion systems.

In the present study, we have focused our attention on a single impurity. It is well-known in quantum parameter estimation theory that entanglement can further enhance the sensitivity of quantum sensors. Thus, in the future, it would be interesting to investigate how the estimation bound can be improved by entangling two ions, a task that is routinely accomplished in trapped ion experiments, and to devise novel interferometric protocols to attain the bound in this case. Furthermore, it would be also interesting to explore the impact of the impurity motion in more detail, for instance, by studying the properties of the Green's functions of the system, as recently undertaken in Ref. [75] as well as via a master equation approach [34]. Using motional states of the ion for sensing the gas temperature is preferable in view of reducing the impact of few-body processes.

ACKNOWLEDGMENTS

This work is supported by the project NE 1711/3-1 of the Deutsche Forschungsgemeinschaft. We are very grateful to T. Wasak for his constructive feedback on our analyses as well as for the insight in the estimation procedure. We also thank R. Gerritsma for feedback on the manuscript.

APPENDIX A: DYNAMICS OF THE ION INTERNAL STATE

In Sec. II, we stated that the Bloch vector is given by $\mathbf{v} = (\text{Re}[v], \text{Im}[v], 0)$. To show this, we consider the time evolution of the density matrix of the composite atom-gas system $\hat{\rho}$. This is given by $\hat{\rho}(t) = \hat{U}(t)\hat{\rho}(0)\hat{U}^\dagger(t)$, where $\hat{U}(t) = e^{-i\hat{H}t/\hbar}$ with $\hat{H} = \hat{H}_B + \hat{H}_P + \hat{H}_I$ the total Hamiltonian. Specifically, we have

$$\hat{\rho}(t) = \frac{1}{2} \begin{pmatrix} e^{\frac{i}{\hbar}(\hat{H}_B + \hat{H}_0)t} \hat{\rho}_B e^{-\frac{i}{\hbar}(\hat{H}_B + \hat{H}_0)t} & e^{\frac{i}{\hbar}(\hat{H}_B + \hat{H}_1)t} \hat{\rho}_B e^{-\frac{i}{\hbar}(\hat{H}_B + \hat{H}_0)t} \\ e^{\frac{i}{\hbar}(\hat{H}_B + \hat{H}_0)t} \hat{\rho}_B e^{-\frac{i}{\hbar}(\hat{H}_B + \hat{H}_1)t} & e^{\frac{i}{\hbar}(\hat{H}_B + \hat{H}_1)t} \hat{\rho}_B e^{-\frac{i}{\hbar}(\hat{H}_B + \hat{H}_1)t} \end{pmatrix}. \quad (\text{A1})$$

The components of the Bloch vector are given by the Hilbert-Schmidt inner product $v_i = \text{Tr}[\hat{\rho}(t)\hat{\sigma}_i]$ with $\hat{\sigma}_i$ $i = x, y, z$ being the Pauli matrices, which yield exactly Eq. (6). Let us note that the trace is taken over both the ion and gas degrees of freedom and where we have exploited the cyclic property of the trace.

We can then use Eq. (A1) to show that the projective measure of the energy yields the expectation value of the SLD. To this end, we define the matrix of a $\pi/2$ -pulse as

$$\hat{R}_{\pi/2}(\theta) = \frac{1}{\sqrt{2}} \begin{pmatrix} e^{i\theta} & 1 \\ 1 & -e^{-i\theta} \end{pmatrix} \quad (\text{A2})$$

and we calculate $\hat{R}_{\pi/2}(\theta)\hat{\rho}(t)\hat{R}_{\pi/2}^\dagger(\theta)$. This gives the following matrix:

$$\hat{\rho}_\theta(t) = \frac{1}{4} \begin{pmatrix} 2 + e^{i\theta} v(t) + e^{-i\theta} v^*(t) & v^*(t) - e^{2i\theta} v(t) \\ v(t) - e^{-2i\theta} v^*(t) & 2 - e^{i\theta} v(t) - e^{-i\theta} v^*(t) \end{pmatrix}. \quad (\text{A3})$$

The projective measure of the energy, that is, on the $\hat{\sigma}_z$ basis, reads

$$\text{Tr}[\hat{\rho}_\theta \hat{\sigma}_z] = \text{Re}[v(t)] \cos(\theta) - \text{Im}[v(t)] \sin(\theta). \quad (\text{A4})$$

By choosing $\theta = \phi + \varphi$ we obtain the desired expectation value of the symmetric logarithmic derivative.

APPENDIX B: REMARKS ON THE NUMERICAL SIMULATIONS

In this section, we provide some pieces of information on the employed numerical methods utilized to assess the quantum signal-to-noise ratio, especially with regard to the diagonalization of the impurity-bath Hamiltonian and decoherence function via the Levitov formula.

1. Finite size system

Let us recall the single-particle Hamiltonians of Eq. (9):

$$\hat{h}_B = -\frac{\hbar^2}{2m} \nabla^2 + V_{\text{ext}}(\mathbf{r}), \quad \hat{h}_\alpha = \hat{h}_B + V_{\text{eff}}^{(\alpha)}(\mathbf{r}). \quad (\text{B1})$$

Despite treating the gas as homogeneous, we solve the eigenvalues equations for a system confined in a sphere with finite size R . The value of the latter can be defined by fixing both the density and the number N_f of fermions in the s -wave state at $T = 0$ giving $N_f/R = \sqrt{2mE_F}/\pi\hbar$. The number of fermions is chosen large enough to achieve the thermodynamic limit for the considered timescales. Specifically, $N_f = 400$ was sufficient.

The eigenstates and eigenenergies satisfying $\hat{h}_B|\phi_n\rangle = \epsilon_n|\phi_n\rangle$ (without V_{ext}) are given by

$$\langle \mathbf{r} | \phi_n \rangle = \sqrt{\frac{1}{2\pi R}} \frac{\sin(k_n r)}{r}, \quad \epsilon_n = \frac{\hbar^2 k_n^2}{2m} \quad (\text{B2})$$

with $k_n R = n\pi$. As far as the eigenstates and eigenenergies of \hat{h}_1 are concerned, analytical solutions are available only in the case of the regularized pseudopotential (see Supplemental Material of Ref. [27] for details). In the case of the ionic impurity with the regularized two-body potential (2), however, we need to numerically diagonalize \hat{h}_1 . Towards this end, we used the MATHEMATICA built-in function NDEIGENSOLVE, as it has been proven to be an efficient and versatile tool for such a task.

2. Computation of the decoherence function

In order to compute the decoherence function $\nu(t)$, we need to evaluate the determinant in Eq. (8) at each time. Towards this aim, we represent the operator $\hat{\mathcal{M}} \equiv 1 - \hat{n} + \hat{n}e^{i\hat{h}_0 t/\hbar}e^{-i\hat{h}_1 t/\hbar}$, of which the determinant has to be assessed, in the basis of eigenstates $|\phi_j\rangle$ of \hat{h}_B . Hence, the corresponding matrix elements read

$$\begin{aligned} \langle \psi_m | \hat{\mathcal{M}} | \psi_n \rangle &= (1 - n_n)\delta_{n,m} + n_m \sum_l^{\mathcal{N}_0} \sum_k^{\mathcal{N}_1} e^{i(E_l - E_k)t/\hbar} \\ &\times \langle \phi_m | \psi_l \rangle \langle \psi_l | \psi_k' \rangle \langle \psi_k' | \phi_n \rangle, \end{aligned} \quad (\text{B3})$$

where $|\psi_l\rangle$ ($|\psi_k'\rangle$) are the eigenstates of \hat{h}_0 (\hat{h}_1) with eigenenergy E_l (E_k'), and the fermionic occupation number of the j th eigenstate is given by

$$n_j = \left\{ \exp \left[\frac{T_F}{T} \frac{1}{\bar{\epsilon}_F} (\bar{\epsilon}_n - \bar{\mu}) \right] + 1 \right\}^{-1}. \quad (\text{B4})$$

Here, for the sake of numerical convenience, we have rescaled (indicated by an overbar) the energies with respect to $\hbar^2/(2ma^2)$ and lengths with respect to the s -wave impurity-bath scattering length a . Moreover, $\bar{\mu}$ denotes the rescaled chemical potential of the Fermi gas that has been determined by solving $\text{Tr}[\hat{n}] = N_f$. In order to determine the right dimension of the Hilbert space \mathcal{N}_B of \hat{h}_B such that the desired numerical accuracy has been reached, we proceeded as follows: once the number of fermions N_f has been fixed, we imposed that $|\text{Tr}[\hat{n}] - N_f| < \epsilon$ with $\epsilon \in (0, 1]$. Specifically, we have chosen $\epsilon = 10^{-4}$, which results in a good tradeoff between accuracy and computational time. The dimensions of the Hilbert spaces $\mathcal{N}_{0,1}$ of $\hat{h}_{0,1}$ are varied arbitrarily up to the value at which the result is convergent. We get for them a number of the same order of \mathcal{N}_B . Albeit the value of \mathcal{N}_B and $\mathcal{N}_{0,1}$ depend on the gas temperature and number of fermions, that is, the higher the temperature, the larger is the Hilbert space dimension, all of them range typically between 500 and 1300.

- [1] P. W. Anderson, Infrared Catastrophe in Fermi Gases with Local Scattering Potentials, *Phys. Rev. Lett.* **18**, 1049 (1967).
- [2] M. Knap, A. Shashi, Y. Nishida, A. Imambekov, D. A. Abanin, and E. Demler, Time-Dependent Impurity in Ultracold Fermions: Orthogonality Catastrophe and Beyond, *Phys. Rev. X* **2**, 041020 (2012).
- [3] J. T. Devreese and A. S. Alexandrov, Fröhlich polaron and bipolaron: recent developments, *Rep. Prog. Phys.* **72**, 066501 (2009).
- [4] A. S. Alexandrov and J. T. Devreese, *Advances in Polaron Physics*, Springer Series in Solid-State Sciences, Vol. 159 (Springer, Berlin, 2010).
- [5] G. Yuval and P. W. Anderson, Exact results for the kondo problem: One-body theory and extension to finite temperature, *Phys. Rev. B* **1**, 1522 (1970).
- [6] A. Rosch, Quantum-coherent transport of a heavy particle in a fermionic bath, *Adv. Phys.* **48**, 295 (1999).
- [7] A. Alexandrov, *Theory of Superconductivity. From Weak to Strong Coupling*. (Institute of Physics Publishing, Bristol, 2003).
- [8] A. S. Alexandrov, High-temperature superconductivity: the explanation, *Phys. Scr.* **83**, 038301 (2011).
- [9] I. Esterlis, S. A. Kivelson, and D. J. Scalapino, A bound on the superconducting transition temperature, *npj Quantum Mater.* **3**, 59 (2018).
- [10] M. Koschorreck, D. Pertot, E. Vogt, B. Fröhlich, M. Feld, and M. Köhl, Attractive and repulsive fermi polarons in two dimensions, *Nature (London)* **485**, 619 (2012).
- [11] M. Cetina, M. Jag, R. S. Lous, I. Fritsche, J. T. M. Walraven, R. Grimm, J. Levinsen, M. M. Parish, R. Schmidt, M. Knap, and E. Demler, Ultrafast many-body interferometry of impurities coupled to a fermi sea, *Science* **354**, 96 (2016).
- [12] F. Scazza, G. Valtolina, P. Massignan, A. Recati, A. Amico, A. Burchianti, C. Fort, M. Inguscio, M. Zaccanti, and G. Roati, Repulsive Fermi Polarons in a Resonant Mixture of Ultracold ^6Li Atoms, *Phys. Rev. Lett.* **118**, 083602 (2017).
- [13] H. S. Adlong, W. E. Liu, F. Scazza, M. Zaccanti, N. D. Opong, S. Fölling, M. M. Parish, and J. Levinsen, Quasiparticle Lifetime of the Repulsive Fermi Polaron, *Phys. Rev. Lett.* **125**, 133401 (2020).
- [14] P. Massignan, M. Zaccanti, and G. M. Bruun, Polarons, dressed molecules and itinerant ferromagnetism in ultracold fermi gases, *Rep. Prog. Phys.* **77**, 034401 (2014).
- [15] R. Schmidt, M. Knap, D. A. Ivanov, J.-S. You, M. Cetina, and E. Demler, Universal many-body response of heavy impurities coupled to a fermi sea: a review of recent progress, *Rep. Prog. Phys.* **81**, 024401 (2018).
- [16] H. Tajima, J. Takahashi, S. I. Mistakidis, E. Nakano, and K. Iida, Polaron problems in ultracold atoms: Role of a fermi sea across different spatial dimensions and quantum fluctuations of a bose medium, *Atoms* **9**, 18 (2021).
- [17] A. Härter and J. Hecker Denschlag, Cold atom-ion experiments in hybrid traps, *Contemp. Phys.* **55**, 33 (2014).
- [18] R. Côté, Chapter two-ultracold hybrid atom-ion systems, *Adv. At. Mol. Opt. Phys.* **65**, 67 (2016).
- [19] M. Tomza, K. Jachymski, R. Gerritsma, A. Negretti, T. Calarco, Z. Idziaszek, and P. S. Julienne, Cold hybrid ion-atom systems, *Rev. Mod. Phys.* **91**, 035001 (2019).
- [20] S. Haze, M. Sasakawa, R. Saito, R. Nakai, and T. Mukaiyama, Cooling Dynamics of a Single Trapped Ion via Elastic

- Collisions with Small-Mass Atoms, *Phys. Rev. Lett.* **120**, 043401 (2018).
- [21] T. Feldker, H. Furst, H. Hirzler, N. V. Ewald, M. Mazzanti, D. Wiater, M. Tomza, and R. Gerritsma, Buffer gas cooling of a trapped ion to the quantum regime, *Nat. Phys.* **16**, 413 (2020).
- [22] P. Weckesser, F. Thielemann, D. Wiater, A. Wojciechowska, L. Karpa, K. Jachymski, M. Tomza, T. Walker, and T. Schaetz, Observation of feshbach resonances between a single ion and ultracold atoms, *Nature (London)* **600**, 429 (2021).
- [23] A. B. Michelsen, M. Valiente, N. T. Zinner, and A. Negretti, Ion-induced interactions in a tomonaga-luttinger liquid, *Phys. Rev. B* **100**, 205427 (2019).
- [24] S. I. Mistakidis, G. C. Katsimiga, G. M. Koutentakis, and P. Schmelcher, Repulsive fermi polarons and their induced interactions in binary mixtures of ultracold atoms, *New J. Phys.* **21**, 043032 (2019).
- [25] U. Bissbort, D. Cocks, A. Negretti, Z. Idziaszek, T. Calarco, F. Schmidt-Kaler, W. Hofstetter, and R. Gerritsma, Emulating Solid-State Physics with a Hybrid System of Ultracold Ions and Atoms, *Phys. Rev. Lett.* **111**, 080501 (2013).
- [26] K. Jachymski and A. Negretti, Quantum simulation of extended polaron models using compound atom-ion systems, *Phys. Rev. Research* **2**, 033326 (2020).
- [27] M. T. Mitchison, T. Fogarty, G. Guarnieri, S. Campbell, T. Busch, and J. Goold, *In Situ* Thermometry of a Cold Fermi Gas via Dephasing Impurities, *Phys. Rev. Lett.* **125**, 080402 (2020).
- [28] S. Schmid, A. Harter, and J. Hecker Denschlag, Dynamics of a Cold Trapped Ion in a Bose-Einstein Condensate, *Phys. Rev. Lett.* **105**, 133202 (2010).
- [29] C. Zipkes, S. Palzer, L. Ratschbacher, C. Sias, and M. Kohl, Cold Heteronuclear Atom-Ion Collisions, *Phys. Rev. Lett.* **105**, 133201 (2010).
- [30] H. Hirzler, R. S. Lous, E. Trimby, J. Perez-Rıos, A. Safavi-Naini, and R. Gerritsma, Observation of Chemical Reactions between a Trapped Ion and Ultracold Feshbach Dimers, *Phys. Rev. Lett.* **128**, 103401 (2022).
- [31] C. Kollath, M. Kohl, and T. Giamarchi, Scanning tunneling microscopy for ultracold atoms, *Phys. Rev. A* **76**, 063602 (2007).
- [32] Y. Sherkunov, B. Muzykantskii, N. d'Ambrumenil, and B. D. Simons, Probing ultracold fermi atoms with a single ion, *Phys. Rev. A* **79**, 023604 (2009).
- [33] M. Krych and Z. Idziaszek, Description of ion motion in a paul trap immersed in a cold atomic gas, *Phys. Rev. A* **91**, 023430 (2015).
- [34] L. Oghittu, M. Johannsen, A. Negretti, and R. Gerritsma, Dynamics of a trapped ion in a quantum gas: Effects of particle statistics, *Phys. Rev. A* **104**, 053314 (2021).
- [35] D. A. Abanin and L. S. Levitov, Fermi-Edge Resonance and Tunneling in Nonequilibrium Electron Gas, *Phys. Rev. Lett.* **94**, 186803 (2005).
- [36] N. d'Ambrumenil and B. Muzykantskii, Fermi gas response to time-dependent perturbations, *Phys. Rev. B* **71**, 045326 (2005).
- [37] D. Leibfried, R. Blatt, C. Monroe, and D. Wineland, Quantum dynamics of single trapped ions, *Rev. Mod. Phys.* **75**, 281 (2003).
- [38] Ch. Schneider, M. Enderlein, T. Huber, and T. Schaetz, Optical trapping of an ion, *Nat. Photonics* **4**, 772 (2010).
- [39] M. G. A. Paris, Quantum estimation for quantum technology, *Int. J. Quantum. Inform.* **07**, 125 (2009).
- [40] G. Toth and I. Apellaniz, Quantum metrology from a quantum information science perspective, *J. Phys. A: Math. Theor.* **47**, 424006 (2014).
- [41] T. Wasak, A. Smerzi, L. Pezze, and J. Chwedenczuk, Optimal measurements in phase estimation: simple examples, *Quant. Info. Proc.* **15**, 2231 (2016).
- [42] M. Mehboudi, A. Sanpera, and L. A. Correa, Thermometry in the quantum regime: recent theoretical progress, *J. Phys. A: Math. Theor.* **52**, 303001 (2019).
- [43] S. L. Braunstein and C. M. Caves, Statistical Distance and the Geometry of Quantum States, *Phys. Rev. Lett.* **72**, 3439 (1994).
- [44] P. Refregier, *Noise Theory and Application to Physics: From Fluctuations to Information* (Springer Science & Business Media, 2012).
- [45] W. Zhong, Z. Sun, J. Ma, X. Wang, and F. Nori, Fisher information under decoherence in bloch representation, *Phys. Rev. A* **87**, 022337 (2013).
- [46] F. Engel, T. Dieterle, T. Schmid, C. Tomschitz, C. Veit, N. Zuber, R. Low, T. Pfau, and F. Meinert, Observation of Rydberg Blockade Induced by a Single Ion, *Phys. Rev. Lett.* **121**, 193401 (2018).
- [47] T. Secker, R. Gerritsma, A. W. Glaetzle, and A. Negretti, Controlled long-range interactions between rydberg atoms and ions, *Phys. Rev. A* **94**, 013420 (2016).
- [48] D. Hu, L. Niu, S. Jin, X. Chen, G. Dong, J. Schmiedmayer, and X. Zhou, Ramsey interferometry with trapped motional quantum states, *Commun. Phys.* **1**, 29 (2018).
- [49] S. van Frank, A. Negretti, T. Berrada, R. Bucker, S. Montangero, J.-F. Schaff, T. Schumm, T. Calarco, and J. Schmiedmayer, Interferometry with non-classical motional states of a Bose-Einstein condensate, *Nat. Commun.* **5**, 4009 (2014).
- [50] A. Retzker, R. C. Thompson, D. M. Segal, and M. B. Plenio, Double Well Potentials and Quantum Phase Transitions in Ion Traps, *Phys. Rev. Lett.* **101**, 260504 (2008).
- [51] A. Klumpp, A. Zampetaki, and P. Schmelcher, Dynamical ion transfer between coupled coulomb crystals in a double-well potential, *Phys. Rev. E* **96**, 032227 (2017).
- [52] P. Weckesser, F. Thielemann, D. Hoenig, A. Lambrecht, L. Karpa, and T. Schaetz, Trapping, shaping, and isolating of an ion coulomb crystal via state-selective optical potentials, *Phys. Rev. A* **103**, 013112 (2021).
- [53] P. Treutlein, T. W. Hansch, J. Reichel, A. Negretti, M. A. Cirone, and T. Calarco, Microwave potentials and optimal control for robust quantum gates on an atom chip, *Phys. Rev. A* **74**, 022312 (2006).
- [54] P. Bohi, M. F. Riedel, J. Hoffrogge, J. Reichel, T. W. Hansch, and P. Treutlein, Coherent manipulation of Bose-Einstein condensates with state-dependent microwave potentials on an atom chip, *Nat. Phys.* **5**, 592 (2009).
- [55] M. M. Muller, R. S. Said, F. Jelezko, T. Calarco, and S. Montangero, One decade of quantum optimal control in the chopped random basis, [arXiv:2104.07687](https://arxiv.org/abs/2104.07687) [quant-ph].
- [56] G. E. Astrakharchik, L. A. P. Ardila, R. Schmidt, K. Jachymski, and A. Negretti, Ionic polaron in a Bose-Einstein condensate, *Commun. Phys.* **4**, 94 (2021).
- [57] L. Ratschbacher, C. Sias, L. Carcagni, J. M. Silver, C. Zipkes, and M. Kohl, Decoherence of a Single-Ion Qubit Immersed in a Spin-Polarized Atomic Bath, *Phys. Rev. Lett.* **110**, 160402 (2013).

- [58] R. S. Lous, I. Fritsche, M. Jag, B. Huang, and R. Grimm, Thermometry of a deeply degenerate fermi gas with a Bose-Einstein condensate, *Phys. Rev. A* **95**, 053627 (2017).
- [59] T. Wasak, K. Jachymski, T. Calarco, and A. Negretti, Magnetic-field gradiometer based on ultracold collisions, *Phys. Rev. A* **97**, 052701 (2018).
- [60] N. B. Jørgensen, L. Wacker, K. T. Skalmstang, M. M. Parish, J. Levinsen, R. S. Christensen, G. M. Bruun, and J. J. Arlt, Observation of Attractive and Repulsive Polarons in a Bose-Einstein Condensate, *Phys. Rev. Lett.* **117**, 055302 (2016).
- [61] M.-G. Hu, M. J. Van de Graaff, D. Kedar, J. P. Corson, E. A. Cornell, and D. S. Jin, Bose Polarons in the Strongly Interacting Regime, *Phys. Rev. Lett.* **117**, 055301 (2016).
- [62] A. Krükow, A. Mohammadi, A. Härter, J. H. Denschlag, J. Pérez-Ríos, and C. H. Greene, Energy Scaling of Cold Atom-Atom-Ion Three-Body Recombination, *Phys. Rev. Lett.* **116**, 193201 (2016).
- [63] J. Pérez-Ríos and C. H. Greene, Universal temperature dependence of the ion-neutral-neutral three-body recombination rate, *Phys. Rev. A* **98**, 062707 (2018).
- [64] J. Pérez-Ríos, Cold chemistry: a few-body perspective on impurity physics of a single ion in an ultracold bath, *Mol. Phys.* **119**, e1881637 (2021).
- [65] R. Côté, V. Kharchenko, and M. D. Lukin, Mesoscopic Molecular Ions in Bose-Einstein Condensates, *Phys. Rev. Lett.* **89**, 093001 (2002).
- [66] J. M. Schurer, A. Negretti, and P. Schmelcher, Unraveling the Structure of Ultracold Mesoscopic Collinear Molecular Ions, *Phys. Rev. Lett.* **119**, 063001 (2017).
- [67] E. R. Christensen, A. Camacho-Guardian, and G. M. Bruun, Charged Polarons and Molecules in a Bose-Einstein Condensate, *Phys. Rev. Lett.* **126**, 243001 (2021).
- [68] T. V. Tscherbul, P. Brumer, and A. A. Buchachenko, Spin-Orbit Interactions and Quantum Spin Dynamics in Cold Ion-Atom Collisions, *Phys. Rev. Lett.* **117**, 143201 (2016).
- [69] V. S. Melezhik and A. Negretti, Confinement-induced resonances in ultracold atom-ion systems, *Phys. Rev. A* **94**, 022704 (2016).
- [70] T. Secker, N. Ewald, J. Joger, H. Fürst, T. Feldker, and R. Gerritsma, Trapped Ions in Rydberg-Dressed Atomic Gases, *Phys. Rev. Lett.* **118**, 263201 (2017).
- [71] N. V. Ewald, T. Feldker, H. Hirzler, H. A. Fürst, and R. Gerritsma, Observation of Interactions between Trapped Ions and Ultracold Rydberg Atoms, *Phys. Rev. Lett.* **122**, 253401 (2019).
- [72] L. Wang, M. Deiß, G. Raithel, and J. H. Denschlag, Optical control of atom-ion collisions using a rydberg state, *J. Phys. B: At., Mol. Opt. Phys.* **53**, 134005 (2020).
- [73] S. Haze, J. Wolf, M. Deiß, L. Wang, G. Raithel, and J. H. Denschlag, Stark spectroscopy of rydberg atoms in an atom-ion hybrid trap, (2019), [arXiv:1901.11069](https://arxiv.org/abs/1901.11069) [physics.atom-ph].
- [74] R. Saito, S. Haze, M. Sasakawa, R. Nakai, M. Raoult, H. Da Silva, O. Dulieu, and T. Mukaiyama, Characterization of charge-exchange collisions between ultracold ${}^6\text{Li}$ atoms and ${}^{40}\text{Ca}^+$ ions, *Phys. Rev. A* **95**, 032709 (2017).
- [75] E. R. Christensen, A. Camacho-Guardian, and G. M. Bruun, Mobile ion in a fermi sea, *Phys. Rev. A* **105**, 023309 (2022).

Cooling dynamics of a free ion in a Bose-Einstein condensate

Lorenzo Oghittu¹, Juliette Simonet^{1,2,3}, Philipp Wessels-Staarmann^{1,2,3},
Markus Drescher^{1,3}, Klaus Sengstock^{1,2,3}, Ludwig Mathey^{1,2,3}, Antonio Negretti¹

¹Zentrum für Optische Quantentechnologien, Universität Hamburg, Luruper Chaussee 149, 22761 Hamburg, Germany,

²Institut für Quantenphysik, Universität Hamburg, Luruper Chaussee 149, 22761 Hamburg, Germany,

³The Hamburg Centre for Ultrafast Imaging, Luruper Chaussee 149, 22761 Hamburg, Germany

(Dated: February 20, 2024)

We investigate the dynamics of an ion moving through a homogeneous Bose-Einstein condensate (BEC) after an initial momentum is imparted. For this, we derive a master equation in the weak-coupling limit and Lamb-Dicke approximation for the reduced density matrix of the ion. We study the time evolution of the ion's kinetic energy and observe that its expectation value, identified as the ion temperature T_{ion} , is reduced by several orders of magnitude in a time on the order of microseconds for a condensate density in the experimentally relevant range between 10^{13} cm^{-3} and 10^{14} cm^{-3} . We characterize this behavior by defining the duration at half maximum as the time required by T_{ion} to reach half of its initial value, and study its dependence on the system parameters. Similarly, we find that the expectation value of the ion's momentum operator is reduced by nine orders of magnitude on the same timescale, making the ion's position converge to a final value. Based on these results, we conclude that the interaction with the bosonic bath allows for cooling and pinning of the ion by decreasing the expectation value of its kinetic energy and velocity, which constitutes a result of direct relevance for current atom-ion experiments.

I. INTRODUCTION

Quantum mixtures of ultracold atoms and ions have attracted the interest of an increasing part of the ultracold quantum matter community in the last few years. Combining the high controllability of trapped ions with the long coherence times of ultracold atomic systems, they provide a fertile platform for the study of both few- and many-body physics and their application to the advancement of quantum technologies arising from the long-ranged character of atom-ion interactions. Some of the most recent theoretical investigations include ab-initio quantum Monte Carlo and multi-configuration time-dependent Hartree methods for bosons as well as diagrammatic techniques for the analysis and characterization of polaronic states [1–3]. More recently, studies have also focused on how the interaction between two ions is mediated by the surrounding gas [4, 5], while proposals to exploit ions in ultracold gases as quantum simulators [6–9] or sensors [10] have been put forward. We refer to Refs. [11, 12] for an overview in the field. As far as experiments are concerned, most of the recent achievements involve the presence of external potentials that tightly trap the ion [13]. In particular, sympathetic cooling was observed in such setups with the ion confined in radio-frequency traps [14, 15] or in optical dipole traps [16, 17]. Similar systems were also employed in the observation and study of few-body processes and chemical reactions between ions and atoms [18–22]. On the other hand, experiments based on the ionization of Rydberg atoms [23, 24] have explored the scenario where no trap is present and the ion is driven by an external electric field, focusing on the transport properties of electrical charges inside a Bose-Einstein condensate [25, 26] and the formation of molecules in Rydberg-atom-ion systems [27, 28]. However, while the

formation and behavior of neutral polarons both in the case of Fermi [29–32] and Bose environments [33–35] has made tremendous progress, the physics of mobile charged impurities in ultracold gases is at an earlier stage compared to its neutral analogous. This is due to the experimental challenges in reaching the ultracold regime involving only a few partial waves, due to the notorious micromotion [36]. Theoretical challenges arise from the fact that the properties of the systems depend not only on the scattering length and effective range of the atom-ion potential, but also on the presence of the long-range tail of the interaction, preventing the use of the pseudopotential approximation [37, 38].

Here, we study the quantum dynamics of a free, i.e., not trapped, ion moving inside a bosonic quantum gas with a finite initial momentum. Let us note that one-dimensional in-depth investigations of the quantum dynamics of the motional degrees of freedom of an ion both at zero and finite temperature interacting with matter waves confined in a double well have been carried out in Refs. [39, 40]. The ion-induced correlated dynamics of a bosonic system after ionization has been analyzed in Ref. [41], where the ion, however, has been treated as a static impurity. Specifically, we resort to the master equation approach developed in Refs. [42, 43] to characterize the evolution of the expectation value of the ion's kinetic energy, velocity and position. Our study is motivated by the recent experimental advances involving untrapped ions in condensates [25, 44], where we note that optical control of the ion movement in the atomic gas can be accomplished by means of optical traps as well [45, 46]. In this work, we are inspired by the specific scenario that originates from the experiment reported by T. Kroker *et al.* in Ref. [44]. As depicted in Fig. 1(a), a laser pulse ionizes some of the ^{87}Rb atoms in a BEC within 215 fs, hence instantly creating

ions inside the bosonic gas with a finite initial kinetic energy determined by the excess energy of the ionization process. For this reason, we focus mostly on the case of the homonuclear system $^{87}\text{Rb}^+ / ^{87}\text{Rb}$, as this is the atomic species utilized in those experiments, but we also provide a brief analysis of the case of ions with a larger mass. We note that although in Refs. [44, 47] the initial kinetic energy of the ion is on the order of a few microelectronvolts, this can be experimentally reduced by an order of magnitude. Fig. 1(b) illustrates that for the corresponding initial momentum the ion can be cooled and pinned within the BEC due to the long range atom-ion interaction arising from the polarizability of the atomic cloud. We characterize the cooling of the ion and find it to be remarkably robust against the initial ion velocity, density and temperature of the BEC as well as the mass ratio between the ion and the atoms.

The paper is organized as follows: in Sec. II we introduce the atom-ion interaction potential and the Hamiltonian describing the hybrid atom-ion system, while in Sec. III we derive the ionic master equation from which the equation of motion of the most relevant observables are obtained. In Sec. IV we analyse and discuss the results of the numerical simulations, while in Sec. V we discuss the experimental implications of the study. Finally, in Sec. VI we summarize our findings and provide an outlook for future analysis.

II. SYSTEM

In this section, we briefly characterize the theoretical treatment of our system. For a more thorough description, we refer the interested reader to Refs. [42, 43].

A. Atom-ion interaction potential

The interaction between a charged and a neutral particle depends on their separation $r = |\mathbf{r}|$. It is described asymptotically by the polarization potential $V(r) = -C_4/r^4$, where $C_4 = \alpha e^2 / (8\pi\epsilon_0)$ with α the static polarizability of the atom, e the electron charge and ϵ_0 the vacuum permittivity. This potential has the characteristic length $R^* = \sqrt{2\mu C_4 / \hbar^2}$ and energy $E^* = \hbar^2 / [2\mu(R^*)^2]$, with μ as reduced mass. The value of R^* is much larger than the length scale of the van der Waals interaction between neutral particles and, for typical atom-ion systems, it is of the order of hundreds of nanometers. In particular, for the $^{87}\text{Rb} / ^{87}\text{Rb}^+$ system we have $R^* \simeq 265.81$ nm and $E^* \simeq k_B \cdot 79$ nK (k_B is the Boltzmann constant). Due to the singularity of the polarization potential and the fact that we shall have to calculate its Fourier transform, we consider the following regularization [42]

$$V_{\text{reg}}(r) = -C_4 \frac{r^2 - c^2}{r^2 + c^2} \frac{1}{(r^2 + b^2)^2}, \quad (1)$$

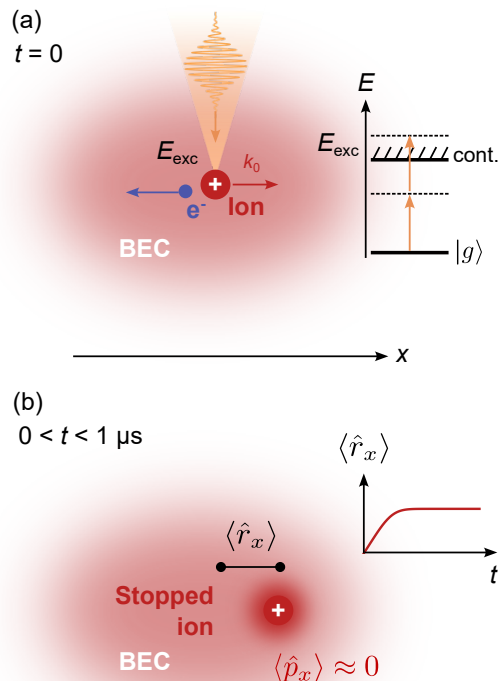


FIG. 1. Proposal for cooling an ion in an ultracold bosonic gas. (a) An atom in a BEC is ionized by an ultrashort laser pulse via a non-resonant two-photon process. The excess energy E_{exc} of the ionization process determines the initial momentum k_0 of the ion in x direction. (b) Subsequently, the ion is slowed down due to the atom-ion interaction arising from the polarizability of the atomic cloud. By deriving a master equation, we can extract the time-evolution of the expectation value of the ion's position $\langle \hat{r}_x \rangle$ and show that it is pinned within a microsecond in a ^{87}Rb BEC.

where the energy spectrum and the atom-ion scattering length a_{ai} are controlled by the parameters b and c [48]. The choice of the values of those parameters is discussed extensively in Ref. [43]. An example of the potential is displayed in the main plot Fig. 2.

The scattering amplitude in the first-order Born approximation is proportional to the Fourier transform of the potential, and is given by

$$f(q) = -\frac{\mu}{2\pi\hbar^2} \int_{\mathbb{R}^3} d\mathbf{r} e^{i\mathbf{q}\cdot\mathbf{r}} V_{\text{reg}}(r) \\ = \frac{c^2\pi(R^*)^2}{(b^2 - c^2)^2 q} \left\{ e^{-bq} \left[1 + \frac{(b^4 - c^4)q}{4bc^2} \right] - e^{-cq} \right\}. \quad (2)$$

An example is shown in the inset of Fig. 2, where $f(q)$ approaches zero for large momenta, while at $qR^* \simeq 7.37$ it exhibits a minimum. The expression of the scattering

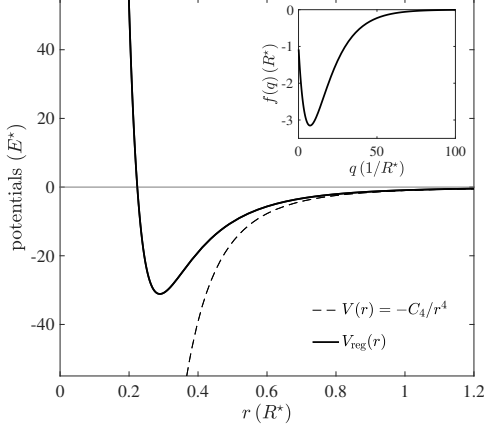


FIG. 2. Main plot: Atom-ion interaction potential in units of E^* as a function of the atom-ion separation r in units of R^* . Dashed line: polarization potential. Solid line: regularized potential in Eq. (1) with parameters $b = 0.07797 R^*$, $c = 0.2239 R^*$, corresponding to an atom-ion scattering length $a_{\text{ai}} \simeq R^*$ and a single two-body bound state with binding energy $E_{\text{BS}} \simeq -1.43 E^*$. Inset: scattering amplitude $f(q)$ [see Eq. (2)] corresponding to the regularized potential in the main plot. Note that f is in units of R^* , whereas q in units of $1/R^*$.

amplitude is used in the derivation of the master equation, as we shall discuss it in Sec. III.

B. Hamiltonian

We consider a non-trapped ion of mass M coupled to an ultracold bosonic gas with mass m , henceforth referred to as bath. The Hamiltonian is the sum of three terms: $\hat{H} = \hat{H}_{\text{ion}} + \hat{H}_{\text{bath}} + \hat{H}_{\text{int}}$, with $\hat{H}_{\text{ion}} = \hat{p}^2/(2M)$,

$$\hat{H}_{\text{bath}} = \int_{\mathbb{R}^3} d\mathbf{r}_b \hat{\Psi}_b^\dagger(\mathbf{r}_b) \left[\frac{\hat{p}_b^2}{2m} + \frac{g}{2} \hat{\Psi}_b^\dagger(\mathbf{r}_b) \hat{\Psi}_b(\mathbf{r}_b) \right] \hat{\Psi}_b(\mathbf{r}_b), \quad (3)$$

and

$$\hat{H}_{\text{int}} = \int_{\mathbb{R}^3} d\mathbf{r}_b \hat{\Psi}_b^\dagger(\mathbf{r}_b) V_{\text{ib}}(\mathbf{r}_b - \hat{\mathbf{r}}) \hat{\Psi}_b(\mathbf{r}_b), \quad (4)$$

where the subscript b indicates the bosons of the bath, $\hat{\mathbf{r}}$ is the position operator of the ion, and V_{ib} represents the two-body potential between the ion and the particles of the bath. Moreover, we assume the bath to be confined in a box of length L and its atoms to interact via contact potential with coupling strength $g = 4\pi\hbar^2 a_{\text{bb}}^s/m$, a_{bb}^s being the three-dimensional (3D) atom-atom s -wave scattering length.

The bosonic field operator can be written as an expansion around the condensate density $n_0 = N_0/L^3$ (N_0 being the number of condensed particles) as

$$\hat{\Psi}_b(\mathbf{r}_b) = \sqrt{n_0} + \delta\hat{\Psi}_b(\mathbf{r}_b), \quad (5)$$

where the fluctuations are described within Bogoliubov theory, i.e.,

$$\delta\hat{\Psi}_b(\mathbf{r}_b) = L^{-3/2} \sum_{\mathbf{q}} \left(u_{\mathbf{q}} \hat{b}_{\mathbf{q}} e^{i\mathbf{q}\cdot\mathbf{r}_b} + v_{\mathbf{q}} \hat{b}_{\mathbf{q}}^\dagger e^{-i\mathbf{q}\cdot\mathbf{r}_b} \right), \quad (6)$$

with $[\hat{b}_{\mathbf{q}}, \hat{b}_{\mathbf{q}'}^\dagger] = \delta_{\mathbf{q},\mathbf{q}'}$. By using Eq. (6) we can rewrite the bath Hamiltonian as follows

$$\hat{H}_{\text{bath}} \approx E_0 + \sum_{\mathbf{q}} \hbar\omega_{\mathbf{q}} \hat{b}_{\mathbf{q}}^\dagger \hat{b}_{\mathbf{q}} \quad (7)$$

with $E_0 = gN_0^2/(2L^3)$ the condensate ground-state energy, and the phononic dispersion relation given by

$$\epsilon(\mathbf{q}) \equiv \hbar\omega_{\mathbf{q}} = \sqrt{\left(\frac{\hbar^2 q^2}{2m} \right)^2 + (\hbar c_s q)^2}, \quad (8)$$

where $c_s = \sqrt{gn_0/m}$ is the speed of sound of the gas. The amplitudes of the Bogoliubov modes are given by [49]

$$u_{\mathbf{q}} = \sqrt{\frac{\hbar^2 q^2/(2m) + gn_0}{2\hbar\omega_{\mathbf{q}}} + \frac{1}{2}} \quad (9)$$

$$v_{\mathbf{q}} = -\sqrt{\frac{\hbar^2 q^2/(2m) + gn_0}{2\hbar\omega_{\mathbf{q}}} - \frac{1}{2}}.$$

Hence, the atomic density operator reads

$$\hat{\Psi}_b^\dagger(\mathbf{r}_b) \hat{\Psi}_b(\mathbf{r}_b) = n_0 + \Delta\hat{n}(\mathbf{r}_b) \quad (10)$$

and we can use the definition in Eq. (5) to write the last term on the right hand side as

$$\Delta\hat{n}(\mathbf{r}_b) = \delta\hat{n}(\mathbf{r}_b) + \delta^2\hat{n}(\mathbf{r}_b) \quad (11)$$

with $\delta\hat{n}(\mathbf{r}_b) = \sqrt{n_0}[\delta\hat{\Psi}_b(\mathbf{r}_b) + \delta\hat{\Psi}_b^\dagger(\mathbf{r}_b)]$ and $\delta^2\hat{n}(\mathbf{r}_b) = \delta\hat{\Psi}_b^\dagger(\mathbf{r}_b)\delta\hat{\Psi}_b(\mathbf{r}_b)$. In our description we only consider the first of the two terms, thereby taking into account only the density fluctuations proportional to the square root of the condensate density n_0 . Let us note that the second order is related to the non-condensed part of the gas. As we pointed out in Ref. [43], its contribution becomes relevant when the gas temperature approaches the critical temperature of condensation from below, and is the only one contributing in the absence of condensation. Here, however, our analysis focuses on gas temperatures much lower than the critical temperature, allowing the contribution of the quadratic terms to be safely neglected. According to Eq. (6), we have

$$\delta\hat{n}(\mathbf{r}_b) = \sqrt{\frac{n_0}{L^3}} \sum_{\mathbf{q}} \left[(u_{\mathbf{q}} + v_{\mathbf{q}}^*) \hat{b}_{\mathbf{q}} e^{i\mathbf{q}\cdot\mathbf{r}_b} + (u_{\mathbf{q}}^* + v_{\mathbf{q}}) \hat{b}_{\mathbf{q}}^\dagger e^{-i\mathbf{q}\cdot\mathbf{r}_b} \right]. \quad (12)$$

At this stage let us remark that we assume that the condensate density is not affected by the presence of the ion

and remains homogeneous. As recently shown in Ref. [1], however, the formation of many-body bound-states can change the bath density around the ion substantially. Such many-body bound-states are not included in the present study, since their formation remains negligible as long as no stimulated resonance processes occur [50]. Under these assumptions, our open system approach is justified.

Finally, the interaction Hamiltonian becomes

$$\begin{aligned}\hat{H}_{\text{int}} &= \int_{\mathbb{R}^3} d\mathbf{r}_b V_{\text{ib}}(\mathbf{r}_b - \hat{\mathbf{r}}) \delta \hat{n}(\mathbf{r}_b) \\ &= \hbar \sum_{\mathbf{q}} \left(\hat{S}_{\mathbf{q}} \hat{b}_{\mathbf{q}} + \hat{S}_{\mathbf{q}}^\dagger \hat{b}_{\mathbf{q}}^\dagger \right)\end{aligned}\quad (13)$$

with

$$\hat{S}_{\mathbf{q}} = \frac{\sqrt{n_0 L^3}}{\hbar} (u_{\mathbf{q}} + v_{\mathbf{q}}^*) e^{i\mathbf{q} \cdot \hat{\mathbf{r}}} c_{\mathbf{q}} \quad (14)$$

and

$$c_{\mathbf{q}} = \frac{1}{L^3} \int_{\mathbb{R}^3} d\mathbf{y} e^{i\mathbf{q} \cdot \mathbf{y}} V_{\text{ib}}(\mathbf{y}). \quad (15)$$

Note that the coefficient $c_{\mathbf{q}}$ is related to the scattering amplitude $f(q)$ by

$$c_{\mathbf{q}} = -\frac{2\pi\hbar^2}{\mu L^3} f(q) \quad (16)$$

As discussed in Sec. II A, we model the two-body atom-ion potential V_{ib} with the regularization of Eq. (1), whose scattering amplitude is given in Eq. (2).

III. IMPURITY MASTER EQUATION

In this section we derive a master equation for the reduced density matrix of the ion. We start from the master equation in the Born and Markov approximation for an impurity in a bosonic bath:

$$\begin{aligned}\frac{d}{dt} \hat{\rho}(t) &= -\frac{i}{\hbar} [\hat{H}_{\text{ion}}, \hat{\rho}(t)] - \sum_{\mathbf{q}} \int_0^t d\tau \Omega_{\mathbf{q}}^2 \left\{ \right. \\ &+ (n_{\mathbf{q}} + 1) \left[e^{i\mathbf{q} \cdot \hat{\mathbf{r}}}, e^{-i\mathbf{q} \cdot \hat{\mathbf{r}}(t, \tau)} \hat{\rho}(t) \right] e^{-i\omega_{\mathbf{q}} \tau} \\ &+ n_{\mathbf{q}} \left[\hat{\rho}(t) e^{-i\mathbf{q} \cdot \hat{\mathbf{r}}(t, \tau)}, e^{i\mathbf{q} \cdot \hat{\mathbf{r}}} \right] e^{-i\omega_{\mathbf{q}} \tau} \\ &+ (n_{\mathbf{q}} + 1) \left[\hat{\rho}(t) e^{i\mathbf{q} \cdot \hat{\mathbf{r}}(t, \tau)}, e^{-i\mathbf{q} \cdot \hat{\mathbf{r}}} \right] e^{i\omega_{\mathbf{q}} \tau} \\ &+ n_{\mathbf{q}} \left[e^{-i\mathbf{q} \cdot \hat{\mathbf{r}}}, e^{i\mathbf{q} \cdot \hat{\mathbf{r}}(t, \tau)} \hat{\rho}(t) \right] e^{i\omega_{\mathbf{q}} \tau} \left. \right\}.\end{aligned}\quad (17)$$

Here, we defined

$$\Omega_{\mathbf{q}}^2 = \frac{|u_{\mathbf{q}} + v_{\mathbf{q}}|^2}{\hbar^2} |c_{\mathbf{q}}|^2 n_0 L^3, \quad (18)$$

while $n_{\mathbf{q}} = [e^{\beta(\epsilon(\mathbf{q}) - \mu_{\text{B}})} - 1]^{-1}$ is the Bose-Einstein occupation number based on the averages over the thermal state of the bath \hat{B}_0 [see also Eq. (B7)]

$$\text{Tr}_{\text{b}} \{ \hat{b}_{\mathbf{q}}^\dagger \hat{b}_{\mathbf{q}'} \hat{B}_0 \} = n_{\mathbf{q}} \delta_{\mathbf{q}, \mathbf{q}'}, \quad (19)$$

with μ_{B} the chemical potential of the bosonic gas at temperature T_{gas} , and $\beta = 1/(k_{\text{B}} T_{\text{gas}})$. We note that Eq. (17) corresponds to the first line of Eq. (41) in Ref. [43] and can be applied to any kind of impurity in interaction with a bath of bosonic atoms by specifying the scattering amplitude in the definition of $c_{\mathbf{q}}$ and the equation of motion of the impurity $\hat{\mathbf{r}}(t, \tau)$. For a detailed derivation we refer to Ref. [43].

A. Lamb-Dicke approximation

In order to render the master equation numerically treatable, we perform the Lamb-Dicke approximation to further simplify it. Such an approximation is based on the assumption that the average wavelength of the atoms in the bosonic bath, corresponding to the de Broglie wavelength $\lambda_{\text{dB}}(T_{\text{gas}})$, is much larger than the spatial extension of the ion, namely the width of the associated wave packet. The validity of this requirement is discussed in Appendix A, while here we proceed with the derivation of the master equation. In the Lamb-Dicke regime, we Taylor expand the products of exponential functions containing $\mathbf{q} \cdot \hat{\mathbf{r}}$ and $\mathbf{q} \cdot \hat{\mathbf{r}}(t, \tau)$ and keep the terms up to second order. For instance, the first commutator in Eq. (17) can be written as

$$\begin{aligned}\left[e^{i\mathbf{q} \cdot \hat{\mathbf{r}}}, e^{-i\mathbf{q} \cdot \hat{\mathbf{r}}(t, \tau)} \hat{\rho}(t) \right] &\simeq \\ i[\mathbf{q} \cdot \hat{\mathbf{r}}, \hat{\rho}(t)] + [\mathbf{q} \cdot \hat{\mathbf{r}}, \mathbf{q} \cdot \hat{\mathbf{r}}(t, \tau) \hat{\rho}(t)] &- \frac{1}{2} [(\mathbf{q} \cdot \hat{\mathbf{r}})^2, \hat{\rho}(t)].\end{aligned}\quad (20)$$

However, due to the assumed spherical symmetry of the bath, the first term on the right hand side of Eq. (20) is zero after the sum over \mathbf{q} is taken, and so are the terms containing odd powers of q_x , q_y or q_z . Hence, the directions are decoupled and the contribution from the first commutator reads $\sum_{\xi} ([\hat{r}_{\xi}, \hat{r}_{\xi}(t, \tau) \hat{\rho}(t)] - [\hat{r}_{\xi}^2, \hat{\rho}(t)]/2)$, $\xi = x, y, z$.

We now explicitly substitute the equation of motion of the free ion $\hat{r}_{\xi}(t, \tau) = \hat{r}_{\xi} - (\hat{p}_{\xi}/M)\tau$ and perform the time integration. We note that the latter is performed analytically in the present study, which is in contrast with the usual approach in the literature [51] and with the previous works [42, 43], where the limit $t \rightarrow \infty$ has been taken. For further details we refer to the Appendix B. Similarly to Ref. [43], we use the master equation to derive the differential equations for the expectation value of the squared momentum \hat{p}_{ξ}^2 along the direction ξ (see

Appendix C for an alternative derivation):

$$\begin{aligned} \frac{d}{dt} \langle \hat{p}_\xi^2 \rangle &= \sum_{\mathbf{q}} \Omega_{\mathbf{q}}^2 q_\xi^2 \left\{ \frac{2\hbar^2}{\omega_{\mathbf{q}}} (2n_{\mathbf{q}} + 1) \sin(\omega_{\mathbf{q}} t) \right. \\ &\quad \left. + \frac{4\hbar}{M\omega_{\mathbf{q}}^2} \left[\omega_{\mathbf{q}} t \cos(\omega_{\mathbf{q}} t) - \sin(\omega_{\mathbf{q}} t) \right] \langle \hat{p}_\xi^2 \rangle \right\} \end{aligned} \quad (21)$$

and for the squared position \hat{r}_ξ^2 and covariance $\hat{c}_\xi = \hat{r}_\xi \hat{p}_\xi + \hat{p}_\xi \hat{r}_\xi$:

$$\begin{aligned} \frac{d}{dt} \langle \hat{r}_\xi^2 \rangle &= \frac{1}{M} \langle \hat{c}_\xi \rangle \\ \frac{d}{dt} \langle \hat{c}_\xi \rangle &= \frac{2}{M} \langle \hat{p}_\xi^2 \rangle + \\ &\quad + \sum_{\mathbf{q}} \Omega_{\mathbf{q}} q_\xi^2 \left\{ \frac{2\hbar}{M\omega_{\mathbf{q}}^2} \left[\omega_{\mathbf{q}} t \cos(\omega_{\mathbf{q}} t) - \sin(\omega_{\mathbf{q}} t) \right] \langle \hat{c}_\xi \rangle \right. \\ &\quad \left. + \frac{2\hbar^2}{M\omega_{\mathbf{q}}^2} (2n_{\mathbf{q}} + 1) \left[\cos(\omega_{\mathbf{q}} t) + \omega_{\mathbf{q}} t \sin(\omega_{\mathbf{q}} t) - 1 \right] \right\}. \end{aligned} \quad (22)$$

In the limit of a large bath, where $L \rightarrow \infty$, the quantized values assumed by the wave vector $q_\xi = 2\pi s_\xi/L$ with $s \in \mathbb{Z}$ become closely spaced. In this regime, the sum over \mathbf{q} can be replaced with the integral $L^3/(2\pi)^3 \int_{\mathbb{R}^3} d\mathbf{q}$. From the expectation value of $\hat{p}^2 = \hat{p}_x^2 + \hat{p}_y^2 + \hat{p}_z^2$, we calculate the ion temperature. The latter, for an untrapped ion, can be defined as the expectation value of the kinetic energy in units of the Boltzmann constant:

$$T_{\text{ion}} = \frac{1}{k_B} \frac{1}{2M} \langle \hat{p}^2 \rangle. \quad (23)$$

For the sake of completeness, we remark that the definition of the ion temperature can change for different systems. For instance, in the case of Paul-trapped ions, both the secular motion and micromotion have to be taken into account (see Ref. [52] for details).

Finally, we report the equations of motion for the first momenta, which are derived in a similar manner

$$\begin{aligned} \frac{d}{dt} \langle \hat{r}_\xi \rangle &= \frac{1}{M} \langle \hat{p}_\xi \rangle \\ \frac{d}{dt} \langle \hat{p}_\xi \rangle &= \sum_{\mathbf{q}} \Omega_{\mathbf{q}}^2 q_\xi^2 \left\{ \frac{2\hbar}{M\omega_{\mathbf{q}}^2} \left[\omega_{\mathbf{q}} t \cos(\omega_{\mathbf{q}} t) - \sin(\omega_{\mathbf{q}} t) \right] \langle \hat{p}_\xi \rangle \right\}. \end{aligned} \quad (24)$$

B. Initial quantum state after ionization

The aim of this section is to describe the density matrix of the ion immediately after ionization of a bosonic quantum gas. We assume the BEC with typical parameters presented in Tab. I is confined in a harmonic potential with trap frequencies $\omega_\xi = 2\pi\nu_\xi$, which is typically realized by an optical dipole trap. In the following, we consider two possible experimental

scenarios for the ionization process: either ionization of a Rydberg excitation or direct ionization with an ultrashort laser pulse. Let us note that once the ion is created, however, it is no longer affected by the optical dipole trap confining the condensate and no additional external potential for the ion is assumed. Hence, the ion is free to move within the BEC. Nonetheless, the ion inherits its spatial extent, as represented by the squared modulus of its wave function, from the former atom in the trapped condensate before ionization. Crucially, the spatial extent of the ion must fulfill the requirements of the Lamb-Dicke approximation at all times, as we discuss in Appendix A. Finally, we assume that the ionization process occurs on a time scale much faster than the atomic dynamics, i.e., we treat it as an instantaneous process.

Ionization via Rydberg states - We begin by considering the case of ionization via Rydberg excitation, for which the initial ionic state can be represented as a thermal state. We assume that, before the ionization, the bosons are in a trapped motional state due to their confinement. At low temperatures, all bosons are described by the same single-particle state, to a very good approximation. If a laser pulse is utilized to excite the internal state of the atoms to a Rydberg state, and if the chosen Rydberg state is such that the corresponding blockade radius is large enough to guarantee a single excitation in the atomic ensemble, then, that excitation is delocalized over the entire atomic cloud. Namely, a giant superposition state is created. The motional state, however, to a very good approximation is the same as before the Rydberg excitation took place. When a second laser pulse is applied to ionize the Rydberg atom as in Ref. [24], the quantum superposition with a single Rydberg excitation is collapsed into a specific product state of the many-body system. Nonetheless, the motional state is still well described by the initial single-particle state of the bosonic ensemble mentioned before, except for an imparted momentum due to the two laser pulses. Specifically, we consider the atom before ionization to be confined in a harmonic trap with trap frequencies $\omega_\xi = 2\pi\nu_\xi$ and single-particle eigenenergies $E_{n_\xi}^{(\xi)} = \hbar\omega_\xi n_\xi$ with $n_\xi = 0, 1, 2, \dots$, that is, we neglect interactions among them. Moreover, we assume that the ionization imparts a momentum $k_{0,\xi}$ along the ξ -direction at $t = t_0$. Assuming that the atom is not completely cooled down to the trap ground state, the density matrix reads

$$\begin{aligned} \hat{\rho}_\xi(t_0) &= \left(1 - e^{-\frac{\hbar\omega_\xi}{k_B T_{\text{gas}}}} \right) e^{ik_{0,\xi} \hat{r}_\xi} \times \\ &\quad \times \sum_{n_\xi} e^{-\frac{E_{n_\xi}^{(\xi)}}{k_B T_{\text{gas}}}} |n_\xi\rangle \langle n_\xi| e^{-ik_{0,\xi} \hat{r}_\xi}, \end{aligned} \quad (25)$$

where $|n_\xi\rangle$ are the states of the harmonic oscillator with frequency ω_ξ and T_{gas} the gas temperature.

The initial value of the squared momentum along the

direction ξ is calculated as the average $\text{Tr}\{\hat{p}_\xi^2 \hat{\rho}_\xi(t_0)\}$ over the initial density matrix $\hat{\rho}_\xi(t_0)$. Using the definition of the momentum operator $\hat{p}_\xi = i\sqrt{\hbar M \omega_\xi/2}(\hat{a}^\dagger - \hat{a})$ and the properties of the trace, we get to the following formula for the initial squared momentum [53]:

$$\langle \hat{p}_\xi^2(t_0) \rangle = \left(1 - e^{-\frac{\hbar \omega_\xi}{k_B T_{\text{gas}}}}\right) \times \sum_n e^{-\frac{\hbar \omega_\xi}{k_B T_{\text{gas}}}} n \left[\frac{\hbar M \omega_\xi}{2} (2n+1) + \hbar^2 k_{0,\xi}^2 \right]. \quad (26)$$

In a similar fashion, we obtain the initial squared position:

$$\langle \hat{r}_\xi^2(t_0) \rangle = \left(1 - e^{-\frac{\hbar \omega_\xi}{k_B T_{\text{gas}}}}\right) \sum_n e^{-\frac{\hbar \omega_\xi}{k_B T_{\text{gas}}}} n \frac{\hbar}{2M \omega_\xi} (2n+1), \quad (27)$$

whereas the initial values of the covariance \hat{c}_ξ is always zero.

Ion	
Kinetic energy	$1.3 \cdot 10^{-7}$ eV
Temperature	1 mK
Excess velocity	530 mm/s
BEC	
Atom number	$3 \cdot 10^4$
Peak density	$2 \cdot 10^{14}$ cm $^{-3}$
Speed of sound	2.7 mm/s
Trap frequencies ν_ξ	120 – 170 Hz
Cloud radius	5 μ m

TABLE I. Typical experimental parameters for the homonuclear system $^{87}\text{Rb}^+ / ^{87}\text{Rb}$. The initial kinetic energy of the $^{87}\text{Rb}^+$ ion corresponds to a two-photon ionization via a virtual intermediate state by an intense femtosecond laser pulse with a duration of 200 fs near the ionization threshold. The parameters of the Bose-Einstein condensate are typical for ^{87}Rb atoms in an optical dipole trap.

Ionization with an ultrashort laser pulse - Another interesting scenario is the ionization procedure employed in Ref. [44], where a femtosecond laser is focused down to a waist $w_0 = 1 \mu\text{m}$, which is small compared to the size of the atomic cloud. Within a single pulse of 215 fs duration, the number of ionized atoms can be precisely tuned with the laser peak intensity. More details of the experimental procedure are reported in Sec. V. In this case, the ionization process can be interpreted as a continuous measurement process, where the focused laser beam with Gaussian envelop $e^{-2\mathbf{r}^2/w_0^2}$ is the probe field [54]. Therefore, the probability of finding the ion

at position \mathbf{r} is given by

$$P(\mathbf{r}) = \sqrt{\frac{2}{\pi w_0^2}} \int_{\mathbb{R}^3} d\mathbf{r}' e^{-\frac{2}{w_0^2}(\mathbf{r}'-\mathbf{r})^2} \langle \mathbf{r}' | \hat{\rho}_{\text{BEC}} | \mathbf{r}' \rangle \quad (28)$$

namely, the convolution between the Gaussian beam and the probability density $\langle \mathbf{r}' | \hat{\rho}_{\text{BEC}} | \mathbf{r}' \rangle$ of the condensate. The initial density distribution of the ion can be therefore identified with Eq. (28), while the initial ion's wave function can be defined, apart from a global phase, as the square root of $P(\mathbf{r})$, with spatial extent determined by the beam-waist. Consider an ultra-cold bosonic gas with experimental parameters as listed in Tab. I that corresponds to the experimental situation reported in Ref. [44]. Hence, the bosonic density distribution is well described by the Thomas-Fermi profile, which reads

$$\langle \mathbf{r}' | \hat{\rho}_{\text{BEC}} | \mathbf{r}' \rangle = n_0 \left[1 - \left(\frac{x'}{R_x} \right)^2 - \left(\frac{y'}{R_y} \right)^2 - \left(\frac{z'}{R_z} \right)^2 \right] \quad (29)$$

in the region defined by the ellipsoid with radii R_ξ ($\xi = x, y, z$), and zero elsewhere. The definitions of R_ξ and other details on the Thomas-Fermi approximation can be found, e.g., in Ref. [55]. The integral in Eq. (28) can be computed numerically in spherical coordinates. As anticipated, we define the initial ion wavefunction as $\Psi_0(\mathbf{r}) = e^{ik_{0,\xi} \hat{r}_\xi} \sqrt{P(\mathbf{r})}$, where we added the contribution of the initial imparted momentum along the ξ direction.

The initial state of the ion is used to calculate the initial conditions for the equations of motion of the expectation values given in Sec. III A. For the parameters considered in our study, however, no significant differences have been observed between the initial states obtained after photoionization of a Rydberg atom or of a ground-state atom with a femtosecond laser pulse. Albeit the numerical analysis in the following section refers to the thermal state (25), we note that the choice of one or the other initial condition does not affect the conclusions we are going to outline in Sec. IV.

IV. RESULTS

In this section, we report on the dynamics of an ion with initial momentum in an ultracold bosonic cloud. The evolution of the ion temperature, velocity and position are obtained by numerically solving Eq. (21) and Eq. (24). We investigate the impact of different experimental parameters such as the initial momentum of the ion k_0 , the density of the atomic cloud n_0 and the atom-ion scattering length a_{ai} on the ion dynamics. Unless stated differently, the system consists of a $^{87}\text{Rb}^+$ ion in a bosonic bath of ^{87}Rb atoms at $T_{\text{gas}} = 1$ nK, with $n_0 = 2 \cdot 10^{14}$ cm $^{-3}$, and $a_{\text{ai}} \simeq R^*$ corresponding to the potential in Fig. 2 (see also Tab. I). Let us note that the results obtained at fixed density do not depend on the specific value of the temperature of the ultracold

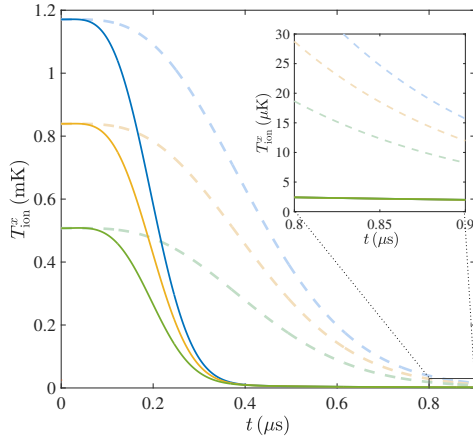


FIG. 3. Ion temperature $T_{\text{ion}}^x = \langle \hat{p}_x^2 \rangle / (2Mk_B)$ as a function of time for $n_0 = 2 \cdot 10^{14} \text{ cm}^{-3}$ (solid lines) and $n_0 = 2 \cdot 10^{13} \text{ cm}^{-3}$ (light dashed lines). (a) The initial ion temperatures correspond to $T_{\text{ion}}^x = 1.17 \text{ mK}$ (blue), $T_{\text{ion}}^x = 0.84 \text{ mK}$ (orange) and $T_{\text{ion}}^x = 0.51 \text{ mK}$ (green). The inset shows a magnification of the main plot in the range from $t = 0.8 \mu\text{s}$ to $t = 0.9 \mu\text{s}$, as indicated. From the latter, we observe that the temperature corresponding to $n_0 = 2 \cdot 10^{14} \text{ cm}^{-3}$ converges to a value of around $2 \mu\text{K}$, independent on the initial condition.

bosonic gas, T_{gas} , which is chosen according to the discussion in Appendix A. Moreover, we consider the momentum imparted at $t = t_0$ to be directed along x , and we focus on the dynamics along the same direction. In fact, although the initial conditions for $T_{\text{ion}}^{y,z}$ may be different from zero depending on the choice of the initial state and the direction of the imparted momentum, the decoupling of the three directions allows us to consider just one direction without any loss of generality [56].

A. Cooling dynamics

We start by comparing the ion temperature as a function of time for different initial conditions.

Initial temperature of the ion - In Fig. 3, the results corresponding to initial ion temperatures in the millikelvin regime are shown. We can observe from the main plot and inset that the time required for T_{ion}^x to converge to $2 \mu\text{K}$ is almost independent on its initial value at $t = t_0$. In other words, the larger the initial momentum, the faster the cooling. On the other hand, the cooling dynamics is strongly affected by the condensate density n_0 , as can be observed by comparing the dark solid lines with the light dashed lines. We refer to Appendix D for a comparison with the dynamics

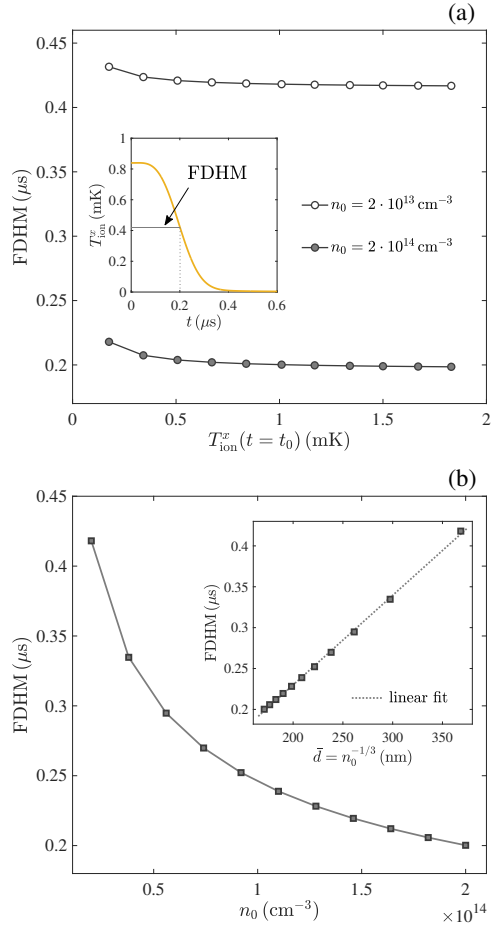


FIG. 4. (a) Main plot: full duration at half maximum (FDHM) for two atomic densities as a function of the initial ion temperature; solid lines connecting the points are a mere guide to the eye. Inset: definition of FDHM. (b) FDHM for $T_{\text{ion}}^x(t = t_0) \simeq 1.01 \text{ mK}$ and $a_{\text{ai}} \simeq R^*$ (gray squares). Main plot: FDHM as a function of the gas density n_0 ; the solid line connecting the points is a mere guide to the eye. Inset: FDHM as a function of the average particle separation $\bar{d} = 1/\sqrt[3]{n_0}$; the dotted line is a linear function fitting the data.

corresponding to lower initial ion temperatures.

Atomic density - To systematically study the cooling dynamics, we define the full duration at half maximum (FDHM) as the time it takes for the ion temperature to reach half of its initial value [see inset of Fig. 4(a)]. Note that small values of the FDHM correspond to higher cooling rates: the larger is the FDHM, the smaller is the atom-ion cross section and vice versa. The time-scale of the cooling dynamics is similar to the average time-scale for classical collisions with one

atom in the bath given by $t = d_{\text{WS}}/v_x(t_0) = 265$ ns for an initial velocity of $v_x(t_0) = 0.4 \text{ ms}^{-1}$ and with $d_{\text{WS}} = (3/(4\pi n_0))^{1/3} = 106$ nm being the Wigner-Seitz radius at a condensate density of $n_0 = 2 \cdot 10^{14} \text{ cm}^{-3}$.

The circles in the main plot of Fig. 4(a) show that the FDHM is barely affected by the initial temperature of the ion. Moreover, the same weak dependence is observed for $n_0 = 2 \cdot 10^{14} \text{ cm}^{-3}$ (full circles) and $n_0 = 2 \cdot 10^{13} \text{ cm}^{-3}$ (empty circles). Figure 4(b) quantifies how effective the cooling of the ion is, depending on the density of the condensate (main plot) and on the mean distance between the atoms (inset). The initial temperature is fixed to $T_{\text{ion}}^x(t_0) \simeq 1.1 \text{ mK}$ and the gray squares are the values of the FDHM for different n_0 (or $\bar{d} = 1/\sqrt[3]{n_0}$ in the inset). As expected, a denser gas ensures a faster cooling (i.e. a smaller FDHM) due to the stronger impact of the atom-ion interaction on the ion dynamics. We observe that the FDHM increases linearly with the mean distance. Both the gas and the ion are treated fully three-dimensionally in the master equation. However, due to the Lamb-Dicke approximation, solutions are given by the tensor product of the density matrices of the three spatial directions. Fig. 4(b) exemplary shows the result for the x direction as the dynamics is effectively one-dimensional for the ion moving into a fixed direction. Because of this, the ion dynamics is characterized by the mean distance between the bosons, which accounts for the rate of atom-ion collisions in one direction: the larger the distance, the larger the FDHM, i.e., the smaller is the cooling rate and vice versa. This is in contrast with the expectation that the cooling rate is linearly proportional to the gas density. In the future it will be interesting to find solutions to solve the master equation without relying on the Lamb-Dicke approximation to investigate the density dependence of the FDHM as well as a maximum capture velocity for the cooling and pinning dynamics.

Atom-ion scattering length - Another feature that we point out is the dependence of the cooling dynamics on the atom-ion scattering length. The recent observation of Feshbach resonances in compound atom-ion systems [17] confirms the possibility of tuning the atom-ion interaction via an external magnetic field. This dependence can be exploited in experiments to achieve a higher cooling rate without changing parameters such as the atomic density or the ion initial temperature. Since the cooling dynamics is closely related to the elastic cross-section, no strong dependence on the scattering length would be expected at high collision energies, where the ion can be treated classically. In contrast, such a dependence could be expected at ion temperatures on the order of μK and below, where fewer partial waves contribute to scattering events and quantum effects become relevant. On this regard, we note that the number of partial waves contributing in the millikelvin regime is on the order of ten. In the main plot of Fig. 5 the non-trivial dependence of the

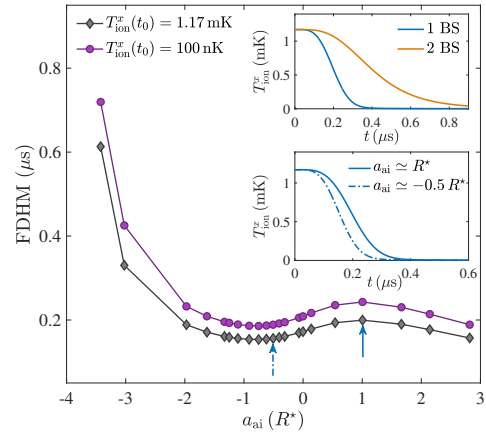


FIG. 5. Main plot: scattering length dependence of the FDHM for $T_{\text{ion}}^x(t_0) = 1.17 \text{ mK}$ (gray diamonds) and $T_{\text{ion}}^x(t_0) = 100 \text{ nK}$ (purple circles). The lines are a mere guide to the eye. Lower inset: time dependence of the ion temperature for two values of the atom-ion scattering length and initial ion temperature $T_{\text{ion}}^x = 1.17 \text{ mK}$. The two values of the scattering length are indicated in the main plot by the two arrows. Upper inset: time dependence of the ion temperature for two regularized potentials supporting a different number of two-body bound states: one bound state with $E_{\text{BS}} \simeq -1.43 E^*$ (blue) and two bound states with $E_{\text{BS},1} \simeq -1.39 E^*$ and $E_{\text{BS},2} \simeq -152.78 E^*$ (orange).

FDHM on a_{ai} is shown for two values of the initial temperature: $T_{\text{ion}}^x(t_0) = 1.17 \text{ mK}$ and $T_{\text{ion}}^x(t_0) = 100 \text{ nK}$, the latter being on the order of the typical energy of the atom-ion potential $E^*/k_B = 79 \text{ nK}$. We observe a similar behavior for the two initial conditions. However, considering values of a_{ai} between $\sim -2 R^*$ and $\sim 2 R^*$, the difference between the maximum and minimum FDHM for the lower initial temperature of the ion is 23% larger compared to the higher initial temperature ($0.057 \mu\text{s}$ and $0.046 \mu\text{s}$, respectively). This shows that the dependence is indeed more pronounced when the collision energy is lower, as expected. The noticeably larger values of the FDHM observed for the two values of a_{ai} below $-2 R^*$ could indicate the failure of the Born approximation due to the strong atom-ion coupling. Another hypothesis to explain the dependence of the FDHM on a_{ai} could be the binding of atoms to the ion. This would increase the effective mass of the ion, which would modify the scattering parameters with the bath as well as the cooling dynamics.

Finally, we consider a regularized atom-ion potential supporting two two-body bound states. In the upper inset of Fig. 5 we can observe that the cooling dynamics does not depend qualitatively on the number of such bound states. Although the FDHM corresponding to two bound states is about twice the value obtained with one bound state, the reduction of T_{ion}^x takes place on

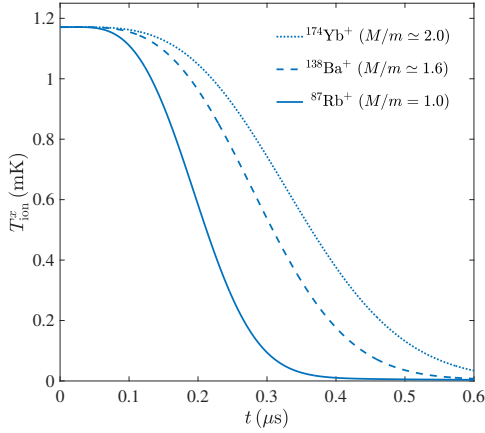


FIG. 6. Time dependence of ion temperature for different ion species immersed in a gas of ^{87}Rb atoms with density $n_0 = 2 \cdot 10^{14} \text{ cm}^{-3}$. The initial ion temperature is $T_{\text{ion}}^x = 1.17 \text{ mK}$. The corresponding values of R^* are the following: 265.81 nm for $^{87}\text{Rb}^+$, 294.67 nm for $^{138}\text{Ba}^+$ and 307.23 nm for $^{174}\text{Yb}^+$.

similar timescales in the two cases. We remark, however, that the choice of the potential with one bound state is justified by the fact that the occupation of deeply bound states is much less likely compared to the occupation of loosely bound states because of the large energy gap between them (see, e.g. [50]).

Ionic species - Similar simulations are repeated for different ionic species moving in the ^{87}Rb atomic gas. In Fig. 6, the time dependence of T_{ion}^x is shown for $^{138}\text{Ba}^+$ and $^{174}\text{Yb}^+$ compared to the rubidium ion considered in the previous analysis. The observed behavior is qualitatively the same, but the plot shows that higher values of the ion-atom mass ratio M/m result in slower cooling. We remark that the use of different ions affects the value of the ratio M/m , hence, the range of validity of the Lamb-Dicke approximation (see Appendix A).

B. Pinning dynamics

Now, we discuss the evolution of the expectation value of the position and momentum of the ion given by Eq. (24). Note that all results are given in one dimension, since the initial momentum k_0 is assumed to be along x .

Ion velocity evolution - In the main plot of Fig. 7, we observe how the ion's velocity decays, reaching a value on the order of $10^{-10} \text{ m s}^{-1}$ at $t = 0.9 \mu\text{s}$. Similar to what was observed for the decay of T_{ion} , the time required

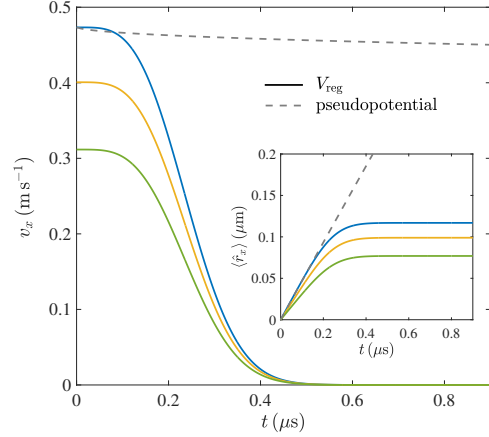


FIG. 7. Time dependence of the ion's velocity $v_x = \langle \hat{p}_x \rangle / M$ (main plot) and position (inset) along the x -direction for different initial ion velocities: $v_x = 0.47 \text{ m s}^{-1}$ (blue), $v_x = 0.40 \text{ m s}^{-1}$ (orange) and $v_x = 0.31 \text{ m s}^{-1}$ (green). Solid lines correspond to a regularized atom-ion potential with $a_{\text{ai}} \simeq R^*$, whereas the gray dashed line corresponds to a neutral impurity in a gas with a short-range pseudopotential with $a_{\text{ai}} \simeq 0.05 R^*$.

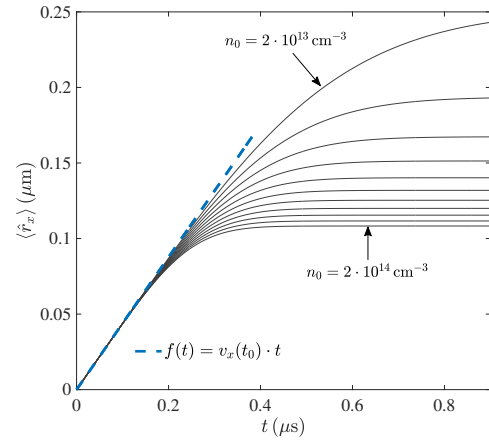


FIG. 8. Time dependence of the ion's position for $T_{\text{ion}}^x(t_0) = 1.17 \text{ mK}$ and different gas densities (solid gray lines). The values of n_0 are chosen uniformly in the interval between the indicated values of $n_0 = 2 \cdot 10^{13} \text{ cm}^{-3}$ and $n_0 = 2 \cdot 10^{14} \text{ cm}^{-3}$. The dashed blue line represents the position of a particle moving at constant velocity.

for the velocity to decay depends only weakly on its initial value. For this reason, the ion's final positions are reached at approximately the same time for all values of $v_x(t_0) = \hbar k_0 / M$, as shown in the inset of Fig. 7. This result is completely different from the dynamics of a neutral impurity in a bosonic bath interacting via a

short-range pseudopotential, as shown in Fig. 7 by the dashed gray lines. On the timescale relevant for the atom-ion dynamics, the neutral impurity does not come to rest, and the neutral impurity moves with constant velocity through the gas (see inset). We attribute this difference to the long-range character of the polarization potential, which cannot be adequately described by taking only the s -wave scattering into account. For a meaningful comparison, we choose a value of $0.05 R^*$ for the impurity-gas scattering length, corresponding roughly to the range of the van der Waals interaction between ^{87}Rb atoms. Note that choosing a scattering length comparable to R^* for the neutral impurity would correspond to the unitary limit, and the validity of the master equation description would likely no longer hold.

Ion position evolution - The onset of the pinning dynamics is affected by the gas density as shown in Fig. 8. There, the dashed blue line represents the position of a particle moving with constant velocity, while the gray solid lines correspond to the ion's position in the presence of a condensate with different densities. The plot shows that, at short times, the ion's position is not affected by the presence of the gas, while at later times it is deflected to its final value at a rate increasing with the density.

Interestingly, the initial linear time dependence of the ion dynamics in the gas is an indication of the polaronic behavior. Specifically, due to its interaction with the bosonic bath, the ion is dressed by phononic excitations in such a way that it can be considered as a quasi particle moving freely within the gas. However, as time evolves, effects such as dephasing of the phonon modes become dominant until the ion comes to rest.

Friction coefficient evolution - Since the motion of the ion cannot be explained by a classical trajectory, we have analyzed the equation more closely for the expectation value of the momentum [second line of Eq. (24)]. That equation can be compared to the classical equation of a particle subject to a friction. On this purpose, we rewrite it as

$$\frac{d}{dt}\langle\hat{p}_\xi\rangle = -\Gamma(t)\langle\hat{p}_\xi\rangle, \quad (30)$$

where we defined the friction $\Gamma(t)$ according to Eq. (24). In Fig. 9 the time dependence of Γ for two values of the scattering length and for a neutral particle is shown. In a classical scenario the friction coefficient would be constant in time, whereas here it is explicitly time-dependent. Since all properties of the atomic bath are constant in time, the time-dependent friction observed here can only be explained by a change in the properties of the impurity. Moreover, we note that the qualitative difference between the friction coefficient corresponding to the neutral and charged particle highlights the key role of the long-range atom-ion potential in our predictions. In the neutral case, the time evolution of the friction

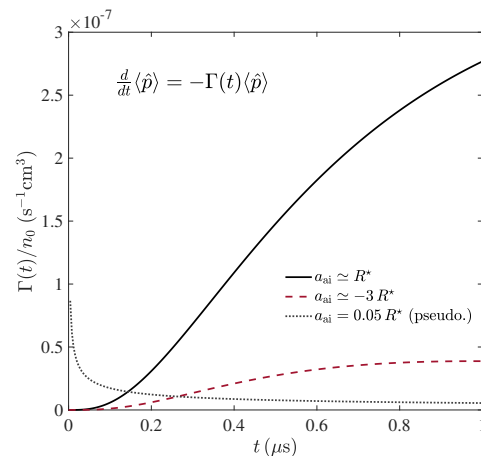


FIG. 9. Time-dependent friction in units of the condensate density n_0 as a function of time for two different atom-ion scattering lengths (solid and dashed) and for a neutral impurity (dotted).

can be associated to the formation of a Bose polaron: as the impurity moves through the condensate, it gets dressed by phononic excitations, resulting in the reduction of the friction coefficient. For the ionic impurity, a transient phase is observed at very short times where the friction is almost zero for both scattering lengths. This phase corresponds to the regime where the particle is not affected by the presence of the gas, as shown in Fig. 8, that is, a polaronic-type behavior. The increase in Γ at longer times is responsible for the pinning dynamics. We note that for large negative scattering lengths, we observe much smaller values of Γ , corresponding to a slower pinning. While for shorter time-scales the Bogoliubov phonon modes behave coherently due to the superfluidity of the bath, at longer times coherence is reduced, which we attribute to dephasing of the phononic modes. Whether this phenomenon is connected to the formation of two-body atom-ion states supported by our regularized interaction is not possible to quantify in the current formulation of the master equation. It will be interesting in the future to investigate whether the formation of many-body bound states as those predicted in Refs. [1–3] occur and to understand if they are responsible of the pinning dynamics we observe in this work. For this, the description of the atomic gas needs to be modified and the back action of the ion on the atomic gas has to be included.

V. EXPERIMENTAL CONSIDERATIONS

In this section, we will describe experimental settings that should allow investigating the cooling and pinning dynamics of an ion in an ultracold bosonic gas. Finally,

previously neglected inelastic processes and their impacts on the ionic dynamics are discussed.

Results validation in future experiments - In order to experimentally validate the calculated dynamics, it is necessary to instantaneously create an ion out of an ultracold bosonic gas with a defined, but tunable, initial velocity v_x . Two-photon ionization via a virtual intermediate state by an intense femtosecond laser pulse with adjustable wavelength gives rise to a tunable excess energy E_{exc} . This results in an adjustable initial velocity of the ion (compare Fig. 1). The experiments in Refs. [44, 47] use ultrashort laser pulses of ~ 200 fs duration and a rather high excess energy of $E_{\text{exc}} = 0.68$ eV, which corresponds to an initial kinetic energy of the ^{87}Rb ion of ~ 4 μeV or an initial temperature of $T_{\text{ion}} = 33$ mK [44]. However, by using an optical-parametric amplifier, the wavelength of the laser pulses can be tuned close to the ionization threshold so that the excess energy is ultimately limited by the bandwidth of the laser pulse due to the time-energy uncertainty relation. A Gaussian laser pulse of 200 fs duration corresponds to a kinetic energy of 115 neV for a ^{87}Rb ion, which relates to an initial temperature of $T_{\text{ion}} = 890$ μK . Such a regime is covered by the initial parameters of our calculations and would allow stopping the ion within the BEC.

In order to resolve the cooling and pinning dynamics of the ion, it needs to be created in a localized region much smaller than the extent of the BEC. This is possible by focusing the laser beam to a diffraction limited spot with a high-resolution microscope objective [44]. Because two 594 nm photons are sufficient to excite the outermost electron of ^{87}Rb just over the ionization threshold, such a region would extend over the distance of ~ 600 nm. Subsequently, it is necessary to trace the position of the ion with a high spatial and temporal resolution on the order of 100 nm and 100 ns, respectively (compare Fig. 8). An ion microscope [57, 58] is capable of directly imaging the ion's position with a sufficient resolution as it does not rely on optical detection, thus surpassing the resolution limit of visible light. However, to avoid constant acceleration of the ion, it is necessary to compensate for electric stray fields as well as possible. Typically, related experiments reach a residual stray field level of $E_{\text{stray}} = 0.1$ V m $^{-1}$ [24]. Such a field would cause an acceleration of $a = eE_{\text{stray}}/M$, yielding an additional velocity of $v = at = 0.1$ m s $^{-1}$ during the calculated time span of $t = 1$ μs that is below the initial velocities assumed here. Thus, nonetheless, a slowing of the ion should be observable experimentally. A more sophisticated approach would need the derivation of a master equation with a constant acceleration term due to the stray field, which is beyond the scope of this work, but an obvious extension for future work.

Inelastic processes - In our analysis, we have studied the cooling dynamics of the ion, which arises from elastic collisions with the atoms of the gas. However, in

the case of homonuclear systems such as $^{87}\text{Rb}^+ / ^{87}\text{Rb}$, resonant charge exchange (RCx) can be relevant [59, 60]. This phenomenon consists of the charge of the ion being transferred to a neutral atom after a collision. To estimate its impact, let us first recall that two-body collisions can be divided into two groups: glancing collisions, where the particles trajectories are slightly deflected, and Langevin collisions, which can be classically represented as the two particles getting close in a spiraling motion and being scattered isotropically. In the same classical picture, Langevin collisions occur when the impact parameter of the collision is smaller than a critical value $b_c = (2C_4/E_{\text{col}})^{1/4}$ [13], where C_4 is the prefactor of the polarization potential and E_{col} is the energy of the collision. It has recently been observed in Ref. [61] that RCx associated with glancing collisions can be the dominant process for collisional energies higher than 100 K $\cdot k_B$, leading to fast cooling of the ion (so-called swap cooling). On the other hand, for lower energies, RCx can only occur by Langevin collisions, with a cross section given by $\sigma_{\text{RCx}} = \sigma_{\text{Lgv}}/2$. For the $^{87}\text{Rb}^+ / ^{87}\text{Rb}$ system with $E_{\text{col}} = 1$ mK $\cdot k_B$, σ_{RCx} is about 10 times smaller than the elastic cross section [13, 59] and remains significantly lower than the latter even for $E_{\text{col}} = 2$ $\mu\text{K} \cdot k_B$, where it reaches 1/3 of the elastic cross section. Hence, resonant charge exchange is never dominant in the energy range of the ion. However, note that the previous reasoning is based on a semi-classical analysis, which is accurate down to 1 mK $\cdot k_B$. A more accurate estimation for lower energies requires studies at the quantum level that are not yet available. Similar arguments can be applied to three-body recombination processes that lead to the formation of molecules. In this regard, experiments involving a trapped $^{87}\text{Rb}^+$ ion immersed in an ultracold cloud of ^{87}Rb atoms [18] showed that the three-body recombination rate is on the order of a second for values of the atomic density, comparable to the ones we considered in this work. Although our study does not involve a trap and our collision energies are lower than the ones considered in the aforementioned experiment, we can assume the formation of molecules not to play a significant role due to the short time scales in which we expect the cooling and pinning dynamics to take place.

VI. SUMMARY AND CONCLUSIONS

We studied the behavior of an ion moving in an ultracold bosonic gas with an initial momentum resulting from an ionization process. To this end, in Sec. III, we derived the quantum master equation reported in Eq. (B10). Based on this equation, we computed the differential equations for the expectation value of the squared momentum [see Eq. (21)] and the expectation value of the position and momentum [see Eq. (24)]. We numerically solved these differential equations for different values of initial momentum k_0 , condensate density n_0 , and atom-

ion scattering length a_{ai} and showed the corresponding results in Sec. IV. As a key observation, we demonstrated that the ion temperature defined as $T_{\text{ion}} = \langle \hat{p}^2 \rangle / (2Mk_{\text{B}})$ decays in time. We quantified this behavior by defining the FDHM (i.e., full duration at half maximum) as the time required for T_{ion} to halve. Interestingly, we found a linear dependence of the FDHM on the mean distance between the bosons. Expanding on our key point of short cooling times, we found that the FDHM is almost independent of the initial temperature of the ion (Fig. 4a), whereas it is noticeably affected by the density of the condensate (Fig. 4b). Similarly, we observed that the ion's velocity drops by nine orders of magnitude in a time that is independent of the ion's initial velocity (Fig. 7), which we attribute to incoherent dynamics of the phonon modes as a consequence of the enhancement of the friction coefficient (Fig. 9). In conclusion, our study predicts the cooling and pinning of the ion due to its interaction with the surrounding ultracold bosonic gas. Moreover, we observed a substantial robustness of the results against the parameters involved. These findings are relevant in view of the upcoming experiments discussed in Sec. V, as the time and length scales of the ion's dynamics are compatible with the expected experimental resolution.

ACKNOWLEDGEMENTS

This work is supported by the project NE 1711/3-1 of the Deutsche Forschungsgemeinschaft (DFG). Moreover, support by the Cluster of Excellence ‘‘CUI: Advanced Imaging of Matter’’ of the DFG — EXC 2056 — project ID 390715994 is acknowledged.

Appendix A: Validity of the Lamb-Dicke approximation

The master equation derived in Sec. III relies on the Lamb-Dicke approximation. We recall that the latter results in the expansion in Eq. (20) and it is based on the assumption that the average wavelength of the atoms in the bath is much larger than the width of the ion. Here, we discuss the fulfillment of such a condition during the evolution of the system in question. Of course, the assumption has to hold regardless of the choice of the initial state. Since the spatial extension of the ion wave function at the initial time must fulfill the approximation as well, this imposes a condition on the temperature of the gas.

Let us consider, for example, the ionization process via a Rydberg state. In order to hold, the Lamb-Dicke approximation imposes that $\lambda_{\text{dB}}(T_{\text{gas}}) \gg \sigma_{\text{av}}$, where σ_{av} is the geometric average of $\sigma_{\xi} = \sqrt{\langle \hat{r}_{\xi}^2 \rangle - \langle \hat{r}_{\xi} \rangle^2}$ along the three directions and represents the width of the ion wave packet (i.e., the standard deviation), while $\lambda_{\text{dB}}(T_{\text{gas}})$ is the de Broglie wavelength of the bosons in the gas at

temperature T_{gas} . A rough estimate is given by considering the ion to be in the ground state of the harmonic trap in Eq. (25). Thus, we have at the initial time $\sigma_{\text{av}} = \sqrt{\hbar / (2M\omega_{\text{av}})}$ with $\omega_{\text{av}} = (\omega_x \omega_y \omega_z)^{1/3}$ being the geometrical average of the harmonic trap frequencies. For a homonuclear system and with the trap frequencies shown in Tab. I, we get the following condition on the gas temperature

$$T_{\text{gas}} \ll \frac{4\pi\hbar M}{k_{\text{B}} m} \omega_{\text{av}}, \quad (\text{A1})$$

which yields a value of T_{gas} on the order of nK. At such a low temperature, the exponential weights in the sum of Eq. (27) barely affect the value of $\langle \hat{r}_{\xi}^2(t_0) \rangle$. For this reason, we can safely use Eq. (A1) as a condition for our system to be in the Lamb-Dicke regime at the initial time. Note that the latter statement could be violated for ion-atom systems with a different mass ratio.

In the case of ionization via an ultrashort laser pulse, the condition for the validity of the Lamb-Dicke approximation can be simply verified by comparing the de Broglie wavelength of the gas with the value of the laser beam waist w_0 . Considering $w_0 = 1 \mu\text{m}$, as it is expected in future experiments, we can impose a condition on T_{gas} . Similarly, the required value is on the order of nK.

The validity of the Lamb-Dicke approximation at later times, however, has to be monitored numerically by solving the equations for the first [Eq. (24)] and second order moments [Eq. (21) and (22)]. In Fig. 10, we show the time evolution of the spatial width of the ion σ_{av} for three different initial temperatures. As it can be observed, the ratio between σ_{av} and the de Broglie wavelength is always on the order of one tenth, confirming that the Lamb-Dicke approximation is rather well justified.

Appendix B: Details on the master equation

For the sake of completeness, let us retrace the main steps of the derivation starting from the von Neumann equation for the density matrix of the total system (ion plus bath) $\hat{\chi}(t)$:

$$\frac{d}{dt} \hat{\chi}(t) = -\frac{i}{\hbar} [\hat{H}, \hat{\chi}(t)]. \quad (\text{B1})$$

Following the standard quantum-optical approach (see, e.g., Ref. [51]), we write the density matrix in the interaction picture as

$$\tilde{\chi}(t) = \hat{U}^\dagger(t) \hat{\chi}(t) \hat{U}(t) \quad (\text{B2})$$

with

$$\hat{U}(t) = \exp \left[-\frac{i}{\hbar} (\hat{H}_{\text{ion}} + \hat{H}_{\text{bath}}) t \right]. \quad (\text{B3})$$

Recalling the definition of the total Hamiltonian $\hat{H} = \hat{H}_{\text{ion}} + \hat{H}_{\text{bath}} + \hat{H}_{\text{int}}$, we obtain the following equation

$$\frac{d}{dt} \tilde{\chi}(t) = -\frac{i}{\hbar} [\hat{H}_{\text{int}}, \tilde{\chi}(t)], \quad (\text{B4})$$

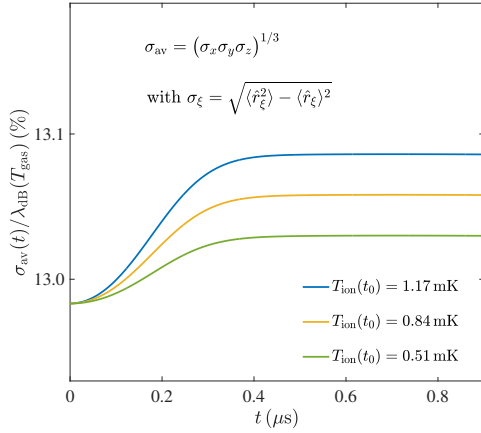


FIG. 10. Average spatial width of the ion as a function of time as a percentage of the atomic de Broglie wavelength $\lambda_{dB}(T_{gas})$ with $T_{gas} = 1$ nK and $n_0 = 2 \cdot 10^{14}$ cm $^{-3}$. The three lines correspond to the three initial temperatures considered in Fig 3(a).

whose formal solution reads

$$\tilde{\chi}(t) = \tilde{\chi}(0) - \frac{i}{\hbar} \int_0^t dt' [\tilde{H}_{int}(t'), \tilde{\chi}(t')]. \quad (\text{B5})$$

Here, \tilde{H}_{int} is the interaction Hamiltonian in the interaction picture.

We now insert Eq. (B5) in Eq. (B4) and we get

$$\begin{aligned} \frac{d}{dt} \tilde{\chi}(t) = & -\frac{i}{\hbar} [\tilde{H}_{int}(t), \tilde{\chi}(0)] \\ & - \frac{i}{\hbar^2} \int_0^t dt' [\tilde{H}_{int}(t), [\tilde{H}_{int}(t'), \tilde{\chi}(t')]]. \end{aligned} \quad (\text{B6})$$

In order to proceed, we assume that at the initial time $t = 0$ the system and the bath are not correlated. This allows the total density matrix to be factorized as $\tilde{\chi}(0) = \tilde{\rho}(0) \otimes \hat{B}_0$, where $\tilde{\rho}(0) = \hat{\rho}(0)$ is the initial density matrix of the ion, while \hat{B}_0 is the initial density matrix of the Bose gas at thermal equilibrium

$$\hat{B}_0 = \frac{e^{-\beta(\hat{H}_{bath} - \mu_G \hat{N})}}{\mathcal{Z}}, \quad \mathcal{Z} = \text{Tr}_b \left\{ e^{-\beta(\hat{H}_{bath} - \mu_G \hat{N})} \right\}, \quad (\text{B7})$$

where $\beta = 1/(k_B T_{gas})$, \hat{N} is the bath number operator and the chemical potential of the gas μ_G is zero for a Bose gas below the critical temperature of condensation. Note that the same assumption was made in Ref. [43], where a Paul-trapped ion immersed in an ultracold gas was considered. In that case, the assumption was well justified, as the ion and the gas are typically prepared separately in experiments, and no interaction occurs before they are brought together. In the present case, we

note that part of the simulations will refer to a scenario where the ion is created after ionizing one of the atoms in the gas. However, the interaction between the gas atoms is weaker and of short-range nature compared to the atom-ion polarization potential. Given the fact that the ionization process occurs on a time scale much shorter than every other time scale in our theoretical treatment, we can reasonably assume that at the very initial moment of the ion generation the interaction between the ion and the bath is weak. Only subsequently, it becomes stronger, but in such a way that the gas state is not significantly altered.

Now, we trace out the bath degrees of freedom from Eq. (B6) obtaining an equation for the reduced density matrix of the ion

$$\frac{d}{dt} \tilde{\rho}(t) = -\frac{1}{\hbar^2} \int_0^t dt' \text{Tr}_b \left\{ [\tilde{H}_{int}(t), [\tilde{H}_{int}(t'), \tilde{\chi}(t')]] \right\}, \quad (\text{B8})$$

and we finally perform the Born and Markov approximations. The Born approximation relies on the fact that the coupling between the ion and the bath is weak and that the bath is very large. Therefore, the factorization $\tilde{\chi}(t') \simeq \tilde{\rho}(t') \otimes \hat{B}_0$ is assumed to be valid at all times t' . Instead, the Markov approximation is based on the assumption that the dynamics of the bath is much faster than the dynamics of the ion. It consists of the replacement $\tilde{\rho}(t') \rightarrow \tilde{\rho}(t)$.

We then get to the so-called Redfield equation for the reduced ion density matrix in the interaction picture:

$$\frac{d}{dt} \tilde{\rho}(t) = -\frac{1}{\hbar^2} \int_0^t dt' \text{Tr}_b \left\{ [\tilde{H}_{int}(t), [\tilde{H}_{int}(t'), \tilde{\rho}(t) \otimes \hat{B}_0]] \right\}. \quad (\text{B9})$$

From this equation, we can explicitly substitute \tilde{H}_{int} and transform back to the Schrödinger picture. After tracing out the bath degrees of freedom, we get to the impurity master equation provided in Eq. (17), where we performed the change of variable $\tau = t - t'$ and $\hat{\mathbf{r}}(t, \tau) = \hat{U}(t) \hat{U}^\dagger(t - \tau) \hat{\mathbf{r}} \hat{U}(t - \tau) \hat{U}^\dagger(t)$.

Here, we report for the interested reader the complete master equation in the Born-Markov and Lamb-Dicke approximation:

$$\begin{aligned} \frac{d}{dt} \hat{\rho}(t) = & -\frac{i}{\hbar} [\hat{H}_S, \hat{\rho}(t)] \\ & - \sum_{\xi=x,y,z} \left\{ \lambda_\xi(t) [\hat{r}_\xi, \hat{\rho}(t) \hat{p}_\xi] - \lambda_\xi^*(t) [\hat{r}_\xi, \hat{p}_\xi \hat{\rho}(t)] \right. \\ & \left. + \phi_\xi(t) \left([\hat{r}_\xi, \hat{r}_\xi \hat{\rho}(t)] - [\hat{r}_\xi, \hat{\rho}(t) \hat{r}_\xi] \right) \right\}, \end{aligned} \quad (\text{B10})$$

where we have introduced the following functions:

$$\begin{aligned}\lambda_\xi(t) &= \sum_{\mathbf{q}} \Omega_q^2 q_\xi^2 \left\{ \frac{2n_q}{m\omega_q^2} [\cos(\omega_q t) + \omega_q t \sin(\omega_q t) - 1] \right. \\ &\quad \left. + \frac{1}{m\omega_q^2} [e^{i\omega_q t} (1 - i\omega_q t) - 1] \right\}, \\ \phi_\xi(t) &= \sum_{\mathbf{q}} \Omega_q^2 q_\xi^2 \left[(2n_q + 1) \frac{\sin(\omega_q t)}{\omega_q} \right].\end{aligned}\tag{B11}$$

The equations in Eq. (21), (22) and (24) are computed by explicitly calculating the expectation value of the corresponding observables with Eq. (B10) and by making use of the canonical commutation relations between the position and momentum operators.

Appendix C: Alternative squared momentum derivation

The same equation for the squared momentum in Eq. (21) can be derived with a different approach. In particular, we can calculate the variation in the ion's energy due to the presence of the gas. Specifically, to second order in the perturbative expansion we have

$$\begin{aligned}\frac{d\langle \hat{H}_{\text{ion}}(t) \rangle}{dt} &= \frac{i}{\hbar} \langle [\hat{H}_{\text{int}}(t), \hat{H}_{\text{ion}}] \rangle \\ &\quad - \frac{1}{\hbar^2} \int_0^t dt' \langle [\hat{H}_{\text{int}}(t'), [\hat{H}_{\text{int}}(t'), \hat{H}_{\text{ion}}]] \rangle,\end{aligned}\tag{C1}$$

where the average value $\langle \dots \rangle$ has to be intended as the trace over a density matrix. By choosing the total system density matrix as the one we defined for the derivation of the master equation, it is straightforward to show that the first term on the right hand side of Eq. (C1) vanishes due to the odd number of bath operators, while the second gives rise to terms proportional to $n_{\mathbf{q}}$ and $(n_{\mathbf{q}} + 1)$. After transforming back to the Schrödinger picture, performing the time integrals and the Lamb-Dicke approximation, one can retrieve Eq. (21).

Appendix D: Dynamics for low initial ion temperatures

Here we discuss the time evolution of the ion temperature obtained for initial values in a regime comparable to $E^*/k_B = 79$ nK and one order of magnitude higher. The results are shown in Fig. 11. Interestingly, the ion

is heated up at short times, meaning that the expectation value of its kinetic energy increases. At later times, the ion temperature exhibits a maximum. This is positioned around $\sim 0.2 \mu\text{s}$ for $n_0 = 2 \cdot 10^{-14} \text{ cm}^{-3}$ and $\sim 0.4 \mu\text{s}$ for $n_0 = 2 \cdot 10^{-13} \text{ cm}^{-3}$. Similarly to what we observed for initial ion energies in the mK-regime, the results in Fig. 11 only slightly depend on the initial temperature, while they are noticeably affected by the density

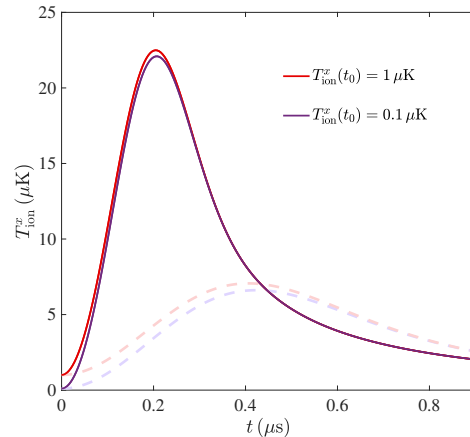


FIG. 11. Ion temperature $T_{\text{ion}}^x = \langle \hat{p}_x^2 \rangle / (2Mk_B)$ as a function of time for $n_0 = 2 \cdot 10^{14} \text{ cm}^{-3}$ (solid lines) and $n_0 = 2 \cdot 10^{13} \text{ cm}^{-3}$ (light dashed lines). The initial ion temperatures correspond to $T_{\text{ion}}^x = 1 \mu\text{K}$ (red) and $T_{\text{ion}}^x = 0.1 \mu\text{K}$ (purple).

of the condensate. In particular, a lower density (light dashed lines) corresponds to a shift towards larger times and flattening of the maximum. The behavior of T_{ion} at short times can be attributed to the long-range and attractive character of the atom-ion interaction generated after the ionization process. Contrarily to a neutral impurity, which interacts with a particle of the bath only when this is at its same position, the increased range of the polarization potential causes the ion to heat up due to the surrounding polarized bath atoms within a radius given by R^* . This dynamical behavior continues until the frequency of collisions with the atoms in the bath is large enough to cool down the moving ion. We note that a similar initial heating, although with a lower peak, is also observed with initial temperatures in the mK-regime. However, the scale of temperatures in the main plot of Fig. 3 does not allow this peaks to be appreciated. It is also important to remark that no maximum is observed in the expectation value of the ion momentum $\langle \hat{p}_x(t) \rangle$, meaning that the heating of the ion at short time does not correspond to an acceleration.

[1] Grigory E. Astrakharchik, Luis A. Peña Ardila, Richard Schmidt, Krzysztof Jachymski, and Antonio Negretti,

“Ionic polaron in a bose-einstein condensate,” *Communications Physics* 4, 94 (2021).

- [2] Esben Rohan Christensen, Arturo Camacho-Guardian, and Georg M. Bruun, “Charged polarons and molecules in a bose-einstein condensate,” *Phys. Rev. Lett.* **126**, 243001 (2021).
- [3] J. M. Schurer, A. Negretti, and P. Schmelcher, “Unraveling the structure of ultracold mesoscopic collinear molecular ions,” *Phys. Rev. Lett.* **119**, 063001 (2017).
- [4] Shanshan Ding, Michael Drewsen, Jan J. Arlt, and G. M. Bruun, “Mediated interaction between ions in quantum degenerate gases,” *Phys. Rev. Lett.* **129**, 153401 (2022).
- [5] Grigory E. Astrakharchik, Luis A. Peña Ardila, Krzysztof Jachymski, and Antonio Negretti, “Many-body bound states and induced interactions of charged impurities in a bosonic bath,” *Nature Communications* **14**, 1647 (2023).
- [6] U. Bissbort, D. Cocks, A. Negretti, Z. Idziaszek, T. Calarco, F. Schmidt-Kaler, W. Hofstetter, and R. Gerritsma, “Emulating solid-state physics with a hybrid system of ultracold ions and atoms,” *Phys. Rev. Lett.* **111**, 080501 (2013).
- [7] A. Negretti, R. Gerritsma, Z. Idziaszek, F. Schmidt-Kaler, and T. Calarco, “Generalized kronig-penney model for ultracold atomic quantum systems,” *Phys. Rev. B* **90**, 155426 (2014).
- [8] A. B. Michelsen, M. Valiente, N. T. Zinner, and A. Negretti, “Ion-induced interactions in a tomonaga-luttinger liquid,” *Phys. Rev. B* **100**, 205427 (2019).
- [9] Krzysztof Jachymski and Antonio Negretti, “Quantum simulation of extended polaron models using compound atom-ion systems,” *Phys. Rev. Research* **2**, 033326 (2020).
- [10] Lorenzo Oghittu and Antonio Negretti, “Quantum-limited thermometry of a fermi gas with a charged spin particle,” *Phys. Rev. Res.* **4**, 023069 (2022).
- [11] R. Côté, “Chapter two-ultracold hybrid atom-ion systems,” *Adv. At. Mol. Opt. Phys.* **65**, 67 (2016).
- [12] Michał Tomza, Krzysztof Jachymski, Rene Gerritsma, Antonio Negretti, Tommaso Calarco, Zbigniew Idziaszek, and Paul S. Julienne, “Cold hybrid ion-atom systems,” *Rev. Mod. Phys.* **91**, 035001 (2019).
- [13] A. Härter and J. Hecker Denschlag, “Cold atom-ion experiments in hybrid traps,” *Contemporary Physics* **55**, 33–45 (2014).
- [14] T. Feldker, H. FÜRST, H. Hirzler, N. V. Ewald, M. Mazzanti, D. Wiater, M. Tomza, and R. Gerritsma, “Buffer gas cooling of a trapped ion to the quantum regime,” *Nature Physics* **16**, 413–416 (2020).
- [15] H. Hirzler, T. Feldker, H. FÜRST, N. V. Ewald, E. Trimby, R. S. Lous, J. D. Arias Espinoza, M. Mazzanti, J. Joger, and R. Gerritsma, “Experimental setup for studying an ultracold mixture of trapped Yb^{+} - ${}^6\text{Li}$,” *Phys. Rev. A* **102**, 033109 (2020).
- [16] J. Schmidt, P. Weckesser, F. Thielemann, T. Schaetz, and L. Karpa, “Optical traps for sympathetic cooling of ions with ultracold neutral atoms,” *Phys. Rev. Lett.* **124**, 053402 (2020).
- [17] Pascal Weckesser, Fabian Thielemann, Dariusz Wiater, Agata Wojciechowska, Leon Karpa, Krzysztof Jachymski, Michał Tomza, Thomas Walker, and Tobias Schaetz, “Observation of feshbach resonances between a single ion and ultracold atoms,” *Nature* **600**, 429–433 (2021).
- [18] Arne Härter, Artjom Krükow, Andreas Brunner, Wolfgang Schnitzler, Stefan Schmid, and Johannes Hecker Denschlag, “Single ion as a three-body reaction center in an ultracold atomic gas,” *Phys. Rev. Lett.* **109**, 123201 (2012).
- [19] Lothar Ratschbacher, Christoph Zipkes, Carlo Sias, and Michael Köhl, “Controlling chemical reactions of a single particle,” *Nature Physics* **8**, 649–652 (2012).
- [20] Tomas Sikorsky, Ziv Meir, Ruti Ben-shlomi, Nitzan Akerman, and Roei Ozeri, “Spin-controlled atom-ion chemistry,” *Nature Communications* **9**, 920 (2018).
- [21] J. Pérez-Ríos, “Cold chemistry: a few-body perspective on impurity physics of a single ion in an ultracold bath,” *Molecular Physics* **119** (2021), 10.1080/00268976.2021.1881637.
- [22] Meirav Pinkas, Or Katz, Jonathan Wengrowicz, Nitzan Akerman, and Roei Ozeri, “Trap-assisted formation of atom-ion bound states,” *Nature Physics* (2023), 10.1038/s41567-023-02158-5.
- [23] K. S. Kleinbach, F. Engel, T. Dieterle, R. Löw, T. Pfau, and F. Meinert, “Ionic impurity in a bose-einstein condensate at submicrokelvin temperatures,” *Phys. Rev. Lett.* **120**, 193401 (2018).
- [24] F. Engel, T. Dieterle, T. Schmid, C. Tomschitz, C. Veit, N. Zuber, R. Löw, T. Pfau, and F. Meinert, “Observation of rydberg blockade induced by a single ion,” *Phys. Rev. Lett.* **121**, 193401 (2018).
- [25] T. Dieterle, M. Berngruber, C. Hölzl, R. Löw, K. Jachymski, T. Pfau, and F. Meinert, “Transport of a single cold ion immersed in a bose-einstein condensate,” *Phys. Rev. Lett.* **126**, 033401 (2021).
- [26] T. Dieterle, M. Berngruber, C. Hölzl, R. Löw, K. Jachymski, T. Pfau, and F. Meinert, “Inelastic collision dynamics of a single cold ion immersed in a bose-einstein condensate,” *Phys. Rev. A* **102**, 041301(R) (2020).
- [27] Nicolas Zuber, Viraatt S. V. Anasuri, Moritz Berngruber, Yi-Quan Zou, Florian Meinert, Robert Löw, and Tilman Pfau, “Observation of a molecular bond between ions and rydberg atoms,” *Nature* **605**, 453–456 (2022).
- [28] Daniel J. Bosworth, Frederic Hummel, and Peter Schmelcher, “Charged ultralong-range rydberg trimers,” *Phys. Rev. A* **107**, 022807 (2023).
- [29] André Schirotzek, Cheng-Hsun Wu, Ariel Sommer, and Martin W. Zwierlein, “Observation of fermi polarons in a tunable fermi liquid of ultracold atoms,” *Phys. Rev. Lett.* **102**, 230402 (2009).
- [30] Marco Koschorreck, Daniel Pertot, Enrico Vogt, Bernd Fröhlich, Michael Feld, and Michael Köhl, “Attractive and repulsive fermi polarons in two dimensions,” *Nature* **485**, 619–622 (2012).
- [31] C. Kohstall, M. Zaccanti, M. Jag, A. Trenkwalder, P. Massignan, G. M. Bruun, F. Schreck, and R. Grimm, “Metastability and coherence of repulsive polarons in a strongly interacting fermi mixture,” *Nature* **485**, 615–618 (2012).
- [32] F. Scazza, G. Valtolina, P. Massignan, A. Recati, A. Amico, A. Burchianti, C. Fort, M. Inguscio, M. Zaccanti, and G. Roati, “Repulsive fermi polarons in a resonant mixture of ultracold ${}^6\text{Li}$ atoms,” *Phys. Rev. Lett.* **118**, 083602 (2017).
- [33] Ming-Guang Hu, Michael J. Van de Graaff, Dhruv Kedar, John P. Corson, Eric A. Cornell, and Deborah S. Jin, “Bose polarons in the strongly interacting regime,” *Phys. Rev. Lett.* **117**, 055301 (2016).
- [34] Nils B. Jørgensen, Lars Wacker, Kristoffer T. Skalmstang, Meera M. Parish, Jesper Levinsen, Rasmus S.

- Christensen, Georg M. Bruun, and Jan J. Arlt, “Observation of attractive and repulsive polarons in a bose-einstein condensate,” *Phys. Rev. Lett.* **117**, 055302 (2016).
- [35] Z. Yan Zou, Yiqi Ni, Carsten Robens, and Martin W. Zwierlein, “Bose polarons near quantum criticality,” *Science* **368**, 190–194 (2020).
- [36] Marko Cetina, Andrew T. Grier, and Vladan Vuletić, “Micromotion-induced limit to atom-ion sympathetic cooling in paul traps,” *Phys. Rev. Lett.* **109**, 253201 (2012).
- [37] Zbigniew Idziaszek, Tommaso Calarco, and Peter Zoller, “Controlled collisions of a single atom and an ion guided by movable trapping potentials,” *Phys. Rev. A* **76**, 033409 (2007).
- [38] Bo Gao, “Universal properties in ultracold ion-atom interactions,” *Phys. Rev. Lett.* **104**, 213201 (2010).
- [39] J. Joger, A. Negretti, and R. Gerritsma, “Quantum dynamics of an atomic double-well system interacting with a trapped ion,” *Phys. Rev. A* **89**, 063621 (2014).
- [40] Mostafa R. Ebgha, Shahpoor Saeidian, Peter Schmelcher, and Antonio Negretti, “Compound atom-ion josephson junction: Effects of finite temperature and ion motion,” *Phys. Rev. A* **100**, 033616 (2019).
- [41] J M Schurer, A Negretti, and P Schmelcher, “Capture dynamics of ultracold atoms in the presence of an impurity ion,” *New Journal of Physics* **17**, 083024 (2015).
- [42] Michał Krych and Zbigniew Idziaszek, “Description of ion motion in a paul trap immersed in a cold atomic gas,” *Phys. Rev. A* **91**, 023430 (2015).
- [43] Lorenzo Oghittu, Melf Johannsen, Antonio Negretti, and Rene Gerritsma, “Dynamics of a trapped ion in a quantum gas: Effects of particle statistics,” *Phys. Rev. A* **104**, 053314 (2021).
- [44] Tobias Kroker, Mario Großmann, Klaus Sengstock, Markus Drescher, Philipp Wessels-Staarmann, and Juliette Simonet, “Ultrafast electron cooling in an expanding ultracold plasma,” *Nature Communications* **12**, 596 (2021).
- [45] T. Schneider, B. Roth, H. Duncker, I. Ernsting, and S. Schiller, “All-optical preparation of molecular ions in the rovibrational ground state,” *Nature Physics* **6**, 275–278 (2010).
- [46] Alexander Lambrecht, Julian Schmidt, Pascal Weckesser, Markus Debatin, Leon Karpa, and Tobias Schaetz, “Long lifetimes and effective isolation of ions in optical and electrostatic traps,” *Nature Photonics* **11**, 704–707 (2017).
- [47] Philipp Wessels, Bernhard Ruff, Tobias Kroker, Andrey K. Kazansky, Nikolay M. Kabachnik, Klaus Sengstock, Markus Drescher, and Juliette Simonet, “Absolute strong-field ionization probabilities of ultracold rubidium atoms,” *Communications Physics* **1**, 32 (2018).
- [48] Note that, to date, the short-range part of the atom-ion potential has not yet been experimentally characterized.
- [49] E. M. Lifshitz and L. P. Pitaevskii, *Course of theoretical physics* [“Landau-Lifshits”]. Vol. 10, Pergamon International Library of Science, Technology, Engineering and Social Studies (Pergamon Press, Oxford-Elmsford, N.Y., 1981) pp. xi+452, translated from the Russian by J. B. Sykes and R. N. Franklin.
- [50] R. Côté, V. Kharchenko, and M. D. Lukin, “Mesoscopic molecular ions in bose-einstein condensates,” *Phys. Rev. Lett.* **89**, 093001 (2002).
- [51] H. J. Carmichael, *Statistical methods in quantum optics. 1*, Texts and Monographs in Physics (Springer-Verlag, Berlin, 1999) pp. xxii+361, master equations and Fokker-Planck equations.
- [52] H A Fürst, N V Ewald, T Secker, J Joger, T Feldker, and R Gerritsma, “Prospects of reaching the quantum regime in li-yb+ mixtures,” *Journal of Physics B: Atomic, Molecular and Optical Physics* **51**, 195001 (2018).
- [53] In the derivation of Eq. (26) we use the Baker-Campbell-Hausdorff (BCH) identity $e^{i\hat{G}\lambda}\hat{A}e^{-i\hat{G}\lambda} = \hat{A} + i\lambda[\hat{G}, \hat{A}] + \frac{(i\lambda)^2}{2!}[\hat{G}, [\hat{G}, \hat{A}]] + \dots$, whose terms of order higher than two are zero for $\hat{G} = \hat{r}_\xi$ and $\hat{A} = \hat{p}^2$.
- [54] Kurt Jacobs and Daniel A. Steck, “A straightforward introduction to continuous quantum measurement,” *Contemporary Physics* **47**, 279–303 (2006).
- [55] Lev Pitaevskii and Sandro Stringari, *Bose-Einstein Condensation and Superfluidity* (Oxford Science Publications, 2016).
- [56] A finite initial temperature along y and z would not have any qualitative effect on our analysis. However, a quantitative study could require the total temperature $T_{\text{ion}} = T_{\text{ion}}^x + T_{\text{ion}}^y + T_{\text{ion}}^z$ to be considered.
- [57] C. Veit, N. Zuber, O. A. Herrera-Sancho, V. S. V. Anasuri, T. Schmid, F. Meinert, R. Löw, and T. Pfau, “Pulsed ion microscope to probe quantum gases,” *Phys. Rev. X* **11**, 011036 (2021).
- [58] Markus Stecker, Hannah Schefzyk, József Fortágh, and Andreas Günther, “A high resolution ion microscope for cold atoms,” *New Journal of Physics* **19**, 043020 (2017).
- [59] R. Côté and A. Dalgarno, “Ultracold atom-ion collisions,” *Phys. Rev. A* **62**, 012709 (2000).
- [60] K. Ravi, Seunghyun Lee, Arijit Sharma, G. Werth, and S. A. Rangwala, “Cooling and stabilization by collisions in a mixed ion-atom system,” *Nature Communications* **3**, 1126 (2012).
- [61] Amir Mahdian, Artjom Krükov, and Johannes Hecker Denschlag, “Direct observation of swap cooling in atom-ion collisions,” *New Journal of Physics* **23**, 065008 (2021).

Bibliography

- [1] T.W. Hänsch and A.L. Schawlow. Cooling of gases by laser radiation. *Optics Communications*, 13(1):68–69, 1975. doi: [https://doi.org/10.1016/0030-4018\(75\)90159-5](https://doi.org/10.1016/0030-4018(75)90159-5). URL <https://www.sciencedirect.com/science/article/pii/0030401875901595>.
- [2] Steven Chu, L. Hollberg, J. E. Bjorkholm, Alex Cable, and A. Ashkin. Three-dimensional viscous confinement and cooling of atoms by resonance radiation pressure. *Phys. Rev. Lett.*, 55:48–51, Jul 1985. doi: 10.1103/PhysRevLett.55.48. URL <https://link.aps.org/doi/10.1103/PhysRevLett.55.48>.
- [3] Naoto Masuhara, John M. Doyle, Jon C. Sandberg, Daniel Kleppner, Thomas J. Greytak, Harald F. Hess, and Greg P. Kochanski. Evaporative cooling of spin-polarized atomic hydrogen. *Phys. Rev. Lett.*, 61:935–938, Aug 1988. doi: 10.1103/PhysRevLett.61.935. URL <https://link.aps.org/doi/10.1103/PhysRevLett.61.935>.
- [4] M. H. Anderson, J. R. Ensher, M. R. Matthews, C. E. Wieman, and E. A. Cornell. Observation of bose-einstein condensation in a dilute atomic vapor. *Science*, 269(5221):198–201, 1995. doi: 10.1126/science.269.5221.198. URL <https://www.science.org/doi/abs/10.1126/science.269.5221.198>.
- [5] K. B. Davis, M. O. Mewes, M. R. Andrews, N. J. van Druten, D. S. Durfee, D. M. Kurn, and W. Ketterle. Bose-einstein condensation in a gas of sodium atoms. *Phys. Rev. Lett.*, 75:3969–3973, Nov 1995. doi: 10.1103/PhysRevLett.75.3969. URL <https://link.aps.org/doi/10.1103/PhysRevLett.75.3969>.
- [6] C. C. Bradley, C. A. Sackett, J. J. Tollett, and R. G. Hulet. Evidence of bose-einstein condensation in an atomic gas with attractive interactions. *Phys. Rev. Lett.*, 75:1687–1690, Aug 1995. doi: 10.1103/PhysRevLett.75.1687. URL <https://link.aps.org/doi/10.1103/PhysRevLett.75.1687>.
- [7] B. DeMarco and D. S. Jin. Onset of fermi degeneracy in a trapped atomic gas. *Science*, 285(5434):1703–1706, 1999. doi: 10.1126/science.285.5434.1703. URL <https://www.science.org/doi/abs/10.1126/science.285.5434.1703>.
- [8] Lev Pitaevskii and Sandro Stringari. *Bose-Einstein Condensation and Superfluidity*. Oxford Science Publications, 2016.
- [9] M. R. Andrews, C. G. Townsend, H.-J. Miesner, D. S. Durfee, D. M. Kurn, and W. Ketterle. Observation of interference between two bose condensates. *Science*,

- 275(5300):637–641, 1997. doi: 10.1126/science.275.5300.637. URL <https://www.science.org/doi/abs/10.1126/science.275.5300.637>.
- [10] J. R. Abo-Shaer, C. Raman, J. M. Vogels, and W. Ketterle. Observation of vortex lattices in bose-einstein condensates. *Science*, 292(5516):476–479, 2001. doi: 10.1126/science.1060182. URL <https://www.science.org/doi/abs/10.1126/science.1060182>.
- [11] Martin W. Zwierlein, Christian H. Schunck, André Schirotzek, and Wolfgang Ketterle. Direct observation of the superfluid phase transition in ultracold fermi gases. *Nature*, 442(7098):54–58, 2006. doi: 10.1038/nature04936. URL <https://doi.org/10.1038/nature04936>.
- [12] Steven Chu. Nobel lecture: The manipulation of neutral particles. *Rev. Mod. Phys.*, 70:685–706, Jul 1998. doi: 10.1103/RevModPhys.70.685. URL <https://link.aps.org/doi/10.1103/RevModPhys.70.685>.
- [13] Claude N. Cohen-Tannoudji. Nobel lecture: Manipulating atoms with photons. *Rev. Mod. Phys.*, 70:707–719, Jul 1998. doi: 10.1103/RevModPhys.70.707. URL <https://link.aps.org/doi/10.1103/RevModPhys.70.707>.
- [14] William D. Phillips. Nobel lecture: Laser cooling and trapping of neutral atoms. *Rev. Mod. Phys.*, 70:721–741, Jul 1998. doi: 10.1103/RevModPhys.70.721. URL <https://link.aps.org/doi/10.1103/RevModPhys.70.721>.
- [15] Cheng Chin, Rudolf Grimm, Paul Julienne, and Eite Tiesinga. Feshbach resonances in ultracold gases. *Rev. Mod. Phys.*, 82:1225–1286, Apr 2010. doi: 10.1103/RevModPhys.82.1225. URL <https://link.aps.org/doi/10.1103/RevModPhys.82.1225>.
- [16] Immanuel Bloch, Jean Dalibard, and Wilhelm Zwerger. Many-body physics with ultracold gases. *Rev. Mod. Phys.*, 80:885–964, Jul 2008. doi: 10.1103/RevModPhys.80.885. URL <https://link.aps.org/doi/10.1103/RevModPhys.80.885>.
- [17] Immanuel Bloch. Ultracold quantum gases in optical lattices. *Nature Physics*, 1(1):23–30, 2005. doi: 10.1038/nphys138. URL <https://doi.org/10.1038/nphys138>.
- [18] Christian Gross and Immanuel Bloch. Quantum simulations with ultracold atoms in optical lattices. *Science*, 357(6355):995–1001, 2017. doi: 10.1126/science.aal3837. URL <https://www.science.org/doi/abs/10.1126/science.aal3837>.
- [19] D. Leibfried, R. Blatt, C. Monroe, and D. Wineland. Quantum dynamics of single trapped ions. *Rev. Mod. Phys.*, 75:281–324, Mar 2003. doi: 10.1103/RevModPhys.75.281. URL <https://link.aps.org/doi/10.1103/RevModPhys.75.281>.
- [20] Alexander Lambrecht, Julian Schmidt, Pascal Weckesser, Markus Debatin, Leon Karpa, and Tobias Schaetz. Long lifetimes and effective isolation of ions in optical and electrostatic traps. *Nature Photonics*, 11(11):704–707, 2017. doi: 10.1038/s41566-017-0030-2. URL <https://doi.org/10.1038/s41566-017-0030-2>.

- [21] F. Diedrich, J. C. Bergquist, Wayne M. Itano, and D. J. Wineland. Laser cooling to the zero-point energy of motion. *Phys. Rev. Lett.*, 62:403–406, Jan 1989. doi: 10.1103/PhysRevLett.62.403. URL <https://link.aps.org/doi/10.1103/PhysRevLett.62.403>.
- [22] Jürgen Eschner, Giovanna Morigi, Ferdinand Schmidt-Kaler, and Rainer Blatt. Laser cooling of trapped ions. *J. Opt. Soc. Am. B*, 20(5):1003–1015, May 2003. doi: 10.1364/JOSAB.20.001003. URL <https://opg.optica.org/josab/abstract.cfm?URI=josab-20-5-1003>.
- [23] Wayne M. Itano, J. C. Bergquist, J. J. Bollinger, and D. J. Wineland. Cooling methods in ion traps. *Physica Scripta*, 1995(T59):106, jan 1995. doi: 10.1088/0031-8949/1995/T59/013. URL <https://dx.doi.org/10.1088/0031-8949/1995/T59/013>.
- [24] T. Feldker, H. Furst, H. Hirzler, N. V. Ewald, M. Mazzanti, D. Wiater, M. Tomza, and R. Gerritsma. Buffer gas cooling of a trapped ion to the quantum regime. *Nature Physics*, 16(4):413–416, 2020. doi: 10.1038/s41567-019-0772-5. URL <https://doi.org/10.1038/s41567-019-0772-5>.
- [25] R. Blümel, J. M. Chen, E. Peik, W. Quint, W. Schleich, Y. R. Shen, and H. Walther. Phase transitions of stored laser-cooled ions. *Nature*, 334(6180):309–313, 1988. doi: 10.1038/334309a0. URL <https://doi.org/10.1038/334309a0>.
- [26] D. J. Wineland, J. C. Bergquist, Wayne M. Itano, J. J. Bollinger, and C. H. Manney. Atomic-ion coulomb clusters in an ion trap. *Phys. Rev. Lett.*, 59:2935–2938, Dec 1987. doi: 10.1103/PhysRevLett.59.2935. URL <https://link.aps.org/doi/10.1103/PhysRevLett.59.2935>.
- [27] H. Häffner, C.F. Roos, and R. Blatt. Quantum computing with trapped ions. *Physics Reports*, 469(4):155–203, 2008. ISSN 0370-1573. doi: <https://doi.org/10.1016/j.physrep.2008.09.003>. URL <https://www.sciencedirect.com/science/article/pii/S0370157308003463>.
- [28] C. Monroe and J. Kim. Scaling the ion trap quantum processor. *Science*, 339(6124):1164–1169, 2013. doi: 10.1126/science.1231298. URL <https://www.science.org/doi/abs/10.1126/science.1231298>.
- [29] Colin D. Bruzewicz, John Chiaverini, Robert McConnell, and Jeremy M. Sage. Trapped-ion quantum computing: Progress and challenges. *Applied Physics Reviews*, 6(2):021314, 05 2019. ISSN 1931-9401. doi: 10.1063/1.5088164. URL <https://doi.org/10.1063/1.5088164>.
- [30] R. Blatt and C. F. Roos. Quantum simulations with trapped ions. *Nature Physics*, 8(4):277–284, 2012. doi: 10.1038/nphys2252. URL <https://doi.org/10.1038/nphys2252>.
- [31] Justin G. Bohnet, Brian C. Sawyer, Joseph W. Britton, Michael L. Wall, Ana Maria Rey, Michael Foss-Feig, and John J. Bollinger. Quantum spin dynamics and entanglement generation with hundreds of trapped ions. *Science*, 352(6291):1297–1301, 2016.

- doi: 10.1126/science.aad9958. URL <https://www.science.org/doi/abs/10.1126/science.aad9958>.
- [32] C. Monroe, W. C. Campbell, L.-M. Duan, Z.-X. Gong, A. V. Gorshkov, P. W. Hess, R. Islam, K. Kim, N. M. Linke, G. Pagano, P. Richerme, C. Senko, and N. Y. Yao. Programmable quantum simulations of spin systems with trapped ions. *Rev. Mod. Phys.*, 93:025001, Apr 2021. doi: 10.1103/RevModPhys.93.025001. URL <https://link.aps.org/doi/10.1103/RevModPhys.93.025001>.
- [33] Andrew D. Ludlow, Martin M. Boyd, Jun Ye, E. Peik, and P. O. Schmidt. Optical atomic clocks. *Rev. Mod. Phys.*, 87:637–701, Jun 2015. doi: 10.1103/RevModPhys.87.637. URL <https://link.aps.org/doi/10.1103/RevModPhys.87.637>.
- [34] M. D. Barrett, J. Chiaverini, T. Schaetz, J. Britton, W. M. Itano, J. D. Jost, E. Knill, C. Langer, D. Leibfried, R. Ozeri, and D. J. Wineland. Deterministic quantum teleportation of atomic qubits. *Nature*, 429(6993):737–739, 2004. doi: 10.1038/nature02608. URL <https://doi.org/10.1038/nature02608>.
- [35] M. Riebe, H. Häffner, C. F. Roos, W. Hänsel, J. Benhelm, G. P. T. Lancaster, T. W. Körber, C. Becher, F. Schmidt-Kaler, D. F. V. James, and R. Blatt. Deterministic quantum teleportation with atoms. *Nature*, 429(6993):734–737, 2004. doi: 10.1038/nature02570. URL <https://doi.org/10.1038/nature02570>.
- [36] R. Côté and A. Dalgarno. Ultracold atom-ion collisions. *Phys. Rev. A*, 62:012709, Jun 2000. doi: 10.1103/PhysRevA.62.012709. URL <https://link.aps.org/doi/10.1103/PhysRevA.62.012709>.
- [37] Bo Gao. Universal properties in ultracold ion-atom interactions. *Phys. Rev. Lett.*, 104:213201, May 2010. doi: 10.1103/PhysRevLett.104.213201. URL <https://link.aps.org/doi/10.1103/PhysRevLett.104.213201>.
- [38] Zbigniew Idziaszek, Tommaso Calarco, Paul S. Julienne, and Andrea Simoni. Quantum theory of ultracold atom-ion collisions. *Phys. Rev. A*, 79:010702, Jan 2009. doi: 10.1103/PhysRevA.79.010702. URL <https://link.aps.org/doi/10.1103/PhysRevA.79.010702>.
- [39] Zbigniew Idziaszek, Tommaso Calarco, and Peter Zoller. Controlled collisions of a single atom and an ion guided by movable trapping potentials. *Phys. Rev. A*, 76:033409, Sep 2007. doi: 10.1103/PhysRevA.76.033409. URL <https://link.aps.org/doi/10.1103/PhysRevA.76.033409>.
- [40] A. Härter and J. Hecker Denschlag. Cold atom-ion experiments in hybrid traps. *Contemporary Physics*, 55(1):33–45, 01 2014. doi: 10.1080/00107514.2013.854618. URL <https://doi.org/10.1080/00107514.2013.854618>.
- [41] R. Côté. Chapter two - ultracold hybrid atom-ion systems. In *Advances in Atomic, Molecular, and Optical Physics*, volume 65, pages 67–126. Academic Press, 2016. doi: <https://doi.org/10.1016/bs.aamop.2016.04.004>. URL <https://www.sciencedirect.com/science/article/pii/S1049250X16300088>.

- [42] Michał Tomza, Krzysztof Jachymski, Rene Gerritsma, Antonio Negretti, Tommaso Calarco, Zbigniew Idziaszek, and Paul S. Julienne. Cold hybrid ion-atom systems. *Rev. Mod. Phys.*, 91:035001, Jul 2019. doi: 10.1103/RevModPhys.91.035001. URL <https://link.aps.org/doi/10.1103/RevModPhys.91.035001>.
- [43] Rianne S. Lous and René Gerritsma. Chapter two - ultracold ion-atom experiments: cooling, chemistry, and quantum effects. In *Advances in Atomic, Molecular, and Optical Physics*, volume 71, pages 65–133. Academic Press, 2022. doi: <https://doi.org/10.1016/bs.aamop.2022.05.002>. URL <https://www.sciencedirect.com/science/article/pii/S1049250X22000027>.
- [44] Christoph Zipkes, Stefan Palzer, Carlo Sias, and Michael Köhl. A trapped single ion inside a bose–einstein condensate. *Nature*, 464(7287):388–391, 2010. doi: 10.1038/nature08865. URL <https://doi.org/10.1038/nature08865>.
- [45] Stefan Schmid, Arne Härter, and Johannes Hecker Denschlag. Dynamics of a cold trapped ion in a bose-einstein condensate. *Phys. Rev. Lett.*, 105:133202, Sep 2010. doi: 10.1103/PhysRevLett.105.133202. URL <https://link.aps.org/doi/10.1103/PhysRevLett.105.133202>.
- [46] Christoph Zipkes, Lothar Ratschbacher, Carlo Sias, and Michael Köhl. Kinetics of a single trapped ion in an ultracold buffer gas. *New Journal of Physics*, 13(5):053020, May 2011. doi: 10.1088/1367-2630/13/5/053020. URL <https://dx.doi.org/10.1088/1367-2630/13/5/053020>.
- [47] Marko Cetina, Andrew T. Grier, and Vladan Vuletić. Micromotion-induced limit to atom-ion sympathetic cooling in paul traps. *Phys. Rev. Lett.*, 109:253201, Dec 2012. doi: 10.1103/PhysRevLett.109.253201. URL <https://link.aps.org/doi/10.1103/PhysRevLett.109.253201>.
- [48] Ziv Meir, Tomas Sikorsky, Ruti Ben-shlomi, Nitzan Akerman, Yehonatan Dallal, and Roei Ozeri. Dynamics of a ground-state cooled ion colliding with ultracold atoms. *Phys. Rev. Lett.*, 117:243401, Dec 2016. doi: 10.1103/PhysRevLett.117.243401. URL <https://link.aps.org/doi/10.1103/PhysRevLett.117.243401>.
- [49] Shinsuke Haze, Mizuki Sasakawa, Ryoichi Saito, Ryosuke Nakai, and Takashi Mukaiyama. Cooling dynamics of a single trapped ion via elastic collisions with small-mass atoms. *Phys. Rev. Lett.*, 120:043401, Jan 2018. doi: 10.1103/PhysRevLett.120.043401. URL <https://link.aps.org/doi/10.1103/PhysRevLett.120.043401>.
- [50] H. Hirzler, T. Feldker, H. Furst, N. V. Ewald, E. Trimby, R. S. Lous, J. D. Arias Espinoza, M. Mazzanti, J. Joger, and R. Gerritsma. Experimental setup for studying an ultracold mixture of trapped Yb^{+6}Li . *Phys. Rev. A*, 102:033109, Sep 2020. doi: 10.1103/PhysRevA.102.033109. URL <https://link.aps.org/doi/10.1103/PhysRevA.102.033109>.
- [51] J. Schmidt, P. Weckesser, F. Thielemann, T. Schaetz, and L. Karpa. Optical traps for sympathetic cooling of ions with ultracold neutral atoms. *Phys. Rev. Lett.*, 124:053402, Feb 2020. doi: 10.1103/PhysRevLett.124.053402. URL <https://link.aps.org/doi/10.1103/PhysRevLett.124.053402>.

- [52] Pascal Weckesser, Fabian Thielemann, Dariusz Wiater, Agata Wojciechowska, Leon Karpa, Krzysztof Jachymski, Michał Tomza, Thomas Walker, and Tobias Schaetz. Observation of feshbach resonances between a single ion and ultracold atoms. *Nature*, 600(7889):429–433, 2021. doi: 10.1038/s41586-021-04112-y. URL <https://doi.org/10.1038/s41586-021-04112-y>.
- [53] Arne Härter, Artjom Krüchow, Andreas Brunner, Wolfgang Schnitzler, Stefan Schmid, and Johannes Hecker Denschlag. Single ion as a three-body reaction center in an ultracold atomic gas. *Phys. Rev. Lett.*, 109:123201, Sep 2012. doi: 10.1103/PhysRevLett.109.123201. URL <https://link.aps.org/doi/10.1103/PhysRevLett.109.123201>.
- [54] Lothar Ratschbacher, Christoph Zipkes, Carlo Sias, and Michael Köhl. Controlling chemical reactions of a single particle. *Nature Physics*, 8(9):649–652, 2012. doi: 10.1038/nphys2373. URL <https://doi.org/10.1038/nphys2373>.
- [55] Tomas Sikorsky, Ziv Meir, Ruti Ben-shlomi, Nitzan Akerman, and Roei Ozeri. Spin-controlled atom–ion chemistry. *Nature Communications*, 9(1):920, 2018. doi: 10.1038/s41467-018-03373-y. URL <https://doi.org/10.1038/s41467-018-03373-y>.
- [56] J. Pérez-Ríos. Cold chemistry: a few-body perspective on impurity physics of a single ion in an ultracold bath. *Molecular Physics*, 119(8):e1881637, 04 2021. doi: 10.1080/00268976.2021.1881637. URL <https://doi.org/10.1080/00268976.2021.1881637>.
- [57] H. Hirzler, R. S. Lous, E. Trimby, J. Pérez-Ríos, A. Safavi-Naini, and R. Gerritsma. Observation of chemical reactions between a trapped ion and ultracold feshbach dimers. *Phys. Rev. Lett.*, 128:103401, Mar 2022. doi: 10.1103/PhysRevLett.128.103401. URL <https://link.aps.org/doi/10.1103/PhysRevLett.128.103401>.
- [58] Meirav Pinkas, Or Katz, Jonathan Wengrowicz, Nitzan Akerman, and Roei Ozeri. Trap-assisted formation of atom–ion bound states. *Nature Physics*, 2023. doi: 10.1038/s41567-023-02158-5. URL <https://doi.org/10.1038/s41567-023-02158-5>.
- [59] N. V. Ewald, T. Feldker, H. Hirzler, H. A. Fürst, and R. Gerritsma. Observation of interactions between trapped ions and ultracold rydberg atoms. *Phys. Rev. Lett.*, 122:253401, Jun 2019. doi: 10.1103/PhysRevLett.122.253401. URL <https://link.aps.org/doi/10.1103/PhysRevLett.122.253401>.
- [60] Limei Wang, Markus Deiß, Georg Raithel, and Johannes Hecker Denschlag. Optical control of atom-ion collisions using a rydberg state. *Journal of Physics B: Atomic, Molecular and Optical Physics*, 53(13):134005, jun 2020. doi: 10.1088/1361-6455/ab7d24. URL <https://dx.doi.org/10.1088/1361-6455/ab7d24>.
- [61] K. Ravi, Seunghyun Lee, Arijit Sharma, G. Werth, and S. A. Rangwala. Cooling and stabilization by collisions in a mixed ion–atom system. *Nature Communications*, 3(1):1126, 2012. doi: 10.1038/ncomms2131. URL <https://doi.org/10.1038/ncomms2131>.
- [62] Amir Mahdian, Artjom Krüchow, and Johannes Hecker Denschlag. Direct observation of swap cooling in atom–ion collisions. *New Journal of Physics*, 23(6):065008,

- Jun 2021. doi: 10.1088/1367-2630/ac0575. URL <https://dx.doi.org/10.1088/1367-2630/ac0575>.
- [63] K. S. Kleinbach, F. Engel, T. Dieterle, R. Löw, T. Pfau, and F. Meinert. Ionic impurity in a bose-einstein condensate at submicrokelvin temperatures. *Phys. Rev. Lett.*, 120:193401, May 2018. doi: 10.1103/PhysRevLett.120.193401. URL <https://link.aps.org/doi/10.1103/PhysRevLett.120.193401>.
- [64] F. Engel, T. Dieterle, T. Schmid, C. Tomschitz, C. Veit, N. Zuber, R. Löw, T. Pfau, and F. Meinert. Observation of rydberg blockade induced by a single ion. *Phys. Rev. Lett.*, 121:193401, Nov 2018. doi: 10.1103/PhysRevLett.121.193401. URL <https://link.aps.org/doi/10.1103/PhysRevLett.121.193401>.
- [65] T. Dieterle, M. Berngruber, C. Hölzl, R. Löw, K. Jachymski, T. Pfau, and F. Meinert. Inelastic collision dynamics of a single cold ion immersed in a bose-einstein condensate. *Phys. Rev. A*, 102:041301, Oct 2020. doi: 10.1103/PhysRevA.102.041301. URL <https://link.aps.org/doi/10.1103/PhysRevA.102.041301>.
- [66] T. Dieterle, M. Berngruber, C. Hölzl, R. Löw, K. Jachymski, T. Pfau, and F. Meinert. Transport of a single cold ion immersed in a bose-einstein condensate. *Phys. Rev. Lett.*, 126:033401, Jan 2021. doi: 10.1103/PhysRevLett.126.033401. URL <https://link.aps.org/doi/10.1103/PhysRevLett.126.033401>.
- [67] Nicolas Zuber, Viraatt S. V. Anasuri, Moritz Berngruber, Yi-Quan Zou, Florian Meinert, Robert Löw, and Tilman Pfau. Observation of a molecular bond between ions and rydberg atoms. *Nature*, 605(7910):453–456, 2022. doi: 10.1038/s41586-022-04577-5. URL <https://doi.org/10.1038/s41586-022-04577-5>.
- [68] Daniel J. Bosworth, Frederic Hummel, and Peter Schmelcher. Charged ultralong-range rydberg trimers. *Phys. Rev. A*, 107:022807, Feb 2023. doi: 10.1103/PhysRevA.107.022807. URL <https://link.aps.org/doi/10.1103/PhysRevA.107.022807>.
- [69] J. M. Schurer, A. Negretti, and P. Schmelcher. Unraveling the structure of ultracold mesoscopic collinear molecular ions. *Phys. Rev. Lett.*, 119:063001, Aug 2017. doi: 10.1103/PhysRevLett.119.063001. URL <https://link.aps.org/doi/10.1103/PhysRevLett.119.063001>.
- [70] Grigory E. Astrakharchik, Luis A. Peña Ardila, Richard Schmidt, Krzysztof Jachymski, and Antonio Negretti. Ionic polaron in a bose-einstein condensate. *Communications Physics*, 4(1):94, 2021. doi: 10.1038/s42005-021-00597-1. URL <https://doi.org/10.1038/s42005-021-00597-1>.
- [71] Esben Rohan Christensen, Arturo Camacho-Guardian, and Georg M. Bruun. Charged polarons and molecules in a bose-einstein condensate. *Phys. Rev. Lett.*, 126:243001, Jun 2021. doi: 10.1103/PhysRevLett.126.243001. URL <https://link.aps.org/doi/10.1103/PhysRevLett.126.243001>.
- [72] Shanshan Ding, Michael Drewsen, Jan J. Arlt, and G. M. Bruun. Mediated interaction between ions in quantum degenerate gases. *Phys. Rev. Lett.*, 129:153401, Oct

2022. doi: 10.1103/PhysRevLett.129.153401. URL <https://link.aps.org/doi/10.1103/PhysRevLett.129.153401>.
- [73] Grigory E. Astrakharchik, Luis A. Peña Ardila, Krzysztof Jachymski, and Antonio Negretti. Many-body bound states and induced interactions of charged impurities in a bosonic bath. *Nature Communications*, 14(1):1647, 2023. doi: 10.1038/s41467-023-37153-0. URL <https://doi.org/10.1038/s41467-023-37153-0>.
- [74] Michał Krych and Zbigniew Idziaszek. Description of ion motion in a paul trap immersed in a cold atomic gas. *Phys. Rev. A*, 91:023430, Feb 2015. doi: 10.1103/PhysRevA.91.023430. URL <https://link.aps.org/doi/10.1103/PhysRevA.91.023430>.
- [75] U. Bissbort, D. Cocks, A. Negretti, Z. Idziaszek, T. Calarco, F. Schmidt-Kaler, W. Hofstetter, and R. Gerritsma. Emulating solid-state physics with a hybrid system of ultracold ions and atoms. *Phys. Rev. Lett.*, 111:080501, Aug 2013. doi: 10.1103/PhysRevLett.111.080501. URL <https://link.aps.org/doi/10.1103/PhysRevLett.111.080501>.
- [76] A. Negretti, R. Gerritsma, Z. Idziaszek, F. Schmidt-Kaler, and T. Calarco. Generalized kronig-penney model for ultracold atomic quantum systems. *Phys. Rev. B*, 90:155426, Oct 2014. doi: 10.1103/PhysRevB.90.155426. URL <https://link.aps.org/doi/10.1103/PhysRevB.90.155426>.
- [77] A. B. Michelsen, M. Valiente, N. T. Zinner, and A. Negretti. Ion-induced interactions in a tomonaga-luttinger liquid. *Phys. Rev. B*, 100:205427, Nov 2019. doi: 10.1103/PhysRevB.100.205427. URL <https://link.aps.org/doi/10.1103/PhysRevB.100.205427>.
- [78] Krzysztof Jachymski and Antonio Negretti. Quantum simulation of extended polaron models using compound atom-ion systems. *Phys. Rev. Res.*, 2:033326, Aug 2020. doi: 10.1103/PhysRevResearch.2.033326. URL <https://link.aps.org/doi/10.1103/PhysRevResearch.2.033326>.
- [79] Trygve Helgaker, Poul Jorgensen, and Jeppe Olsen. *Molecular electronic-structure theory*. John Wiley & Sons, 2000.
- [80] Trygve Helgaker, Sonia Coriani, Poul Jørgensen, Kasper Kristensen, Jeppe Olsen, and Kenneth Ruud. Recent advances in wave function-based methods of molecular-property calculations. *Chemical Reviews*, 112(1):543–631, 01 2012. doi: 10.1021/cr2002239. URL <https://doi.org/10.1021/cr2002239>.
- [81] Michał Tomza, Christiane P. Koch, and Robert Moszynski. Cold interactions between an yb^+ ion and a li atom: Prospects for sympathetic cooling, radiative association, and feshbach resonances. *Phys. Rev. A*, 91:042706, Apr 2015. doi: 10.1103/PhysRevA.91.042706. URL <https://link.aps.org/doi/10.1103/PhysRevA.91.042706>.
- [82] Oleg P. Makarov, R. Côté, H. Michels, and W. W. Smith. Radiative charge-transfer lifetime of the excited state of $(\text{NaCa})^+$. *Phys. Rev. A*, 67:042705, Apr 2003. doi: 10.

- 1103/PhysRevA.67.042705. URL <https://link.aps.org/doi/10.1103/PhysRevA.67.042705>.
- [83] Michał Krych, Wojciech Skomorowski, Filip Pawłowski, Robert Moszynski, and Zbigniew Idziaszek. Sympathetic cooling of the ba^+ ion by collisions with ultracold rb atoms: Theoretical prospects. *Phys. Rev. A*, 83:032723, Mar 2011. doi: 10.1103/PhysRevA.83.032723. URL <https://link.aps.org/doi/10.1103/PhysRevA.83.032723>.
- [84] H. D. L. Lamb, J. F. McCann, B. M. McLaughlin, J. Goold, N. Wells, and I. Lane. Structure and interactions of ultracold yb ions and rb atoms. *Phys. Rev. A*, 86:022716, Aug 2012. doi: 10.1103/PhysRevA.86.022716. URL <https://link.aps.org/doi/10.1103/PhysRevA.86.022716>.
- [85] Soulef Jellali, H ela Habli, Leila Mejrissi, Mahmoud Mohery, Brahim Oujia, and Florent Xavier Gad ea. Theoretical study of the srl^+ molecular ion: structural, electronic and dipolar properties. *Molecular Physics*, 114(20):2910–2923, 10 2016. doi: 10.1080/00268976.2016.1203035. URL <https://doi.org/10.1080/00268976.2016.1203035>.
- [86] H. Kreek and William J. Meath. Charge-Overlap Effects. Dispersion and Induction Forces. *The Journal of Chemical Physics*, 50(6):2289–2302, 12 1969. ISSN 0021-9606. doi: 10.1063/1.1671379. URL <https://doi.org/10.1063/1.1671379>.
- [87] Robert J. Buehler and Joseph O. Hirschfelder. Bipolar expansion of coulombic potentials. *Phys. Rev.*, 83:628–633, Aug 1951. doi: 10.1103/PhysRev.83.628. URL <https://link.aps.org/doi/10.1103/PhysRev.83.628>.
- [88] F. H. Mies. Molecular theory of atomic collisions: Fine-structure transitions. *Phys. Rev. A*, 7:942–957, Mar 1973. doi: 10.1103/PhysRevA.7.942. URL <https://link.aps.org/doi/10.1103/PhysRevA.7.942>.
- [89] O. Dulieu and A. Osterwalder. *Cold Chemistry: Molecular Scattering and Reactivity Near Absolute Zero*. Theoretical and Computational Chemistry Series. Royal Society of Chemistry, 2017. ISBN 9781782625971. URL <https://books.google.de/books?id=Fs9CDwAAQBAJ>.
- [90] Christopher R. Ekstrom, J org Schmiedmayer, Michael S. Chapman, Troy D. Hammond, and David E. Pritchard. Measurement of the electric polarizability of sodium with an atom interferometer. *Phys. Rev. A*, 51:3883–3888, May 1995. doi: 10.1103/PhysRevA.51.3883. URL <https://link.aps.org/doi/10.1103/PhysRevA.51.3883>.
- [91] Peng Zhang and Alexander Dalgarno. Static dipole polarizability of ytterbium. *The Journal of Physical Chemistry A*, 111(49):12471–12476, 12 2007. doi: 10.1021/jp0750856. URL <https://doi.org/10.1021/jp0750856>.
- [92] William F. Holmgren, Melissa C. Revelle, Vincent P. A. Lonij, and Alexander D. Cronin. Absolute and ratio measurements of the polarizability of na, k, and rb with an atom interferometer. *Phys. Rev. A*, 81:053607, May 2010. doi: 10.1103/PhysRevA.81.053607. URL <https://link.aps.org/doi/10.1103/PhysRevA.81.053607>.

- [93] Maxwell D. Gregoire, Ivan Hromada, William F. Holmgren, Raisa Trubko, and Alexander D. Cronin. Measurements of the ground-state polarizabilities of cs, rb, and k using atom interferometry. *Phys. Rev. A*, 92:052513, Nov 2015. doi: 10.1103/PhysRevA.92.052513. URL <https://link.aps.org/doi/10.1103/PhysRevA.92.052513>.
- [94] E. Czuchaj, J. Sienkiewicz, and W. Miklaszewski. Non-local pseudopotentials for electron-rare gas atom interaction. *Chemical Physics*, 116(1):69–78, 1987. ISSN 0301-0104. doi: [https://doi.org/10.1016/0301-0104\(87\)80069-1](https://doi.org/10.1016/0301-0104(87)80069-1). URL <https://www.sciencedirect.com/science/article/pii/0301010487800691>.
- [95] Edward A. Mason and Earl W. McDaniel. *Transport Properties of Ions in Gases*. John Wiley & Sons, Ltd, 1988. ISBN 978-3-527-60285-8. doi: <https://doi.org/10.1002/3527602852>. URL <https://onlinelibrary.wiley.com/doi/book/10.1002/3527602852>.
- [96] C. Greene, U. Fano, and G. Strinati. General form of the quantum-defect theory. *Phys. Rev. A*, 19:1485–1509, Apr 1979. doi: 10.1103/PhysRevA.19.1485. URL <https://link.aps.org/doi/10.1103/PhysRevA.19.1485>.
- [97] Chris H. Greene, A. R. P. Rau, and U. Fano. General form of the quantum-defect theory. ii. *Phys. Rev. A*, 26:2441–2459, Nov 1982. doi: 10.1103/PhysRevA.26.2441. URL <https://link.aps.org/doi/10.1103/PhysRevA.26.2441>.
- [98] M J Seaton. Quantum defect theory. *Reports on Progress in Physics*, 46(2):167, feb 1983. doi: 10.1088/0034-4885/46/2/002. URL <https://dx.doi.org/10.1088/0034-4885/46/2/002>.
- [99] Bo Gao. General form of the quantum-defect theory for $-1/r^\alpha$ type of potentials with $\alpha > 2$. *Phys. Rev. A*, 78:012702, Jul 2008. doi: 10.1103/PhysRevA.78.012702. URL <https://link.aps.org/doi/10.1103/PhysRevA.78.012702>.
- [100] Bo Gao. Quantum-defect theory for $-1/r^4$ -type interactions. *Phys. Rev. A*, 88:022701, Aug 2013. doi: 10.1103/PhysRevA.88.022701. URL <https://link.aps.org/doi/10.1103/PhysRevA.88.022701>.
- [101] Zbigniew Idziaszek, Andrea Simoni, Tommaso Calarco, and Paul S Julienne. Multichannel quantum-defect theory for ultracold atom-ion collisions. *New Journal of Physics*, 13(8):083005, aug 2011. doi: 10.1088/1367-2630/13/8/083005. URL <https://dx.doi.org/10.1088/1367-2630/13/8/083005>.
- [102] Ming Li, Li You, and Bo Gao. Multichannel quantum-defect theory for ion-atom interactions. *Phys. Rev. A*, 89:052704, May 2014. doi: 10.1103/PhysRevA.89.052704. URL <https://link.aps.org/doi/10.1103/PhysRevA.89.052704>.
- [103] Robin Côté. From classical mobility to hopping conductivity: Charge hopping in an ultracold gas. *Phys. Rev. Lett.*, 85:5316–5319, Dec 2000. doi: 10.1103/PhysRevLett.85.5316. URL <https://link.aps.org/doi/10.1103/PhysRevLett.85.5316>.

- [104] M. P. Langevin. Une formule fondamentale de theorie cinetique. *Ann. Chim. Phys.*, 8, 1905.
- [105] Erich Vogt and Gregory H. Wannier. Scattering of ions by polarization forces. *Phys. Rev.*, 95:1190–1198, Sep 1954. doi: 10.1103/PhysRev.95.1190. URL <https://link.aps.org/doi/10.1103/PhysRev.95.1190>.
- [106] Thomas F. O'Malley, Larry Spruch, and Leonard Rosenberg. Modification of Effective-Range Theory in the Presence of a Long-Range (r^{-4}) Potential. *Journal of Mathematical Physics*, 2(4):491–498, 12 2004. ISSN 0022-2488. doi: 10.1063/1.1703735. URL <https://doi.org/10.1063/1.1703735>.
- [107] Richard M. Spector. Exact solution of the schrödinger equation for inverse fourth-power potential. *Journal of Mathematical Physics*, 5(9):1185–1189, 1964. URL <https://doi.org/10.1063/1.1704224>.
- [108] D. Blume and Chris H. Greene. Fermi pseudopotential approximation: Two particles under external confinement. *Phys. Rev. A*, 65:043613, Apr 2002. doi: 10.1103/PhysRevA.65.043613. URL <https://link.aps.org/doi/10.1103/PhysRevA.65.043613>.
- [109] E. L. Bolda, E. Tiesinga, and P. S. Julienne. Effective-scattering-length model of ultracold atomic collisions and feshbach resonances in tight harmonic traps. *Phys. Rev. A*, 66:013403, Jul 2002. doi: 10.1103/PhysRevA.66.013403. URL <https://link.aps.org/doi/10.1103/PhysRevA.66.013403>.
- [110] S. Earnshaw. On the nature of the molecular forces which regulate the constitution of the luminiferous ether. *Trans. Camb. Phil. Soc.*, 7:97, Jan 1848.
- [111] F.M. Penning. Die glimmentladung bei niedrigem druck zwischen koaxialen zylindern in einem axialen magnetfeld. *Physica*, 3(9):873–894, 1936. ISSN 0031-8914. doi: [https://doi.org/10.1016/S0031-8914\(36\)80313-9](https://doi.org/10.1016/S0031-8914(36)80313-9). URL <https://www.sciencedirect.com/science/article/pii/S0031891436803139>.
- [112] Wolfgang Paul. Electromagnetic traps for charged and neutral particles. *Rev. Mod. Phys.*, 62:531–540, Jul 1990. doi: 10.1103/RevModPhys.62.531. URL <https://link.aps.org/doi/10.1103/RevModPhys.62.531>.
- [113] N.W. McLachlan. *Theory and Application of Mathieu Functions*. Clarendon Press, 1947. URL <https://books.google.de/books?id=pCXEvwEACAAJ>.
- [114] Alejandro Bermudez, Philipp Schindler, Thomas Monz, Rainer Blatt, and Markus Müller. Micromotion-enabled improvement of quantum logic gates with trapped ions. *New Journal of Physics*, 19(11):113038, nov 2017. doi: 10.1088/1367-2630/aa86eb. URL <https://dx.doi.org/10.1088/1367-2630/aa86eb>.
- [115] H. J. Carmichael. *Statistical methods in quantum optics. 1*. Texts and Monographs in Physics. Springer-Verlag, Berlin, 1999. ISBN 3-540-54882-3. doi: 10.1007/978-3-662-03875-8. URL <https://doi.org/10.1007/978-3-662-03875-8>. Master equations and Fokker-Planck equations.

- [116] H.P. Breuer and F. Petruccione. *The Theory of Open Quantum Systems*. OUP Oxford, 2007. ISBN 9780199213900. URL <https://books.google.de/books?id=DkcJPwAACAAJ>.
- [117] E. M. Lifshitz and L. P. Pitaevskiĭ. *Course of theoretical physics [“Landau-Lifshits”]. Vol. 10*. Pergamon International Library of Science, Technology, Engineering and Social Studies. Pergamon Press, Oxford-Elmsford, N.Y., 1981. ISBN 0-08-020641-7; 0-08-026480-8. Translated from the Russian by J. B. Sykes and R. N. Franklin.
- [118] Gerald D. Mahan. *Many-Particle Physics*. Physics of Solids and Liquids. Springer New York, NY, 2000. ISBN 978-0-306-46338-9. doi: 10.1007/978-1-4757-5714-9.
- [119] Steffen Patrick Rath and Richard Schmidt. Field-theoretical study of the bose polaron. *Phys. Rev. A*, 88:053632, Nov 2013. doi: 10.1103/PhysRevA.88.053632. URL <https://link.aps.org/doi/10.1103/PhysRevA.88.053632>.
- [120] R. Schmidt, J. D. Whalen, R. Ding, F. Camargo, G. Woehl, S. Yoshida, J. Burgdörfer, F. B. Dunning, E. Demler, H. R. Sadeghpour, and T. C. Killian. Theory of excitation of rydberg polarons in an atomic quantum gas. *Phys. Rev. A*, 97:022707, Feb 2018. doi: 10.1103/PhysRevA.97.022707. URL <https://link.aps.org/doi/10.1103/PhysRevA.97.022707>.
- [121] T.S Evans and D.A Steer. Wick’s theorem at finite temperature. *Nuclear Physics B*, 474(2):481–496, 1996. ISSN 0550-3213. doi: [https://doi.org/10.1016/0550-3213\(96\)00286-6](https://doi.org/10.1016/0550-3213(96)00286-6). URL <https://www.sciencedirect.com/science/article/pii/0550321396002866>.
- [122] J. Joger, H. Fürst, N. Ewald, T. Feldker, M. Tomza, and R. Gerritsma. Observation of collisions between cold li atoms and yb^+ ions. *Phys. Rev. A*, 96:030703, Sep 2017. doi: 10.1103/PhysRevA.96.030703. URL <https://link.aps.org/doi/10.1103/PhysRevA.96.030703>.
- [123] Tobias Kroker, Mario Großmann, Klaus Sengstock, Markus Drescher, Philipp Wessels-Staarmann, and Juliette Simonet. Ultrafast electron cooling in an expanding ultracold plasma. *Nature Communications*, 12(1):596, 2021. doi: 10.1038/s41467-020-20815-8. URL <https://doi.org/10.1038/s41467-020-20815-8>.
- [124] Kurt Jacobs and Daniel A. Steck. A straightforward introduction to continuous quantum measurement. *Contemporary Physics*, 47(5):279–303, 2006. doi: 10.1080/00107510601101934. URL <https://doi.org/10.1080/00107510601101934>.
- [125] Mark T. Mitchison, Thomás Fogarty, Giacomo Guarnieri, Steve Campbell, Thomas Busch, and John Goold. In situ thermometry of a cold fermi gas via dephasing impurities. *Phys. Rev. Lett.*, 125:080402, Aug 2020. doi: 10.1103/PhysRevLett.125.080402. URL <https://link.aps.org/doi/10.1103/PhysRevLett.125.080402>.
- [126] D. A. Abanin and L. S. Levitov. Fermi-edge resonance and tunneling in nonequilibrium electron gas. *Phys. Rev. Lett.*, 94:186803, May 2005. doi: 10.1103/PhysRevLett.94.186803. URL <https://link.aps.org/doi/10.1103/PhysRevLett.94.186803>.

- [127] N. d'Ambrumenil and B. Muzykantskii. Fermi gas response to time-dependent perturbations. *Phys. Rev. B*, 71:045326, Jan 2005. doi: 10.1103/PhysRevB.71.045326. URL <https://link.aps.org/doi/10.1103/PhysRevB.71.045326>.
- [128] Philippe Réfrégier. *Noise Theory and Application to Physics: From Fluctuations to Information*. Advanced Texts in Physics. Springer New York, NY, 2012. doi: <https://doi.org/10.1007/978-0-387-22526-5>. URL <https://link.springer.com/book/10.1007/978-0-387-22526-5>.
- [129] Matteo G. A. Paris. Quantum estimation for quantum technology. *International Journal of Quantum Information*, 07(supp01):125–137, 2009. doi: 10.1142/S0219749909004839. URL <https://doi.org/10.1142/S0219749909004839>.
- [130] Géza Tóth and Iagoba Apellaniz. Quantum metrology from a quantum information science perspective. *Journal of Physics A: Mathematical and Theoretical*, 47(42):424006, oct 2014. doi: 10.1088/1751-8113/47/42/424006. URL <https://dx.doi.org/10.1088/1751-8113/47/42/424006>.
- [131] Tomasz Wasak, Augusto Smerzi, Luca Pezzé, and Jan Chwedeńczuk. Optimal measurements in phase estimation: simple examples. *Quantum Information Processing*, 15(5):2231–2252, 2016. doi: 10.1007/s11128-016-1248-5. URL <https://doi.org/10.1007/s11128-016-1248-5>.
- [132] Mohammad Mehboudi, Anna Sanpera, and Luis A Correa. Thermometry in the quantum regime: recent theoretical progress. *Journal of Physics A: Mathematical and Theoretical*, 52(30):303001, jul 2019. doi: 10.1088/1751-8121/ab2828. URL <https://dx.doi.org/10.1088/1751-8121/ab2828>.
- [133] Samuel L. Braunstein and Carlton M. Caves. Statistical distance and the geometry of quantum states. *Phys. Rev. Lett.*, 72:3439–3443, May 1994. doi: 10.1103/PhysRevLett.72.3439. URL <https://link.aps.org/doi/10.1103/PhysRevLett.72.3439>.
- [134] Tomasz Wasak, Krzysztof Jachymski, Tommaso Calarco, and Antonio Negretti. Magnetic-field gradiometer based on ultracold collisions. *Phys. Rev. A*, 97:052701, May 2018. doi: 10.1103/PhysRevA.97.052701. URL <https://link.aps.org/doi/10.1103/PhysRevA.97.052701>.
- [135] A. J. Daley, P. O. Fedichev, and P. Zoller. Single-atom cooling by superfluid immersion: A nondestructive method for qubits. *Phys. Rev. A*, 69:022306, Feb 2004. doi: 10.1103/PhysRevA.69.022306. URL <https://link.aps.org/doi/10.1103/PhysRevA.69.022306>.
- [136] K Knakkergaard Nielsen, L A Peña Ardila, G M Bruun, and T Pohl. Critical slowdown of non-equilibrium polaron dynamics. *New Journal of Physics*, 21(4):043014, apr 2019. doi: 10.1088/1367-2630/ab0a81. URL <https://dx.doi.org/10.1088/1367-2630/ab0a81>.

- [137] Frederik Nathan and Mark S. Rudner. Universal lindblad equation for open quantum systems. *Phys. Rev. B*, 102:115109, Sep 2020. doi: 10.1103/PhysRevB.102.115109. URL <https://link.aps.org/doi/10.1103/PhysRevB.102.115109>.
- [138] H A Fürst, N V Ewald, T Secker, J Joger, T Feldker, and R Gerritsma. Prospects of reaching the quantum regime in li-yb+ mixtures. *Journal of Physics B: Atomic, Molecular and Optical Physics*, 51(19):195001, sep 2018. doi: 10.1088/1361-6455/aadd7d. URL <https://dx.doi.org/10.1088/1361-6455/aadd7d>.
- [139] Artjom Krüchow, Amir Mohammadi, Arne Härter, Johannes Hecker Denschlag, Jesús Pérez-Ríos, and Chris H. Greene. Energy scaling of cold atom-atom-ion three-body recombination. *Phys. Rev. Lett.*, 116:193201, May 2016. doi: 10.1103/PhysRevLett.116.193201. URL <https://link.aps.org/doi/10.1103/PhysRevLett.116.193201>.
- [140] Sourav Dutta, Rahul Sawant, and S. A. Rangwala. Collisional cooling of light ions by cotrapped heavy atoms. *Phys. Rev. Lett.*, 118:113401, Mar 2017. doi: 10.1103/PhysRevLett.118.113401. URL <https://link.aps.org/doi/10.1103/PhysRevLett.118.113401>.
- [141] Philipp Wessels, Bernhard Ruff, Tobias Kroker, Andrey K. Kazansky, Nikolay M. Kabachnik, Klaus Sengstock, Markus Drescher, and Juliette Simonet. Absolute strong-field ionization probabilities of ultracold rubidium atoms. *Communications Physics*, 1(1):32, 2018. doi: 10.1038/s42005-018-0032-5. URL <https://doi.org/10.1038/s42005-018-0032-5>.
- [142] Lê Huy Nguyễn, Amir Kalev, Murray D. Barrett, and Berthold-Georg Englert. Micromotion in trapped atom-ion systems. *Phys. Rev. A*, 85:052718, May 2012. doi: 10.1103/PhysRevA.85.052718. URL <https://link.aps.org/doi/10.1103/PhysRevA.85.052718>.
- [143] J. Joger, A. Negretti, and R. Gerritsma. Quantum dynamics of an atomic double-well system interacting with a trapped ion. *Phys. Rev. A*, 89:063621, Jun 2014. doi: 10.1103/PhysRevA.89.063621. URL <https://link.aps.org/doi/10.1103/PhysRevA.89.063621>.
- [144] Vladimir S. Melezhik, Zbigniew Idziaszek, and Antonio Negretti. Impact of ion motion on atom-ion confinement-induced resonances in hybrid traps. *Phys. Rev. A*, 100:063406, Dec 2019. doi: 10.1103/PhysRevA.100.063406. URL <https://link.aps.org/doi/10.1103/PhysRevA.100.063406>.
- [145] Vladimir S. Melezhik. Improving efficiency of sympathetic cooling in atom-ion and atom-atom confined collisions. *Phys. Rev. A*, 103:053109, May 2021. doi: 10.1103/PhysRevA.103.053109. URL <https://link.aps.org/doi/10.1103/PhysRevA.103.053109>.
- [146] P. W. Anderson. Infrared catastrophe in fermi gases with local scattering potentials. *Phys. Rev. Lett.*, 18:1049–1051, Jun 1967. doi: 10.1103/PhysRevLett.18.1049. URL <https://link.aps.org/doi/10.1103/PhysRevLett.18.1049>.

- [147] Michael Knap, Aditya Shashi, Yusuke Nishida, Adilet Imambekov, Dmitry A. Abanin, and Eugene Demler. Time-dependent impurity in ultracold fermions: Orthogonality catastrophe and beyond. *Phys. Rev. X*, 2:041020, Dec 2012. doi: 10.1103/PhysRevX.2.041020. URL <https://link.aps.org/doi/10.1103/PhysRevX.2.041020>.
- [148] Jozef T Devreese and Alexandre S Alexandrov. Fröhlich polaron and bipolaron: recent developments. *Reports on Progress in Physics*, 72(6):066501, may 2009. doi: 10.1088/0034-4885/72/6/066501. URL <https://dx.doi.org/10.1088/0034-4885/72/6/066501>.
- [149] Marco Koschorreck, Daniel Pertot, Enrico Vogt, Bernd Fröhlich, Michael Feld, and Michael Köhl. Attractive and repulsive fermi polarons in two dimensions. *Nature*, 485(7400):619–622, 2012. doi: 10.1038/nature11151. URL <https://doi.org/10.1038/nature11151>.
- [150] Marko Cetina, Michael Jag, Rianne S. Lous, Isabella Fritsche, Jook T. M. Walraven, Rudolf Grimm, Jesper Levinsen, Meera M. Parish, Richard Schmidt, Michael Knap, and Eugene Demler. Ultrafast many-body interferometry of impurities coupled to a fermi sea. *Science*, 354(6308):96–99, 2016. doi: 10.1126/science.aaf5134. URL <https://www.science.org/doi/abs/10.1126/science.aaf5134>.
- [151] F. Scazza, G. Valtolina, P. Massignan, A. Recati, A. Amico, A. Burchianti, C. Fort, M. Inguscio, M. Zaccanti, and G. Roati. Repulsive fermi polarons in a resonant mixture of ultracold ${}^6\text{Li}$ atoms. *Phys. Rev. Lett.*, 118:083602, Feb 2017. doi: 10.1103/PhysRevLett.118.083602. URL <https://link.aps.org/doi/10.1103/PhysRevLett.118.083602>.
- [152] Haydn S. Adlong, Weizhe Edward Liu, Francesco Scazza, Matteo Zaccanti, Nelson Darkwah Oppong, Simon Fölling, Meera M. Parish, and Jesper Levinsen. Quasi-particle lifetime of the repulsive fermi polaron. *Phys. Rev. Lett.*, 125:133401, Sep 2020. doi: 10.1103/PhysRevLett.125.133401. URL <https://link.aps.org/doi/10.1103/PhysRevLett.125.133401>.
- [153] Corinna Kollath, Michael Köhl, and Thierry Giamarchi. Scanning tunneling microscopy for ultracold atoms. *Phys. Rev. A*, 76:063602, Dec 2007. doi: 10.1103/PhysRevA.76.063602. URL <https://link.aps.org/doi/10.1103/PhysRevA.76.063602>.
- [154] Y. Sherkunov, B. Muzykantskii, N. d’Ambrumenil, and B. D. Simons. Probing ultracold fermi atoms with a single ion. *Phys. Rev. A*, 79:023604, Feb 2009. doi: 10.1103/PhysRevA.79.023604. URL <https://link.aps.org/doi/10.1103/PhysRevA.79.023604>.
- [155] Rianne S. Lous, Isabella Fritsche, Michael Jag, Bo Huang, and Rudolf Grimm. Thermometry of a deeply degenerate fermi gas with a bose-einstein condensate. *Phys. Rev. A*, 95:053627, May 2017. doi: 10.1103/PhysRevA.95.053627. URL <https://link.aps.org/doi/10.1103/PhysRevA.95.053627>.

- [156] Richard Schmidt, Michael Knap, Dmitri A Ivanov, Jih-Shih You, Marko Cetina, and Eugene Demler. Universal many-body response of heavy impurities coupled to a fermi sea: a review of recent progress. *Reports on Progress in Physics*, 81(2): 024401, jan 2018. doi: 10.1088/1361-6633/aa9593. URL <https://dx.doi.org/10.1088/1361-6633/aa9593>.
- [157] L. Ratschbacher, C. Sias, L. Carcagni, J. M. Silver, C. Zipkes, and M. Köhl. Decoherence of a single-ion qubit immersed in a spin-polarized atomic bath. *Phys. Rev. Lett.*, 110:160402, Apr 2013. doi: 10.1103/PhysRevLett.110.160402. URL <https://link.aps.org/doi/10.1103/PhysRevLett.110.160402>.
- [158] Jesús Pérez-Ríos and Chris H. Greene. Universal temperature dependence of the ion-neutral-neutral three-body recombination rate. *Phys. Rev. A*, 98:062707, Dec 2018. doi: 10.1103/PhysRevA.98.062707. URL <https://link.aps.org/doi/10.1103/PhysRevA.98.062707>.
- [159] T. Schneider, B. Roth, H. Duncker, I. Ernsting, and S. Schiller. All-optical preparation of molecular ions in the rovibrational ground state. *Nature Physics*, 6(4):275–278, 2010. doi: 10.1038/nphys1605. URL <https://doi.org/10.1038/nphys1605>.
- [160] André Schirotzek, Cheng-Hsun Wu, Ariel Sommer, and Martin W. Zwierlein. Observation of fermi polarons in a tunable fermi liquid of ultracold atoms. *Phys. Rev. Lett.*, 102:230402, Jun 2009. doi: 10.1103/PhysRevLett.102.230402. URL <https://link.aps.org/doi/10.1103/PhysRevLett.102.230402>.
- [161] C. Kohstall, M. Zaccanti, M. Jag, A. Trenkwalder, P. Massignan, G. M. Bruun, F. Schreck, and R. Grimm. Metastability and coherence of repulsive polarons in a strongly interacting fermi mixture. *Nature*, 485(7400):615–618, 2012. doi: 10.1038/nature11065. URL <https://doi.org/10.1038/nature11065>.
- [162] Ming-Guang Hu, Michael J. Van de Graaff, Dhruv Kedar, John P. Corson, Eric A. Cornell, and Deborah S. Jin. Bose polarons in the strongly interacting regime. *Phys. Rev. Lett.*, 117:055301, Jul 2016. doi: 10.1103/PhysRevLett.117.055301. URL <https://link.aps.org/doi/10.1103/PhysRevLett.117.055301>.
- [163] Nils B. Jørgensen, Lars Wacker, Kristoffer T. Skalmstang, Meera M. Parish, Jesper Levinsen, Rasmus S. Christensen, Georg M. Bruun, and Jan J. Arlt. Observation of attractive and repulsive polarons in a bose-einstein condensate. *Phys. Rev. Lett.*, 117: 055302, Jul 2016. doi: 10.1103/PhysRevLett.117.055302. URL <https://link.aps.org/doi/10.1103/PhysRevLett.117.055302>.
- [164] Zoe Z. Yan, Yiqi Ni, Carsten Robens, and Martin W. Zwierlein. Bose polarons near quantum criticality. *Science*, 368(6487):190–194, 2020. doi: 10.1126/science.aax5850. URL <https://www.science.org/doi/abs/10.1126/science.aax5850>.
- [165] Jean Dalibard, Yvan Castin, and Klaus Mølmer. Wave-function approach to dissipative processes in quantum optics. *Phys. Rev. Lett.*, 68:580–583, Feb 1992. doi: 10.1103/PhysRevLett.68.580. URL <https://link.aps.org/doi/10.1103/PhysRevLett.68.580>.

-
- [166] Klaus Mølmer, Yvan Castin, and Jean Dalibard. Monte carlo wave-function method in quantum optics. *J. Opt. Soc. Am. B*, 10(3):524–538, Mar 1993. doi: 10.1364/JOSAB.10.000524. URL <https://opg.optica.org/josab/abstract.cfm?URI=josab-10-3-524>.
- [167] T. Secker, R. Gerritsma, A. W. Glaetzle, and A. Negretti. Controlled long-range interactions between rydberg atoms and ions. *Phys. Rev. A*, 94:013420, Jul 2016. doi: 10.1103/PhysRevA.94.013420. URL <https://link.aps.org/doi/10.1103/PhysRevA.94.013420>.
- [168] T. Secker, N. Ewald, J. Joger, H. FÜRST, T. Feldker, and R. Gerritsma. Trapped ions in rydberg-dressed atomic gases. *Phys. Rev. Lett.*, 118:263201, Jun 2017. doi: 10.1103/PhysRevLett.118.263201. URL <https://link.aps.org/doi/10.1103/PhysRevLett.118.263201>.

Eidesstattliche Versicherung / Declaration on oath

Hiermit versichere ich an Eides statt, die vorliegende Dissertationsschrift selbst verfasst und keine anderen als die angegebenen Hilfsmittel und Quellen benutzt zu haben.

Sofern im Zuge der Erstellung der vorliegenden Dissertationsschrift generative Künstliche Intelligenz (gKI) basierte elektronische Hilfsmittel verwendet wurden, versichere ich, dass meine eigene Leistung im Vordergrund stand und dass eine vollständige Dokumentation aller verwendeten Hilfsmittel gemäß der Guten wissenschaftlichen Praxis vorliegt. Ich trage die Verantwortung für eventuell durch die gKI generierte fehlerhafte oder verzerrte Inhalte, fehlerhafte Referenzen, Verstöße gegen das Datenschutz- und Urheberrecht oder Plagiate.

Hamburg, den 06.03.2024



Unterschrift der Doktorandin / des Doktoranden